The Development and Characterisation of Microelectrodes for Extreme Environments

Charlotte L. Brady

Degree of Doctor of Philosophy

The University of Edinburgh

2013

Declaration

I hereby declare that the work presented in this thesis is my own unless otherwise credited and that the work has not been submitted for any other degree or professional qualification.

Charlotte L. Brady

February 2013

Abstract

Microelectrodes have been found to be a valuable tool in a variety of analytical studies. Their advantages over macro-sized electrodes are well known, including their enhanced mass transport properties (due to their ubiquitous hemispherical diffusion) which lead to steady state responses without external convection. They also exhibit high signal-to-noise ratios (greater sensitivities), furthering their analytical application. Microelectrode arrays are analytical devices with multiple electrodes. There are suitable for practical sensing with all the benefits of microelectrodes but with greater currents, leading to greater ease of measurement.

To produce a reliable electroanalytical device the microelectrode response must be reproducible, a fundamental property based on the quality control of their production. Square microelectrode and array fabrication techniques have been developed for this purpose. This research discusses the fabrication and development of closely spaced arrays of square microelectrodes. Simulated and measured responses are compared and used to characterize electrode and array responses by cyclic voltammetry, electrical impedance spectroscopy and current-time transients. Measurements on variably spaced arrays allow insight into overlap of hemispherical diffusion from individual electrodes and the subsequent effect including peak current output on the array device. By studying these devices key insights into the mass transport properties of single square microelectrodes and microelectrode arrays were gained.

This study also prepares and develops microelectrodes from materials appropriate for use in the extreme environments of molten salts and concentrated nitric acid solutions. These robust electrodes were developed for use in hydro- and pyro-chemical techniques for nuclear fuel

reprocessing. These results demonstrate the practical uses for microelectrode systems across a wide range of chemical systems and in extreme conditions.

Acknowledgements

There are many people I'd like to thank for the last few years. Firstly, my supervisor, Professor Andy Mount, without whom none of this would have happened. From within the group I'd like to thank Dr Helena Woodvine and Ilka Schmueser for use of their simulation data and contributions to developing the aqueous electrochemical analyses. Similarly I'd like to thank my second supervisor, Professor Colin Pulham, as well as Andrew Relf and Dr Damion Corrigan for ideas in the molten salt set-up. I hope they enjoy the use of the system in the future. I would also like to thank Dr John Henry for electrochemical advice and banter.

I would like to thank the engineers at the Scottish Microelectronics Centre: Dr Jonathan Terry, creator of my electrodes and all-round magician and Professor Anthony Walton. Without the two of them I would have had nothing to work with.

The people who kept me sane: Kate Fisher, Dr Adam Wilson, Dr Alexander Delf, Ilka again, Miriam Kaatz, Dr Louisa Reissig, Michael Doig, Dean Wood, David Blair, Dr Andrew Gray.

The man I blame for everything as he said I'd enjoy a PhD: Dr David Whiteman.

The people who have done more for me than I will ever be able to express: Dr John Thomson and Johnny Cockayne.

The one who keeps me going still: Richard Perry, without whom I would be lost.

Common Abbreviations

CV cyclic voltammogram
EIS Electrical Impedance Spectroscopy
SCE Saturate Calomel Electrode

Constants

R Gas constant (8.314 $JK^{-1}mol^{-1}$)
F Faraday constant (96485 $Cmol^{-1}$)

Symbols

E potential
i current
Z impedance
T temperature
c concentration
k rate constant
t time
A Area
D diffusion coefficient
r radius
n number of electrons
$\mathbf{R_{S}}$, $\mathbf{R_{CT}}$, $\mathbf{R_{NL}}$ solution, charge transfer, non-linear resistance
$\mathbf{C_{DL}}$ double layer capacitance
W Warburg impedance

Chapter 1: Introduction

1.1 Background

Microelectrodes are electrodes where at least one of the electrode's dimensions is on a micrometre scale. Invented between 1918 and 1919 by Ida Henrietta Hyde, the first female researcher at Harvard Medical School, they were first used as a tool for stimulating and recording electrical signals in cells[1]. This technique was developed further for monitoring different types of cells and tissues.[2]

However, it was not until 1981 that the electrochemical properties of microelectrodes were properly analysed[3]. Wightman described the additional benefits of microelectrodes, beyond the convenience of electrodes with dimensions of comparable scale to cells[4]. Interest in microelectrodes for electrochemical research increased dramatically from this point, and research particularly flourished in the area of reaction modelling at electrode/electrolyte interfaces[5].

With this heightened interest there were improvements in fabrication technologies. With these fabrication developments there was a broadening of relevant applications to microelectrode analysis. Microelectrodes can now be designed for specific purposes, as discussed below. With these varying designs however it is imperative that the electrodes can be fully characterised and their response understood.

1.2 Applications of Microelectrodes

The applications of microelectrodes have increased with both a greater understanding of the properties and the wider range of designs available, which have enabled applications in small molecule sensing[6], trace heavy metal analysis[7,8], oxygen content of oceanic waters[9] and neuronal sensors[10].

The majority of microelectrode applications have been in the fields of biological and medical sciences. Initially microelectrodes were used to study tissues and physiological chemical signalling.[2] This field of research has continued to grow, with work being done to probe neurons[11] and record neural activity over time[12]. Microelectrode probes have been used *in vitro* in tissues, such as the retina, to understand the neural networks[13] and *in vivo* to monitor electrical signals in rats.[14]

Biologically essential chemicals such as glucose, glutamate and lactose have been sensed using microelectrodes by modifying the electrode surfaces with enzymes selective to the small molecule of interest.[15] These molecules are essential for brain chemistry and fluctuations in their concentrations can indicate serious medical consequences. Microelectrodes have been designed and optimised to be minimally invasive in the detection of fluctuations in the oxygen pressure in living tissues.[16] As a non-invasive diagnostic technique microelectrodes have been used to monitor concentrations in secreted bodily fluids such as sweat.[17] This takes advantage of the fact that microelectrodes need only a small volume of sample for analysis.

Detection of biological structures, such as cells, with microelectrodes has been documented. Dielectrophoresis is the separation of polarizable particles on application of a non-uniform electrical field. By changing the frequency of fields, selection of substances of interest can occur. This process has been used to detect differences in cell types[18] such as tumour cells from healthy cells due to differences in cell physiology.[19] Using electrical fields generated by microelectrodes such as interdigitated microelectrode arrays, the detection of the cell transport due to an electrical field can be analysed.

Microelectrode devices can be designed for particular applications and this gives great benefit, particularly in biology. The substrate the device is attached to can be modified to fit the purpose, such as using ceramic as an inflexible, insulating, substrate[20] for precise placement of microelectrodes, or indeed the opposite, using a flexible, stretchable substrate such as polydimethylsiloxane[21] to simulate tissue injuries through deformation. Implantable electrodes are required to be biocompatible and stable. The need for flexible substrates that do not compress nerves and minimize abrasions with movement can lead to substrates made from biocompatible polymers such as polyimide or liquid crystal polymer.[22] Such implantable biocompatible microelectrode devices can lead to some truly extraordinary applications, such as giving rats the ability to sense infrared wavelengths.[23]

Given that microelectrodes can be used to detect small concentrations it follows that this can be applied to areas other than biology. Indeed, a lot of work has been done in sensing environmental samples. The study of metals such as copper, cadmium, lead and zinc in natural waters using electrochemical techniques began in the 1970s using mercury electrodes.[24] The benefit of these techniques over non-electrochemical methods was that the samples could be analysed without pre-treatment. By using microelectrodes in these studies the amount of mercury required, selected as the electrode due to its wide reductive potential range and alloying capabilities, could be minimised, minimising the environmental hazard. In addition gel integrated microelectrodes (GIMEs) were developed that have mercury plated on iridium microelectrodes with an agarose gel layer on the surface.[25] The gel layer prevents organic substances from reaching the microelectrodes. Iridium has a low solubility in mercury, a metal known for making amalgams and was therefore an appropriate substrate.[26] Platinum has also been used as a substrate.[27] Bare gold microelectrodes have been used for mercury detection in freshwater samples[28] and for copper (II) ion detection from soil samples.[29]

The benefit of microelectrodes over macroelectrodes lies not only in reducing absolute mercury quantities, but in the increased sensitivities of microelectrodes. This is due to their enhanced diffusion profiles, discussed in Chapter 2 (Section 2.2). Some microelectrodes are fabricated using a wire set in glass, applicable to oxygen content and pH measurements.[9] However, the fabrication of most microelectrodes for environmental sensing is done through microlithographic methods as this allows for greater control over the final device.[30] After fabrication the microelectrodes can then be modified, such as plating mercury films onto the solid metal substrate.

Not only metal ions can be detected in aquatic environmental samples. Microelectrode devices can be modified to selectively detect other species in samples of interest. Biofilms formed by bacterial growth have been added to a microelectrode and the vitality of the bacteria used to measure the toxicity of their environment.[31] The oxygen reduction current was measured after subjecting the biofilm modified electrodes to samples and changes in current response due to bacterial death were used as a measure of the toxicity of the sample. Using microelectrodes modified with enzymes bound in conducting polymers the presence of pesticides was detected at a limit of $1\text{x}10^{-17}$ M.[32]

The importance of detecting small concentrations is not only relevant in environmental or biological science, but food science as well. Microelectrodes have been able to detect the presence of the Escherichia coli O157:H7 bacteria in food sources such as ground beef.[33] The properties of cylindrical microelectrodes set in glass have been used to detect vanillin, an artificial flavouring additive, in dehydrated pudding powder, using organic solvents to extract the species.[34] The herbicide paraquat, now banned in the EU, has been detected using microelectrodes in lemon and orange juices[35] and apple and potato samples.[36] Given the usefulness of microelectrodes for sensing heavy metals in environmental samples, they have also been applied to mineralised honey samples for the same purpose. Untreated honey samples require a water content of at least 20% for valid sensing. In addition to viscosity issues, the metal complexing leads to difficulties in testing in untreated honey samples.[37] Using a gold microelectrode with a surface modified using bismuth, lead ions were detected in wine samples.[38] Microelectrodes have also been used to study the changing conditions of samples. Camembert samples mature in 15-35 days and microelectrodes have been used to monitor the ripening process, from rind to core, through observation of the E_h/pH gradients.[39]

1.3 Microelectrode Design & Fabrication

Since the first microelectrode was invented device fabrication has developed along two fundamental production paths. One is based on the initial microelectrode fabrication, while the other has arisen from improved technological methods of microfabrication using photolithographic processing and masks.

The initial design of the microelectrode consisted of a glass pipette encapsulating a wire that was drawn out, stretching the wire and lowering the surface area of the tip. This is still the basis for many microelectrode devices that are made today. The tip of the wire that acts as the electrode is polished to the required area and shape. The geometry of these microelectrodes is usually a planar disc however hemispheres, cones and rings have all been developed from this basic principle.[40] A selection of the various possible geometries is shown in Figure 1-1.

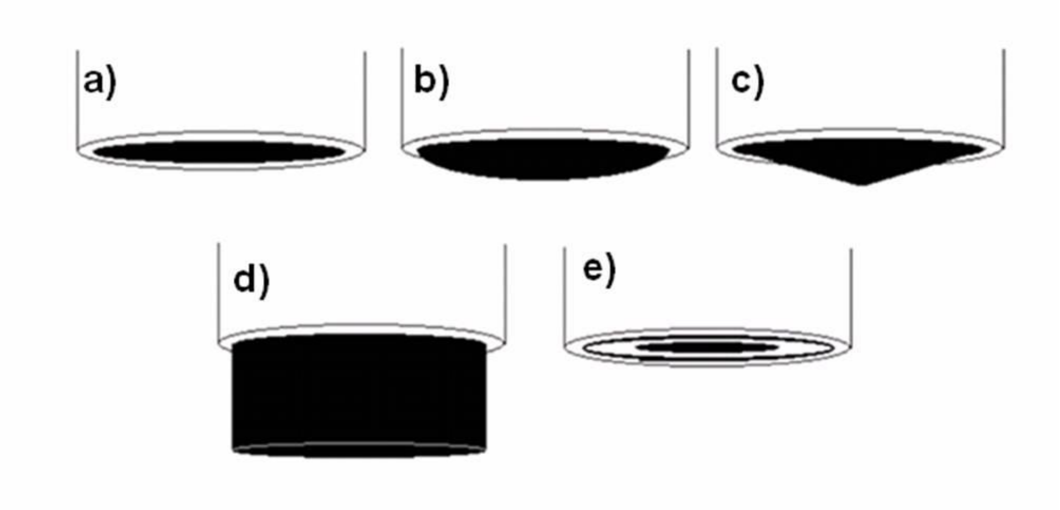

Figure 1-1: Various electrode geometries based on the production method of a wire encapsulated in glass. Seen here: a) disc, b) hemisphere, c) cone, d) cylinder and e) ring-disc.

There are several methods of producing disc microelectrodes with this fabrication process. The easiest to produce are created by using a pipette puller which can control the final length and width of the stretched pipette. Alternatives include encapsulating a fine wire in glass.[3] This is done by placing a wire in a glass capillary that is sealed at one end, and attached to a vacuum pump at the other.[40] The capillary is then heated until the glass melts around the wire, allowing the sides of the wire to be protected, with one end of the wire acting as the electro-active contact.

The sealed end is then polished so the metal is revealed. The polishing is continued until the electrode surface is uniform, as monitored by electron microscopy. The polishing of the surface typically produces a cone shaped electrode and the area and shape of the electrode is controlled by the polishing. Characterisation of the electrode is usually done through scanning electron microscopy and voltammetry[41]. The SEM technique allows the uniformity of the surface and the contact between the insulating glass and the wire sides to be monitored, as seen in Figure 1-2. Steady-state voltammetry allows the diffusion limited current to be determined using a redox species with known diffusion coefficient, which can be used to estimate the surface area of the microelectrode.

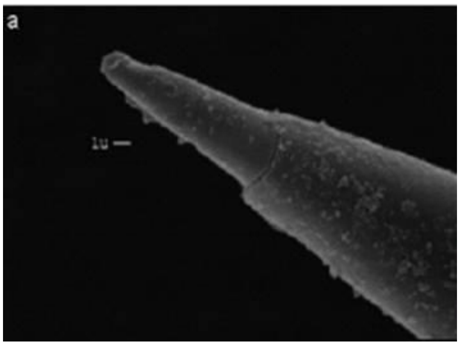

Figure 1-2: Tungsten microelectrode tip plated in platinum and characterised by SEM[42]

There are both advantages and disadvantages to this production technique. The foremost advantage is the ease of production. The process is relatively simple and fast. Most commercial disposable microelectrodes for biological and room temperature solution analysis are created through this fabrication process. The major disadvantage in this process is the lack of reproducibility in the production technique. Each metal wire encased in glass is drawn out separately and polished. Even with the use of electron microscopy to monitor the surface texture of the final product the electrodes will have different areas of metal as each electrode has to be polished individually, giving rise to variations.

The other disadvantage is for use in systems under extreme conditions. Due to the two materials used in the production, metal and glass, upon severe heating the different coefficients of thermal expansion mean that separation can occur. This would allow redox species access the sides of the metal wire changing the active surface area and transport characteristics of the electrode in an uncontrolled manner. Effectively the traditional design of the microelectrode would be inappropriate for the high temperature and corrosive conditions used in this thesis.

The other general method of microelectrode production is based on the patterning and etching of metal and insulator layers through photolithography[43,44,45]. Devices are typically produced on silicon wafers by the layering of conducting layers and using light-sensitive chemicals and masks to pattern the layer to the desired electrode specifications.

Electrode geometries, spacing and position are all defined by the mask. This means that by using the same mask, devices with electrodes of reproducible shape, size and placement can be made. In addition a mask can be designed to produce arrays of electrodes on the single silicon chip. Arrays of microelectrodes sum the currents of each of the active microelectrodes, allowing higher currents through the system whilst retaining the benefits of single microelectrodes. For sensing under extreme conditions the selection of appropriate materials can produce robust devices. The specifics of these fabrication methods will be discussed in Chapter 3 (Section 3.1).

The fabrication method can have a profound effect on the suitability of a manufactured device for certain applications. The shape, reproducibility of the signal and material properties are all critical considerations when designing a new microelectrode device.

1.4 The Nuclear Fuel Cycle

Nuclear fuel is an important contributor to power generation across the world. It is less environmentally damaging than the fossil fuels in common usage in terms of the amount of greenhouse gas emission (which is essentially all in plant construction and decommissioning) and is therefore considered a "low carbon" fuel. However, the long lifetimes of radioactive waste, the dangers of proliferation, and past accidents have led to unpopularity and there uncertainties in the industry about the future of nuclear power.[46] That said, many consider nuclear fuel as an important step in the progression from fossil fuels to renewable sources as global energy demand continues to increase.[47]

Induced fission is the reaction when a neutron collides with an atomic nucleus resulting in fragmentation and energy release. Along with the nuclear fragments, nuclear fission produces neutrons that can then go on to collide with more uranium atoms, allowing further reactions to occur. The fission reaction is shown schematically in Figure 1-3.

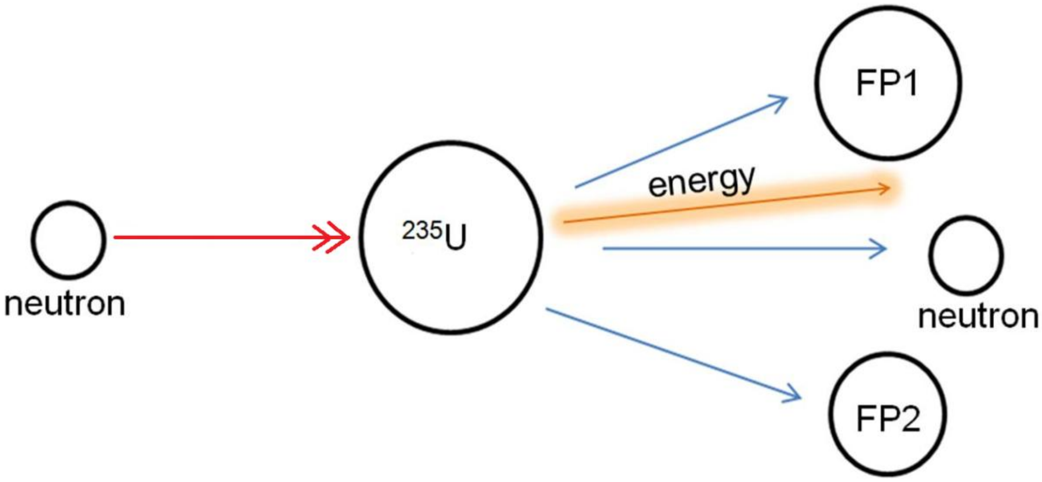

Figure 1-3: Nuclear fission of uranium-235. Bombarded with neutrons, the atom splits producing fission products, neutrons and energy. Particles not to scale.

In the nuclear fuel cycle mined uranium ore is processed to make uranium suitable as a fuel for fission. There are three naturally occurring isotopes of uranium: ^{234}U (a daughter nuclide of the ^{238}U decay series), ^{235}U and ^{238}U. Of these only ^{235}U is fissile, capable of undergoing fission when subject to thermal neutron irradiation. ^{238}U however, is the most abundant uranium isotope, with a natural abundance of 99.3%.[48]

The mined ore is milled to produce “yellowcake”, a mixture of concentrated uranium oxide species. The milling process includes leaching in strong acid or alkali, dissolving the uranium and separating ions such as radionuclides from the decay series. The yellowcake can then go on to be enriched and made suitable as nuclear fuel.

Enrichment of ^{235}U allows the proportion of the isotope to be increased in the uranium oxide mixture from the 0.7% found naturally up to 5%, for a typical light water reactor. The enrichment process uses UF_6 in gaseous form. The enrichment is performed through a process of gas centrifugation, allowing the complexes with different isotopes to be separated due to their difference in mass. The enriched uranium is removed while the remaining UF_6 is enriched further. Gas centrifugation is a large source of the by-product of depleted uranium.

At the time of writing the UK has sixteen working nuclear reactors, including one Magnox reactor that uses un-enriched uranium metal as a fuel. The other reactors, a single pressurised water reactor and fourteen advanced gas-cooled reactors, require enriched UO_2 fuel.[49]

After the fission has occurred what is left of the fuel rod is either disposed of or reprocessed.[50] Disposal requires storage of the radioactive waste for very long times, to allow the activity to drop to safe levels. Used fuel is ~96% uranium, ~1% plutonium and ~3% fission products. Due to the radioactivity the used fuel produces a lot of heat and so it is stored in water pools to allow this heat to dissipate. Fuel and fuel rods are considered high level waste. Waste allocated for disposal is conditioned for handling or transportation. The conditioning process involves conversion to a stable solid, lowering the volume. The waste is then vitrified before storage, to be eventually disposed of in a geologically appropriate underground site.

An alternative to disposing of all the used fuel is to separate the uranium and plutonium from the fission products and add them to the uranium oxide for enrichment, effectively recycling the used fuel. The uranium from the used fuel still contains some ^{235}U, at a proportion higher than found naturally. While plutonium is unsafe to separate and collect, it can be used as a mixed oxide fuel (MOX), combining the two metals as oxides. MOX has a reactivity similar to the UO_2 fuel used in light water reactors. MOX is used widely throughout Europe and Japan and can be used in conjunction with the UO_2 fuel after some modification to a plant.

1.4.1 Nuclear Fuel Reprocessing

After fission the remaining spent uranium oxide is present in a mixture of fission products.[51,52] These elements are in the mass number range from 72 (zinc) to 161 (terbium) with the maximum yields for strontium, Sr^{90}, and caesium, Cs^{137}. There are also neutron rich radioactive nucleotides within these fission products that can then decay into other species. Some plutonium is also produced[53]. The used fuel can either be disposed of or recyclable species can be separated from the remaining waste.

The bulk of global nuclear fuel reprocessing is performed through the Plutonium and Uranium Recovery by Extraction (PUREX) process, or variations. This technique uses solvent extraction for the separation of uranium and plutonium from the fission products. The fuel is dissolved in concentrated nitric acid, which acts as the aqueous phase. Uranium and plutonium preferentially dissolve into the organic phase, typically tri-n-butyl phosphate in kerosene, separating them from the fission products left in the aqueous stream. After separation the actinide nitrates are converted back to oxides and can then be used in MOX. The methods of fuel separation that use an aqueous phase are generally referred to as hydroprocessing.

An alternative process for fuel recovery is to use different media for the extraction of the fissile actinides: namely molten salts. As these non-aqueous solvents are at high temperatures the processes are termed pyroprocessing. In this context pyroprocessing involves the separation of fuel through electrolysis. The used fuel is dissolved in molten salt and the uranium ions in the melt are electrochemically collected at cathodes. Those cathodes with accumulated metal deposits can then go on to be used in reactors designed for metallic fuel, such as fast reactors.

There are advantages and disadvantages associated with the two separation methods. Pyroprocessing produces a lower volume of high level waste than hydroprocessing, which is a significant advantage.[54] The downside is the large energy use required for the high temperature method. There are also debates as to the benefits of accumulating plutonium in the waste (pyroprocessing) or the fuel (hydroprocessing). Pyroprocessing produces fuel eminently suitable for fast reactors.[54] These types of reactors are currently used in South Korea and across Asia[55] whereas the infrastructure for hydroprocessing is in place in most European[56] and American systems, making a change in technique less likely at the current time.

There are four broad descriptions of nuclear generators. The first generation is the original design for the nuclear reactor, such as the Magnox type. The second generation reactors were improvements to the first designs and were produced up to the 1990s. Generation III reactors again follow on from predecessors in improving the efficiency, technology and safety. In the United Kingdom after 2023 only one of the active reactors is still scheduled to be operational with the others having reached the end of their lifetimes.[49] Generation IV reactors are currently being designed and reviewed and will be implemented as national nuclear programmes develop. An additional concern for the Generation IV reactor designs that has been largely neglected in nuclear power history is the sustainability of the reactor and minimising the ecological consequences of the operation. It is an aim that the designs for the future plants will be efficient in terms of both future sustainability and energy production.

One of the proposed methods to minimise waste in the system is to have a closed fuel cycle where every aspect of the cycle results in complete reprocessing and minimal waste for storage. To that end, it is important to be able to monitor every part of the cycle. The need for adequate sensors is essential to allow issues to be spotted as early in the cycle as possible and prevent expensive shut downs. With the fabrication of robust microelectrode devices these fuel reprocessing systems, whether acid or molten salt based, could be analysed and monitored.

1.5 Molten Salt Systems

Molten salts are most frequently used as a liquid medium in metal refining from ores. The melt is an inorganic ionic salt, elevated to high temperatures so that it is in the electrically conductive liquid phase. This allows the salt to act as a solvent for any dissolved metal ion species. To lower working temperatures for reactions fused molten salts are often used. These are mixtures of different salts such as potassium chloride and lithium chloride that will lower the melting temperature significantly with respect to a single pure salt species. Eutectic molten salt is the term used to refer to the composition of ionic salts that produces the lowest melting temperature.

Electrochemistry in molten salts has been studied for decades. Understanding the media is important for understanding the kinetics of chemical reactions. Due to the high temperatures involved, and the need for vigorous exclusion of impurities, measuring the physical properties of molten salts is very difficult. The reliability of measured properties has increased with improving technology though simulations are still used.[57] The physical properties include the densities[58] and viscosities.[59] The most common eutectic mixtures are binary mixtures of alkali chlorides, such as lithium chloride and potassium chloride, though sodium chloride and caesium chloride species are also analysed.[60] Ternary mixtures are also used.[61] Chloride salts are more common than fluoride salts, which have higher melting points and are highly corrosive.[62]

The redox chemistry of metals, typically rare earth metals (REMs) – the lanthanides and actinides, have been studied in molten salts. They are sometimes used as analogues for radioactive elements,[63] though they have uses in their own right, primarily in magnetics, and the separation and purification of rare earths has been studied. This includes studying the Eu (III)/Eu(II) couple[64] and the Sm(III)/Sm(II) couple.[63] In addition reduction from the REM most stable oxidation state to the metal have been studied for electroplating.[65,66,67,68,69] These reactions have been studied using macroelectrodes of materials that are chemically inert to the molten salt environment such as glassy carbon, tungsten, or graphite or aluminium, an electrode material that can form alloys with the REMs.

Studies of nuclear materials have also been performed. These range from uranium[70,71,72] and plutonium[73] electrochemistry in eutectic salts in isolation from other redox active materials to mixtures of actinides[74,75] and rare earth metals[76,77,78,79] in the salt. Some genuine used fuel has also been studied.[80] The separation of the mixtures and reduction of the metals using electrochemical techniques on macroelectrodes have been the focus of these studies and analysis with microelectrodes has not been developed in this area.

1.6 References

---

[1] I. H. Hyde. Biol. Bull., 40 (3), 1921 p130-133 http://www.biolbull.org/cgi/reprint/40/3/130

[2] P.B. Bradley, M.D., J. Elkes, M.D. Electroencephalography and Clinical Neurophysiology. Volume 5, Issue 3, August 1953, Pages 451–456 http://dx.doi.org/10.1016/0013-4694(53)90091-1

[3] C.G. Zoski. Electroanalysis, 14 (15-16), 2002 p1041-1051 **DOI:**10.1002/1521-4109(200208)14:15/16<1041::AID-ELAN1041>3.0.CO;2-8

[4] R.M. Wightman. Analytical Chemistry. 53 (9), 1981 p1125A-1134A **DOI:**10.1021/ac00232a004

[5] J. Heinze. Angew. Chem. Int. Ed. Engl. 32, 1993 p1268-1288 **DOI:**10.1002/anie.199312681

[6] K.L. Ewalt, R.W. Haigis, R. Rooney, D. Ackley, M. Krihak. Analytical Biochemistry, 289, 2001 p162-172 **DOI:**10.1006/abio.2000.4927

[7] Pascal Salaün, Britta Planer-Friedrich, Constant M.G. van den Berg. Analytica Chimica Acta, 585, 2007 p312–322 doi:10.1016/j.aca.2006.12.048

[8] R.F. Domingos, M.F. Benedetti, J.P. Croué, J.P. Pinheiro. Analytica Chimica Acta 521, 2004 p77–86 doi:10.1016/j.aca.2004.05.027

[9] Clare E. Reimers, Chem Rev. 107, 2007 p590-600 **DOI:** 10.1021/cr050363n

---

[10] M. Bove, M. Grattarola, S. Martinoia, G. Verreschi. Bioelectrochemistry and Bioenergetics 38 (2), 1995 p255-265 **DOI:**10.1016/0302-4598(95)01848-9

[11] K.D Wise, A.M. Sodagar, Y. Yao, M.N Gulari, G.E. Perlin, K. Najafi. Proceedings of the IEEE. Vol. 96, No. 7, July 2008 p1184-1202 **DOI:** 10.1109/JPROC.2008.922564

[12] C. Xu, W. Lemon, C. Liu. Sensors and Actuators A, Volume 96, Issue 1, 31 January 2002, Pages 78-85 http://dx.doi.org/10.1016/S0924-4247(01)00766-X

[13] D. Gunning, C. Adams, W. Cunningham, K. Mathieson, V. O'Shea, K.M. Smith, E.J. Chichilnisky, A.M. Litke, M. Rahman. Nuclear Instruments and Methods in Physics Research Section A. Volume 546, Issues 1–2, 1 July 2005, Pages 148-153 http://dx.doi.org/10.1016/j.nima.2005.03.021

[14] K.C. Cheung, P. Renaud, H. Tanila, K. Djupsund. Biosensors and Bioelectronics. Volume 22, Issue 8, 15 March 2007, Pages 1783–1790 http://dx.doi.org/10.1016/j.bios.2006.08.035

[15] O.M. Schuvailo, O.O. Soldatkin, A. Lefebvre, R. Cespuglio, A.P. Soldatkin. Analytica Chimica Acta, Volumes 573–574, 28 July 2006, Pages 110-116 http://dx.doi.org/10.1016/j.aca.2006.03.034

[16] A Dittmar, S Mangin, C Ruban, W.H Newman, H.F Bowman, V Dupuis, G Delhomme, N.F Shram, R Cespuglio, N Jaffrezic-Renault, Ph

---

Roussel, D Barbier, C Martelet. Sensors and Actuators B: Chemical, Volume 44, Issues 1–3, October 1997, Pages 316-320 http://dx.doi.org/10.1016/S0925-4005(97)00224-4

[17] A.P.R. de Souza, A.S. Lima, M.O. Salles, A.N. Nascimento, M. Bertotti. Talanta. Volume 83, Issue 1, 15 November 2010, Pages 167–170 http://dx.doi.org/10.1016/j.talanta.2010.09.001

[18] M.K. Andrews, P.D. Harris. Electroanalysis Volume 10, Issue 16, pages 1112–1118, November 1998 **DOI:** 10.1002/(SICI)1521-4109(199811)10:16<1112::AID-ELAN1112>3.0.CO;2-Z

[19] Elisa Morganti ; Cristian Collini ; Romina Cunaccia ; Leandro Lorenzelli. Proc. SPIE 6592, Bioengineered and Bioinspired Systems III, 65920O (May 22, 2007) **DOI:**10.1117/12.724123

[20] J.J. Burmeister, G.A. Gerhardt. TrAC Trends in Analytical Chemistry, Volume 22, Issue 8, September 2003, Pages 498-502 http://dx.doi.org/10.1016/S0165-9936(03)00904-X

[21] Z. Yu, C. Tsay, S.P. Lacour, S. Wagner, B. Morrison. MRS Proceedings. Volume 926 (2006) http://dx.doi.org/10.1557/PROC-0926-CC07-02

[22] M.M.R. Howlader, T.E. Doyle, S. Mohtashami, J.R. Kish. Sensors and Actuators B. Volume 178, 1 March 2013, Pages 132–139 http://dx.doi.org/10.1016/j.snb.2012.12.051

[23] E.E. Thomson, R. Carra, M.A.L. Nicolelis. Nature Communications 4, Article number: 1482 **DOI:** 10.1038/ncomms2497

---

[24] M. Pesavento, G. Alberti, R. Biesuz. Analytica Chimica Acta, Volume 631, Issue 2, 12 January 2009, Pages 129-141 http://dx.doi.org/10.1016/j.aca.2008.10.046

[25] M-L. Tercier-Waeber, F. Confalonieri, M. Koudelka-Hep, J. Dessureault-Rompre´, F. Graziottin, J. Buffle. Electroanalysis 20, 2008, No. 3, 240– 258 **DOI:** 10.1002/elan.200704067

[26] C. Belmont, M.-L. Tercier, J. Buffle, G.C. Fiaccabrino, M. Koudelka-Hep. Analytica Chimica Acta, Volume 329, Issue 3, 20 August 1996, Pages 203-214 http://dx.doi.org/10.1016/0003-2670(96)00116-X

[27] Kwang-Seok Yun, Hong-Jeong Kim, Segyeong Joo, Juhyoun Kwak and Euisik Yoon Japanese Journal of Applied Physics 39 (2000) pp. 7159-7163 **DOI:** 10.1143/JJAP.39.7159

[28] Albrecht Uhlig, Uwe Schnakemberg and Rainer Hintsche Electroanalysis 1997, 9, No. 2 p125-129 **DOI:** 10.1002/elan.1140090207

[29] J. Orozco, C. Fernández-Sánchez, C. Jiménez-Jorquera Sensors 2010, 10, 475-490 **DOI:**10.3390/s100100475

[30] R. Feeney, S.P. Kounaves. Electroanalysis 12, 2000, No. 9, 677– 684 **DOI:** 10.1002/1521-4109(200005)12:9<677::AID-ELAN677>3.0.CO;2-4

[31] F.J. Del Campo, O. Ordeig, N. Vigués, N. Godino, J. Mas, F. X. Muñoz. Sensors and Actuators B: Chemical, Volume 126, Issue 2, 1 October 2007, Pages 515-521 http://dx.doi.org/10.1016/j.snb.2007.03.038

---

[32] Karen A. Law, Séamus P. J. Higson Biosensors and Bioelectronics 20 (2005) 1914–1924 http://dx.doi.org/10.1016/j.bios.2004.08.048

[33] M. Varshney, Y. Li, B. Srinivasan, S. Tung. Sensors and Actuators B: Chemical. Volume 128, Issue 1, 12 December 2007, Pages 99–107 http://dx.doi.org/10.1016/j.snb.2007.03.045

[34] L Agüı́, J.E López-Guzmán, A González-Cortés, P Yáñez-Sedeño, J.M Pingarrón. Analytica Chimica Acta. Volume 385, Issues 1–3, 5 April 1999, Pages 241–248 http://dx.doi.org/10.1016/S0003-2670(98)00643-6

[35] D. De Souza, S.A.S. Machado. Analytica Chimica Acta. Volume 546, Issue 1, 1 August 2005, Pages 85–91 http://dx.doi.org/10.1016/j.aca.2005.05.020

[36] D.De Souzaa, S.A.S. Machadoa, R.C. Pires. Talanta. Volume 69, Issue 5, 15 July 2006, Pages 1200–1207 http://dx.doi.org/10.1016/j.talanta.2005.12.045

[37] G. Sanna, M. I. Pilo, P. C. Piu, A. Tapparo , R. Seeber. Analytica Chimica Acta 415 (2000) 165–173 http://dx.doi.org/10.1016/S0003-2670(00)00864-3

[38] M. O. Salles, A. P. R. de Souza, J. Naozuka, P. V. de Oliveira, M. Bertotti. Electroanalysis 2009, 21, No. 12, 1439 – 1442 **DOI:** 10.1002/elan.200804575

[39] S. Abraham, R. Cachon, B. Colas, G. Feron, J. De Coninck. International Dairy Journal. Volume 17, Issue 8, August 2007, Pages 954–960 http://dx.doi.org/10.1016/j.idairyj.2006.12.010

---

[40] K. Štulík, C. Amatore, K. Holub, V. Mareček, W. Kutner. Pure Appl. Chem., 72(8), 2000 p1483–1492 **DOI**:10.1351/pac200072081483

[41] O. Köster, W. Schuhmann, H. Vogt, W. Mokwa. Sensors and Actuators B. 76, 2001 p573-581 **DOI**:10.1016/S0925-4005(01)00637-2

[42] A. Hermans, R. M. Wightman. Langmuir. 2006, 22, 10348-10353 **DOI**: 10.1021/la061209e

[43] A. Berduque, Y.H. Lanyon, V. Beni, G. Herzog, Y.E. Watson, K. Rodgers, F. Stam, J. Alderman, D.W.M. Arrigan. Talanta 71, 2007 p1022-1030 **DOI**:10.1016/j.talanta.2006.05.090

[44] G. Buß, M.J. Schöning, H. Lüth, J.W. Schultze. Electrochimica Acta 44, 1999 p3899-3910 doi:10.1016/S0013-4686(99)00097-3

[45] J. Orozco, G. Suárez, C. Fernández-Sánchez, C. McNeil, C. Jiménez-Jorquera. Electrochimica Acta. 53, 2007, p729–736 doi:10.1016/j.electacta.2007.07.049

[46] L. Mez. Energy Policy, Volume 48, September 2012, Pages 56-63 http://dx.doi.org/10.1016/j.enpol.2012.04.047

[47] Ferenc L. Toth, Hans-Holger Rogner. Energy Economics, Volume 28, Issue 1, January 2006, Pages 1-25 http://dx.doi.org/10.1016/j.eneco.2005.03.004

[48] Nature's Building Blocks, John Emsley, p 481.

---

[49] Nuclear Power in the United Kingdom http://www.world-nuclear.org/info/inf84.html accessed on 22/02/2013

[50] P. Högselius. Energy Policy, Volume 37, Issue 1, January 2009, Pages 254-263 http://dx.doi.org/10.1016/j.enpol.2008.09.043

[51] S. M. Jeong, S.B. Park, S.S. Hong, C.S. Seo, S.W. Park. Journal of Radioanalytical and Nuclear Chemistry, 268 (2), 2006 p349–356 **DOI:** 10.1007/s10967-006-0172-z

[52] H. Schmieder, U. Galla. Journal of Applied Electrochemistry. 30, 2000 p201-207 DOI: 10.1023/A:1003834914332

[53] W. Marshall. Nuclear Power Technology. Volume 1: Reactor Technology. 6th Edition. Oxford University Press.

[54] T. Inoue. Progress in Nuclear Energy, Volume 40, Issues 3–4, April–May 2002, Pages 547-554 http://dx.doi.org/10.1016/S0149-1970(02)00049-5

[55] K. Nagarajan, B.P. Reddy, S. Ghosh, G. Ravisankar, K.S. Mohandas, U.K. Mudali, K.V.G. Kutty, K.V.K. Viswanathan, C.A. Babu, P. Kalyanasundaram, P.R.V. Rao, B. Raj. Energy Procedia. Volume 7, 2011, Pages 431–436 http://dx.doi.org/10.1016/j.egypro.2011.06.057

[56] Dominique Warin. IOP Conf. Series: Materials Science and Engineering 9 (2010) 012063 doi:10.1088/1757-899X/9/1/012063

[57] N Galamba, C A Nieto de Castro, James F Ely. J. Chem. Phys. **122**, 224501 (2005) http://dx.doi.org/10.1063/1.1924706

---

[58] E. R. Van Artsdalen, I. S. Yaffe. J. Phys. Chem., 1955, 59 (2), pp 118–127 DOI: 10.1021/j150524a007

[59] V. M. B. Nunes, M. J. V. Lourenço, F. J. V. Santos, C. A. Nieto de Castro. J. Chem. Eng. Data, 2003, 48 (3), pp 446–450 **DOI:** 10.1021/je020160l

[60] H. Ito, Y. Hasegawa. J. Chem. Eng. Data, 2001, 46 (5), pp 1203–1205 **DOI:** 10.1021/je010092n

[61] M. Jafarian, M. G. Mahjani, F. Gobal, I. Danaee. Journal of Applied Electrochemistry. October 2006, Volume 36, Issue 10, pp 1169-1173 **DOI:** 10.1007/s10800-006-9192-1

[62] V. Constantin, A-M. Popescu, M. Olteanu. Journal of Rare Earths, Volume 28, Issue 3, June 2010, Pages 428-434 http://dx.doi.org/10.1016/S1002-0721(09)60127-7

[63] G. Cordoba, C. Caravaca. Journal of Electroanalytical Chemistry, Volume 572, Issue 1, 15 October 2004, Pages 145-151 http://dx.doi.org/10.1016/j.jelechem.2004.05.029

[64] S.A. Kuznetsov, M. Gaune-Escard. Electrochimica Acta, Volume 46, Issue 8, 31 January 2001, Pages 1101-1111 http://dx.doi.org/10.1016/S0013-4686(00)00708-8

[65] Y. Castrillejo, M.R. Bermejo, E. Barrado, A.M. Martínez, Electrochimica Acta, Volume 51, Issue 10, 1 February 2006, Pages 1941-1951 http://dx.doi.org/10.1016/j.electacta.2005.07.004

---

[66] P. Masset, C. Apostolidis, R.J.M. Konings, R. Malmbeck, J. Rebizant, J. Serp, J-P. Glatz. Journal of Electroanalytical Chemistry, Volume 603, Issue 2, 15 May 2007, Pages 166-174 http://dx.doi.org/10.1016/j.jelechem.2007.01.028

[67] M.R. Bermejo, J. Gómez, A.M. Martínez, E. Barrado, Y. Castrillejo. Electrochimica Acta, Volume 53, Issue 16, 30 June 2008, Pages 5106-5112 http://dx.doi.org/10.1016/j.electacta.2008.02.058

[68] Z. -Y. Qiao, S. Duan, D. Inman. Journal of Applied Electrochemistry. Volume 19, Issue 6, November 1989 p937-939 **DOI:** 10.1007/BF01007944

[69] M.R. Bermejo, J. Gómez, J. Medina, A.M. Martínez, Y. Castrillejo. Journal of Electroanalytical Chemistry, Volume 588, Issue 2, 15 March 2006, Pages 253-266 http://dx.doi.org/10.1016/j.jelechem.2005.12.031

[70] B Prabhakara Reddy, S Vandarkuzhali, T Subramanian, P Venkatesh. Electrochimica Acta, Volume 49, Issue 15, 30 June 2004, Pages 2471-2478 http://dx.doi.org/10.1016/j.electacta.2004.02.002

[71] P. Masset, D. Bottomley, R. Konings, R. Malmbeck, A. Rodrigues, J. Serp, J-P. Glatz. J. Electrochem. Soc. 2005 152(6): A1109-A1115; **DOI:**10.1149/1.1901083

[72] K. Serrano, P. Taxil. Journal of Applied Electrochemistry April 1999, Volume 29, Issue 4, pp 497-503 **DOI:** 10.1023/A:1003402029895

---

[73] G. Bourgès, D. Lambertin, S. Rochefort, S. Delpech, G. Picard. Journal of Alloys and Compounds, Volumes 444–445, 11 October 2007, Pages 404-409 http://dx.doi.org/10.1016/j.jallcom.2006.10.095

[74] Y. Sakamura, T. Hijikata, K. Kinoshita, T. Inoue, T.S. Storvick, C.L. Krueger, J.J. Roy, D.L. Grimmett, S.P. Fusselman, R.L. Gay. Journal of Alloys and Compounds, Volumes 271–273, 12 June 1998, Pages 592-596 http://dx.doi.org/10.1016/S0925-8388(98)00166-2

[75] O. Shirai, T. Iwai, Y. Suzuki, Y. Sakamura, H. Tanaka. Journal of Alloys and Compounds, Volumes 271–273, 12 June 1998, Pages 685-688 http://dx.doi.org/10.1016/S0925-8388(98)00187-X

[76] P. Masset, R.J.M. Konings, R. Malmbeck, J. Serp, J-P Glatz. Journal of Nuclear Materials, Volume 344, Issues 1–3, 1 September 2005, Pages 173-179 http://dx.doi.org/10.1016/j.jnucmat.2005.04.038

[77] S.A. Kuznetsov, M. Gaune-Escard. Journal of Nuclear Materials, Volume 389, Issue 1, 15 May 2009, Pages 108-114 http://dx.doi.org/10.1016/j.jnucmat.2009.01.015

[78] S.A. Kuznetsov, H. Hayashi, K. Minato, M. Gaune-Escard. Journal of Nuclear Materials, Volume 344, Issues 1–3, 1 September 2005, Pages 169-172 http://dx.doi.org/10.1016/j.jnucmat.2005.04.037

[79] S.A. Kuznetsov, H. Hayashi, K. Minato, M. Gaune-Escard. Electrochimica Acta, Volume 51, Issue 12, 25 February 2006, Pages 2463-2470 http://dx.doi.org/10.1016/j.electacta.2005.07.028

---

[80] M. Kurata, T. Inoue, J. Serp, M. Ougier, J-P Glatz. Journal of Nuclear Materials, Volume 328, Issues 2–3, 1 July 2004, Pages 97-102 http://dx.doi.org/10.1016/j.jnucmat.2004.03.013

Chapter 2: Theory

This chapter will briefly explain the electrochemical theory behind the analysis performed in this thesis.

2.1 Electrochemistry

2.1.1 Three Electrode System

The three electrode system allows for accurate analysis at a single electrode, denoted as the working electrode. A voltage is applied between the working and a reference electrode. For this the reference electrode needs to have a fixed potential. Since the reference electrode potential is constant this results in control of the working electrode potential and hence the Fermi level. The voltage is therefore the potential of the working electrode with respect to the reference electrode. This controls the electrode reaction, whose rate is measured by the current passing between the working electrode and a third electrode, denoted the counter electrode.

The reference electrode in all aqueous experiments throughout this thesis is a saturated calomel electrode, unless otherwise stated. The calomel reference electrode has the redox reaction:

$$Hg_2Cl_{2(s)} + 2e^- \rightleftarrows 2Hg_{(l)} + 2Cl^-_{(aq)}$$

Equation 2-1

By ensuring that large amounts of the three species, Hg_2Cl_2, Hg and Cl^- are present in the electrode the Fermi level of the reference electrode is fixed, which gives a fixed reference potential through the Nernst equation (Equation 2-2).

$$E = E^{\circ'} + \frac{RT}{nF}\ln\left[\frac{c_{ox}}{c_{\mathrm{Re}\,d}}\right]$$

Equation 2-2

Where E is the applied potential, R is the gas constant (8.314 $JK^{-1}mol^{-1}$), T is the temperature is Kelvin, n is the number of electrons in the reaction, F is the Faraday Constant (96485 $Cmol^{-1}$), and c is the concentration of species Ox or Red in the bulk solution. $E^{\circ\prime}$ is the formal potential of the reaction in question. It is related to the standard electrode potential of the reaction, E^{θ}, when the ratio of c_{ox}/c_{red} is unity, and takes into account the activity coefficients of species present. E^{θ} is the reaction potential under standard conditions. When the concentrations are very large E does not change.

A counter electrode supplies the current required by the working electrode. The counter electrode has a large area in comparison to the working electrode, as the current is proportional to area this helps ensure that the current is limited by the electrochemical reaction at the working electrode. The counter electrode is a platinum gauze in all aqueous experiments in this study.

2.2 Microelectrode Characteristics

Microelectrodes produce a characteristically different response compared to standard sized electrode, beyond that expected by a simple reduction in electrode area. The characteristics of a microelectrode compared to a macroelectrode are lower currents and higher current densities, lower capacitance, increased signal to noise and enhanced diffusion of electroactive substances to the electrode surface.

Current is related to electrode area, so it follows that the currents produced by a microelectrode will be much lower than those observed for a macroelectrode. Indeed most microelectrode currents are in the range of nano Amps. In addition the critical dimension for disc shaped microelectrodes is the radius. The current is directly proportional to the radius of the disc.[1] In macroelectrodes the current is proportional to the area (r^2 if the electrode is disc shaped).[2] This means that microelectrodes produce higher current densities, or current per area than macroelectrodes.

In every electrochemical system there is a solution resistance, which determines how the field is distributed and the effects of migration in the electrochemical cell. In aqueous solutions with background electrolyte the solution resistance can be considered negligible. In non-polar solvents the solution resistance can be appreciably bigger, which can significantly impede electrochemical investigations in these media. The solution resistance leads to an iR drop in the solution between the working electrode and reference electrode, which depends on both the current (i) passed through the cell and the resistance of the solution (R). The reduction in current as a function of the microelectrode's area decreases this iR drop. In addition, the higher current densities allow for enhanced ion transport which reduces the iR drop. The use of microelectrodes therefore allows more of the potential applied to perform electrochemical processes at the electrode surface as opposed to being distributed in the solution due to the iR drop in the system.

Capacitance is a property which describes the storage of electrical charge. At an electrode/electrolyte interface, when an electrode surface becomes charged ions of opposing charge align at the electrode surface, forming an ionic layer at the electrode/electrolyte interface. This electrical double layer acts as a capacitor. Once charged this allows the potential difference between the electrode and bulk solution to drop rapidly at the surface. This ensures that all of the applied potential is available for electron transfer (Faradaic) processes at the electrode surface. The charging current dies away with a time constant of $\tau = R_S C_{DL}$, where R_S is the solution resistance and C_{DL} is the capacitance of the double layer. However, during potential sweep voltammetry as the potential is always changing there is always charging (non-faradaic) current. If the concentration of redox active material is low, or fast scan rates are used, analysis of the faradaic process can then be difficult. To minimize the effect of the charging current it is necessary to reduce the capacitance.

This capacitance is related to the area of a microelectrode. Therefore a microelectrode will have a significantly lower capacitance compared to a macroelectrode due to its size. As the current is directly proportional to the radius of a disc microelectrode, as opposed to being proportional to the area of a macroelectrode, the signal to noise (Faradaic to non-Faradaic current) increases as r decreases.

This reduced capacitance means that both the charging current and the time required to charge the double layer are both reduced. This allows for increased signal-to-noise ratio and faster response from the electrodes making them more sensitive than macroelectrodes and more suitable for analysing reactions with fast electron transfer kinetics.

Mass transport is the term used to describe motion of a redox active substance from the bulk solution to the electrode surface for reaction due to diffusion, migration, and convection. Mass transport is one of two main factors affecting the rate of an electrochemical reaction with the other being the electron transfer rate at the solution-electrode interface. Diffusion occurs after any substance at the electrode-solution interface has reacted, and a concentration gradient is set up between the bulk solution and the electrode surface. In an electrode system transport of these molecules can be enhanced by stirring, increasing convection, though there is always some transport present due to natural convection. The mass transport rates to a microelectrode are very fast due to diffusion, comparable to that of a standard electrode rotating at a rate of thousands of rpm[3], which makes natural convection effects less important.

When material at an electrode is consumed the diffusion layer develops and increases as more material near the electrode is used. The thickness of the diffusion layer is proportional to the square root of time.[4] At a macroelectrode the current decays by $t^{-1/2}$ and eventually the thickness of the diffusion layer becomes large and the current drops towards zero. In practise, there is always some natural convection in the solution so the current will not reach zero. However, for a small electrode surface when a concentration gradient is established the thickness of the diffusion layer soon grows to a scale similar to the electrode. A hemispherical diffusion field then arises. This diffusion field is more efficient than linear diffusion at bringing reactive material to the electrode surface and steady state diffusion is established as evidenced by a time independent response in a cyclic voltammogram. This allows the mass transport effects of a redox reaction to be separated from the electron transfer effects and simplifies the analysis of reactions. These diffusion layer thickness and shapes can be seen figuratively in Figure 2-1.

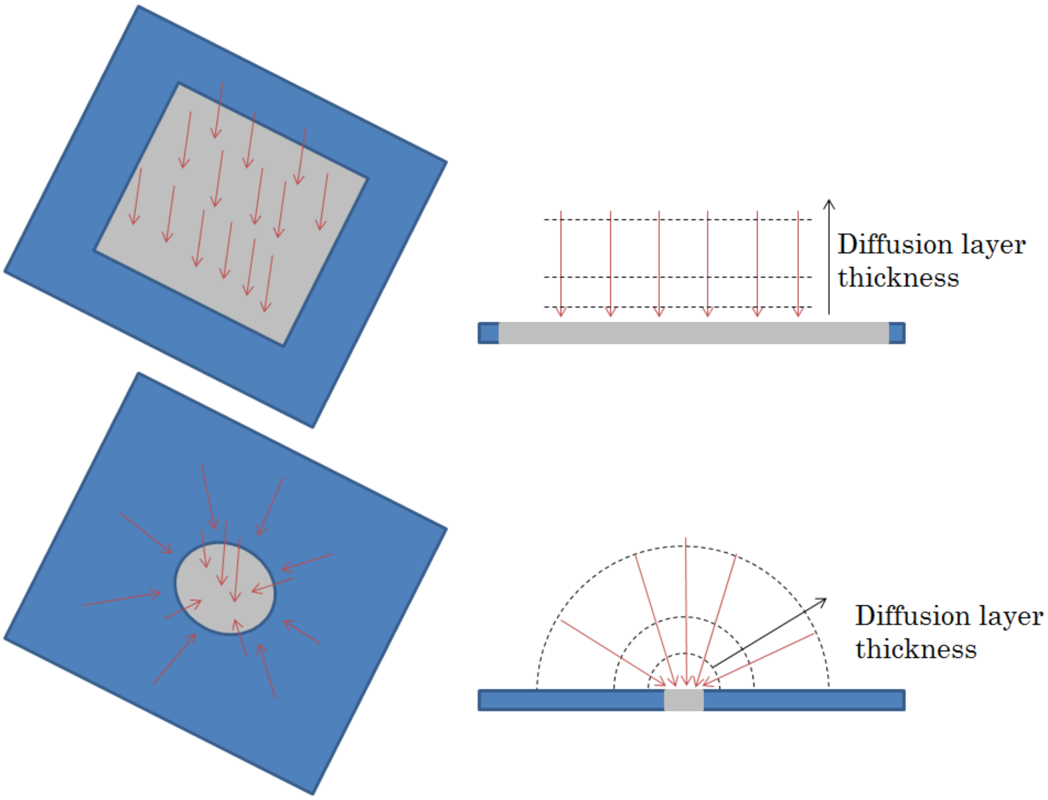

Figure 2-1: Diffusion layer growth and profiles at an electrode. As the diffusion layer grows (black lines) species diffuse (red arrows) travelling to an electrode surface (grey). In the top figure diffusion layer thickness is smaller than the electrode and species diffuse linearly. In the bottom figure the diffusion layers are of a similar scale to the electrode and so a hemispherical diffusion profile develops.

2.3 Electrochemical Techniques

2.3.1 Cyclic Voltammetry

In cyclic voltammetry the potential is swept at the working electrode from a fixed starting potential to a fixed upper limit before being swept backwards to a lower limit at a constant sweep rate, and the current response, i, is measured throughout. The voltages are selected to cause an electroactive species to undergo a redox reaction giving a diagnostic profile. A cyclic voltammogram is produced which is a plot of current versus potential.

Cyclic voltammetry on a macroelectrode has been studied and used for many years. It can provide valuable information about the potentials of reactions and the diffusion properties of chemical species. Taking a general one electron oxidation reaction of A oxidising to B (Equation 2-3) in solution, if the applied potential, E, is swept through the standard reaction potential, E^{θ}, the current response changes with E.

$$A \rightleftarrows B + e^-$$

Equation 2-3

Current is determined by the equation:

$$|i| = nFAc_A k_{ox}$$

Equation 2-4

Where, $|i|$ is the magnitude of current, A is the area of the electrode, and c_A is the concentration of A at the electrode surface. k_{ox} is the rate constant for the oxidation reaction. When E is much more negative than

E^{θ} then no current passes. As E approaches E^{θ} the current response is governed by k_{ox}, the rate of the oxidation which is calculated as:

$$k_{ox} = k^{\theta} \exp\left[\frac{\alpha_{ox} nF\left(E - E^{\theta}\right)}{RT}\right]$$

Equation 2-5

Where, k^{θ} is the standard rate constant for the electron transfer and α_{ox} is the transfer coefficient that describes the position of the transition state along the reaction co-ordinate between 0 and 1.[2]

As E is made more positive the current rises exponentially with E. The reaction rate is controlled by the rate of the charge transfer reaction at the electrode. As species A is oxidised, however more must diffuse to the electrode surface from solution before it can react, which becomes progressively harder as depletion occurs. As the potential is swept further beyond E^{θ} this diffusion layer grows into the bulk solution and the rate determining step of the reaction, that effectively limits the current response, is the diffusion to the electrode surface, described by the rate of mass transfer, k_{MT}. For a macroelectrode, current drops with time as the diffusion layer thickness grows. The two rate controlling aspects of the reaction, k_{MT} and k_{ox}, makes the well-known curved and peaked response of current, shown in Figure 2-2.

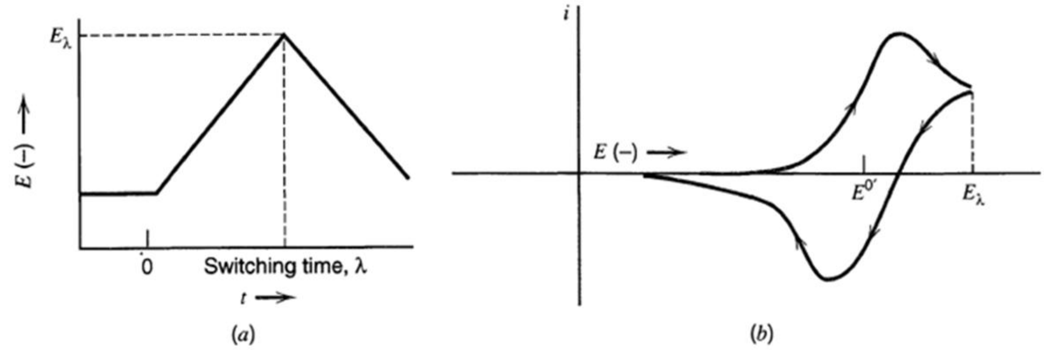

Figure 2-2: (a) Cyclic potential sweep. (b) Resulting cyclic voltammogram[5]

Cyclic voltammograms of microelectrodes have a characteristic shape that distinguishes them from macroelectrodes, as shown in Figure 2-3. Due to the enhanced hemispherical diffusion at a microelectrode, the species in the bulk of the solution is transported to the electrode surface much faster than in the case of a macroelectrode and mass transport is steady state. This means that the rate of diffusion of new material to the surface is time independent therefore k_{MT} is constant. There is no peak to the current response and the reaction becomes a wave-shape.

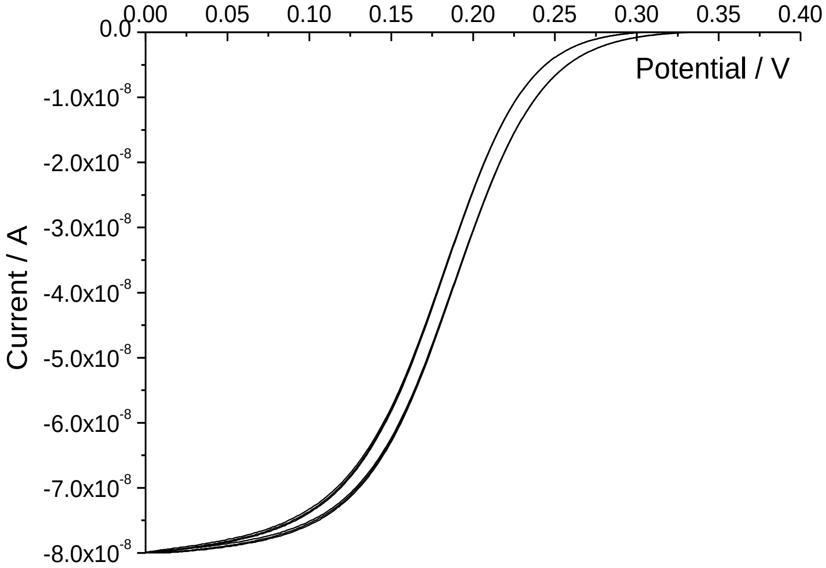

Figure 2-3: CV of a 50 µm platinum microelectrode in 50 mM ferricyanide solution versus a saturated calomel electrode showing the characteristic time independent response.

Experimentally the limiting current of a microelectrode is defined as the difference in height of an oxidation or a reduction wave on a cyclic voltammogram. The equation used for this calculation has also been adapted for various microelectrode shapes, such as hemispheres and rings.[1] The equation for calculating the limiting current of a disc microelectrode was derived by Oldham[6] using a disc shaped electrode[7] (Equation 2-6).

$$i_L = 4r_o nFDc_\infty$$

Equation 2-6

Where i_L is the limiting current, r_o is the radius of the electrode. D is the diffusion coefficient for the redox species in solution and c_∞ is the bulk concentration.

The electrodes produced for this study and characterised previously within the group are square shaped so the disc microelectrode equation needs to be modified to describe the observed limiting current. To that end the radius property, r_o, was replaced in the equation by l where l is the length of a side of a square electrode and using simulations, validated by experimentation, a numerical value, B, was introduced to the equation as a geometric factor.[8] For a square B=2.63. The final equation for the limiting current of a square microelectrode is shown in Equation 2-7.

$$i_L = BnFDlc_\infty$$

Equation 2-7

Metal deposition on a microelectrode has a typical shape associated with the voltammetry, shown in Figure 2-4[9]. Metal is deposited initially akin to the reduction wave seen above with limiting current. However metal ions will continue to reduce, depositing as long as potentials are cathodic. The electrode therefore increases in size as the metal deposited forms a new active surface on the electrode. This creates an increasing current response. Once the potential is swept forward beyond the E^{θ} of the reaction the anodic potential allows the deposited metal to be stripped off again in a sharp peak of positive current.

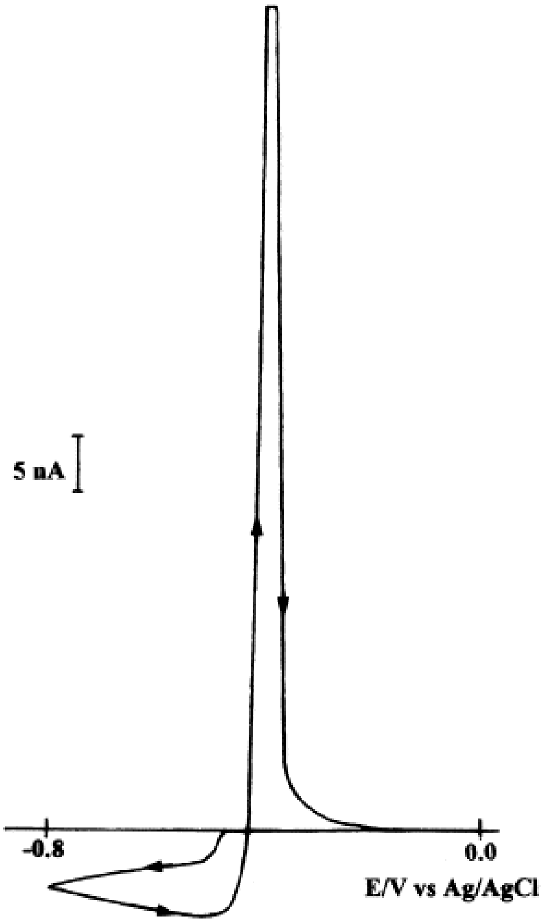

Figure 2-4: Typical cyclic voltammogram of metal deposition and stripping with hemispherical diffusion to the electrode.[9]

2.3.2 Electrical Impedance Spectroscopy

Electrochemical impedance spectroscopy is an analytical technique that allows the characterisation of an extensive range of phenomena at electrode surfaces, and can even allow separate analysis of simultaneous processes at a single electrode[10]. The term resistance (R) is used to describe the opposition to the flow of current in a conductor. Resistance is defined by Ohm's law as

$$R = \frac{E}{i}$$

Equation 2-8

However, resistance only describes this opposition if the current is direct. If an alternating current is present then a phase difference between the oscillating potential and the oscillating current produces an imaginary component to the response. The complex property of impedance must therefore be used to describe the opposition in terms of the resistance (real) and the reactance (imaginary).

An oscillating sinusoidal potential, E(t), induces an oscillating current, i(t). The impedance, Z, therefore can be described by Equation 2-9.

$$Z(f) = \frac{E(t)}{i(t)} = \frac{E_{amp}\sin(2\pi ft)}{i_{amp}\sin(2\pi ft + \theta)}$$

Equation 2-9

Where f is the frequency of the oscillation, E_{amp} is the maximum amplitude of the potential, i_{amp} is the maximum amplitude of the current and θ is the phase difference between the two sinusoidal waves.

Mathematically impedance can be described in terms of the expression below:

$$Z(f) = Z'\sin(2\pi ft) - Z''\cos(2\pi ft)$$

Equation 2-10

where Z’ is the real, in-phase, and –Z” is the imaginary, out-of-phase, component. This allows the impedance to be plotted as a vector using Z’ and –Z” as the (x,y) axes. This is known as a Nyquist plot, and is a common form of presenting impedance data graphically.

The impedance through a macroelectrode can be described by analysing the response in terms of an equivalent electrical circuit. An equivalent circuit is found from a model of the fundamental response and is used to understand the properties of the electrochemical system. Although circuits are derived fundamentally the features give insight into physical processes. A simple capacitor is the simplest impedance response as is shown in Figure 2-5.

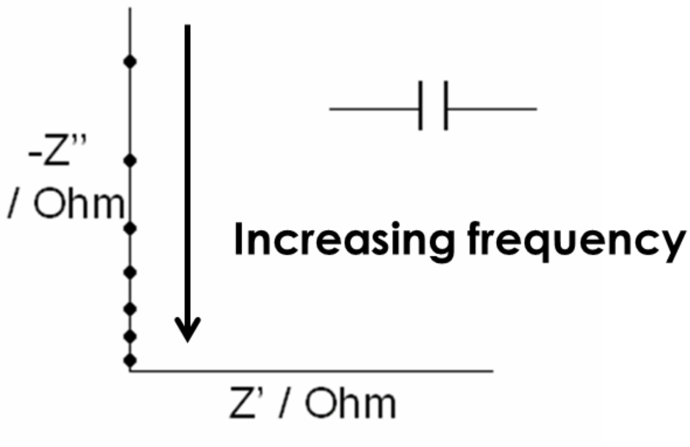

Figure 2-5: The impedance plot of a capacitor

A capacitor in an electrical circuit model is considered to model the double layer of ions that forms at the surface of an electrode. If a capacitor is put in series with a resistor then the response is shifted along the Z' axis as the total impedance is the sum of both resistor and capacitor properties, shown in Figure 2-6. Resistors in the circuit can model various properties of the electrochemical cell, such as the electrolyte resistance and a charge transfer resistance.

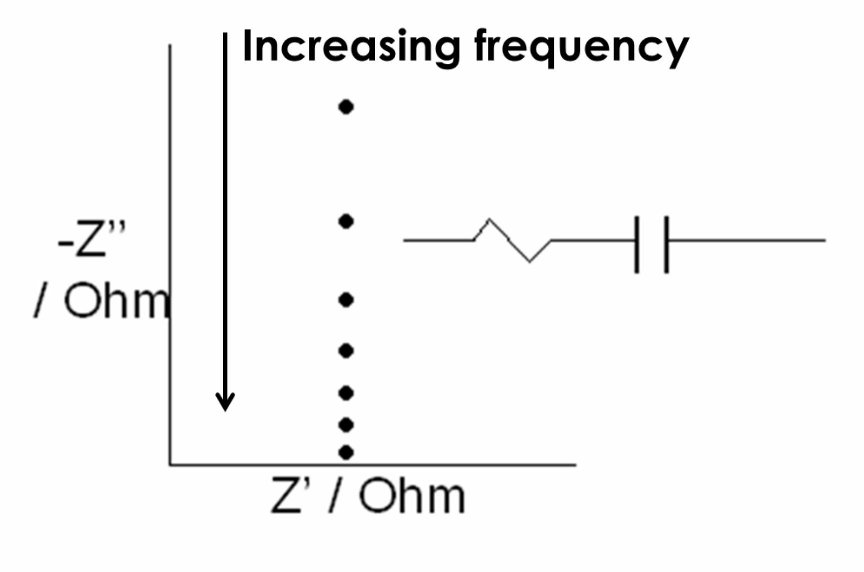

Figure 2-6: The impedance plot of a capacitor and resistor in series

If instead a resistor is put in parallel to the capacitor then there are two possible paths along the circuit. As the flow of current will always follow the path of least resistance, the path taken depends on the frequency. At high frequencies the path containing the capacitor is the favourable path but as the frequency decreases the capacitor begins to charge, when the capacitor is fully charged it will block the flow of current effectively presenting an extremely high resistance. Once the capacitor is charged the current finds the resistor to be the easier path to flow through. At low frequencies the capacitor is charged and so the resistor is favoured. In terms of the real system, the double layer needs to charge before electron transfer at the electrode can occur, so this is a circuit element typically found for charge transfer resistances.

A real circuit is more complicated than just one resistor and one capacitor. When there is an initial electrolyte resistance the current must flow through this before the charge transfer or double layer charging, this will affect the plot by shifting it by R_1 from the zero point on the Z'-axis, as shown in Figure 2-7. Before the double layer charges the voltage is applied between the working electrode and reference electrode across the solution. This is the solution resistance.

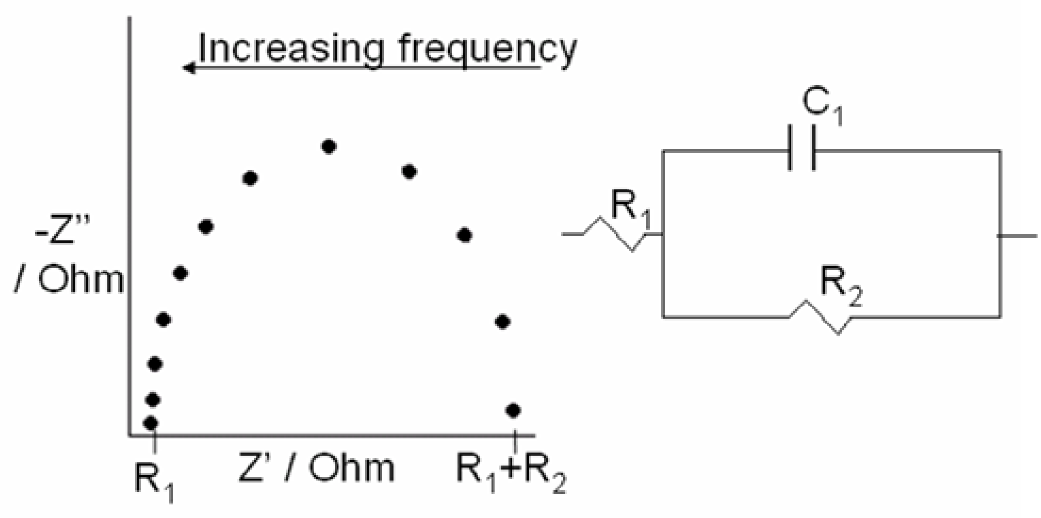

Figure 2-7: The impedance of a capacitor and resistor in parallel. The current must first pass through a resistor which shifts the results along the Z'-axis from zero.

In the impedance plot of a macroelectrode there is an additional factor, the Warburg impedance (W) that gives the plot a region of linear response at a 45° angle. This describes the linear diffusion to the electrode surface from the bulk solution, by mass transport. It is a common element for modelling electrochemical systems and is used to model semi-infinite linear diffusion.

All the factors described combine to give a final equivalent circuit of a macroelectrode as shown below where R_S is the resistance of the solution, R_{CT} is the resistance of the charge transfer reaction, relatable to the electron transfer processes at an electrode, and C_{DL} is the capacitance of the double layer at the electrode surface. This is known as the "Randles' circuit" and is shown in Figure 2-8.[2]

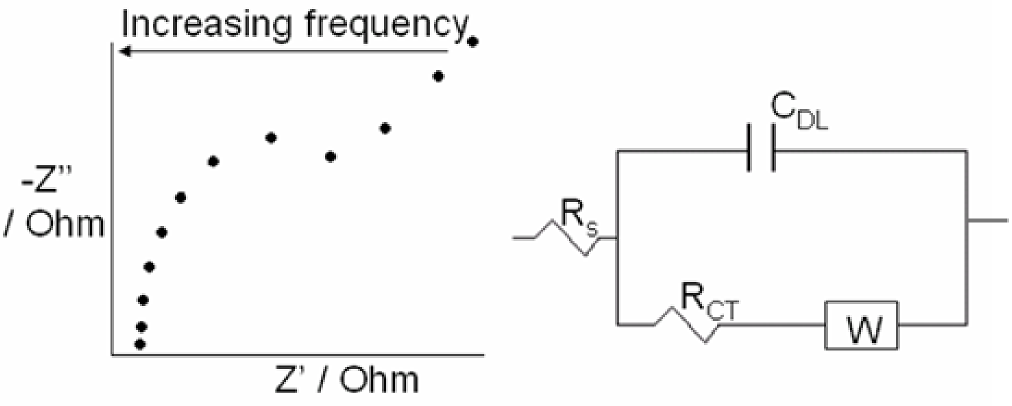

Figure 2-8: The impedance of a macroelectrode and the equivalent circuit describing the system.

The microelectrode response is slightly different[11] to the macroelectrode response as microelectrodes have different mass transport properties. As linear diffusion rapidly develops into hemispherical diffusion the Warburg impedance, which continually increases with time, does not describe the response. Instead a hemispherical approximation is used and a resistor is placed in parallel to the Warburg component as the response on the Nyquist plot returns to the x-axis[12]. Although this is an approximation it is a good fit over the frequency range and can be used to find physical parameters from the circuit. This resistor, R_{NL}, describes the non-linear diffusion to the microelectrode as can be seen in Figure 2-9.

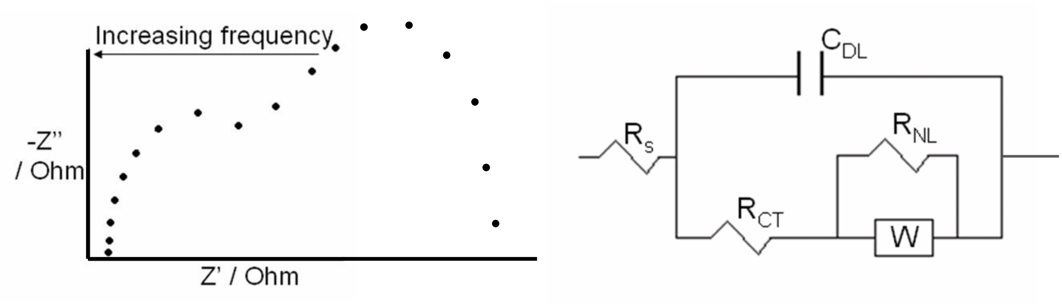

Figure 2-9: The impedance of a microelectrode and the equivalent circuit describing the system.

2.3.3 Chronoamperometry

Potential step voltammetry or chronoamperometry, is the measurement of the current response of an electrode with time as the potential is stepped from one value to another, typically across potentials relevant to a redox process where the species is electrochemically inactive at the first potential, E_1.

Taking the general equation of A oxidising to B (Equation 2-3), if the potential is stepped from E_1 to a potential, E_2, where A is rapidly oxidised to B, then the concentration of A at the surface of the electrode is rapidly depleted to a fixed value defined by E_2, often zero, and fresh species, A, reacts as soon as diffusion brings it to the electrode interface. The current-time profile will show a large peak in current at short timescales, as A is oxidised, before dropping as A is depleted. The Cottrell equation (Equation 2-11) describes the current response as a function of time under mass transport control by linear diffusion:

$$|i| = \frac{nFA\sqrt{D_A}c_A}{\sqrt{\pi t}}$$

Equation 2-11

Note that as t tends to ∞, $|i|$ tends to 0 A.

Chronoamperometry is a complementary technique to both cyclic voltammetry and EIS as it gives information about the current response at the electrode and the rapidly evolving diffusion layer.

2.4 References

---

[1] J. Heinze. Angew. Chem. Int. Ed. Engl. 32, 1993 p1268-1288
DOI:10.1002/anie.199312681

[2] A. C. Fisher. Electrode Dynamics. Oxford University Press. Section 1.2

[3] R.J. Forster. Chemical Society Reviews. 1994 p289-297
DOI:10.1039/CS9942300289

[4] A.J. Bard, L. R. Faulkner. Electrochemical Methods: Fundamentals and Applications. John Wiley & Sons, 1980, Section 1.4.3

[5] A.J. Bard, L. R. Faulkner. Electrochemical Methods: Fundamentals and Applications. John Wiley & Sons, 1980, Section 6.1

[6] K.B. Oldham. J. Electroanal. Chem. 122, 1981 p1–17
doi:10.1016/S0022-0728(81)80136-2

[7] A.J. Bard, L. R. Faulkner. Electrochemical Methods: Fundamentals and Applications. John Wiley & Sons, 1980, section 5.3.2.

[8] H.L. Woodvine. Development and Characterisation of Microelectrode and Nanoelectrode Systems (2011) University of Edinburgh

[9] M.Antonietta Baldo, Carlo Bragato, Gian A. Mazzocchin, Salvatore Daniele Electrochimica Acta Volume 43, Issue 23, 30 July 1998, Pages 3413–3422 http://dx.doi.org/10.1016/S0013-4686(98)00087-5

[10] H. Zhou, R.D. Tilton, L.R. White. Journal of Colloid and Interface Science. 297, 2006 p819-831 doi:10.1016/j.jcis.2005.11.024

---

[11] P. Łoś, G. Żabińska, A. Kisza, L. Christie, A. Mount, P.G. Bruce. Phys. Chem. Chem. Phys. 2 2000 p5449-5454 **DOI:** 10.1039/b004235h

[12] L. Christie, P. Los, P.G. Bruce. Electrochimica Acta. 1995 (40) p2159-2164 http://dx.doi.org/10.1016/0013-4686(95)00157-A

Chapter 3: Experimental Methods and Materials

This chapter will set out the fabrication of the single microelectrodes and microelectrode arrays used in this thesis. The electrochemical methodologies used practically to characterise the microelectrode responses are also detailed.

3.1 Microelectrode Fabrication and Development

There are several designs of microelectrodes used within this study. Each batch of electrodes was fabricated by Dr Jonathan Terry at the Scottish Microelectronics Centre. The fabrication methods are documented here.

The first step in the fabrication of the electrode devices was the isolation of the carrier wafer. This was done by thermal oxidation, that is the growth of a silicon oxide layer on the silicon wafer. The wafers used were three inch diameter <100> n-type silicon (IDB Technologies). The oxide layer acts as an insulator between the silicon platform and the electrical device. The oxide layer was grown by wet oxidation in a furnace at 1100 °C. An O_2/H_2 mixture was pumped through a quartz tube furnace containing the silicon wafers. The oxidising mixture reacts at the silicon surface to produce silicon dioxide. As the oxide is produced on the surface, the O_2/H_2 has to diffuse thorough this layer to react with more silicon. The thicker the required layer the longer this process takes (500 nm takes 40 minutes, 1000 nm takes 2 hours, 30 minutes).

Metal deposition on the device substrate can be achieved either by electron beam evaporation or sputtering. Both these techniques produce thin films of metal. The metal required for electrodes is deposited after a thin layer of another metal that acts as an adhesion layer between the silicon oxide and the required metal. A thin adhesion layer can relax the stress of a subsequent thick metal film, thereby reducing the chance of the film peeling off after deposition. Sputtering uses high energy argon ions (Ar^+) to bombard a large metal target physically knocking out the metal atoms. These atoms are then transported *in vacuo* until they deposit on the process wafers. The coverage of the metal atoms is wide ranging and ensures they hit the substrate. Electron beam evaporation uses a magnetic field to direct a beam of electrons, causing them to hit a small crucible filled with the required metal. The metal in the crucible is heated and atoms are released. These atoms are then transported to the substrate, building up a thin film. E-beam evaporation uses only a small crucible of the metal, making it more efficient for platinum deposition due to the high cost of the metal. Tungsten devices had metal deposition performed via sputtering while platinum devices used electron beam evaporation. Adhesion layers were deposited by the same method as the electrode metal. The two steps were performed without breaking the vacuum of the deposition system to ensure no oxide build-up on the surface of the adhesion metal. Film thickness of metal deposited through electron beam evaporation was measured during the deposition process by a quartz crystal microbalance within the machine. Sputtered film thicknesses were measured after deposition using a profilometer.

The patterning of layers on the device was performed using photolithographic techniques. This used light-sensitive chemicals, called photoresists. Using masks, light was shone onto specific areas of the photoresist to chemically change it, making it soluble in a suitable developer solution. This can then be developed, leaving certain areas still blocked. Unless stated, the photoresist used in fabricating the electrodes in this body of work is Megaposit SPR 350 (Microchem, Chestech). There are two processes for patterning devices: pattern and etch, or lift off processing.

The pattern and etch process ensured that the metal is only in well-defined areas of the final device. The initial process was to deposit the metal layers – both adhesion and required metal. Afterwards photoresist was applied to the substrate. The photoresist was exposed through a mask and developed, leaving it present over the required areas. The now revealed metal could then be etched away and the photoresist protected the areas that were to be kept. The reactive ion etch tool (JLS RIE 80) uses high energy plasma to break surface bonds and the volatile products were removed by evacuation. Reactive ion etching is predominantly a chemical process where reactive ions combine with the atoms of the material being etched to form volatile compounds. These compounds are pumped away by the vacuum system. The chemistry selected is dependent on the species being etched. Afterwards the remaining photoresist was removed and the device was coated in a passivation layer. Passivation layers are electrically resistive, chemically inert layers that ensure only the defined electrode will be electroactive on the device. The areas where metal needs to be revealed on the device were then cut out of the passivation, again using masking of photoresist and selective etching. The pattern and etch process is summarised in Figure 3-1.

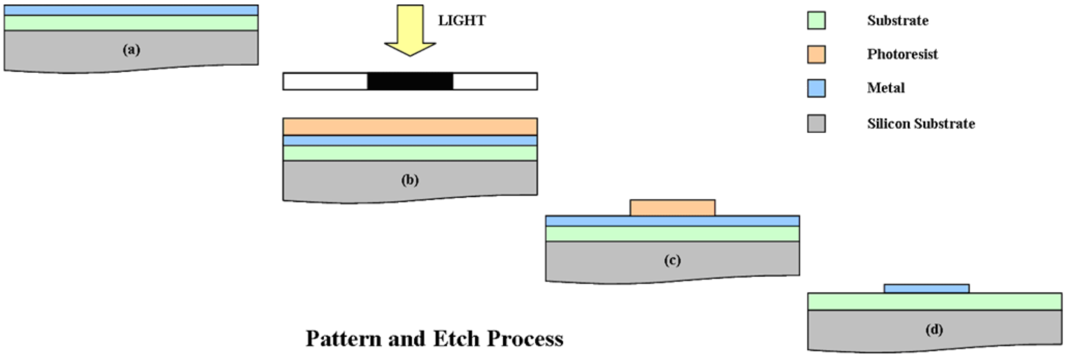

Figure 3-1: Schematic of the pattern and etch process

The lift off process involved laying down a layer before the photoresist, called a lift off resist (LOR-5B, Microchem, Chestech). This layer had a different solubility to the photoresist and created a dual layer profile after the developing step. These layers were put down and patterned before the metal deposition step. The metal was then deposited in the patterned areas. The dual layer resist profile ensured that when the film was deposited across the substrate it formed discontinuous films. This made removal of the resists straightforward and left metal in the required areas across the device without etching. A passivation layer was then added and the required holes were cut out using etching. The lift off resist process is summarised in Figure 3-2.

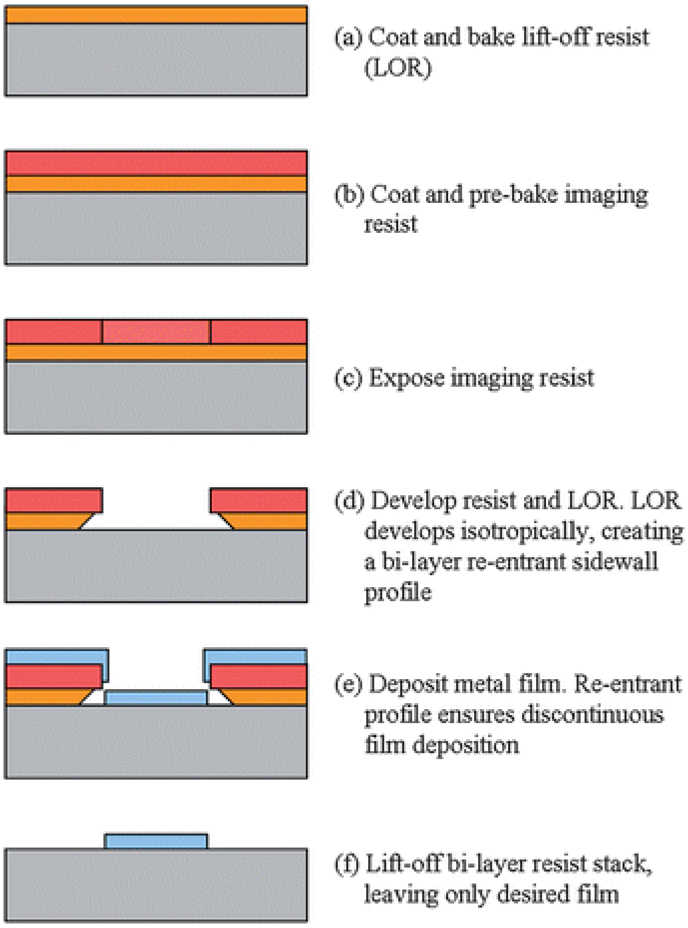

Figure 3-2: Schematic of the lift off resist process.[2]

The lift off resist process was used to deposit a metal across the surface of a device such as is required in arrays. The resolution of patterns was less good using this method, over the pattern and etch process, however it removes the metal etching step which can be difficult with platinum and tungsten based devices.[1]

Film thicknesses of silicon oxide, silicon nitride and Parylene were measured using a reflectometer (Nanospec 3000). The layer of interest is measured after deposition as standard procedure within the cleanroom. After fabrication all microelectrodes were coated in a protective layer of photoresist. The wafers were then diced to produce the individual devices. The devices are stored with this protective layer that can then be removed before use in a three step dissolution process using acetone, isopropanol and deionised water.

3.1.1 Platinum Squares

Single platinum square microelectrodes are the starting point for developing a theory for the response of electrode of this specific shape. Work has been done previously in the group using these electrodes.[8] These microelectrodes were 50 µm in edge length and used Parylene (Parylene C, SCS coatings) as a passivation layer. Parylene is a polymer used frequently in sensing devices for biocompatible applications. Parylene is the trade name for the polymers with the monomeric unit of para-xylylene. The deposition of Parylene is via a vapour deposition polymerisation process. The solid dimer is heated until it becomes a dimeric gas at 150 °C and 1.0 Torr. This is then pyrolised to monomeric gas at 680 °C and 0.5 Torr. The hot monomeric gas enters the coating chamber which is at ambient temperature. The cooling allows the gas to polymerise as a solid on all surfaces, including the intended substrate. The mask for the fabrication of these devices can be seen in Figure 3-3.

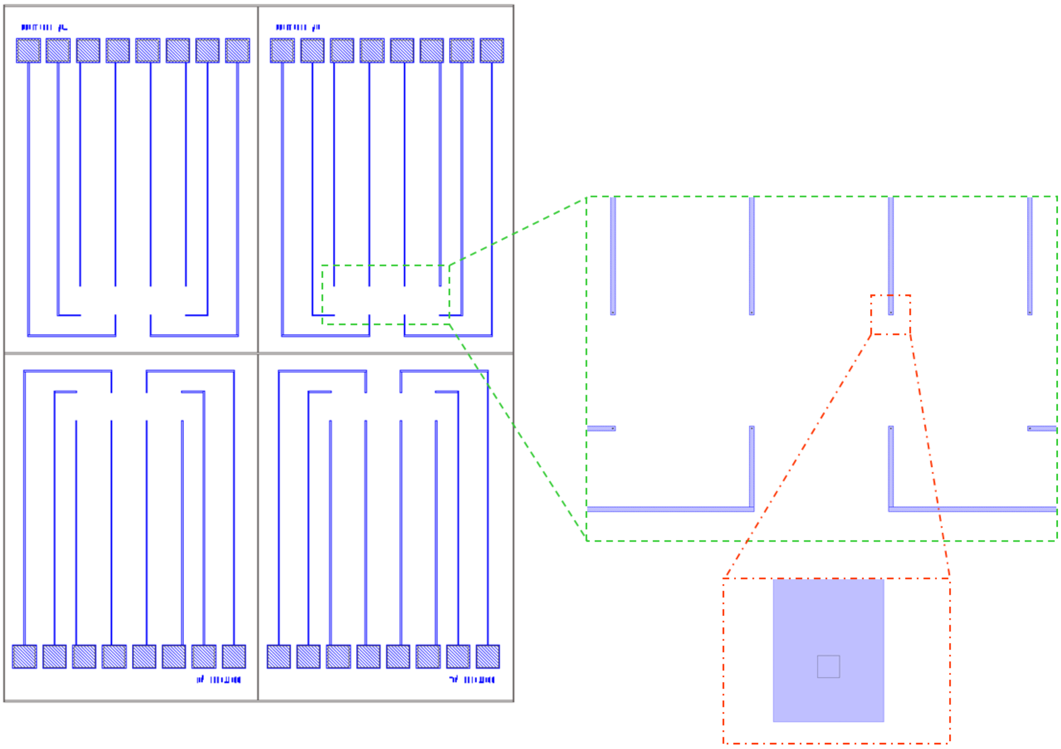

Figure 3-3: The mask design of platinum microelectrodes with eight electrodes to a device, four devices patterned on a single wafer.

The adhesion layer deposited on to the wafer was chromium, to a thickness of 2-3 nm. The platinum was then added to 250 nm. The device was fabricated using the pattern and etch process. Parylene was deposited as a passivation layer to a thickness of 500 nm.

A second design platinum single square device was fabricated after testing of the previous batch had shown significant issues with the Parylene passivation layer, discussed in Chapter 4 (Section 4.2.1). The Parylene was subject to lifting off, increasing the electrode area. It also appeared to show some electro-activity during characterisation of the devices which was not ideal. Instead the Parylene was replaced by an alternative passivation layer, silicon nitride. “Silicon nitride” covers a broad range of stoichiometric (Si_3N_4) and non-stoichiometric ratios of silicon and nitride. This is a common ceramic material used in the semiconductor industry. It has relatively low thermal expansion coefficient, high strength across a broad temperature range and low thermal conductivity. Silicon rich silicon nitride was deposited in a furnace via low pressure chemical vapour deposition. Silicon rich silicon nitride films have lower stress than the stoichiometric ratio. The feed gases for this process were dichlorosilane (10 sccm) and ammonia (15 sccm) at a temperature of 800 °C and pressure of 100 mT to create a silicon-rich silicon nitride layer. Deposition time for a 500 nm layer is 5 hours.

These devices were characterised and used in Chapters 5 and 6. The mask used to fabricate these devices can be seen in Figure 3-4. These electrodes were fabricated using the lift off resist process. The silicon oxide was grown to a thickness of 1000 nm. The adhesion layer metal was changed from chromium to titanium and was deposited to a thickness of 10 nm. The platinum was deposited at a thickness of 200 nm and the silicon nitride at a thickness of 500 nm. This design was used to pattern devices with several electrode lengths: 10, 20, 30, 50 and 100 μm edge by control of the mask defining the square shape.

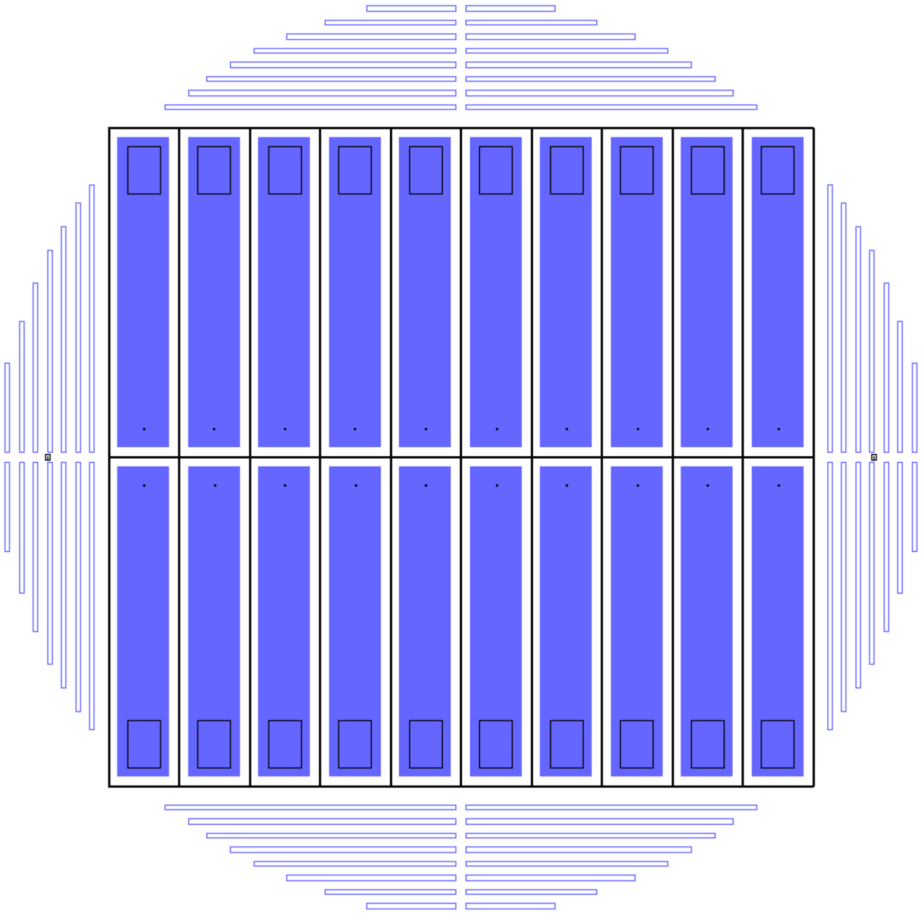

Figure 3-4: The mask design of platinum microelectrodes with single electrodes to a device and twenty devices patterned on a wafer.

3.1.2 Platinum Arrays

Platinum arrays were fabricated using the lift off process. The arrays had metal underneath the entirety of the passivation layer so each exposed area of metal would act as an electrode, but each response would be summed and connected to the system via a single contact pad at the top of the array. This is seen schematically in Figure 3-5.

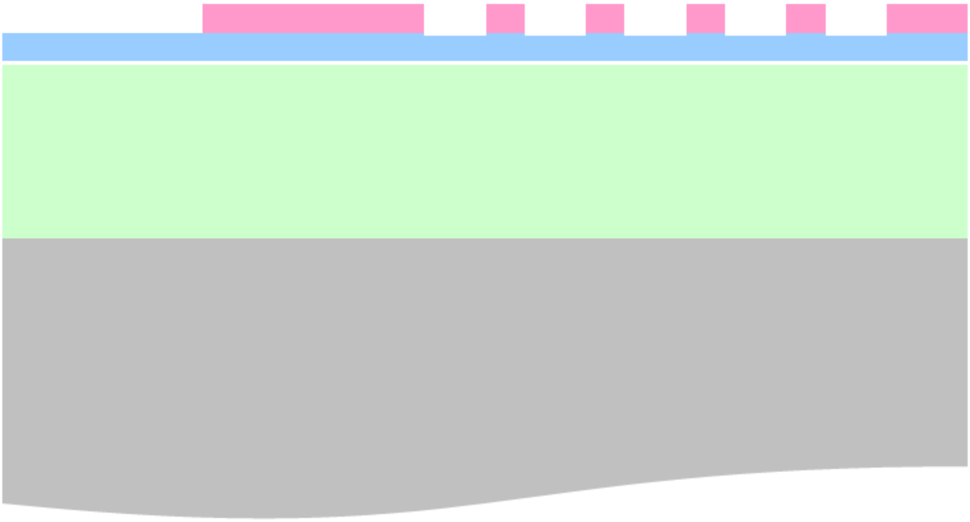

Figure 3-5: Cross-section representation to illustrate how the individual electrode areas on an array are connected to the contact pad, where the grey is the silicon wafer platform, the green indicates the silicon oxide layer, the blue is the electrode and contact pad metal and the pink is the passivation layer. Layers not to scale.

Figure 3-6 shows the mask design of platinum microelectrode arrays with twenty devices patterned on a wafer. The first design of platinum array suffered from the blanket coverage of metal deposition produced by this process. After dicing the wafer, devices had a band of metal around the perimeter that acted as additional electrode area. This was prevented in a second design by using an additional mask to define the edges of an array device. The design was used to fabricate the microelectrode array devices characterised in Chapter 7.

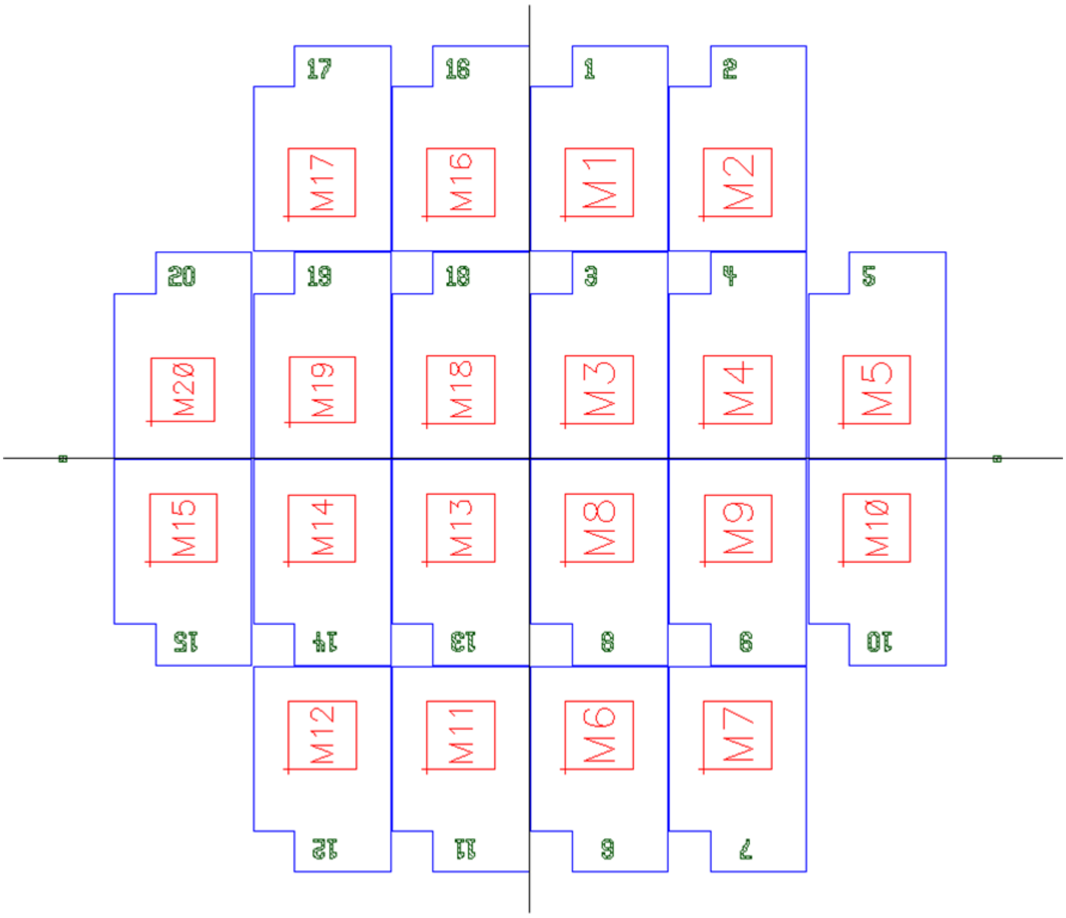

Figure 3-6: The mask design of platinum microelectrode arrays with twenty devices patterned on a wafer.

The array patterning was produced by using three masks to describe the metal deposition area, the device area and the passivation area. This patterning defines the organisation of electrodes on the array. The templates of these masks can be seen in Figure 3-7.

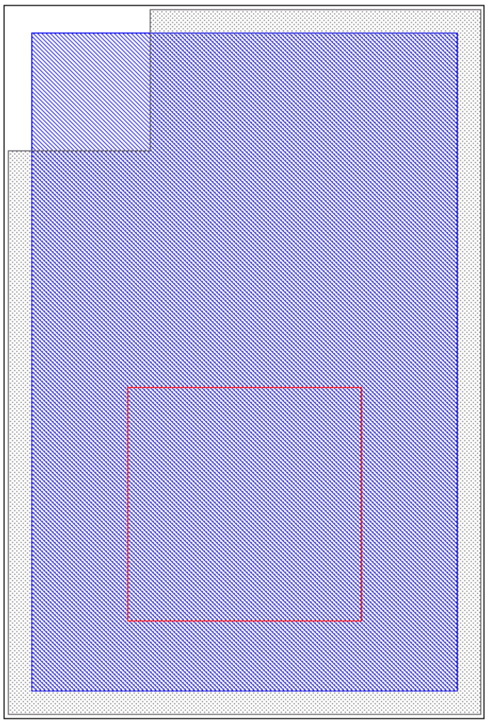

Figure 3-7: The masks used to define the device and passivation (grey), metal (blue), array (red) areas.

The platinum arrays had a silicon oxide layer of 1000 nm. The adhesion layer was titanium to a thickness of 10 nm, and platinum was deposited as an electrode material to a thickness of 50 nm. The arrays used silicon nitride as a passivation layer, to a thickness of 500 nm, as discussed for the platinum squares.

3.1.3 Tungsten Squares

There were two designs of tungsten square microelectrode devices used in Chapter 8. The first discussed was fabricated by processes very similar to the final design of platinum electrodes, using the lift off resist process, but with a tungsten deposition step rather than platinum. The mask for fabricating these devices can be seen in Figure 3-8.

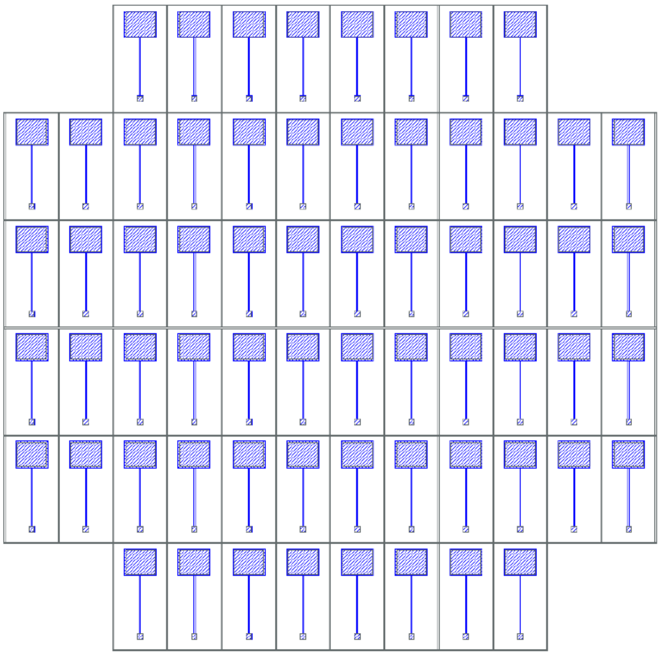

Figure 3-8: Mask layout for 64 single tungsten electrode devices per wafer. Blue structures represent metal, grey structures define contact holes in the surrounding passivation.

The adhesion layer metal was titanium and was deposited to a thickness of 10 nm. The tungsten was deposited to a thickness of 200 nm and the silicon nitride to a thickness of 500 nm. This design was used to pattern devices with electrode length of 500 µm.

The second device design was based on a previously fabricated device and used the same mask as used for the original platinum microelectrodes. The mask design can be seen in Figure 3-3. These devices were fabricated using a pattern and etch process. The adhesion layer metal was titanium and was deposited at a thickness of 10 nm. The tungsten was deposited at a thickness of 200 nm and the silicon nitride at a thickness of 500 nm. This design was used to pattern devices with electrode length of 50 µm.

3.2 Electrochemistry Experimental Set-up

The three electrode system containing a microelectrode device as a working electrode, a saturated calomel electrode (SCE) (Scientific Laboratory Supplies) as a reference electrode and a platinum gauze (Alfa Aesar, VWR) as a counter electrode as shown in Figure 3-9. This set-up is used for all room temperature characterisations in this research and is held in a Faraday cage (made in house) to minimise electrical noise as the current at a microelectrode are typically small and susceptible to noise. When collecting multiple device responses they were all placed in solutions at the same time for the same duration. They were held in solution by a custom made lid with attached crocodile clips.

All electrochemical measurements were collected using a potentiostat. Aqueous experiments were collected using an Autolab PGSTAT30 (Eco Chemie) with frequency resonance analyser and multiplex module. High temperature experiments were collected using an Autolab PGSTAT12 (Eco Chemie) potentiostat.

Figure 3-9: The experimental set up of the three electrode system including microelectrode in a Faraday cage for room temperature aqueous characterisation.

3.3 Electrochemical Reactions

3.3.1 Pre-treatment

Before use in electrochemical systems the protective photoresist layer had to be removed from the microelectrodes. This layer was applied to protect the devices during dicing. The layer was removed in three steps: soaking in acetone, soaking in isopropanol and rinsing in distilled water.

The pre-treatment and development of a cleaning process for the microelectrode devices is discussed at length in Chapter 4. The final electrochemical cleaning process was to scan potentials between the limits of the solvent window in a 1.0 M sulfuric acid solution (VWR, 98%) until the magnitude of the current response no longer increased with additional scans.

3.3.2 Potassium Ferricyanide Reaction

In testing new working electrodes it is practical to take a benchmark reversible couple as a standard to use as basis for comparison with other electrodes. With the microelectrodes work has been done within the group to characterise these electrodes in room temperature aqueous solutions.[2] This previous work was performed using the one electron reversible reaction of potassium ferricyanide and potassium ferrocyanide which is often considered an electrochemical standard[3,4,5,6]. The standard reduction potential of the reaction is 436 mV at pH 7. The diffusion coefficient of potassium ferricyanide in background electrolyte under ambient laboratory temperature is $D = 6.98 \times 10^{-6}$ cm^{2}s^{-1}.[7]

$$[Fe(CN)_6]^{3-} + e^- \rightleftarrows [Fe(CN)_6]^{4-}$$

Equation 3-1

Solutions of 10 mM potassium ferricyanide (99% Sigma Aldrich) in a 0.1 M potassium chloride (99% Fisher Scientific) background electrolyte solution were produced for characterisation. Cyclic voltammetry was performed at various scan rates from 100.0 - 1.0 mVs^{-1}. The potential was scanned from 0.350 V to 0.00 V to observe the redox reaction.

Electrical Impedance Spectroscopy (EIS) was used to characterise the electrodes including the changing diffusional response over time. EIS in ferricyanide solution was performed over DC potentials from 0.150 V to 0.225 V with a rms amplitude of 0.01 V to cover the potentials around E^{θ} as found by cyclic voltammetry. The frequency ranged from 1000.0 Hz to 0.01 Hz, using 40 frequencies in a logarithmic distribution.

Chronoamperometry was used to measure the current response of the microelectrodes devices over time. The potential was stepped from 0.35 V to 0.00 V, 0.10 V, 0.17V, 0.19 V and 0.25 V to cover the potential range of the ferricyanide reduction. The current response was measured for 20 seconds at intervals of 0.01 second.

3.3.3. Nitric Acid Reactions

In Chapter 5 platinum square microelectrodes are used to analyse nitric acid systems. The microelectrodes were pre-treated by cycling in 3.0 M nitric acid (Fisher Chemical, analytical reagent grade, specific gravity 1.42). The data were collected in a Faraday cage to minimise electrical noise and were collected at ambient laboratory temperature.

For silver electrochemistry, to prevent the reaction of chloride ions with silver ions, producing insoluble silver chloride, a double junction reference electrode (Scientific Laboratory Supplies) was used with a saturated calomel electrode within the inner compartment and 3.0 M nitric acid solution in the outer compartment. This prevented contamination both of the reference electrode and of the solution.

Cyclic voltammetry was performed in solutions of 3.0 M nitric acid. Silver deposition studies were performed using a 10 mM solution of silver nitrate (Sigma-Aldrich, 99+%) in 3.0 M nitric acid. Voltammetry was performed at various scan rates from 100.0 - 1.0 mVs^{-1}. Nitric-nitrous acid solutions were produced by making the appropriate concentration of nitric acid and then adding sodium nitrite (Sigma-Aldrich, ≥99%) as required to produce the intended HNO_3/HNO_2 concentration ratios.

3.4 Computational Simulations

Microelectrode responses were simulated via finite element methods using commercial software, COMSOL Multiphysics 3.2b for Linux (COMSOL, Inc., Burlington, MA). The limiting currents for square electrodes of various sizes were determined by simulating steady state diffusion in a 3 dimensional representation of the solution neighbouring the microelectrode. Due to symmetry, only a quarter of the electrode surface was simulated. The space around that quarter was large enough to accommodate the developing and expanding diffusion field. This field was simulated using a user defined adaptive mesh. These simulations demonstrated that higher currents were found for square microelectrodes than discs of equivalent area due to enhanced diffusion at the electrode edges, particularly corners. The numerical values for current at square microelectrodes are used in Chapter 5 (Section 5.3) and Chapter 7 (Section 7.3) for comparison to experimentally derived currents. Steady state responses were simulated by Dr Helena Woodvine and are discussed further in her thesis[8].

Transient responses of microelectrode currents were simulated using the same software (Version 3.5a) by Ilka Schmueser. These simulations calculated the time-dependent diffusional fluxes and therefore the changing current response of single square microelectrodes and arrays of different sizes as the potential was stepped to initiate complete reaction at the surface and the onset of steady state diffusion. These simulations used a user defined mesh. The transient responses can be seen in Chapter 5 (Section 5.3.2) and Chapter 7 (Section 7.3.4) for comparison with experimentally derived responses.

3.5 Analysis of Electrochemical Data

Cyclic voltammograms were collected on the Autolab potentiostats and the associated GPES software was used for initial analysis of these data.

Origin software was used for data presentation within this thesis and any differentiation or integration of current response, as seen in Chapter 6 (Section 6.3.3). In addition, Origin was used to calculate current densities and normalised currents such as those found in Chapter 7 (Section 7.3).

EIS data was collected on the Autolab potentiostats and iterative fitting within the associated FRA software was used to fit the data to equivalent circuits, as discussed in Chapter 7 (Section7.3.2). The equivalent circuits used are shown in Figure 3-10.

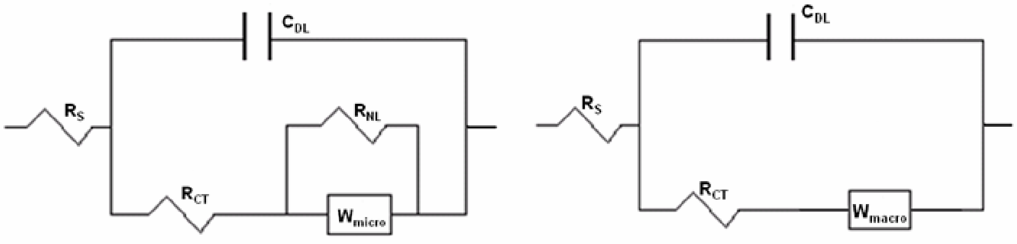

Figure 3-10: Equivalent circuits used to fit impedance response. The equivalent circuits are applicable to microelectrode (left) and macroelectrode (right) behaviour.

From these fits to equivalent circuits, values for R_S, R_{CT}, R_{NL}, C_{DL}, W_{macro} and W_{micro} were obtained as appropriate. If required, the impedance response was fitted for selected frequency ranges or with high frequency weighting selected if these data were more accurate. For example, values of R_{CT} required a frequency weighting to be obtained.

3.5.1 Fundamental Fits to Equivalent Circuit Parameters

The fundamental equations that describe how the non-linear and charge transfer resistances of microelectrode arrays should vary with E_{DC} have been previously derived within the group.[2] Two possible expressions were used: the "thermodynamic fit" (Equation 3-2) and the "kinetic fit" (Equation 3-3). As the non-linear resistance is controlled by thermodynamics, only Equation 3-2 is applicable whilst for charge transfer kinetics either Equation 3-2 or 3-3 can apply to the charge transfer resistance. The kinetic fit contains the transfer coefficient property of α_{ox} as the equation is derived from the k_{red} equation (Equation 3-4).

$$R_X = \frac{R_X^{\min}}{4}\left[2 + \exp\left(\frac{F\left(E_{dc} - E^0\right)}{RT}\right) + \exp\left(\frac{F\left(E_{dc} - E^0\right)}{RT}\right)\right]$$

Equation 3-2

$$R_X = \frac{R_X^{\min}}{2}\left(\exp\left(\frac{-\alpha_{ox}F\left(E_{dc} - E^0\right)}{RT}\right) + \left(\frac{\left(1-\alpha_{ox}\right)F\left(E_{dc} - E^0\right)}{RT}\right)\right)$$

Equation 3-3

$$k_1 = k^0 \exp\left(+\frac{\alpha_{ox}F\left(E - E^0\right)}{RT}\right)$$

Equation 3-4

The iteratively fitted values of R_{NL} were plotted against E_{DC} using Origin and these equations were applied. The results of this can be seen in Chapter 7 (Section 7.3.2.1).

Resistances have units of ohms. Capacitances have units of farads. The Warburg coefficient has units of $\Omega.s^{-½}$. Warburg values obtained from fitting with the FRA software are reported as Y_0. Y is the admittance, which is the inverse of the impedance.[9] Y_0 is the magnitude of the admittance at ω=1 rads^{-1} and is reported in $S.s^{-½}$. This can be converted to Warburg coefficient, σ, using Equation 3-5.

$$\sigma = \frac{1}{\sqrt{2} \times Y_0}$$

Equation 3-5

as the Warburg impedance can be written as[10]:

$$\left|Z_W\right| = \frac{\sqrt{2}\sigma}{\omega^{\frac{1}{2}}}$$

Equation 3-6

3.6 References

---

[1] Sami Franssila. Introduction to Microfabrication. John Wiley and Sons. 2005 edition.

[2] H.L. Woodvine, J.G. Terry, A.J. Walton and A.R. Mount, Analyst, (2010) 135 p1058-1065 **DOI:** 10.1039/b924342a

[3] D. Lowinsohn, H.E.M. Peres, L. Kosminsky, T.R.L.C. Paixão, T.L. Ferreira, F.J. Ramirez-Fernandez, M. Bertotti. Sensors and Actuators B, 113 (2006) p80-87 http://dx.doi.org/10.1016/j.snb.2005.02.024

[4] D. Lantiat, V. Vivier, C. Laberty-Robert, D. Grosso, C. Sanchez. ChemPhysChem 2010 Vol 11 p1971–1977 **DOI:** 10.1002/cphc.200900929

[5] M. Boillot, S. Didierjean, F. Lapicque. Journal of Applied Electrochemistry. December 2004, Volume 34, Issue 12, pp 1191-1197 **DOI:** 10.1007/s10800-004-9304-8

[6] Z. A. Rotenberg, A. V. Dribinskii, V. P. Lukovtsev, N. S. Khozyainova. Russian Journal of Electrochemistry. August 2000, Volume 36, Issue 8, pp 879-882 **DOI:** 10.1007/BF02757062

[7] O. Köster, W. Schuhmann, H. Vogt, W. Mokwa. Sensors and Actuators B: Chemical, Volume 76, Issues 1–3, 1 June 2001, Pages 573-581 http://dx.doi.org/10.1016/S0925-4005(01)00637-2

[8] H.L. Woodvine. Development and Characterisation of Microelectrode and Nanoelectrode Systems (2011) University of Edinburgh

---

[9] Evgenij Barsoukov, J. Ross Macdonald. Impedance Spectroscopy: Theory, Experiment and Applications. Wiley-Interscience. 2nd edition

[10] Electrochemical Methods: Fundamentals and Applications. A.J Bard, L.R Faulkner. 2nd Edition. Section 10.3.

Chapter 4: Optimisation of Microelectrode Cleaning Process

This chapter documents the development of an electrochemical cleaning protocol for platinum microelectrode devices. The mechanisms of microelectrode pre-treatment and the importance of these procedures to device performance are also discussed. In addition, the pre-treatment of tungsten microelectrode devices for high temperature studies is discussed.

4.1 Introduction

Microelectrodes are a sensitive analytical tool. As such any pre-treatments, specifically dealing with the cleanliness of the device, can be of great significance. Given the high sensitivity of a microelectrode any accumulated deposits on the surface prior to use will reduce the efficiency of the device. Therefore, to minimise device contamination, dust and airborne particles must be minimised during device storage. Handling is also an issue. Gloves are required to be worn to prevent skin-based chemicals, particularly oils, contaminating the device.

Microelectrodes fabricated from lithographic techniques are more challenging than macroelectrodes to clean as the standard electrode polishing methods are impossible. Microelectrodes produced by alternative fabrication methods can still present challenges in pre-treatment. In particular, with respect to wires set in glass microelectrodes, mechanical abrasion at the junction of the metal and the insulator can lead to cracking or fracture. Polishing the electrode can also change the electrode shape and area, changing the current response. Some literature reports for pre-treatment of wires set in glass via polishing with alumina exist[1,2] but without any description of how effective these processes were.

Electrochemical pre-treatment of microelectrodes, or "activating the surface,[3]" occurs by applying a sequence of varying electrode potentials. This procedure allows impurities to be desorbed from the electrode surface while, in addition, the formation and reduction of metal oxide films and the production of gases on the electrode surface aids in the further cleaning and activation of the metal surface. Repetition leads to steady oxide layer currents as the electrode is activated and all impurities have been removed so no further area can be revealed.

Chemical cleaning of macroelectrodes and microelectrodes involves changing the chemical environment of the electrode surface. The presence of a reductive or oxidative environment is used to change the character of the electrode surface. Chemical cleaning can dissolve matter on a surface, or it may affect an oxide layer.[4]

4.2 Platinum Electrode Pre-treatment

During fabrication the devices were kept in a clean room which controls the concentration of pollutants in the air. Clean rooms are specially designed areas for manufacturing or research of materials sensitive to atmospheric pollutants. The clean room at the Scottish Microelectronics Centre where the devices are fabricated is an M 2.5 grade clean room which means that particles of 0.5 μm in the air are limited to 353 per cubic metre (10 particles per cubic foot). After fabrication the finished devices are coated with a layer of photoresist, to protect the devices during storage. Once the devices are to be used the photoresist layer is dissolved in a three-step process as described in Chapter 3 (Section 3.3.1).

4.2.1 Platinum Microelectrode Electrochemical Cleaning in Electrolyte

The microelectrodes used for aqueous system analysis were initially cleaned by electrochemical cycling within and outside the solvent window of a 0.1 M potassium chloride electrolyte. This protocol was established previously as an appropriate methodology for microelectrode cleaning based on the existing literature[5]. However, due to the limitations of the Parylene insulation layer as discussed in Chapter 3 (Section 3.1.1) the current had to be controlled at the potentials of the solvent limit where the current peaked. This limited the formation of bubbles of hydrogen and oxygen produced at these potentials and so limited the lift-off of the passivation layer.

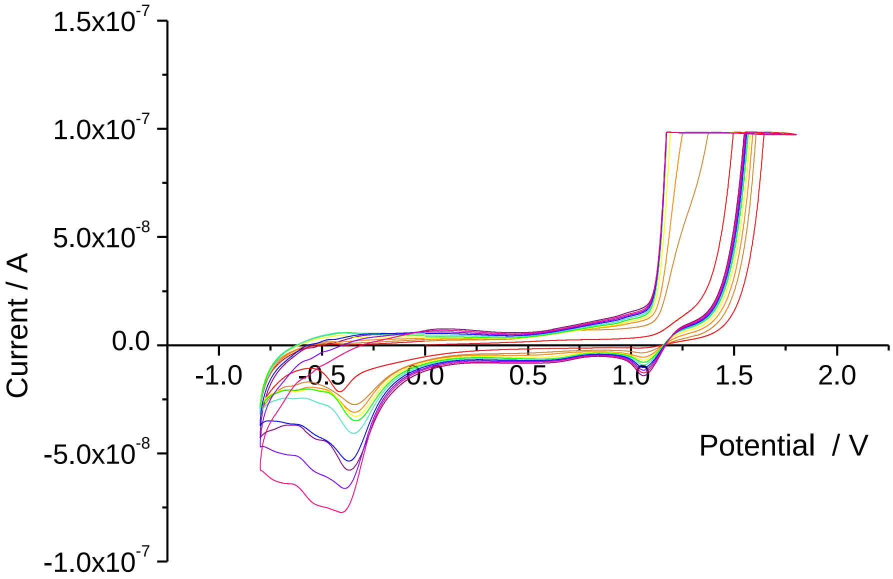

Figure 4-1: Successive cyclic voltammetry scans of a platinum square microelectrode with 50 µm edge in a degassed 0.1M KCl solution. Scan rate 100 mVs^{-1}.

The cyclic voltammogram of the platinum microelectrode shown in Figure 4-1 has several features of note. The first and most distinctive feature is the increasing peak height as more scans are recorded (from red through the spectrum to purple). Higher currents show an increasing effective electroactive area and therefore demonstrate the validity of this cleaning method. The peak at 1.3 V, with current limited to 100 nA, is the most prominent feature on the CV. This corresponds to oxygen evolution, where the upper limit of current is controlled by the potentiostat settings using internal resistors. The current response at the negative potential limit was expected to show hydrogen evolution. However, the potential is not extended far enough and only the reduction peaks of hydrogen adsorption on the platinum crystal faces is observed.[6] There is also an unexpected reduction small peak at 1.1 V which must be due to a reaction associated with the Parylene layer. Parylene is electrochemically unresponsive[7] but degradation products may be electrochemically active. This electrochemical reactivity, in addition to other factors discussed previously, demonstrates the unsuitability of Parylene for these microelectrode devices. Subsequent designs of platinum microelectrode devices used an alternative passivation layer of silicon nitride. Subsequently this reduction peak disappeared and was not present in future scans.

Platinum arrays were designed and fabricated as detailed in Chapter 3 (Section 3.1.2). Initially the cleaning protocol used was that performed on the platinum single squares, with the current controlled at a higher limit, to accommodate the higher current outputs of an array. Typical cyclic voltammograms for this protocol can be seen in Figure 4-2.

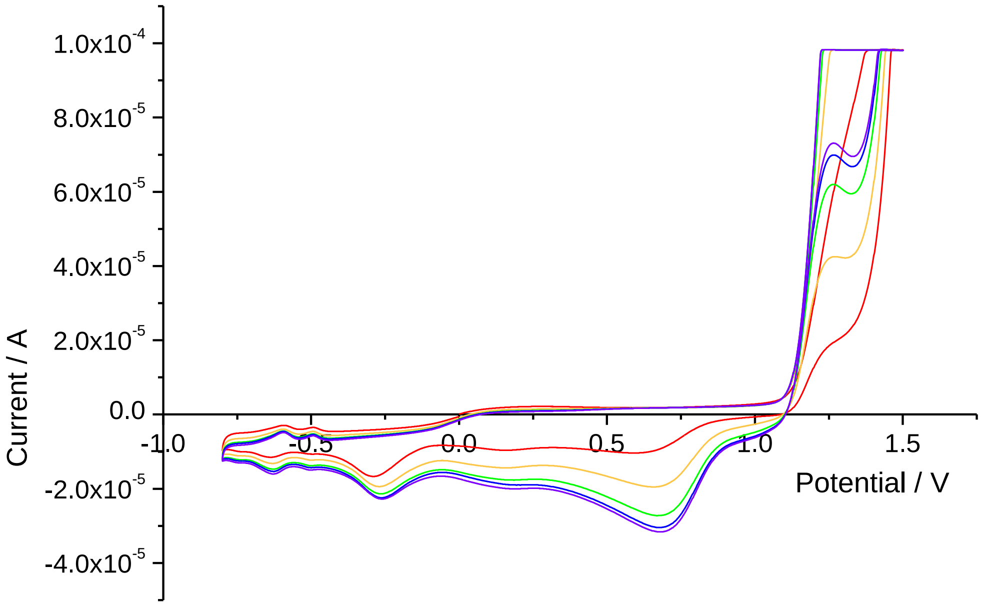

Figure 4-2: Successive cyclic voltammetry scans (red to purple) of an array of platinum square microelectrodes with length 30 μm with 2D spacing in 0.1M KCl solution purged with argon. Scan rate 100 mVs^{-1}.

The first difference to note in changing from a single square device to an array is that the current has increased dramatically. The oxygen evolution peak remains at high positive potentials. The platinum oxide reduction peak at 0.67 V is more pronounced than before. This is likely due to the arrays producing a peak rather than a wave-like response and is discussed in Chapter 7. The hydrogen adsorption peaks found previously are still present between -0.2 and -0.8 V, though their relative peak heights have changed. These peaks are due to absorption on different crystal faces of the platinum metal and the change in heights may be due to changes in the availability of each crystal face in polycrystalline platinum.[3]

The cleaning protocol of an array was modified to remove the step of purging the air from the system using Argon gas. It was found that the presence of oxygen in the system had no discernible effect on the characterisation of the electrodes and so the step was removed for simplicity.

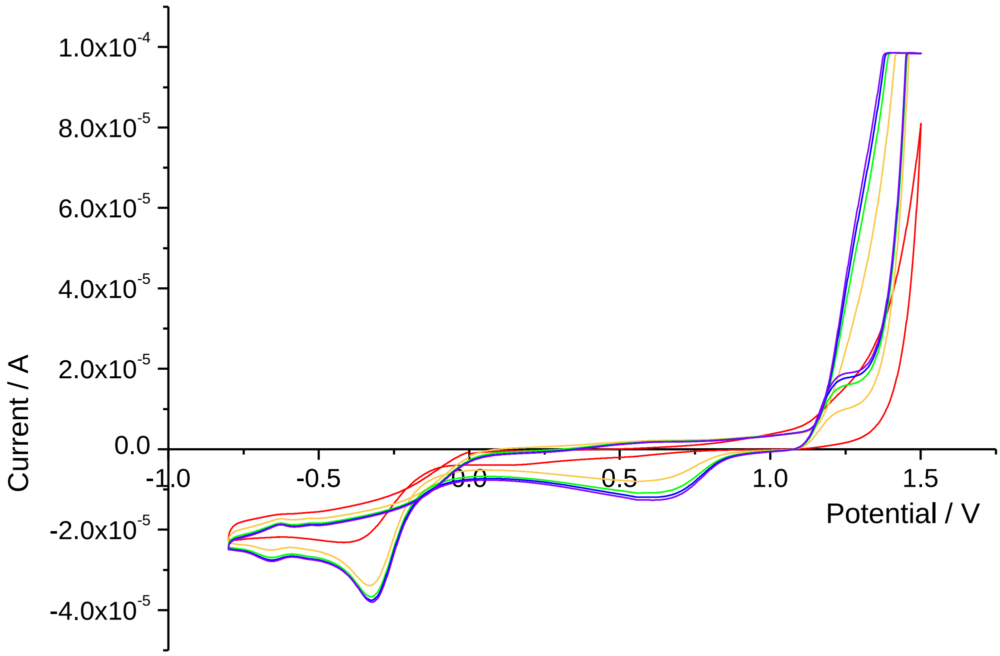

Figure 4-3: Successive cyclic voltammetry scans (red to purple) of an array of platinum square microelectrodes with edge 50 µm with 2D spacing in 0.1M KCl solution. Scan rate 100 mVs^{-1}.

Figure 4-3 shows the cleaning of an array of square platinum electrodes of edge 50 µm with 2D spacing in potassium chloride solution without the degassing step. A peak due to the oxygen reduction reaction at -0.28 V occurs, which has the effect of increasing the current in comparison to the deoxygenated CV seen previously.

The cleaning protocol was extended to the negative potential of -1.0 V, where hydrogen evolution would occur. By extending the potential to this solvent limit more bubbles will be produced, this time of hydrogen, increasing the possibilities of chemical reduction and of bubbles removing particulate matter from the electrode surface. Figure 4-4 shows a typical cyclic voltammogram across this extended range of potentials at a scan rate of 100 mVs^{-1}.

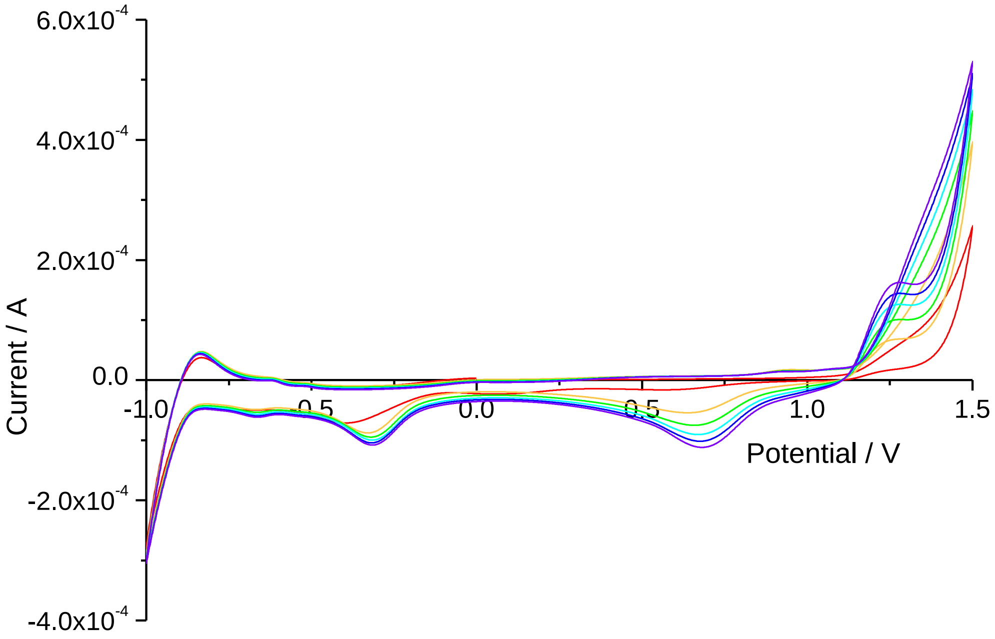

Figure 4-4: Successive cyclic voltammetry scans (red to purple) of an array of platinum square microelectrodes with edge 20 μm with 1D spacing in 0.1M KCl solution. Scan rate 100 mVs^{-1}.

The time to cleanliness of an electrode using this KCl cleaning protocol is variable and it can take anything from 20 to 200 scans to achieve a repeatable current response, as indicated by the size and shape of platinum oxide reduction peak at 0.68 V. The cleanliness of an electrode is observable under a microscope and reinforces the importance of an appropriately treated metal surface. The observable difference between dirty and clean electrodes can be seen in Figure 4-5.

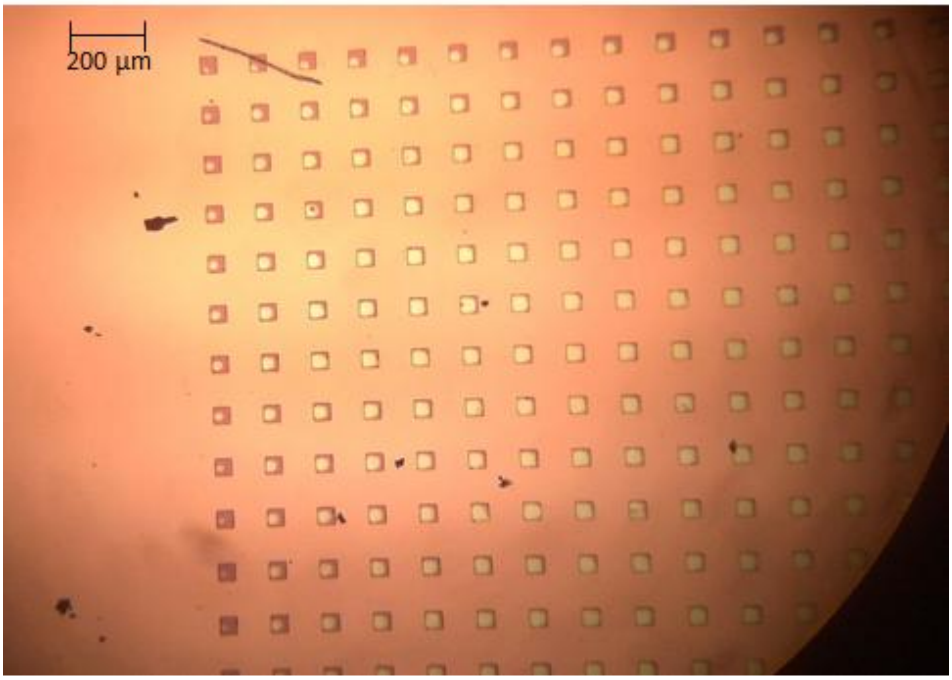

Figure 4-5: Image of the edge of a 50 µm edge 2D platinum square microelectrode array after some electrochemical cleaning in potassium chloride solution. The difference between dirty (around the edge) and clean (in the array) electrodes is apparent.

4.2.2 Platinum Microelectrode Electrochemical Cleaning in Sulfuric Acid

The potassium chloride cleaning protocol provided clean microelectrode devices but the time taken for cleaning could vary widely, sometimes taking a day. With the replacement of Parylene with silicon nitride passivation in the microelectrode device design a more chemically rigorous, method could be developed. Sulfuric acid pre-treatments have been used in the literature previously[8,9,10,11]. Cycling within and outside the electrochemical window in 0.1 M sulfuric acid solution was tested as a suitable cleaning process. Typical cyclic voltammograms for this can be seen in Figure 4-6.

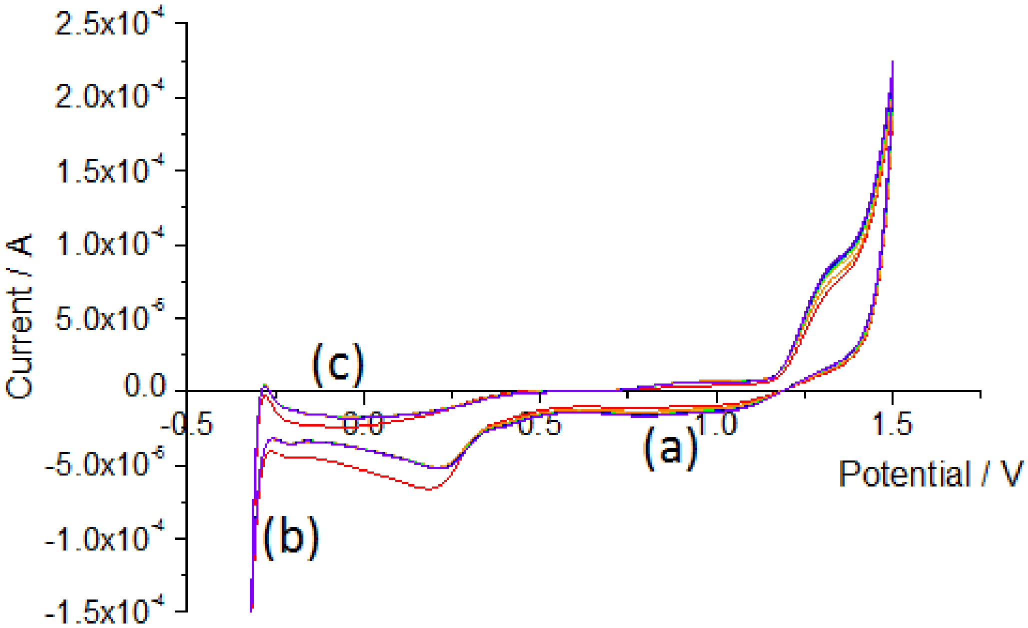

Figure 4-6: Successive cyclic voltammetry scans (red to purple) of an array of platinum square microelectrodes with edge 30 µm and 1D spacing in 0.1 M H_2SO_4 solution. Scan rate 100 mVs^{-1}.

This is a typical profile of a platinum electrode in sulfuric acid[3]. Near 1.5 V there is a typical onset of oxygen evolution, preceded on the forward scan by a peak signifying adsorbed oxygen and/or a platinum oxide layer being formed. The reverse of this process is shown by the small peak at 0.8 V, (a). Once the height of this peak is reproducible on subsequent scans it is taken to show that the electrode area is fixed and no further metal can be activated by electrochemical cleaning. At the opposite potential limit the onset of hydrogen evolution can be observed (b) and the signature peaks of hydrogen adsorption and the subsequent de-adsorption as the potential returns to zero, (c).

These characteristics ensure that the cleanliness of the electrodes can be monitored during the cycling in acidic solution. As the scans progress there is an observable change in current response, specifically the height of reaction peaks which indicates the enhanced area due to the cleaning process. As this current change stabilises, and the peak heights stop changing, this is taken to show a clean electrode.

Typically, cleaning in sulfuric acid takes less scans, and therefore less time, than the potassium chloride cleaning. This is highly dependent on the initial state of the device, however especially if there is excess photoresist remaining. It must be remembered that electrochemical cleaning can only clean an active electrode surface, not a passivated surface where electrochemistry cannot occur. Subsequent electrochemical cleaning of platinum microelectrode devices used the sulfuric acid protocol and this was established as the optimal method.

4.3 Cleaning Mechanism

Given that cleaning of the fabricated microelectrode devices cannot be performed by polishing as you would a standard macroelectrode, the efficiency of cleaning by chemical or electrochemical means is important. It has been found to be easier to clean arrays with electrodes of 100 µm than with 10 µm edges, i.e. smaller microelectrode devices required more scans of an electrochemical cleaning procedure to reach the same peak heights as devices with microelectrodes of larger areas.

It is thought that the cleaning mechanism in electrochemical cleaning is such that the electrochemical reactions occur at the bare metal sections and dirt in the form of particulates is removed, revealing more electrode as the reactions continue. However, if initially there is no active material exposed, i.e. if the electrode is entirely covered by dirt, the electrode will remain unresponsive. It is far more likely that this can occur over the smaller areas of the 10µm than the 100µm length electrodes.

SEM images, shown in Figure 4-7, demonstrate that after cleaning and characterisation in potassium ferricyanide solution some electrodes that appear to remain unclean with dark material covering the bright electrodes on array with microelectrodes of 10 µm edges. In comparison the array with microelectrodes of 100 µm edges is comparatively clean with only some residue remaining at the very edges of some electrodes.

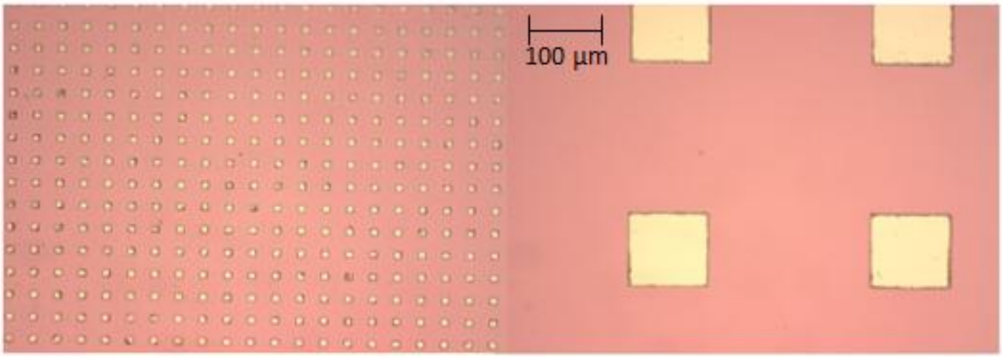

Figure 4-7: SEM images of arrays of platinum square microelectrodes with length 10 µm and 100 µm with 2D spacing.

The cleaning mechanism is hypothesised to come from the limits of the solvent window in the cyclic voltammogram, where the oxygen and hydrogen gases were produced. The bubbles of gas formed allowed particulate matter to become dislodged and diffuse away from the electrode surface. To test this potential step voltammetry was used to change the potential in pulses, setting it to the maximum oxidative potential of the CV and then to the maximum reductive potential. These potentials allowed the gaseous products to be formed, without passing through the intervening potentials. The resulting current-time response of an array in sulfuric acid cleaning solution can be seen in Figure 4-8. The increase in current response indicates that O_2 and H_2 evolution is increased and therefore a greater electrode area had been revealed.

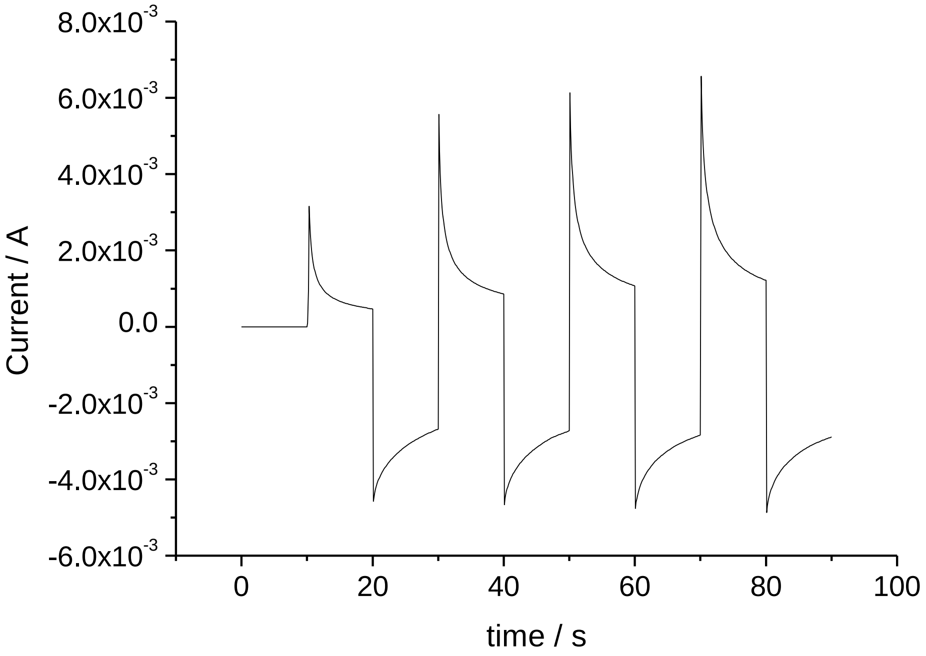

Figure 4-8: Current–time response of an array of platinum square microelectrodes with 20 µm edge and 2D spacing in 0.1 M H_2SO_4, with potentials switched between 1.5 V and -0.5 V.

It can be seen qualitatively that the peak heights of the current-time transients increase with subsequent potential switches. Given that the total area of the array is known this technique could be adapted to test the cleanliness of an electrode, by monitoring the charge passed over a set time period and comparing to an ideal calculated value.

4.4 Validity of Cleanliness As Measured By EIS

The thoroughness of the cleaning was observable during the collection and analysis of electrical impedance spectroscopy (EIS) as described in Chapter 2 (Section 2.3.2). It was found that with very clean arrays the first semicircular feature of the EIS, at high frequencies, describing the double layer capacitance and charge transfer resistance was reduced significantly until data collected within a set frequency range eventually became too small to reliably fit to an equivalent circuit. This is due to the increase in effective electrode area and/or the increase in charge transfer rate constant due to a cleaner surface. This can be seen in Figure 4-9.

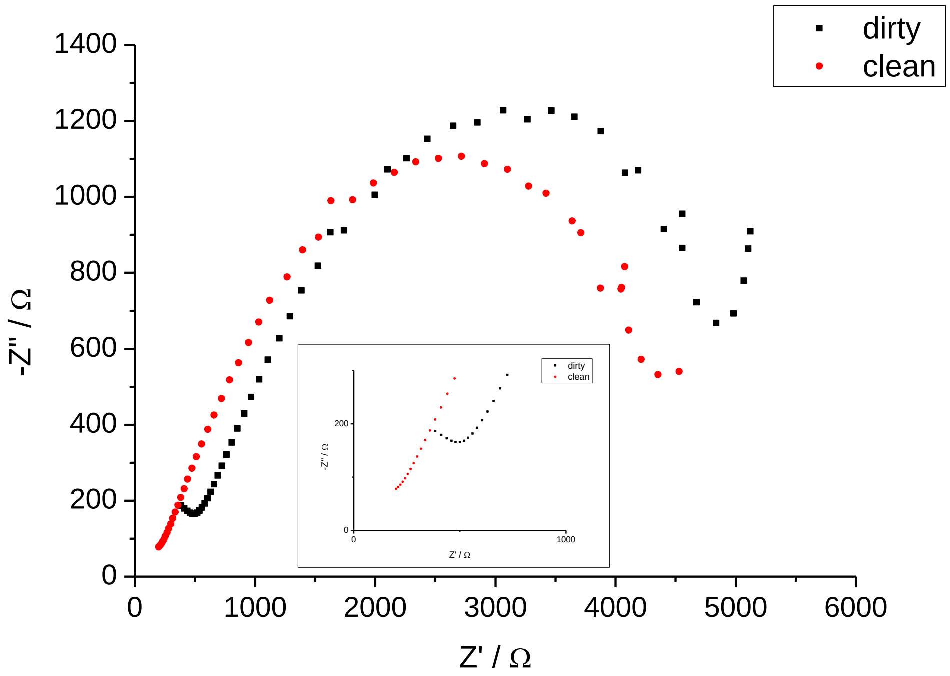

Figure 4-9: The EIS response at a fixed E_{DC} of an array of platinum square microelectrodes with 50 µm edge and 4D spacing in 10 mM potassium ferricyanide solution before and after cleaning in 1.0 M H_2SO_4. Inset shows change to high frequency features of R_{CT} and C_{DL} in parallel. The cleaning process has reduced both the real and imaginary components to the impedance.

The cleanliness of the electrode can dramatically reduce the charge transfer resistance, so that at high frequencies it is only the diffusional response of the electrode that is visible on the Nyquist plot. As well as the shift along the Z'-axis corresponding to the reduction in resistance, or real component, there also appears to be a small reduction in the imaginary component to the impedance response, demonstrated by the slight shift down the Z"-axis.

While this technique gives valuable information about the electrode response this technique was considered inappropriate for routine measurement of the cleaning efficiency of these protocols. The technique was time-consuming as the electrode must be transferred to a potassium ferricyanide solution and impedance data collection was relatively slow. The ability to initially judge the end of the cleaning process by CV within the cleaning solution is therefore considered to be the optimal approach.

4.5 Tungsten Microelectrode Pre-treatment

The platinum electrodes and arrays are designed for aqueous, ambient temperature systems as platinum is inert under these conditions. For the higher temperature, molten salt, studies tungsten was considered to be a more appropriate metal for use in electrodes. This is due primarily to the lower cost of tungsten in comparison to platinum, allowing for more efficient use of resources when testing a new system. Tungsten is a refractory metal and is chemically inert under extreme conditions. Tungsten is frequently used as an inert electrode on the macro-scale in molten salt systems. At room temperature however there is a natural oxide layer that is electrochemically insulating making it a poor metal for room temperature systems.

The salt used in high temperature studies is anhydrous and oxygen present can cause significant corrosive effects. It is highly important to therefore minimise the tungsten oxide layer in pre-treatment however it should be noted that under the 500 °C lithium chloride-potassium chloride fused molten salt conditions the electrode is in the sealed system as the salt heats up and goes through a cleaning process. The high temperature of the system, the length of time to reach this temperature and the release of oxygen or water from the salt mean that some tungsten oxide formation is inevitable.

An attempt was made initially to clean tungsten microelectrodes through the same method as the platinum for comparison, with the potassium chloride electrolyte cleaning protocol. These microelectrodes had been previously used and were over a year old so their oxide layer will have been relatively thick. The cleaning was found to be inappropriate for the metal as the only signal showed high resistance and the current output was a factor of two lower when compared to the current at a platinum electrode of the same area. The oxide layer is therefore insulating the metal to a high degree. The comparison of the two electrode metals in potassium chloride solution can be seen in Figure 4-10 below.

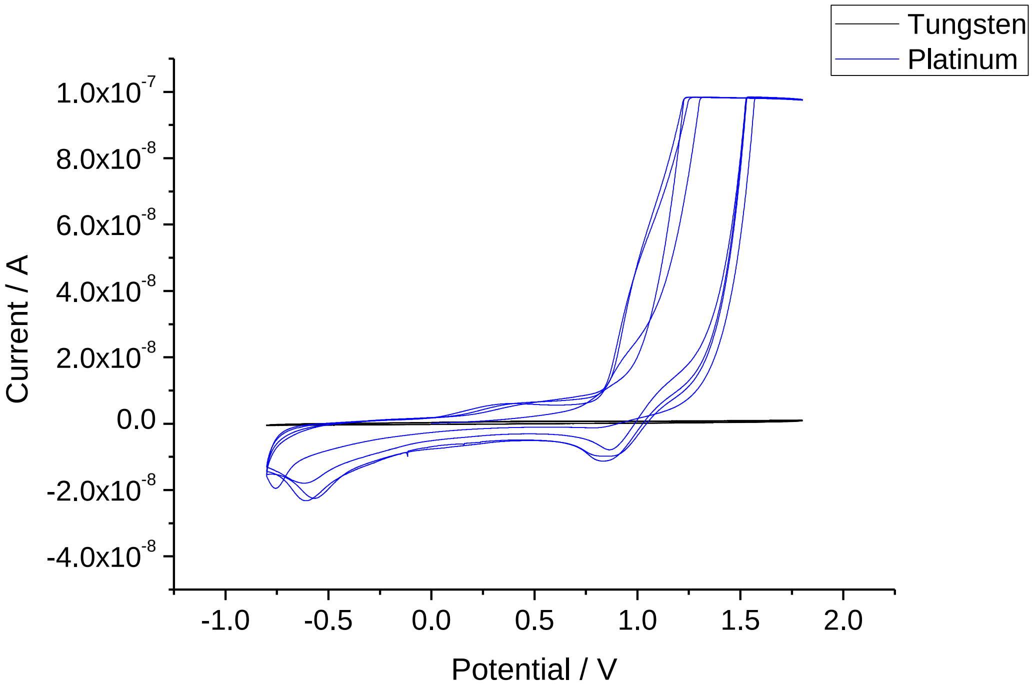

Figure 4-10: Cyclic voltammogram of electrode cycling in potassium chloride solution showing current output of two metals. Scan rate 100 mVs^{-1}.

Anik and Osseo-Asare[12] have constructed a pH-Eh diagram of tungsten, seen in Figure 4-11. From this it appears that within the solvent limits, at the dashed lines, pure tungsten is not stable in aqueous solutions of any pH.

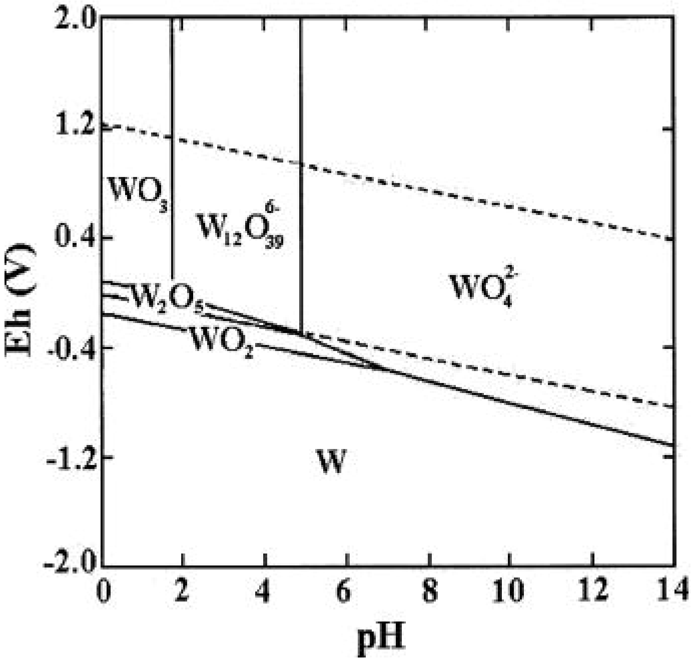

Figure 4-11: Eh-pH diagram for tungsten-water[12]

However, if a tungsten oxide, such as the WO_4^- ion, could be removed from the electrode surface by dissolution, this could reveal tungsten underneath with minimal oxide coverage. Therefore chemical cleaning with various solutions were tried, to remove tungsten oxide build up.

Newly fabricated tungsten microelectrodes, where the surface oxide should be thin and stored with a photoresist protective layer, were used to find the best cleaning solution. The initial solution was 0.1 M potassium chloride electrolyte as used previously. The electrode was stored in the solution for an hour.

Electrochemical cycling in potassium chloride solution was repeated, shown in Figure 4-12, as a method of visualising how electroactive the tungsten electrode was and therefore how much oxide was present. The electrode shows higher initial currents in comparison to the old electrode used previously consistent with a thick passivating oxide layer. The current response of the tungsten electrode was seen to reduce in magnitude as voltammetry in potassium chloride continued (scans go from red to purple). This is expected, due to the oxide formation in the cyclic voltammetry, but the initial scan gives information about the chemically treated layer.

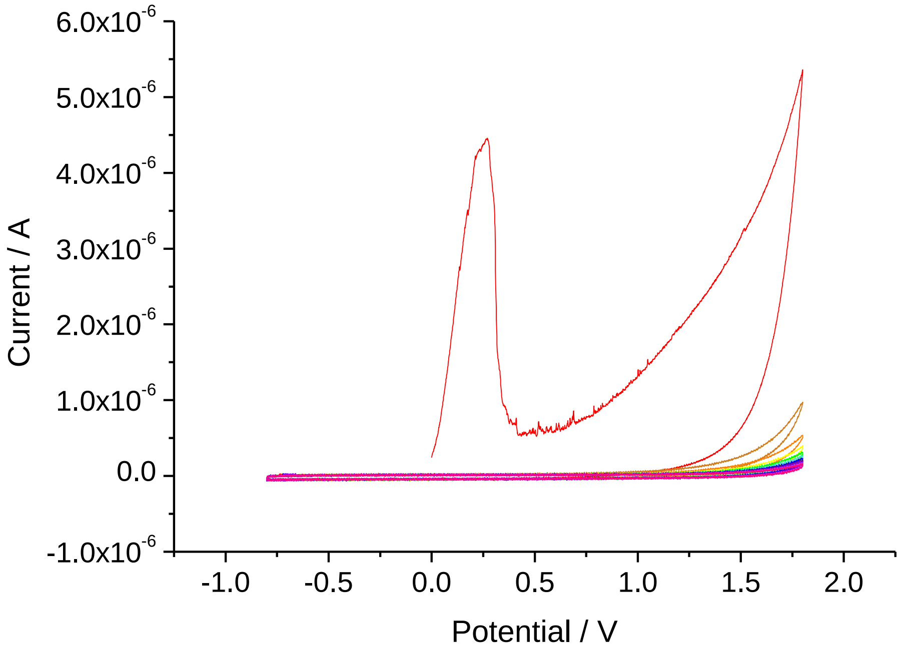

Figure 4-12: Cyclic voltammogram of 50 μm edge tungsten electrode cycling in potassium chloride solution after chemical cleaning in the solution. Scan rate 100 mVs^{-1}.

Literature of sensitive tungsten analytical tools showed two potential cleaning agents: concentrated hydrofluoric acid[13] and highly concentrated potassium hydroxide solution[12]. There have been papers reporting that hydrofluoric acid would etch away the silicon nitride passivation layer on the tungsten device, this method was therefore discounted.[14] Silicon nitride however does appear to resist potassium hydroxide etching.[15]

An acidic solution will form WO_3, from the E_h-pH diagram, and this could be verified in acids less dangerous than HF. Therefore a solution of 1.0 M sulfuric acid was used for an acidic chemical treatment, as used for electrochemical cleaning in the platinum microelectrodes. Chemical treatment in sulfuric acid produced no visible bubbles. After it was suspended in solution for an hour it was cycled in potassium chloride, shown in Figure 4-13. This electrode showed very low currents in comparison to the KCl–cleaned solution indicating that the acidic solution promoted a thick WO_3 film formation, as expected.

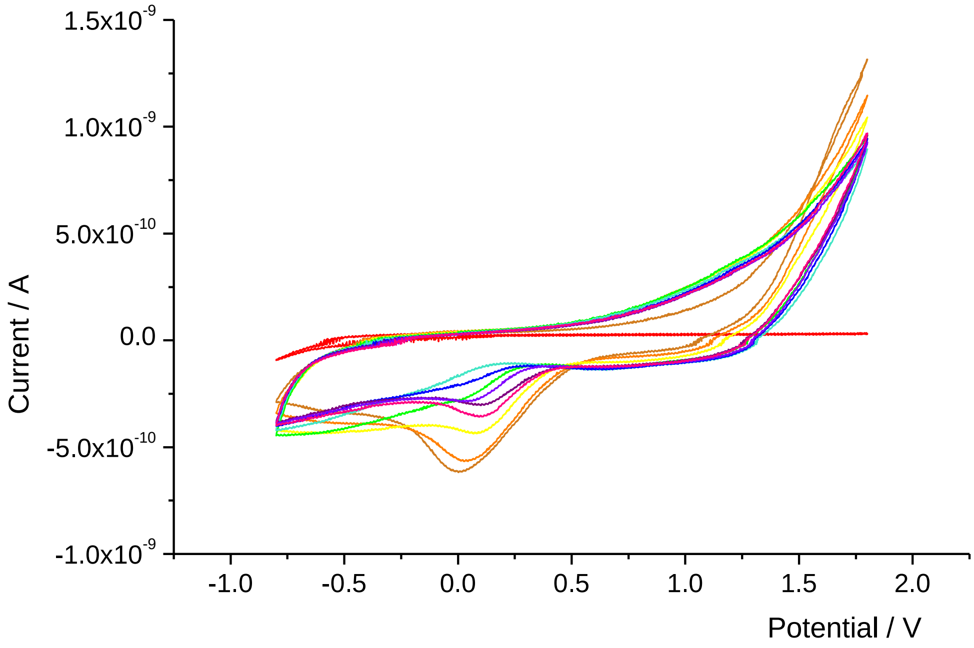

Figure 4-13: Cyclic voltammogram of 50 µm edge tungsten electrode cycling in potassium chloride solution after chemical cleaning in sulfuric acid solution (successive scans from red to purple). Scan rate 100 mVs^{-1}.

Chemical cleaning in 6.0 M potassium hydroxide solution was performed by soaking a device in solution for an hour. Afterwards the electrode surface cleanliness was characterised by cyclic voltammetry, seen in Figure 4-14. The cyclic voltammetry showed much greater current output, suggesting that the oxide layer had indeed been removed to a greater extent, due to the likely dissolution of WO_4^{2-}.

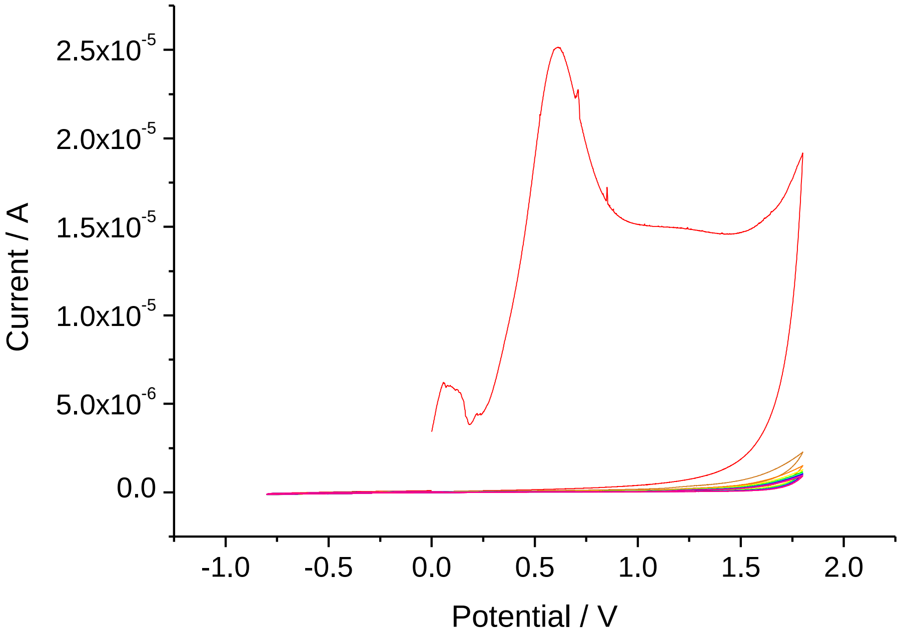

Figure 4-14: Cyclic voltammogram of 50 μm edge tungsten electrode cycling in potassium chloride solution after chemical cleaning in potassium hydroxide solution(successive scans from red to purple). Scan rate 100 mVs^{-1}.

Observation of the device during the chemical cleaning however showed bubbles forming on the edge of the device suggesting that a chemical reaction was occurring, but at an area other than the active electrode area. The fact that the bubbles were large enough to be visible suggested a relatively vigorous reaction. This can be seen in Figure 4-15.

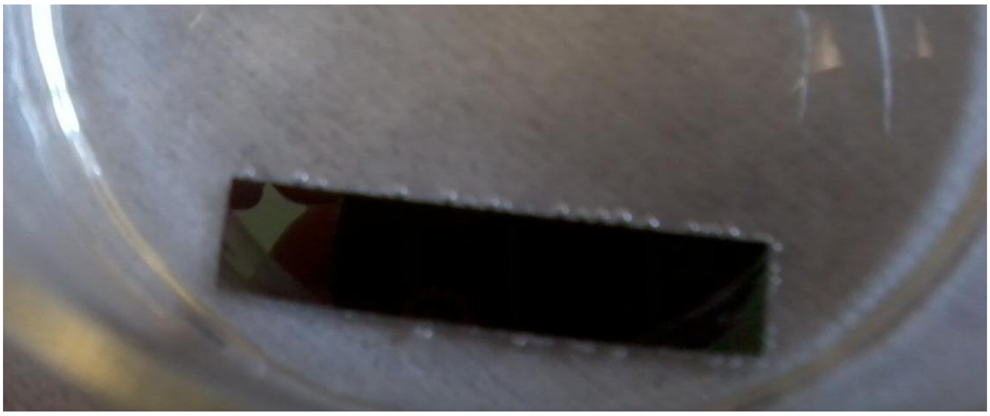

Figure 4-15: Image of the tungsten microelectrode device in a 6 M solution of potassium hydroxide solution after ten minutes. The bubbles around the device suggest a reaction occurring, not on the electrode.

The device was studied under a USB digital microscope, with images seen in Figure 4-16, to check for any observable effect of corrosion from the potassium hydroxide solution. In comparison to the device cleaned in potassium chloride the edge shows a roughened surface, suggesting that a chemical attack was occurring.

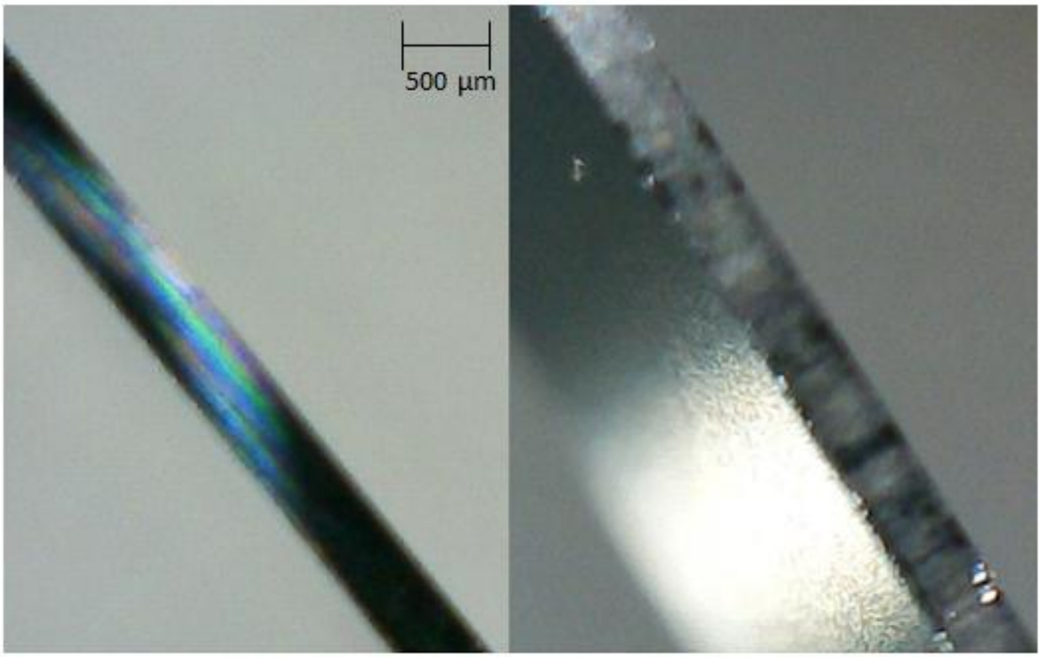

Figure 4-16: Image under a USB microscope. The microelectrode device edge after chemical cleaning in potassium hydroxide solution on the right looks rougher than that of the KCl cleaning performed on the device seen on the left.

The electrode was checked for signs of corrosion using the scanning electron microscope. The SEM image for the potassium hydroxide solution soaked device can be seen in Figure 4-17, compared to the potassium chloride cleaned electrode. The metal of the electrode and the silicon nitride passivation layer both appear to be in good condition though there does appear to be some unusual build up at the edges of the electrode.

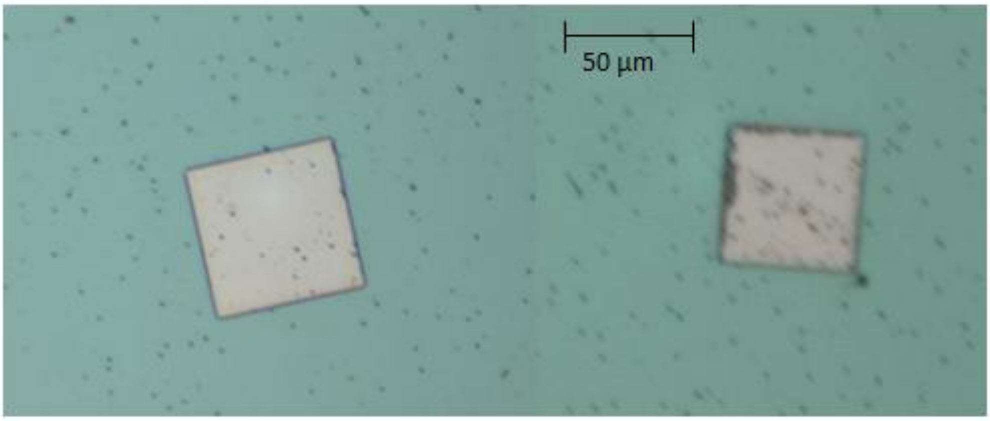

Figure 4-17: SEM images of the tungsten microelectrodes after cleaning procedures. The electrode on the left was cleaned in potassium chloride solution. The electrode on the right was cleaned in potassium hydroxide solution.

The microelectrode edges still appear to be well defined. Therefore the most likely reaction occurring was that after the wafer was diced into separate devices, which exposes silicon to chemical attack at the edges. This should have little or no effect on the electrode response unless products of this chemical attack are soluble.

The comparison of the electrochemical cycling after chemical cleaning in the three solutions can be seen in Figure 4-18 below. The effectiveness of the oxide removal is apparent and the KOH-cleaned electrode shows higher initial overall currents in comparison to the other cleaning protocols, with sulfuric acid showing the most passivation as expected.

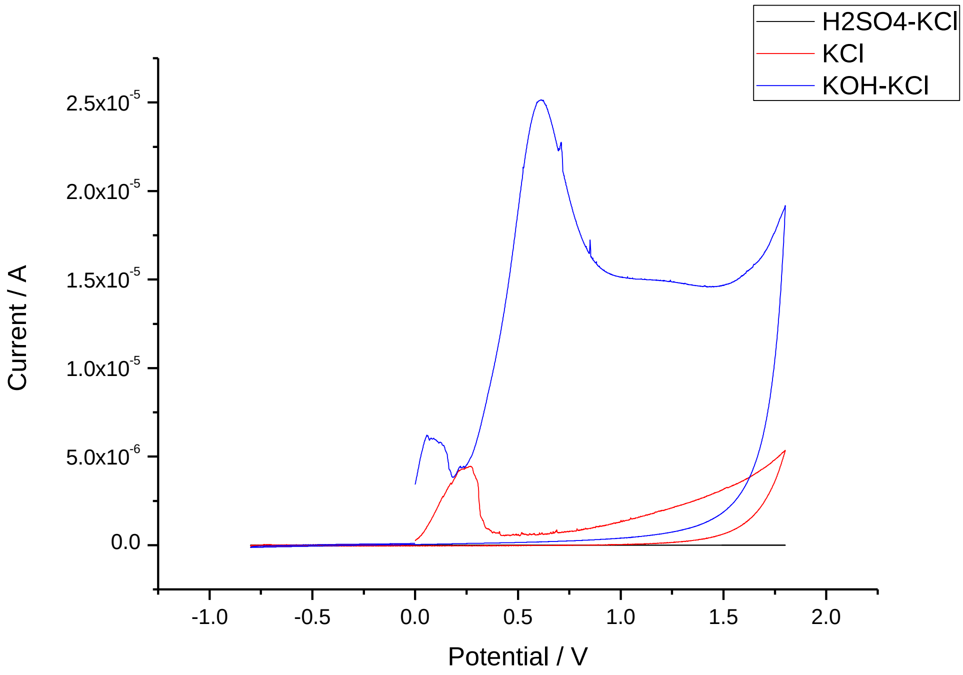

Figure 4-18: Cyclic voltammogram in potassium chloride solution for comparison of cleaning methodologies.

The validity of the cleaning protocols was also characterised by Electrical Impedance Spectroscopy (EIS) in 0.1 M potassium chloride solution. Impedance was measured at a DC potential of 0.25 V. The non-faradaic impedance gives information about the surface roughness of the electrode as well as the cleanliness. Figure 4-19 shows the difference in cleaning methods by EIS. The KCl cleaned and KOH-KCl cleaned electrodes show very similar responses but the KCl cleaned electrode shows a higher Z', the real component of the impedance, shifting it across the Z'-axis due to a higher value of R_{CT} consistent with a passivating oxide layer. The higher resistance accounts for the lower current outputs found in the CVs recorded.

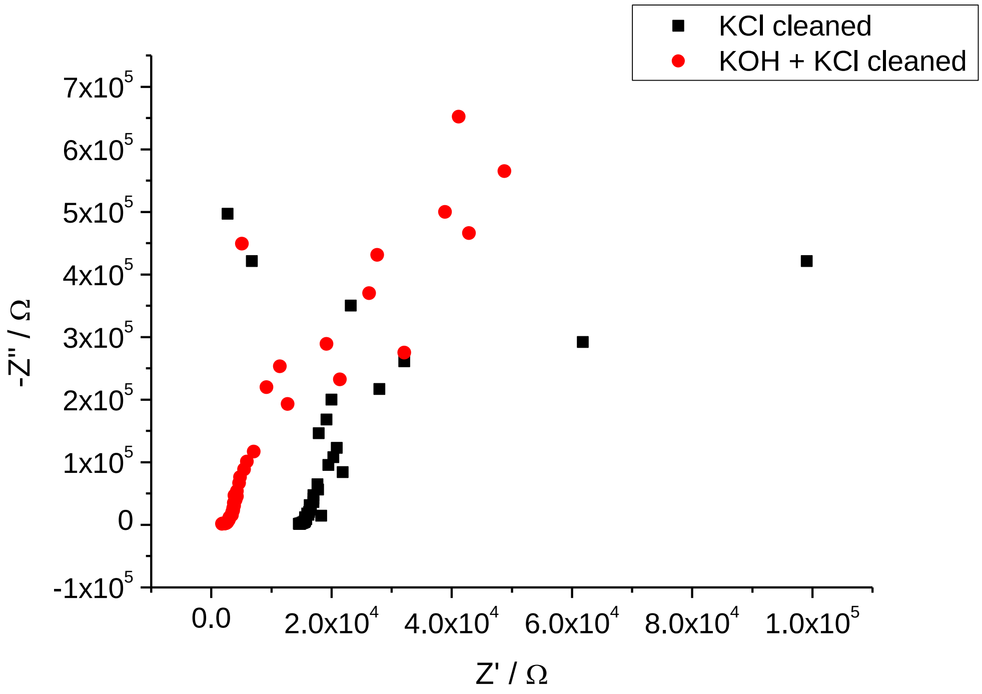

Figure 4-19: Nyquist plot of non-faradaic impedance of tungsten microelectrodes in potassium chloride solution, cleaned through different methods.

The tungsten microelectrode device cleaned in sulfuric acid solution also was characterised using EIS in potassium chloride solution however the signal was very noisy and much larger than that of the other two microelectrodes cleaned using alternative solutions. This huge impedance gave no useful data other than to indicate that a thick oxide film has been formed.

4.6 Conclusion

The importance of having clean microelectrodes for sensitive analytical measurements cannot be underestimated. The pre-treatment of microelectrodes is a valuable area of study and development. It is important that delicate, highly responsive devices be prepared and treated correctly. Several factors have found to be important in making the electrodes as efficient as possible including handling, storage and cleaning protocols.

Handling requires care due to the silicon wafer base of the devices. A high aspect ratio and typical silicon bonding mean that the devices have low mechanical strength and can be considered quite brittle. Therefore their handling should be minimised. In terms of chemical robustness the silicon nitride passivation layer is good protection for the device however gloves should still be worn to prevent skin-based oil from touching the electrode metal.

Microelectrode devices should be stored in a way that preserves the integrity of the electrode surface after production including minimising the formation of surface oxides by exposure to the environment. To ensure this the electrodes are kept with a protective photoresist layer until use. After use, although the devices cannot re-enter the clean room, they are stored to minimise the particulate build up from dust. In addition to these simple measures the electrodes undergo electrochemical pre-treatment steps to activate the electrode surface.

Cleaning of the platinum microelectrode was developed from a potassium chloride procedure used previously in the group. The optimum cleaning regime was found to be in 1.0 M sulfuric acid solution, using cyclic voltammetry to observe the metal oxide layer formation and reduction.

Once this response is stable no further electrode area can be activated and the electrode surface is considered to be clean.

In cleaning electrode arrays the cleaning process was found to be more efficient with larger electrodes, with 100 µm edge squares cleaning faster and better than 10 µm. This lends weight to the theory that the cleaning mechanism is via the formation of oxygen and hydrogen gases above the solvent window potential limits. As these bubbles are produced they dislodge any particulates on the surface. However if an electrode is completely blocked it is far less likely to be able to be electrochemically active and cannot produce the gases to clear the particulates. This is far more likely to occur on electrodes with relatively small areas. This can also lead to inactive elements on an array which would lead to a lower current response than expected.

Tungsten electrodes were also pre-treated to minimise a blocking oxide layer that forms naturally at room temperature. The methodologies that were used for the platinum electrodes were found to be inappropriate. Instead chemical soaking in 6 M potassium hydroxide solution appeared to remove a large amount of the oxide, resulting in higher current outputs. However, surface protection to avoid spontaneous oxide build up was considered a better strategy than trying to remove thick oxide layers that had formed.

4.7 References

---

[1] P. Łoś, G. Żabińska, A. Kisza, L. Christie, A. Mount, P.G. Bruce. Phys. Chem. Chem. Phys. 2 2000 p5449-5454 **DOI:** 10.1039/b004235h

[2] Z. Xie, S. Holdcroft. Journal of Electroanalytical Chemistry. 568, 2004, p247–260 http://dx.doi.org/10.1016/j.jelechem.2004.01.019

[3] Electrochemical Methods: Fundamentals and Applications. A.J Bard, L.R Faulkner. 2nd Edition. Section 13.6.

[4] Electrochemistry. J. Koryta, J Dvořak, V. Boháčková. English edition, 1970. p282

[5] O. Köster, W. Schuhmann, H. Vogt, W. Mokwa. Sensors and Actuators B. 76 (2001) 573-581 http://dx.doi.org/10.1016/S0925-4005(01)00637-2

[6] F. G. Will. Journal of the Electrochemical Society. 112 (1965) p451-455 **doi:** 10.1149/1.2423567

[7] Parylene technical document. Accessed from http://www.paryleneinc.com/pdf/PDS_Dimer_International.pdf at 22/01/2013

[8] C. Gabrielli, M. Keddam, N. Portail, P. Rousseau, H. Takenouti, V. Vivier. Journal of Physical Chemistry B. 110 (2006) p20478-20485 **DOI:** 10.1021/jp063055h

[9] D. Lowinsohn, H.E.M. Peres, L. Kosminsky, T.R.L.C. Paixão, T.L. Ferreira, F.J. Ramirez-Fernandez, M. Bertotti. Sensors and Actuators B, 113 (2006) p80-87 http://dx.doi.org/10.1016/j.snb.2005.02.024

---

[10] E. Komarova, K. Reber, M. Aldissi, A. Bogomolova Biosensors and Bioelectronics 25 (2010) p1389–1394 **doi**:10.1016/j.bios.2009.10.034

[11] P. Yu, G. Wilson. Faraday Discussions, 2000, 116, 305-317
DOI: 10.1039/b001611j

[12] M. Anik, K. Osseo-Asare Journal of The Electrochemical Society, 149 6 B224-B233 (2002) **doi**: 10.1149/1.1471544

[13] E. Paparazzo*, L. Moretto, S. Selci, M. Righini, I. Farne Vacuum 52 (1999) 421-426 http://dx.doi.org/10.1016/S0042-207X(98)00325-X

[14] D. M. Knotter, T. J. J. (Dee) Denteneer. Journal of the Electrochemical Society 148 (2001) F43-F46 **doi**: 10.1149/1.1348262

[15] C. Biasotto, J.A. Diniz, A.M. Daltrini, S.A. Moshkalev, M.J.R. Monteiro Thin Solid Films 516 (2008) p7777-7782 **doi**:10.1016/j.tsf.2008.03.010

Chapter 5: The Characterisation of Platinum Square Microelectrodes for Room Temperature Analysis

Previous work[1] has established the theoretical and experimental response of a 50 µm edge length square microelectrodes. In this chapter devices of single square microelectrodes with varying edge lengths were fabricated and characterised in potassium ferricyanide solution using cyclic voltammetry, electrical impedance spectroscopy and potential step voltammetry. Observed microelectrode responses were compared to simulated limiting currents to determine how square microelectrode response varies with edge length.

5.1 Introduction

Microelectrodes are an invaluable tool for electrochemical sensing and analysis. Their features and development have been described at length in Chapter 1. The microelectrodes in this study are novel due to their square shape. Square microelectrodes have been shown to have higher current responses than discs of the same area[1]. This advantage of square microelectrodes over other 2D shapes is thought to arise from their enhanced diffusion at corners. For these electrodes the analytical response was determined (Equation 2-7), though it remains to be established whether this equation applies at all values of edge length, or whether enhanced diffusion cause an increase in the geometric value, B, as edge length, L, decreases.

As diffusion to microelectrodes is enhanced at the edges and specifically the corners of the electrode, so increasing the relative proportion of edge leads to higher current densities. As the improved diffusion profile of microelectrodes is the primary reason for their advantages over macroelectrodes the enhancement of the diffusion profile through optimised electrode design offers a means to optimise the current response for a given electrode area. This enhanced current density at the edge of a microelectrode has been shown through simulation[2] and observed in electrochemical impedance spectroscopic studies[3]. The correlation of electrode size with electrochemical response has largely been limited to variations of discs and spherical electrodes[4]. There is very little literature to fully characterise the square electrode architecture.

The square microelectrodes in this study have been designed to have reproducible shapes and the shape itself is optimised. The larger current densities and enhanced mass transport should make these electrodes suitable for a wide range of applications once characterised.

5.2 Methodology

5.2.1 Electrode Fabrication

The square platinum electrode design with silicon nitride passivation was produced as described in Chapter 3 (Section 3.1.1), with metal deposited underneath the passivation layer, across the substrate, and an electrode area cut out of the passivation layer. The square electrode devices produced were 35 mm in length as can be seen in Figure 5-1, where the contact pad is clearly visible, along with a microscope image showing a 50 µm x 50 µm square microelectrode.

Figure 5-1: Square microelectrode device with contact pad. Microscope image shows a 50 µm edge microelectrode.

5.2.2 Experimental Techniques

All platinum square microelectrodes were cleaned by cycling in sulfuric acid solution, the method developed in Chapter 4. All experiments were performed in a Faraday cage to minimise electrical noise. All data were collected at ambient laboratory temperature as apparatus to control the temperature was incompatible with the Faraday cage set-up. The electrodes were characterised electrochemically in a solution of 10 mM potassium ferricyanide in 0.1 M KCl electrolyte using cyclic voltammetry, potential step voltammetry and EIS as documented in Chapter 3 (Section 3.3.2). COMSOL simulations, also discussed in Chapter 3 (Section 3.4), were compared to the experimental responses.

5.3 Results & Discussion

5.3.1 Initial Characterisation

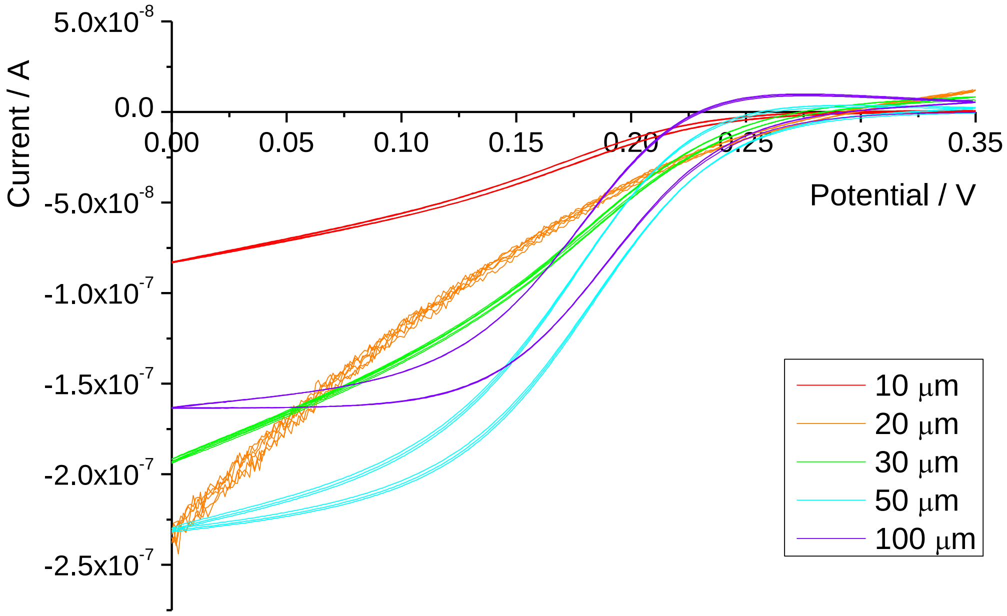

Figure 5-2: Cyclic voltammogram of platinum square microelectrodes of changing electrode edge in potassium ferricyanide solution at a scan rate of 5 mVs^{-1}.

Figure 5-2 shows the initial voltammetry responses, after cleaning, of the platinum microelectrodes in potassium ferricyanide at a 5 mVs^{-1} scan rate. Unexpectedly there is no clear correlation between electrode edge and current response, with the 50 μm edge electrode yielding the greatest current, while the 100 μm electrode showed a maximum current less than the 30 μm electrode. The 20 μm edge electrode showed a very noisy signal that likely indicated a connection issue, which presented a continuous challenge to the microelectrode analysis throughout the work. The scan rate effect on current for the 10, 20, 30, 50, and 100 μm edge square electrodes can be seen in Figure 5-3.

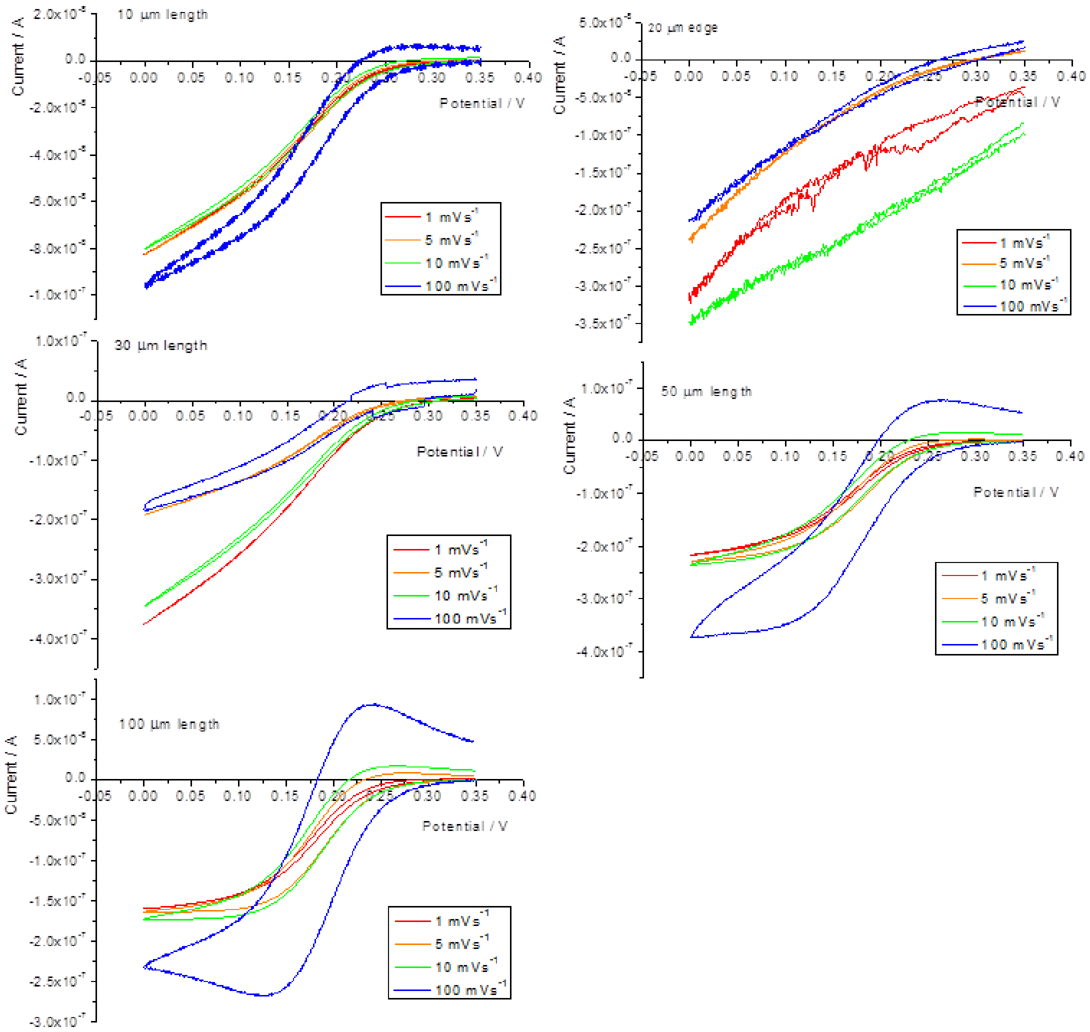

Figure 5-3: Cyclic voltammograms of 10, 20, 30, 50, and 100 µm edge square microelectrodes in potassium ferricyanide solution at various scan rates.

The 30 µm edge electrode shows a large limiting current increase during the data collection. This could be due to issues with the electrode definition, such as dirt falling off and revealing more electroactive area, or fractures developing in the passivation layer. The 20 µm edge electrode continues to show a resistive response, indicating a poor connection or surface insulating film.

As the scan rate was increased it can be seen that the current response changed significantly for some electrodes. The higher scan rate shows a more peak-like response rather than the sigmoidal response of the lower scan rates. This is particularly noticeable for the 50 and 100 μm edge electrodes. For all microelectrodes the lower scan rates show similar responses with minimal change in the current magnitude and shape of the plot between 1 and 10 mVs^{-1} scans, suggesting that the microelectrodes are subject to the same diffusion field at these timescales. At high scan rates the response appears peak-like as the potential changes too quickly for the electrode to exhibit a hemi-spherical diffusional response. This is due to the diffusion layer thickness, δ, first being smaller than the critical dimension of the microelectrode i.e. the electrode edge length, and then becoming larger.

The time for the transition to hemispherical diffusion is based on the relationship of $t = l^2/D$ where l is the electrode length and D is the diffusion coefficient[5]. For the 100 μm edge electrode in the solution (D= 6.98 x10^{-6} cm^{2}s^{-1} for potassium ferricyanide) the time for the diffusion layer thickness to approach the electrode edge length is of the order of 14 seconds. At a scan rate of 100 mVs^{-1}, this is beyond the time for the cyclic voltammogram which explains the peaked response as being due to the effects of time dependent linear diffusion. The 50 μm edge electrode can develop hemispherical diffusion around 3.5 seconds, comparable to the timescale of the CV, which explains the intermediate response between wave and peak.

The potential sweep rate also causes the charging current to be a factor. This charging current is then superimposed onto the faradaic current. This is due to the charging current being proportional to the scan rate, as shown by Equation 5-1.[6]

$$| i_c | = AC_{DL}\nu$$

Equation 5-1

Where | i_C | is the charging current, A is the area, C_{DL} is the capacitance of the double layer and ν is the scan rate.

At lower scan rates the 50 and 100 μm electrodes show the expected sigmoidal response of microelectrodes with mass transport limited currents. The shape of the 10 and 30 μm electrode responses however are stretched or smeared out and do not show the sigmoidal shape expected. This smearing of the peak suggests that charge transfer is inhibited and the reaction rate slowed. This is possibly due to insulating material on the electrode surface that affects the rate of electron transfer.

The measured limiting currents of these electrodes are generally much higher than those expected from COMSOL simulated current outputs. Table 5-1 shows the observed limiting currents, averaged from the 5 mVs^{-1} scans, and the computationally simulated response. These values are consistent with the equation of limiting current of a square microelectrode (Equation 2-7).

Electrode Length / μm	Observed Limiting Current / A	COMSOL Simulated Current / A
10	8.38 x10^{-8}	1.56 x10^{-8}
30	3.53 x10^{-7}	4.70 x10^{-8}
50	2.34 x10^{-7}	7.78 x10^{-8}
100	1.73 x10^{-7}	1.56 x10^{-7}

Table 5-1: Summary of the observed limiting currents from cyclic voltammetry and the simulated currents from COMSOL for each length square microelectrode.

In fact, on close visual inspection, the device was found to have multiple flaws in the silicon nitride passivation layer, shown in Figure 5-4, exposing the platinum underneath, allowing it to act as additional electrode area. In effect, these devices were acting as random arrays, or ensembles, of platinum microelectrodes, with a range of electrode shapes and sizes acting to sum the overall current response.

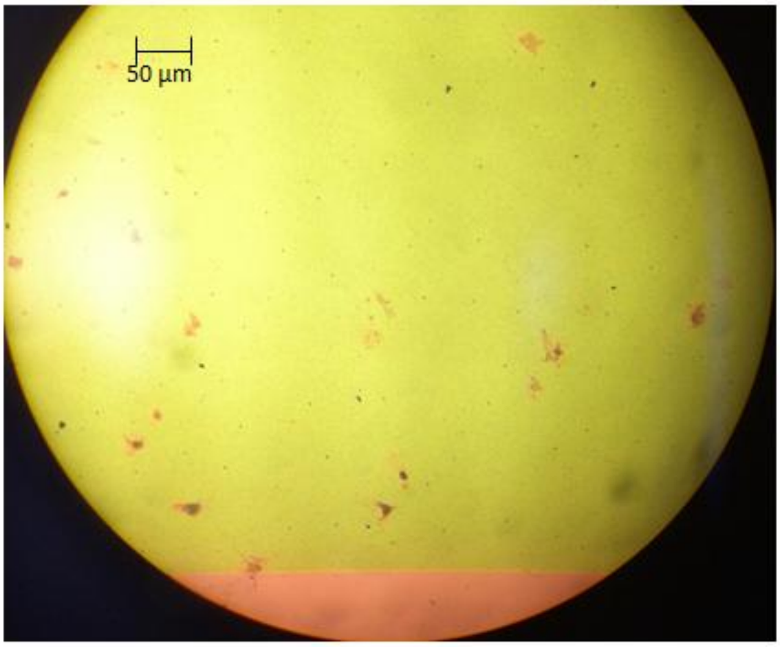

Figure 5-4: Image of damaged silicon nitride layer on microelectrode device. Pink colouring indicates defects in the layer, revealing the metal below.

The holes in the silicon nitride layers were found on each device made on the silicon wafer. This batch had therefore had an issue during fabrication. These blotchy flaws are in the of the order of tens of micrometre in length, comparable to the intended microelectrodes, which explains why the currents are larger than predicted by simulations. The measured currents are only slightly higher than the simulated currents suggesting that many of these flaws were either partially or fully insulated. The revealed electrode area was either unclean or the flaws only contributed slightly to the electrode.

Given that microelectrodes of small area are more difficult to clean electrochemically than microelectrodes of larger areas (activation of the surface), as discussed in the previous chapter (Section 4.3), it could be that many of the small fractures do not penetrate to the metal layer. This would leave the majority of flaws electrochemically inactive.

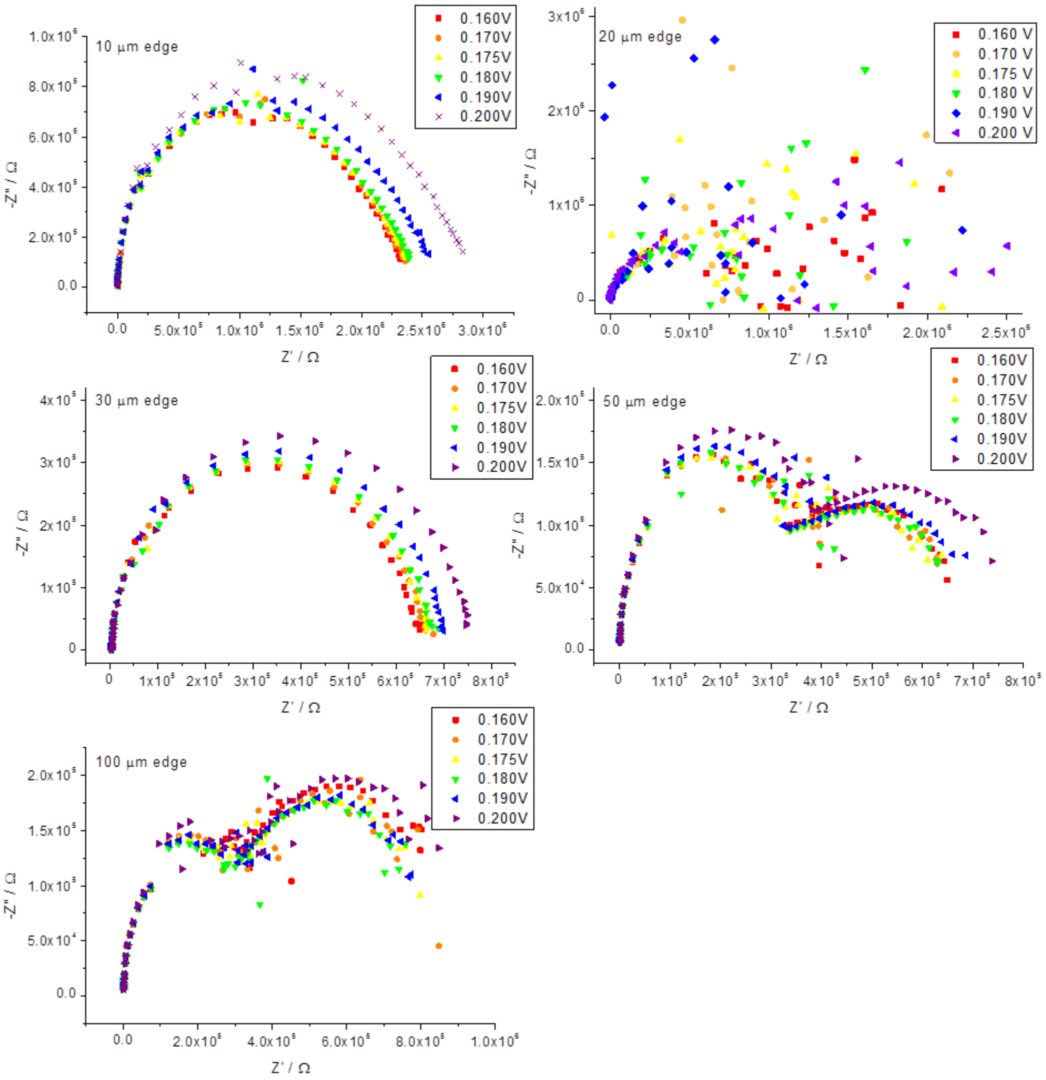

Figure 5-5: EIS response of 10, 20, 30, 50, and 100 µm edge square microelectrodes in potassium ferricyanide solution.

Electrical impedance spectroscopy was used to further characterise the square electrodes. This can be seen in Figure 5-5. The expected microelectrode response, as discussed in Chapter 2, is only observed with the 50 and 100 µm microelectrodes, as seen in the CVs in Figure 5-3. The equivalent circuit describing this response can be seen in Figure 5-6. The initial feature on the Nyquist plot, at high frequencies, corresponding to a resistor and capacitor in parallel on an equivalent circuit, is visible in each response. However the second feature, at lower frequencies, which describes the mass-transport properties of the microelectrode, is only apparent in the 50 and 100 µm length microelectrodes. The very large, scattered response of the 20 µm edge microelectrode shows the connection issues apparent in the CVs.

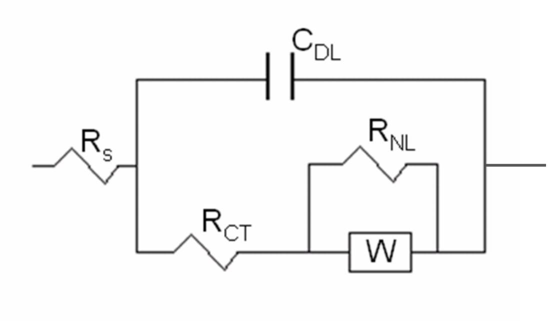

Figure 5-6: The equivalent circuit describing the impedance response of a microelectrode.

In Chapter 4 (Section 4.4) it was shown that unclean electrodes produce Nyquist plots with larger R_{CT}-C_{DL} features. Effectively, the unclean electrodes had kinetically slower responses, producing higher resistances and lower currents. Figure 5-7 shows the EIS response for the 10, 30, 50 and 100 µm edge electrodes at a fixed E_{DC}, 0.160 V. At this E_{DC} it can be seen that the 10 µm edge microelectrode has a larger impedance response than the others, indicative of the low current seen in the CV in Figure 5-2.

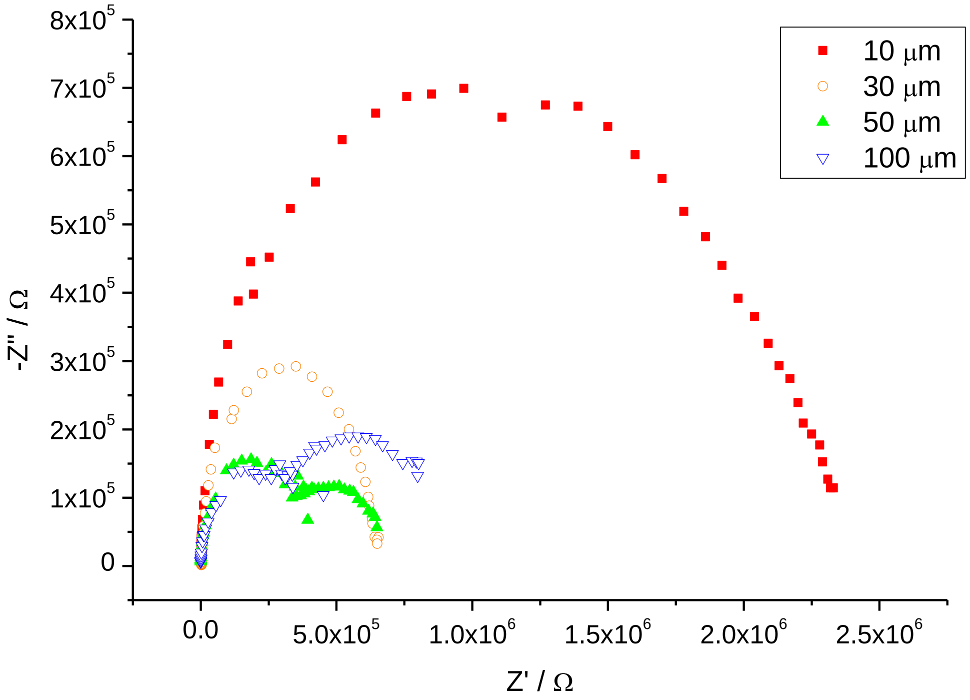

Figure 5-7: Nyquist plots for the 10, 30, 50 and 100 µm edge electrodes at a fixed E_{DC}, 0.160 V.

Given the difficulties in cleaning small areas of electrode it is possible that the defects observed in the passivation layer are not cleaned/activated during pre-treatment. These features would therefore contribute to a large R_{CT}-C_{DL} feature. A large number of these defects would greatly enhance this feature, this is effectively what is seen on the responses of the 10 and 30 µm electrodes. In addition the 50 µm electrode also shows a R_{CT}-C_{DL} feature greater in magnitude than that of the diffusion controlled region. This may again be attributed to areas of unclean electrode surface due to damaged areas of silicon nitride.

5.3.2 Second Batch Characterisation

Characterisation was repeated with a new batch of microelectrodes via cyclic voltammetry and potential step chronoamperometry. Figure 5-8 shows the voltammetry responses of the platinum microelectrodes in potassium ferricyanide at a 5 mVs^{-1} scan rate. Again there is no correlation between electrode length and current, with the 30 μm length microelectrode producing the largest limiting current and 20 μm the smallest.

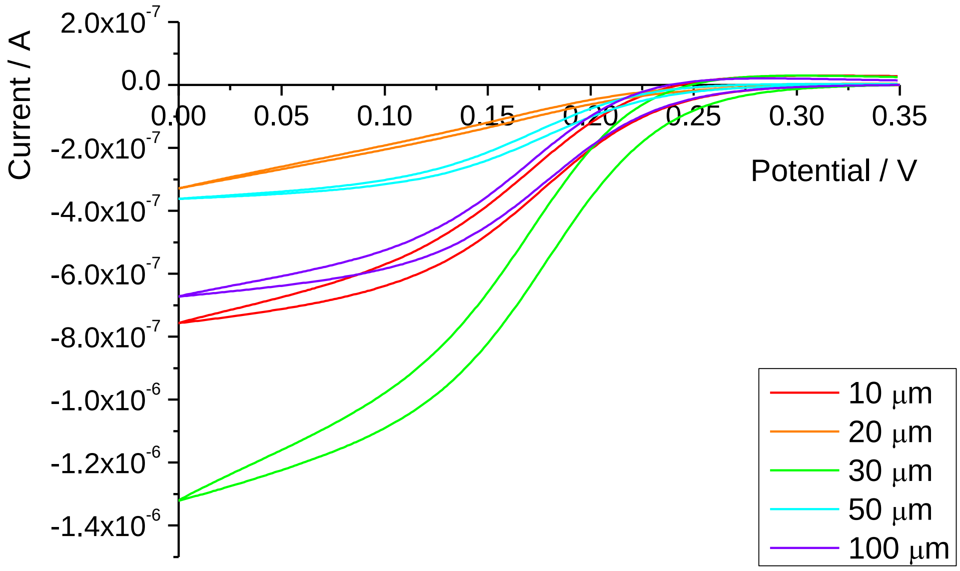

Figure 5-8: Cyclic voltammogram of platinum square microelectrodes of changing electrode length in potassium ferricyanide solution at a scan rate of 5 mVs^{-1}.

The scan rate effect on current for the 10, 30, 50, and 100 μm length square electrodes can be seen in Figure 5-9 below. The shapes of the CV plots again show the change in response from faster to slower scan rates. The 100 mVs^{-1} scan rates again show peak-like responses as the electrode is subject to linear diffusion. In contrast the 5 mVs^{-1} scan rates show the steady state, sigmoidal currents consistent with mass-transport limited current. Interestingly the 20 µm electrode shows an unusual shape, with the reduction reaction smeared, similar to the batch characterised previously. This may be due to insufficient cleaning of the electrode.

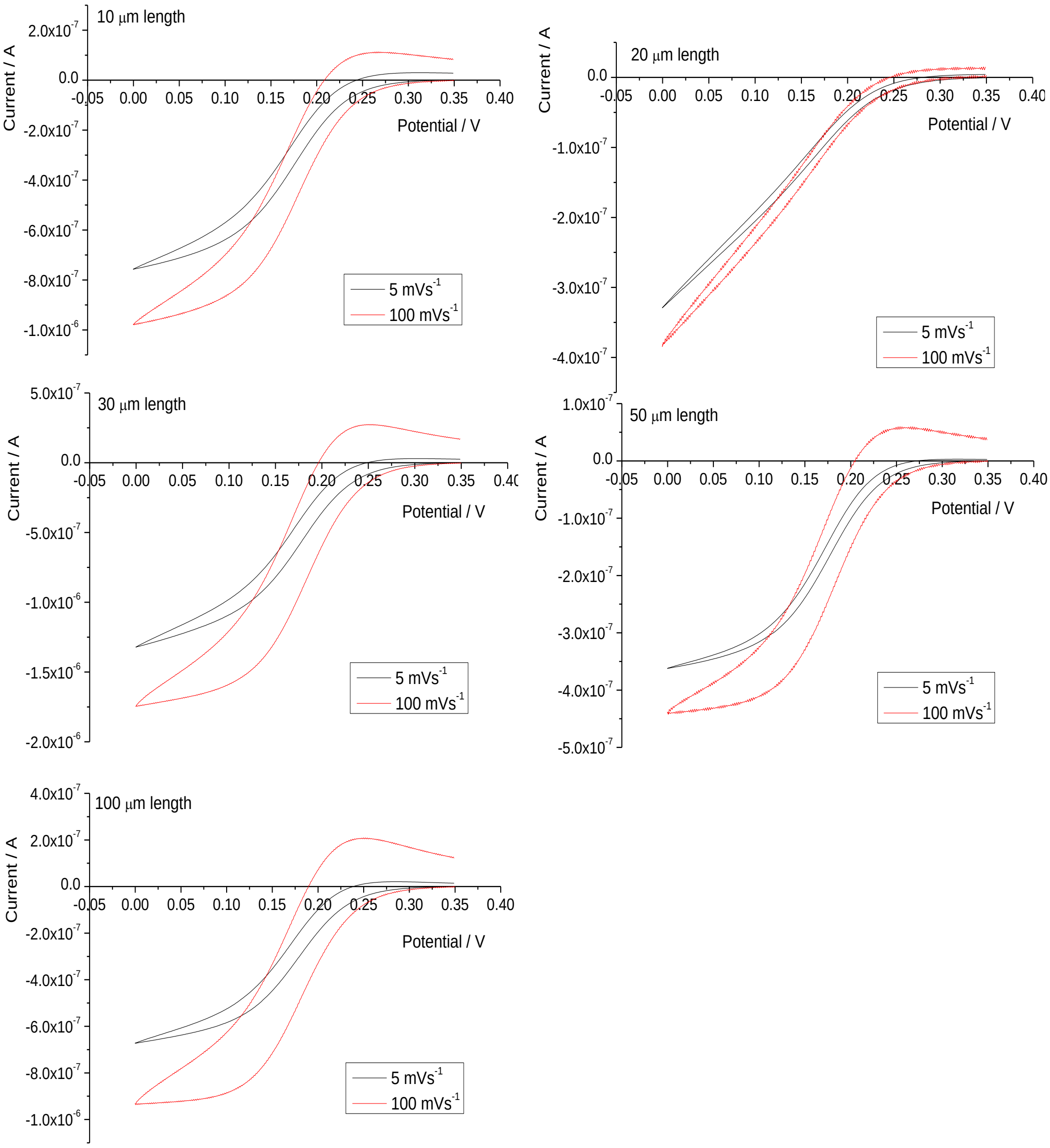

Figure 5-9: Cyclic voltammograms of 10, 20, 30, 50, and 100 µm square microelectrodes in potassium ferricyanide solution at various scan rates.

The limiting currents of the microelectrodes can again be compared to the COMSOL simulations and are summarized in Table 5-2. It can be seen that the observed limiting currents are higher than the simulated and, in fact, are higher again than the electrodes characterised previously.

Electrode Length / μm	Primary Observed Limiting Current / A	Secondary Observed Limiting Current / A	COMSOL Simulated Current / A
10	8.38×10^{-8}	7.87×10^{-7}	1.56×10^{-8}
20	--	3.33×10^{-7}	3.12×10^{-8}
30	3.53×10^{-7}	1.35×10^{-6}	4.70×10^{-8}
50	2.34×10^{-7}	3.65×10^{-7}	7.78×10^{-8}
100	1.73×10^{-7}	6.93×10^{-7}	1.56×10^{-7}

Table 5-2: Summary of the observed limiting currents from cyclic voltammetry during primary and secondary characterisation and the simulated currents from COMSOL for each length square microelectrode.

Once again, on inspection of the device showed that the silicon nitride passivation layer was damaged, allowing the platinum underneath to react and act as additional active electrode area. These areas were larger than those found in the batch fabricated previously. Rather than patches with numerous small breakages, these were single fractures, on a similar scale to the microelectrodes.

Figure 5-10: Image of the 10 µm length square microelectrode (circled bottom left) relative to the breakage in the passivation layer.

These large breakages in the silicon nitride will clearly contribute significantly to the current response of the device. Also, due to their large size, they clean as efficiently as the electrodes, or in the case of defects as shown in Figure 5-10 possibly more efficiently than the intended electrode, and so will give a large and clear response.

The current-time transients of the square microelectrodes were collected and are shown in Figure 5-11. The transients displayed are for the 10, 20, 50 and 100 µm length electrodes. As the potential was stepped with increasing amplitude it can be seen that, as expected, the larger the cathodic potential step the greater the reduction current.

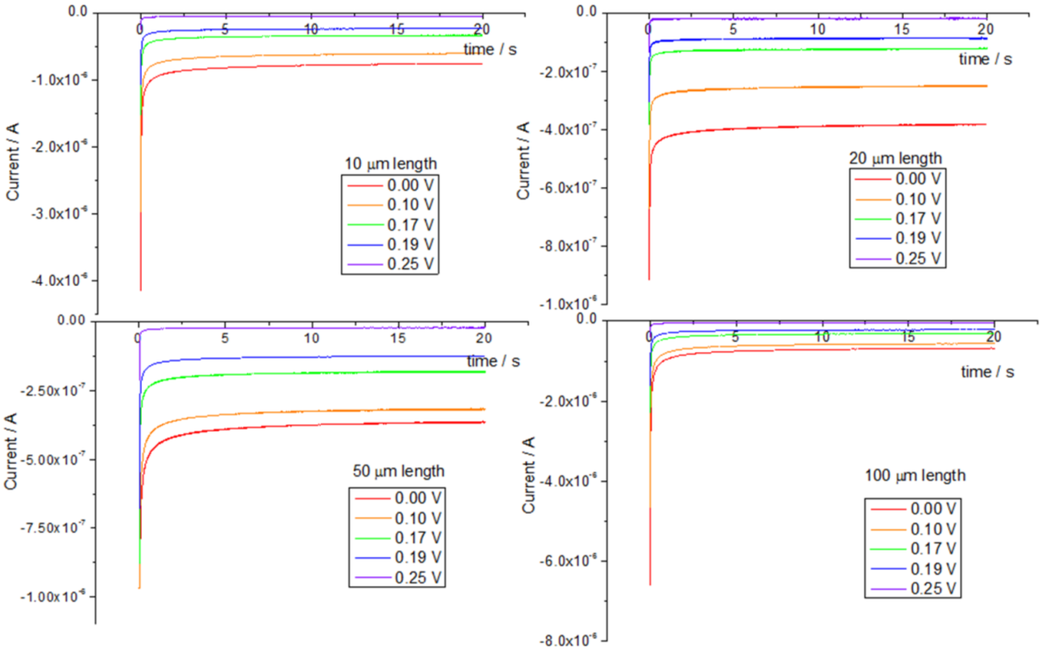

Figure 5-11: Chronoamperometry response of 10, 20, 50, and 100 µm square microelectrodes in potassium ferricyanide solution stepped to various potentials.

The current response of the electrodes can be seen more clearly on the logarithmic scales shown in Figure 5-12. The potential here is stepped to a potential that ensures the system is under diffusional control, 0.00 V, with all the potassium ferricyanide depleted instantaneously at the electrode surface.

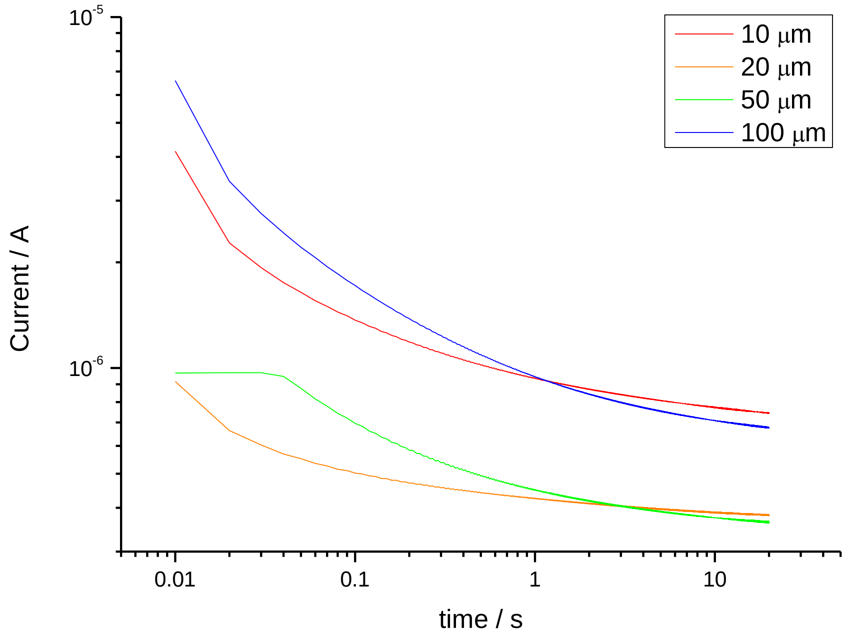

Figure 5-12: Chronoamperometry response of 10, 20, 50, and 100 μm square microelectrodes in potassium ferricyanide solution stepped to 0.00 V.

The measured current-time transients were compared to COMSOL simulated responses based on diffusion to a microelectrode using a reactive species with diffusion coefficient $D = 6.98*10^{-10}$ m^2s^{-1} and a bulk concentration of $[c] = 10$ $molm^{-3}$. Due to the additional exposed electrode area of the microelectrode devices the simulated time dependent responses are much smaller however, qualitatively they can be seen to follow a broadly similar shape, shown in Figure 5-13. This shows that the devices reach a steady state response over a relatively short time scale.

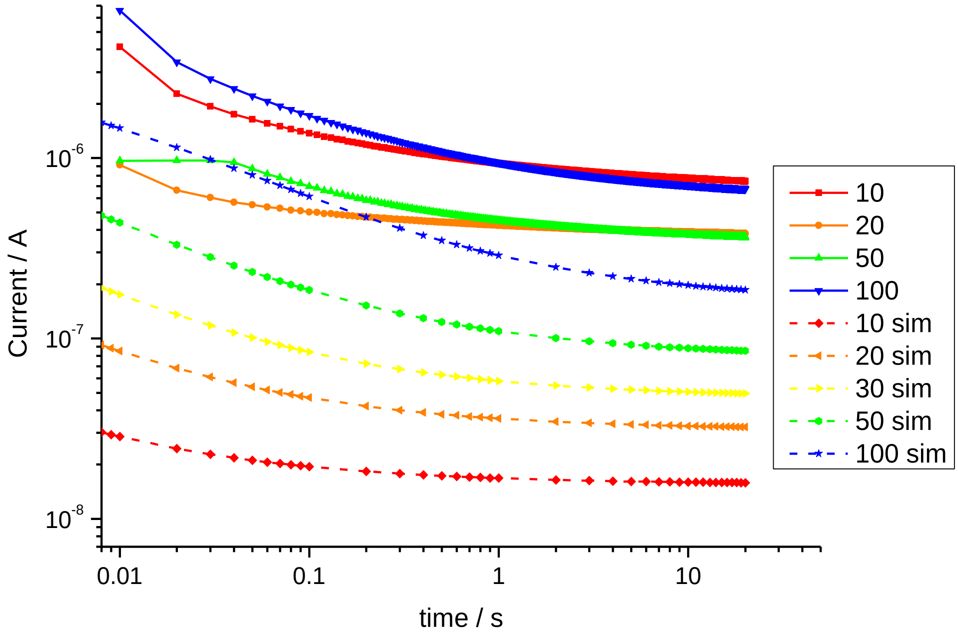

Figure 5-13: Observed and simulated response of 10, 20, 50, and 100 µm square microelectrodes in potassium ferricyanide solution stepped to 0.00 V.

The Cottrell equation (Equation 5-2) describes the current response due to linear diffusion to a macroelectrode. Linear diffusion has a profile where diffusion layer thickness increases proportionally to the square root of time[7]. Therefore the current decays proportionally $t^{-1/2}$ and so eventually should drop to zero current as the diffusion layer thickness extends and t→∞.

$$i = \frac{nFAc_A\sqrt{D_A}}{\sqrt{\pi t}}$$

Equation 5-2

A plot of |i| vs. $t^{-1/2}$ when the potential is stepped to a potential that ensures the system is under diffusional control, 0.00 V, with all the potassium ferricyanide depleted instantaneously at the electrode surface should provide a straight line through the origin if an electrode exhibits behaviour as described by the Cottrell equation. Figure 5-14 shows these plots for the microelectrode systems.

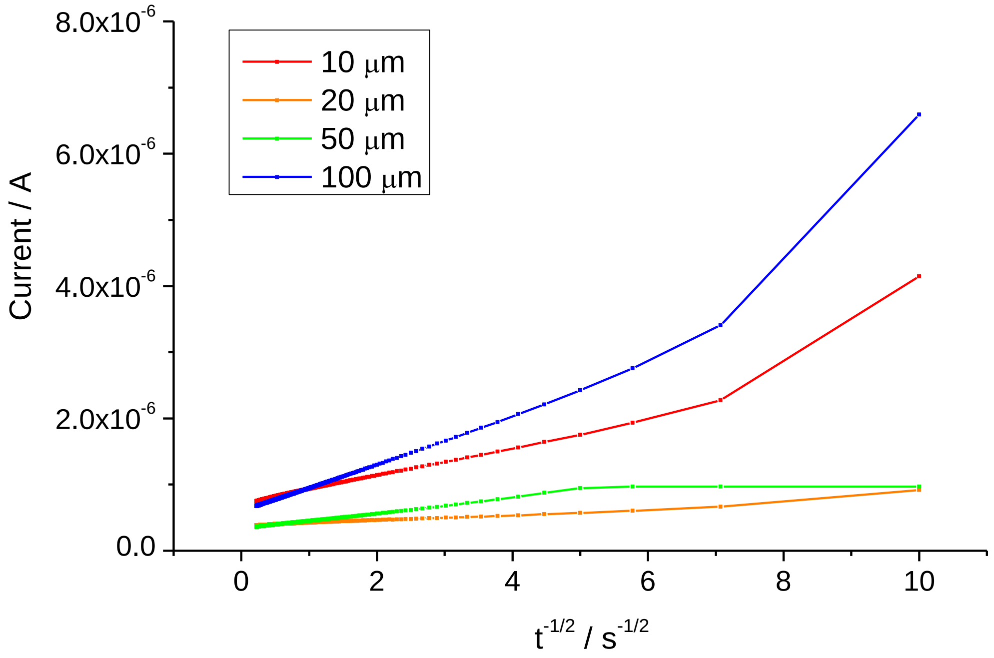

Figure 5-14: Plot of |i| vs. $t^{-1/2}$ when the potential is stepped from 0.35 V to 0.00 V.

Rather than the linear response through the origin the plot, as expected, shows a curved response where the current does not decay to zero. This is because in microelectrode disc theory, the current response over time is described by Equation 5-3[8] with the current dropping to the steady state limiting current, expected as t→∞.

$$i(t) = \frac{nFA\sqrt{D}c_{\infty}}{\sqrt{\pi t}} + 4nFDc_{\infty}r$$

Equation 5-3

where *r* is the radius of a microdisc. Here it can be seen that at short timescales, where $t^{1/2}$ is large, the first part of the equation will dominate the current response, giving macroelectrode-like linear diffusion. At longer timescales, as $t^{1/2}\rightarrow 0$ the time dependent part of the equation will decrease and the time independent part of the equation will dominate. This equation describes the two diffusion profiles at the disc microelectrodes: linear and hemispherical. The square microelectrode however does not have a radius. The equation is therefore modified to use the approximate equation of the square microelectrode limiting current as discussed in Chapter 2 (Equation 2-7). This modification can be seen in Equation 5-4.

$$i(t) = \frac{nFA\sqrt{D}c_{\infty}}{\sqrt{\pi t}} + 2.63nFDcl$$

Equation 5-4

In the case of the experimental data it can be seen that, while the limiting current of the square microelectrodes is unknown, the limiting current of the device can be approximated from the chronoamperometry response at long timescales. The limiting current estimated from the chronoamperometry response is summarized with currents observed in cyclic voltammetry in Table 5-3.

Electrode Length / μm	Observed CV Limiting Current / A	Estimated limiting current at t = 20 s / A	Ratio
10	6.87×10^{-7}	7.47×10^{-7}	0.92:1
20	3.67×10^{-7}	3.79×10^{-7}	0.97:1
50	3.38×10^{-7}	3.68×10^{-7}	0.92:1
100	6.00×10^{-7}	6.74×10^{-7}	0.89:1

Table 5-3: Summary of the observed limiting currents from cyclic voltammetry and chronoamperometry for electrodes of length 10, 20, 50, 100 μm.

There is good agreement between the observed limiting current from cyclic voltammetry and the values derived from the potential step to 0.00 V. The slightly higher current magnitudes from chronoamperometry indicate that some flaws in the passivation layer are sufficiently large that they take longer to reach a steady state current than the microelectrode, beyond t= 20 seconds for this data collection. Figure 5-14 also shows the current is still decreasing.

5.4 Conclusions

As this study shows, photolithographic manufacture of single microelectrodes can present a significant challenge. When depositing electrode metal across the substrate before a layer of insulator, as in the lift off process (described in Section 3.1) it is clear that the passivation layer is critical to defining the electrode area and that any flaws in it can have a notable effect on the quantitative response of the device.

As the first steps to making square microelectrodes however, the results are promising. The devices are electrochemically active and sensitive. While not quantifiable to a known active electrode area, the data displays microelectrode characteristics in cyclic voltammetry, impedance and potential step chronoamperometry.

Cyclic voltammetry showed devices with current magnitudes similar to those predicted by simulation of mass transport limited microelectrode responses. The responses were very sensitive, although the shapes of the plots were affected significantly by the electrode cleanliness. The cyclic voltammetry data also showed the effect of scan rate on the current, with high scan rates showing increased non-faradaic currents consistent with the capacitance expected.

Electrical impedance spectroscopy showed some microelectrode character from the device with the diffusion controlled region of the Nyquist plot displaying the non-linear resistance characteristic of steady state mass transport. This shows hemispherical diffusion, which is significantly different from linear diffusion to the electrode and what gives microelectrodes their advantage in sensing and measuring over macroelectrodes. In addition the results give credence to the theory, discussed in Chapter 3, that thorough cleaning of electrodes can have a significant effect on the device response. An unclean electrode can show kinetically slow responses during impedance spectroscopy and the Nyquist plot is subsequently dominated by a large -RC- feature.

Potential step chronoamperometry showed the changing response of the microelectrodes with time. There was a noticeable difference between the microelectrode response and the linear diffusion described by the Cottrell equation, indicating that hemispherical diffusion profiles developed relatively quickly at the microelectrodes. This hemispherical diffusion was shown to be time independent and gave reasonable agreement with the limiting currents found via cyclic voltammetry, albeit with some contribution from flaws in the insulator, which give rise to further active electrode area.

Together this data established the principle of microelectrode fabrication through photolithography. There remains to be addressed issues with insulator fidelity to achieve quantitative single microelectrode responses, but the fast sensitive properties of the devices opens up the potential for their use in sensing for extreme environments, as will be studied in the next chapter.

5.5 References

---

[1] H.L. Woodvine, J.G. Terry, A.J. Walton and A.R. Mount, Analyst, (2010) 135 p1058-1065 **DOI:** 10.1039/b924342a

[2] I.J. Cutress, R.G. Compton. Journal of Electroanalytical Chemistry, 645 (2010) p159-166 http://dx.doi.org/10.1016/j.jelechem.2010.05.007

[3] J.V. Ferrari, H.G. De Melo, M. Keddam, M.E. Orazem, N. Pébère, B. Tribollet, V. Vivier. Electrochimica Acta, 60 (2012) p244-252 http://dx.doi.org/10.1016/j.electacta.2011.11.053

[4] A. Molina, J. Gonzalez, M. C. Henstridge, R. G. Compton. Journal of Physical Chemistry C (2011) 115 p4054–4062 **DOI:** 10.1021/jp109587b

[5] C.G. Zoski, A.M. Bond, E. T. Allinson, K.B. Oldham. Analytical Chemistry, (1990) 62 p37-45. **DOI:** 10.1021/ac00200a008

[6] Electrochemical Methods: Fundamentals and Applications. A.J Bard, L.R Faulkner. 2nd Edition. Section 6.2.4

[7] Electrochemical Methods: Fundamentals and Applications. A.J Bard, L.R Faulkner. 2nd Edition. Section 5.2.1

[8] H.L. Woodvine. Development and Characterisation of Microelectrode and Nanoelectrode Systems (2011) University of Edinburgh

Chapter 6: Characterisation of Platinum Square Microelectrodes in Nitric Acid Media

In this chapter the single square microelectrode devices characterised previously are used to study a corrosive acid system, namely nitric acid. Nitric acid systems are used in the PUREX processing of nuclear fuel (discussed in Section 1.4.1) but there is currently no method for on-line detection in these systems. This would be a requirement for a robust engineering system and the development of microelectrode sensor systems for redox species detection is a valuable area of study. To prove this principle, the microelectrodes were assessed for their ability to monitor the deposition and stripping of silver in nitric acid and to detect the amount of nitric and nitrous acid in the medium.

6.1 Introduction

Microelectrodes have fundamental properties, discussed in Chapter 2, that make them a potential on-line sensor technology for extreme conditions such as highly concentrated acids. Due to the relatively low solution resistances and small double layer capacitances found with microelectrodes, these systems will have negligible non-Faradaic responses, giving greatly increased sensitivity to redox-active materials. Furthermore, their steady state response, independent of system convection makes quantification in harsh environment a real possibility.

As outlined in Section 1.4.1, during PUREX nuclear fuel reprocessing used fuel and fission products are dissolved in concentrated nitric acid, which converts them into metal nitrates. These metal nitrates then go through a solvent extraction process to separate the uranium and plutonium from fission products which remain dissolved in the acid.

Due to the importance of the system it is necessary to be able to monitor and fully understand the mechanisms and reactions during this reprocessing. This would ensure a safe and efficient industrial process. Concentrated nitric acid is subject to decay via the reactions[1]:

$$2HNO_{3(aq)} \rightleftarrows 2NO_{(g)} + 3/2O_{2(g)} + H_2O_{(l)}$$

Equation 6-1

$$2HNO_{3(aq)} \rightleftarrows N_2O_{4(g)} + 1/2O_{2(g)} + H_2O_{(l)}$$

Equation 6-2

This decay allows for a variety of additional chemical species in the media that can affect the stability of the mixture.

Nitric acid is a very useful reactive media. Nitrate, NO_3^-, can be reduced to a number of different products depending on the number of electrons transferred in the reaction[1], as shown in the Figure 6-1 below.

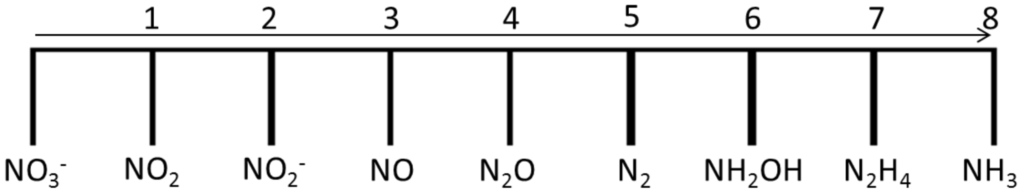

Figure 6-1: Typical reduction products of nitrate with increasing number of electrons in the reaction.

The products can have an effect on the chemical nature of the acidic solution. There has been much debate in the literature as to the mechanisms and products of nitrate reduction. Selectivity for the reduction product of nitrate can depend on the pH, concentration of nitrate in solution, electrode material[2] and the species in the solution.[3] The typical reaction in low pH, low nitrate concentration on a platinum electrode with a significant overpotential is the direct reduction to ammonia.[4] This reaction is highly dependent on NO production. NO adsorbs very strongly on platinum and further reactions to ammonia or hydroxylamine become possible. If however, the concentration of nitrate is increased NO is found in solution, rather than as NO_{ads}, and reactions to N_2 and N_2O are possible.[4]

At concentrations of nitric acid above 4 M the acid degrades to produce nitrite (NO_2^-) ions[4]. The presence of NO_2^- in the solution can create a reaction with nitrate groups to produce more NO_2^- ions by the reactions in Equation 6-3[5].

$$\begin{gathered} 2HNO_2 + 2H^+ \rightleftarrows 2NO^+ + 2H_2O \\ 2NO^+ + 2e^- \rightleftarrows 2NO \\ \underline{H^+ + NO_3^- + 2NO + H_2O \rightleftarrows 3HNO_2} \\ NO_3^- + 3H^+ + 2e^- \rightleftarrows HNO_2 + H_2O \end{gathered}$$

Equation 6-3

The presence of nitrite can lower current efficiencies of electrochemical reductions in nitric acid and interfere with analysis of mechanisms.[6] Nitrite itself also degrades in solutions of high acidity and high nitrate concentration to produce the colourless N_2O_4 and brown NO_2 gases.[7] This occurs by the reactions:

$$2H^+_{(aq)} + 2NO_2^-{}_{(aq)} \rightleftarrows NO_{(g)} + NO_{2(g)} + H_2O_{(l)}$$

Equation 6-4

$$2NO_{2(g)} \rightleftarrows N_2O_{4(g)}$$

Equation 6-5

$$2H^+_{(aq)} + NO_2^-{}_{(aq)} + NO_3^-{}_{(aq)} \rightleftarrows N_2O_{4(g)} + H_2O_{(l)}$$

Equation 6-6

In any concentrated nitric acid processes, including PUREX, HNO_2 is always present and concentration levels must therefore be monitored to detect or to prevent degradation of the solvent, and to assess the redox state of the system.

Platinum microelectrodes were used to study and characterise nitric acid systems to determine if they can be used for this monitoring. Initial studies involved scanning within the solvent window to characterise the nitric acid electrochemistry. Silver was selected as an ideal plating/stripping reaction and detection via deposition was studied using a one electron reaction before the nitric-nitrous acid mixture was probed to understand reactions in the solution. Of particular interest was whether the microelectrode systems would be able to withstand the harsh nitric acid environment to provide a microelectrode measurement system with sufficient longevity to enable practical deployment.

6.2 Methodology

6.2.1 Electrodes

The electrodes used in this study were discussed in Chapter 5. They were fabricated as described in Chapter 3 (Section 3.1.1) and were the second batch characterised in Chapter 5. These devices were platinum square microelectrodes however the previous characterisation found some holes in the silicon nitride passivation layer. These holes lead to an effective increased surface area for the electrode. Nonetheless the devices were electroactive and gave microelectrode-like steady-state responses.

6.2.2 Experimental Techniques

Platinum square microelectrodes were pre-treated by cycling in 3.0 M nitric acid (Fisher Chemical, analytical reagent grade, specific gravity 1.42). The data were collected in a Faraday cage to minimise electrical noise. A water bath to control the temperature was incompatible with this set-up and so data was collected at ambient laboratory temperature.

To prevent the reaction of chloride ions and silver ions, producing insoluble silver chloride, a double junction reference electrode was used with a saturated calomel electrode as the inner compartment and 3.0 M nitric acid solution in the second compartment. This prevented contamination of the solution by the reference electrode.

6.2.2.1 Cyclic Voltammetry

Cyclic voltammetry was performed in solutions of 3.0 M nitric acid. Silver deposition studies were performed in a 10 mM solution of silver nitrate (Sigma-Aldrich, 99+%) in 3.0 M nitric acid. The voltammetry was performed at various scan rates from 100.0 - 1.0 mVs^{-1}. Analysis of the nitric-nitrous acid systems was performed by making the appropriate concentration of nitric acid and then adding sodium nitrite (Sigma-Aldrich, ≥99%) to produce the intended NO_3^-/NO_2^- ratios.

The nitrite is subject to decay by Equation 6-7[5]. Therefore initial concentrations of nitrite in solution should be taken as an upper limit.

$$3H^+_{(aq)} + 3NO_2^-{}_{(aq)} \rightleftarrows 2NO_{(g)} + H^+_{(aq)} + NO_3^-{}_{(aq)} + H_2O_{(l)}$$

Equation 6-7

6.3 Results & Discussion

6.3.1 Cleaning performance, cycling in 3.0 M HNO3

Given the theory discussed in Chapter 4 that it is the production of hydrogen and oxygen bubbles during the cleaning process that removes particulate matter from the metal surface, the microelectrodes were pre-treated in nitric acid, akin to the methodologies described previously, by cycling between the solvent limits. As the system to be characterised was in 3.0 M nitric acid, this was the solution used to clean the platinum square microelectrodes. A representative cleaning scan is shown in Figure 6-2.

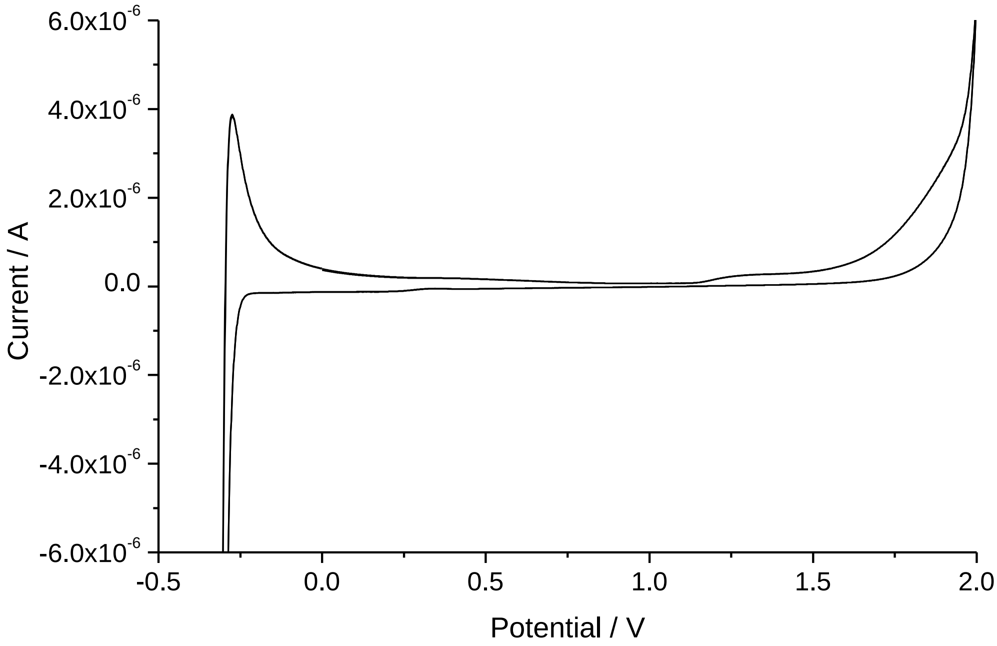

Figure 6-2: Platinum microelectrode response to nitric acid medium. The scanning of the potential window was used as a cleaning method akin to those found in Chapter 4.

The electrochemical window is defined between the gaseous oxygen and hydrogen production at 2.0 V and -0.25 V respectively. Between these solvent limits it can be seen in that there are small reduction and oxidation waves at -0.15 V and 0.00 V showing hydrogen adsorption on the platinum. An oxidation peak at 1.35 V shows oxygen adsorbed on the electrode surface however there is no visible reduction peak. It is worth noting that there is no detectable reduction of the nitrate group in the nitric acid.

6.3.2 Silver plating

Initial analysis of the lifetimes of the devices involved taking a simple one electron plating/stripping reaction and comparing the microelectrode response after sustained use in the acidic media. Using a 10x10^{-3} M solution of $AgNO_3$ in 3.0 M HNO_3, silver was plated on the square platinum microelectrode and stripped off in the reverse reaction. The scan rate was varied to monitor the response of the microelectrode, as can be seen in Figure 6-3.

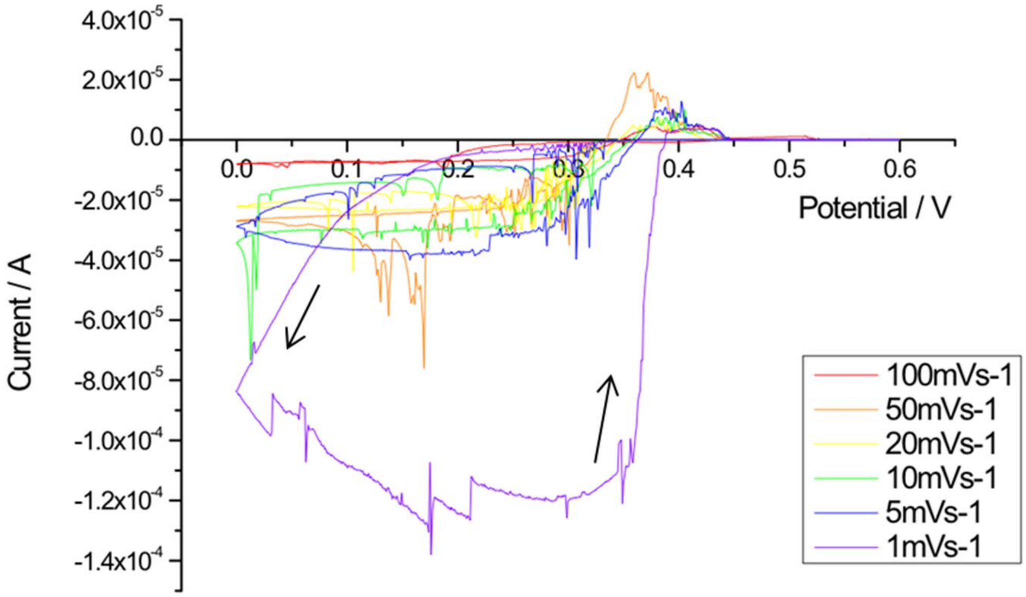

Figure 6-3: Platinum microelectrode response during the plating and stripping of silver at various scan rates.

The change in scan rate shows that as the potential was changed more slowly the amount of charge passed and quantity of silver that was plated increases. It is clear that the main features of these CVs are the steady state reduction current seen at fast sweep rates below +0.3 V, consistent with mass transport limited silver plating, and the associated oxidising peak above +0.35 V consistent with silver stripping. At slower scan rates the current increases greatly with time indicative of an increase in the electrode area due to silver plating and dendrite formation. There are also several spikes during the cathodic currents that are likely due to silver dendrite deposits falling off the electrode and in to the bulk solution. Indeed, solid silver was observed in solutions after electrochemical analysis. This would also explain why the reverse peaks of the stripping reaction are noticeably smaller.

The electrode was then stored in 3.0 M nitric acid solution overnight and the plating/stripping response was re-measured to see if the device had been corroded by the acid media. If there had been a chemical effect on the silicon nitride insulation layer more platinum would likely have been revealed on the device, as the platinum layer covering the device connects to the contact pad. This metal would act as an additional electrode surface and current responses would therefore increase.

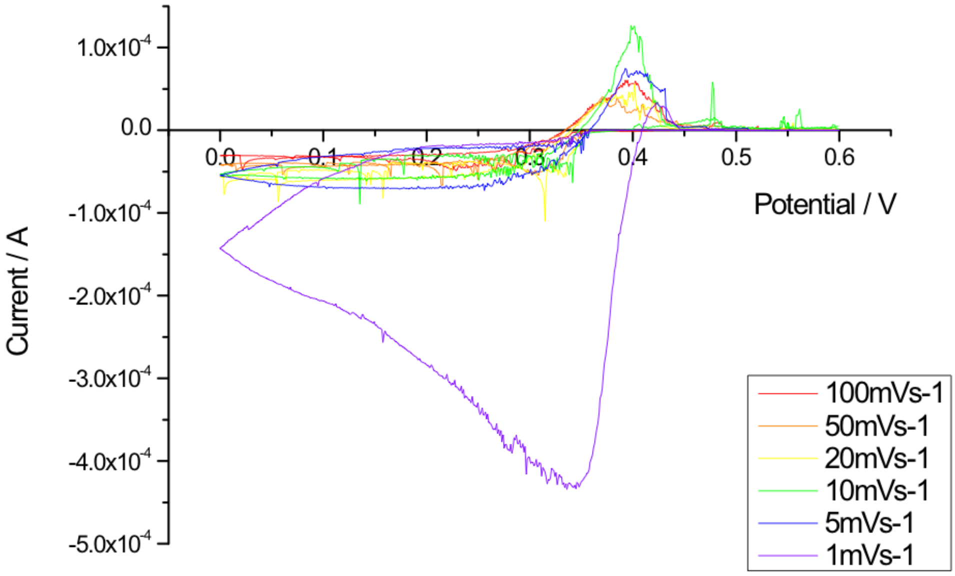

Figure 6-4: Platinum microelectrode response during the plating and stripping of silver at various scan rates after prolonged contact with the 3.0 M HNO_3 solution.

Figure 6-4 shows the response of the device after 18 hours submerged in 3.0 M nitric acid solution. It is seen that the current response to scan rate remains qualitatively similar. However, in terms of current magnitude, there is a distinct increase, from 1.4x10^{-4} to 4.3x10^{-4} A at 1 mVs^{-1} scan rate. The increase in current, summarised Table 6-1, suggests that a greater electrode area was available for reactions to occur.

Scan rate / mVs-1	**Day 1 Silver Plating Charge / C**	**Day 2 Silver Plating Charge / C**	**Relative increase between Day 1 and Day 2**
100	4.010 x10^{-5}	2.061 x10^{-4}	5.1
50	3.189 x10^{-4}	5.322 x10^{-4}	1.7
20	6.610 x10^{-4}	1.722 x10^{-3}	2.6
10	1.389 x10^{-3}	3.135 x10^{-3}	2.3
5	3.099 x10^{-3}	6.299 x10^{-3}	2
1	4.795 x10^{-2}	1.253 x10^{-1}	2.6

Table 6-1: Charge passed during plating on a single platinum microelectrode on subsequent day after storage in 3.0 M nitric acid with changing scan rate.

The silver plating shows much higher currents and deposition charges on the second usage. As the solution has been kept the same it seems unlikely that this is due to a concentration change in the amount of silver available for plating. Observation under the microscope, as shown in Figure 6-5, shows minimal corrosion of the electrode after extended periods of time in the nitric acid. There were also no obvious sign that the silicon nitride insulation layer had been degraded. It is possible that the improved currents are due to the cleaning procedure of cycling potentials in the acid on the second day allowed for greater electrode area availability than on the first day of analysis. However for future studies with the microelectrodes no device was used for more than a single day of study to minimise any possible effects of corrosion or passivation layer degradation.

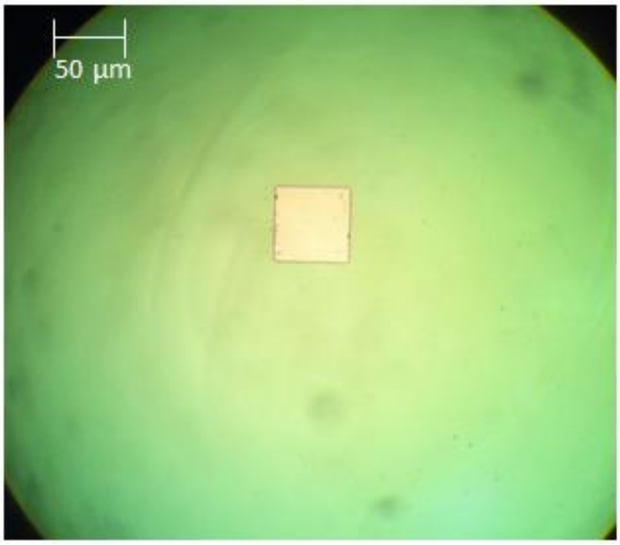

Figure 6-5: Photo of the 50 µm platinum square microelectrode after two days usage and storage in 3.0 M nitric acid solution.

When the working electrode was passing anodic current it was noted that a reaction was occurring at the counter electrode with significant vigour. This reaction produced a dark brown species, most likely reduction of nitric acid to nitrogen dioxide gas that then diffused through the solution away from counter electrode.

6.3.3 Characterisation of the Nitric-Nitrous Acid System

Cyclic voltammetry was then used to study different compositions of mixed nitric-nitrous acid solutions. Figure 6-6 shows the CV for various concentrations of NO_2^- in nitric acid at a 5 mVs^{-1} scan rate.

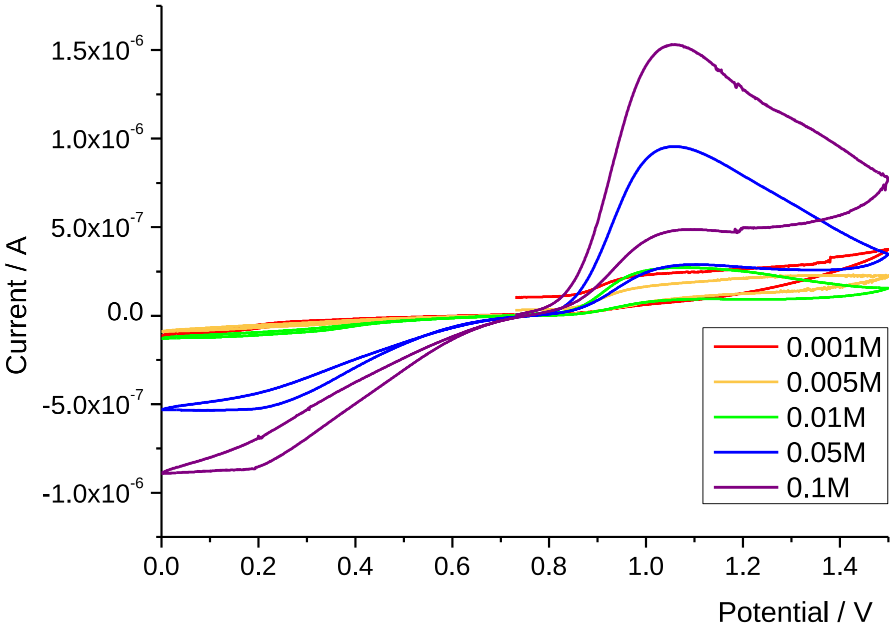

Figure 6-6: CV of the nitric-nitrous acid system with a 3.0 M concentration of HNO_3 and changing concentrations of HNO_2.

The largest feature is an oxidation peak at +1.05 V. This is a peak rather than a wave, which is unusual for microelectrodes, and is not present in the HNO_3-only scan. Given the dependency of this peak on HNO_2 concentration, this is most likely the oxidation of HNO_2 to nitrate, the reverse of Equation 6-3. It is likely that there is an accompanying adsorption to the electrode surface at potentials above 1.05 V that is causing the peaked response. As adsorption increases it poisons the electrode and reduces the current. This species then de-sorbs as the potential is swept to negative potentials.

The other main feature is the reduction wave below +0.8 V. In fact this is made up of more than one reduction wave, found by differentiating the current response to see the change in gradient of the current. This differentiated response is shown in Figure 6-7. The negative peaks indicate where the gradient of the current response was highest and therefore the half wave potential of each reduction reaction.

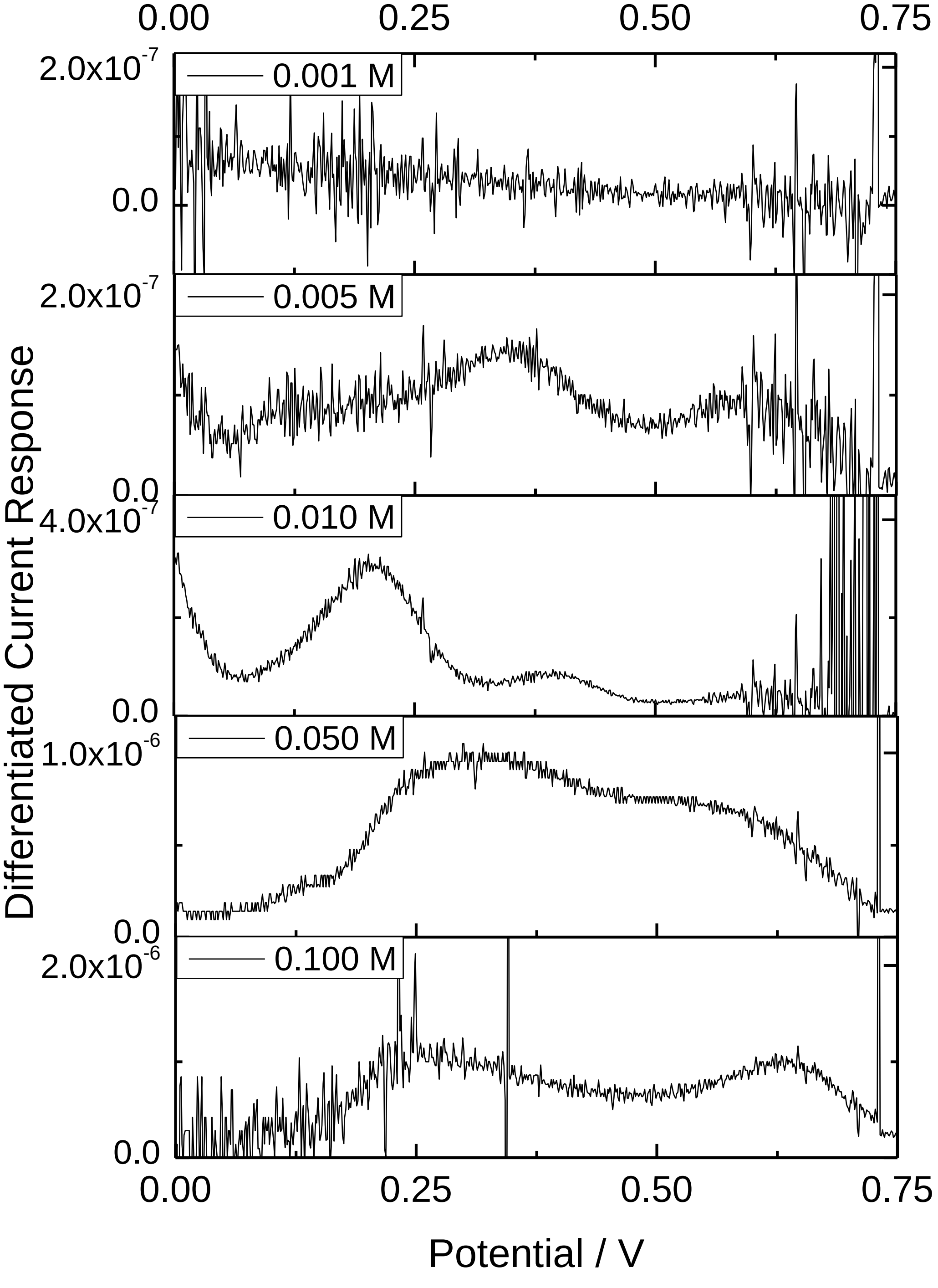

Figure 6-7: The differentiated current response showing reductions in the nitric-nitrous acid mixture with changing HNO_2 concentration. The peaks indicate a reaction occurring.

The first observation is that at a concentration of 0.001 M of HNO_2 the differentiated current response shows no measurable features, demonstrating the detection limit of the device. Analysis of the 0.005 M HNO_2 solution and at higher concentrations there are at least two cathodic reactions, one with a wave at a half wave potential between 0.63 and 0.58 V. This first wave can be attributed to the reduction of HNO_3 to HNO_2, according to Equation 6-3.

A second wave is found at 0.39 – 0.34 V at the concentrations of 0.005 M and 0.010 M. Work using macroelectrodes to study the nitric-nitrous acid mixture found two reduction peaks only, within 0.1 - 0.2 V of each other.[5] They attribute the second peak to the reduction of HNO_2 to NO. While the separation is greater in this case than in the literature, the 0.39 – 0.34 V wave is likely the nitrite reduction reaction.

$$NO_2^-{}_{(aq)} + 2H^+{}_{(aq)} + e^- \rightleftarrows NO_{(g)} + H_2O_{(l)}$$

Equation 6-8

The current at these two reduction potentials (0.60 V and 0.335 V) was measured and a linear response to HNO_2 concentration was found for both, as shown in Figure 6-8. This indicates that the reduction reactions are both first order with respect to HNO_2 concentration. This is consistent with the fact that Equation 6-3 requires HNO_2 as a catalyst to promote HNO_3 reduction and that no reduction current was observed in the absence of HNO_2 (Figure 6-2).

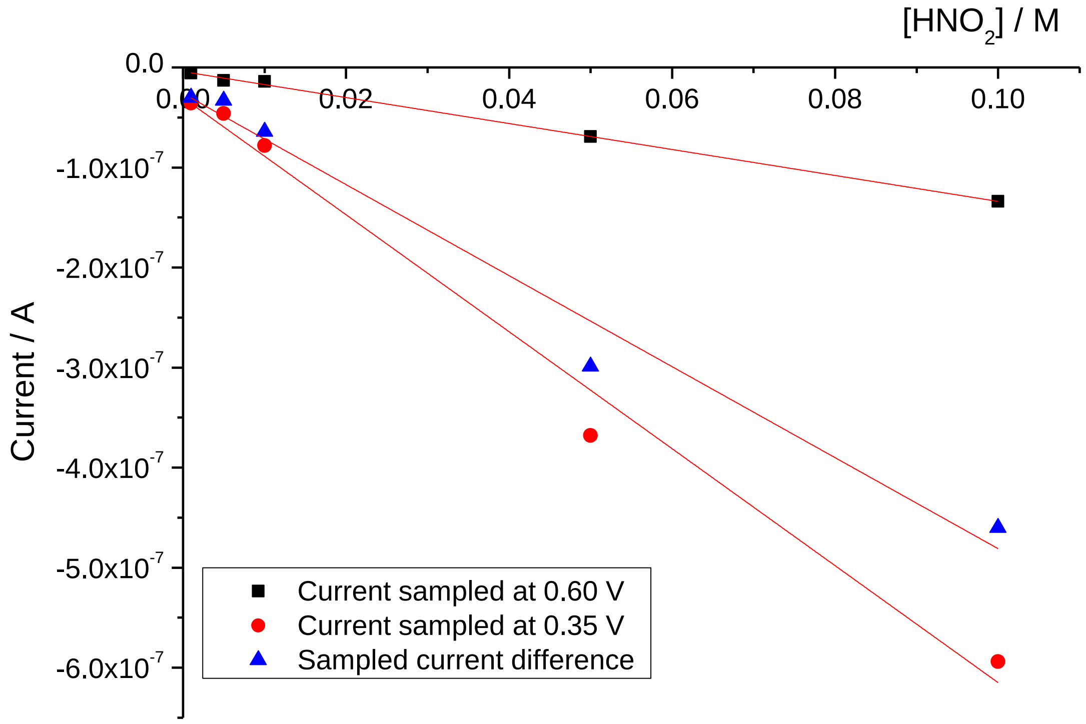

Figure 6-8: Graph of sampled current at a fixed potential with changing concentration of HNO_2.

NO has been found to go through further reductions with the products dependent on the form of the NO. NO_{ads} has been found, strongly adsorbed to platinum surfaces.[4] In solution NO can be reduced to alternative products.[8] Further reaction waves at potentials less than 0.3 V are therefore attributed to NO reducing. On opening the faraday cage it was found that vigorous bubbling of colourless, foul-smelling, gas was observed from the microelectrode device, most likely NO_x gas.

The acid system was also studied by changing the concentration of nitric acid and fixing the concentration of HNO_2, Figure 6-9. The concentration of HNO_2 was kept at 0.01 M and the concentration of HNO_3 was changed. The concentrations studied were 3.0, 2.0, 1.5, 1.0, 0.5, 0.1 M.

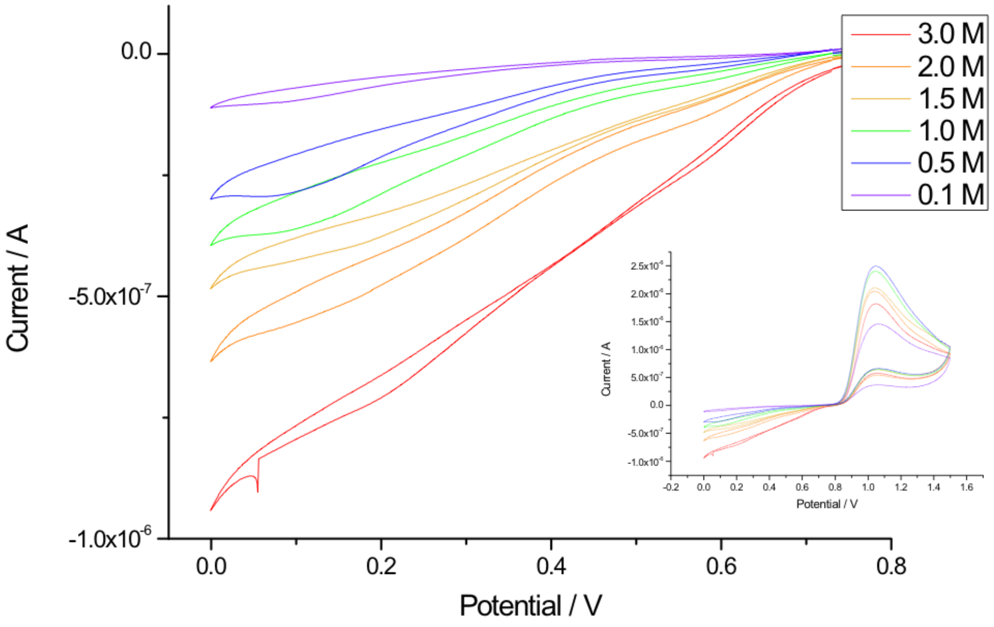

Figure 6-9: Cyclic voltammogram at 5 mVs^{-1} scan rate of the nitric-nitrous acid system with changing concentration of HNO_3. Inset shows peaks relative to the oxidation peak.

As expected, there is still an oxidation seen at 1.05 V that shows the autocatalytic oxidation of NO_2^- to nitrate ions. Changing the concentration of HNO_3 appears to have a similar effect to changing the HNO_2 concentration, in that the reduction wave magnitude increases. This is again consistent with reduction of HNO_3 catalysed by HNO_2. Again the onset of waves was found by differentiating the current response to see the gradient change of the current. This differentiated current response is shown in Figure 6-10.

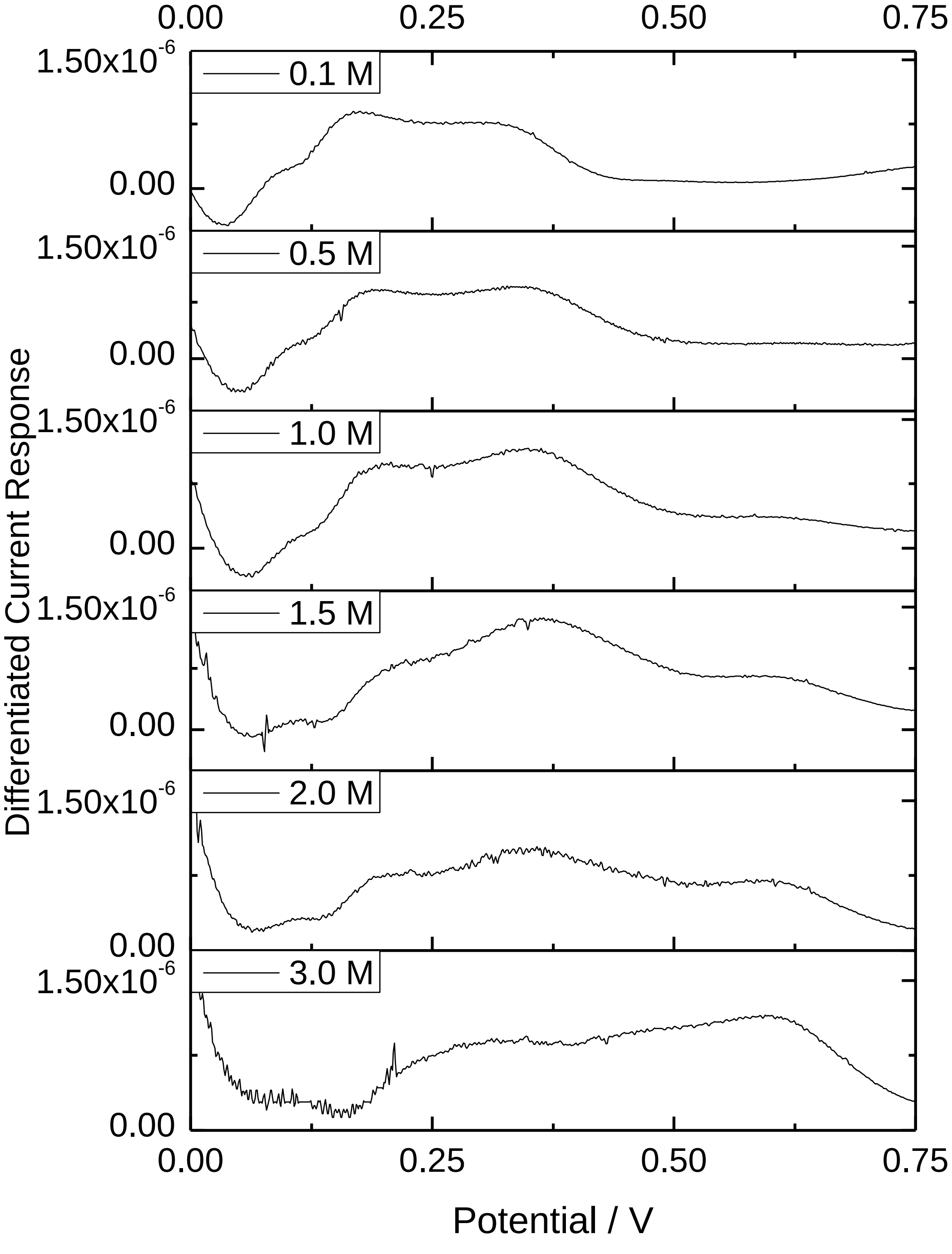

Figure 6-10: The differentiated current response showing reductions in the nitric-nitrous acid mixture with changing nitrate concentration.

There are two reduction waves found at each concentration at 0.6 V and 0.35 V. These were also found previously, in Figure 6-7, and were assigned to the reduction of nitrate to NO_2^- and the reduction of NO_2^- to NO. Both of the differential peaks increase in height with increasing nitric acid concentration, indicating greater current magnitudes. The current magnitude at these potentials increases linearly with nitric acid concentration, as seen in Figure 6-11. This indicates that the reduction reactions are both first order with respect to nitric acid concentration.

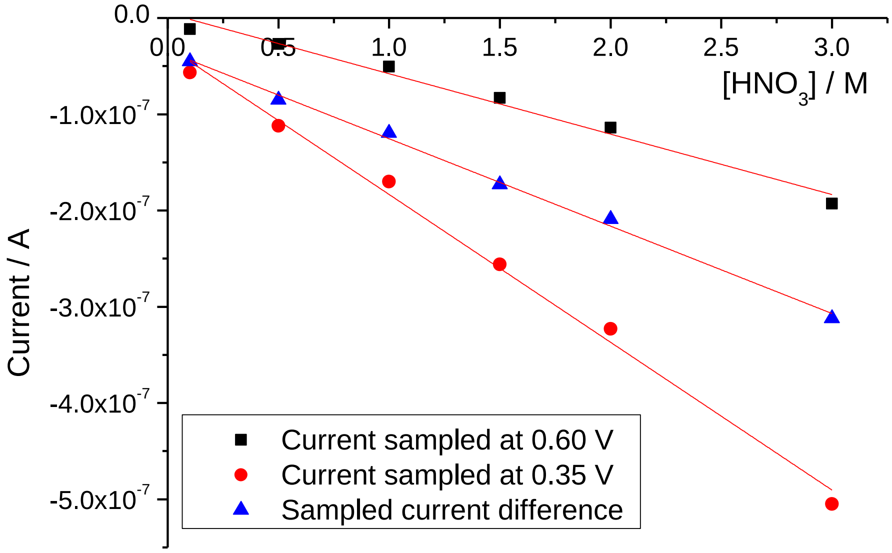

Figure 6-11: Graph of sampled current at a fixed potential with changing concentration of nitric acid.

There are further reduction reactions visible in the differentiated current as the potential is swept towards 0.0 V. These are likely due to NO reductions.[4] In the low nitric acid concentration solutions there is a reduction, at 0.17 – 0.20 V, which decreases in magnitude until disappearing as the nitric acid concentration rises. This wave is likely due to a further reduction reaction made possible by the low concentration of nitrate. This demonstrates that microelectrodes can be used to study acid mixtures and see quantitative changes in reduction reactions of NO_3^-.

The oxidation peak present in both Figure 6-6 and Figure 6-9 was further analysed by sampling the current before and after the peak. It became apparent that the sampled current showed a dependency on HNO_2 concentration beyond the sensitivity of the electrode, but not on changing nitric acid concentration. This is shown in Figure 6-12. This indicates selectivity in the reaction for nitrite, consistent with it being due to the nitrite oxidation, as postulated previously.

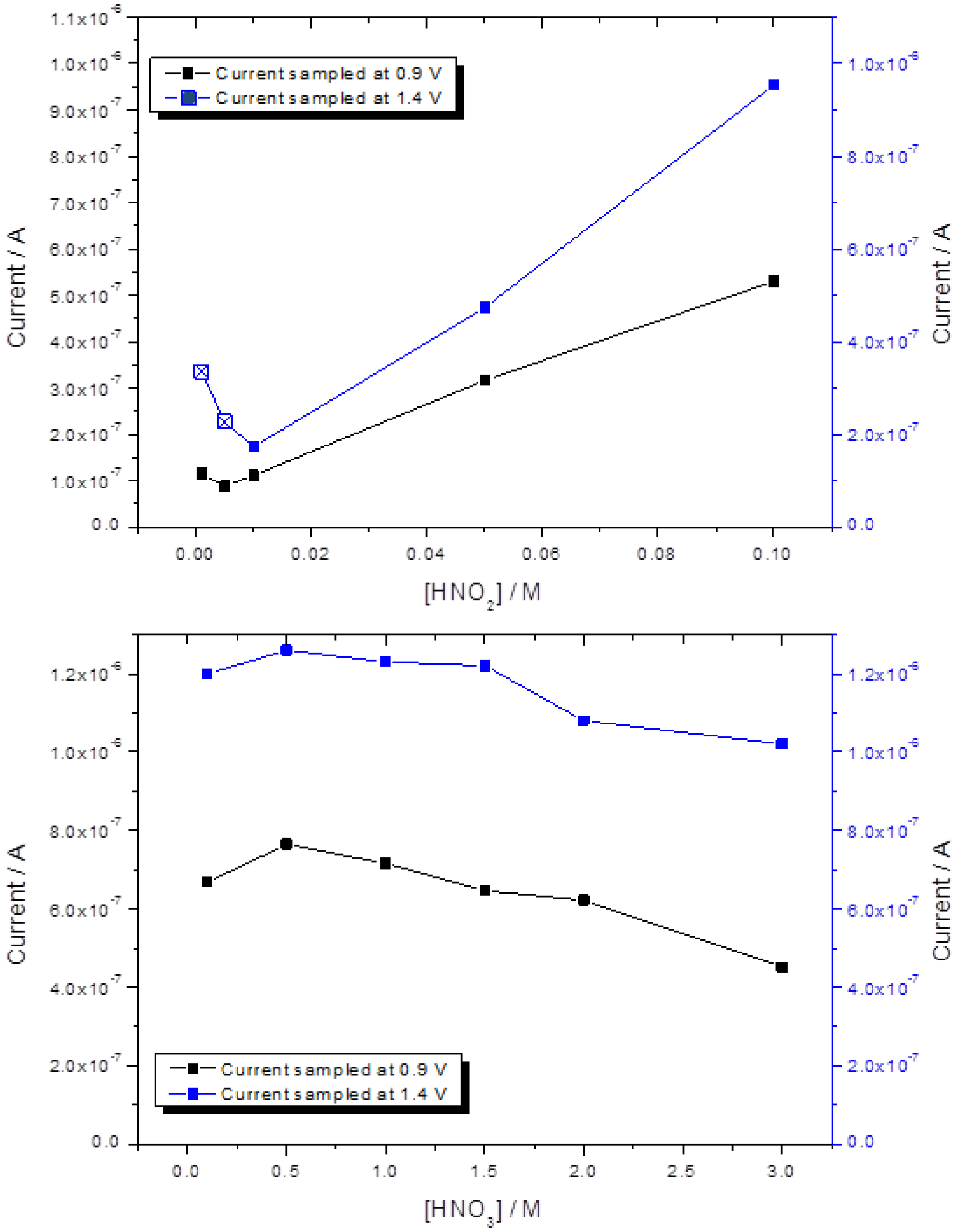

Figure 6-12: Graph of sampled current during oxidation at fixed potentials with changing concentration of HNO_2 and HNO_3. Points below 0.01 M HNO_2 sampled at 1.4 V are considered below the detection limit, have a different symbol, and therefore do not show a real effect.

In terms of material resistance to chemical attack the microelectrode devices were not extensively tested, however visual observation of the device, shown in Figure 6-13, after electrochemistry in the HNO_2/HNO_3 mixtures shows that the square microelectrode remains clearly defined.

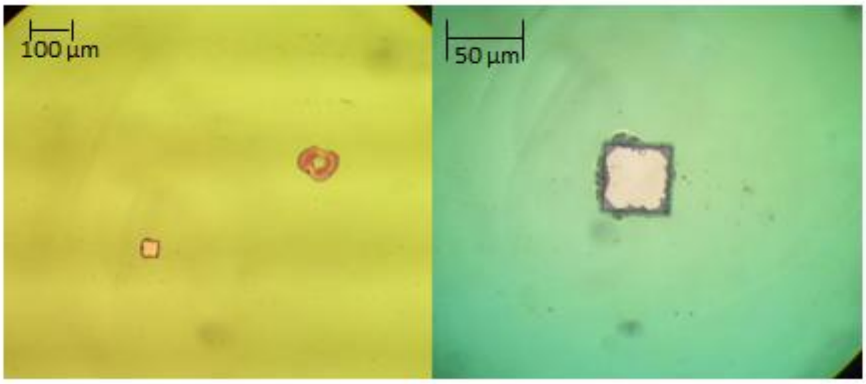

Figure 6-13: Images of the 50 µm edge platinum microelectrode device after electrochemical analysis in the nitrous-nitric acid system. The left image shows the patterned electrode and a nearby defect in the nitride passivation layer. The right image shows a close up of the square electrode.

A dark coloured side product of the nitrate reduction appears to have built up around the edges of electroactive metal on the device, including on flaws in the silicon nitride. These flaws were discussed in Chapter 5. Observation after repeated experimentation on another device the dark build up was again found, shown in Figure 6-14.

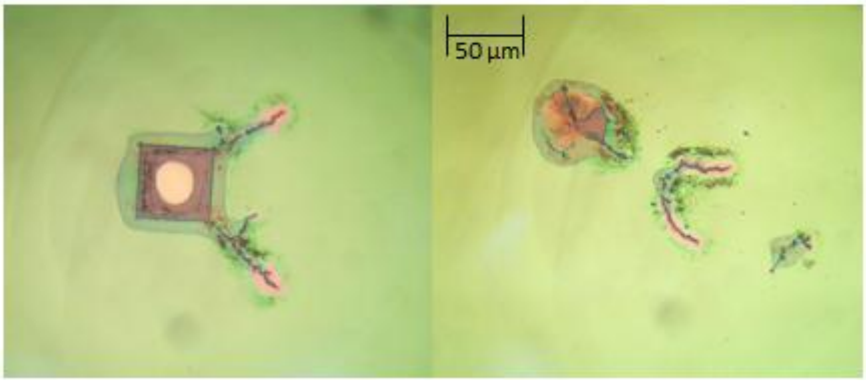

Figure 6-14: Images of a 50 µm edge platinum microelectrode device after electrochemical analysis in the nitrous-nitric acid system. The left image shows the patterned electrode and cracks in the nitride passivation layer. The right image shows other flaws of the nitride layer, some revealing platinum metal below.

The images show that in addition to the dark build up where platinum is revealed at the silicon nitride surface as seen previously there are cracks in the passivation layer where corrosion through the layer occurs. This may be due to pinhole defects in the nitride layer that arise during production, which suggests that modification of the processing is required to ensure a high quality passivation layer and ensure the active electrode area is limited to the intended electrode surface.

This indicates that the electrode system is capable of withstanding the corrosive acid medium over the course of several hours. There are some signs of cracking of the silicon nitride which may limit the lifetimes of the devices, though these cracks are not extensive.

6.4 Conclusions

The applicability of platinum microelectrodes to evaluate electrochemical processes in a complex system, used in the PUREX reprocessing procedure for separation of nuclear fuel, was assessed. Nitric acid is a useful medium but presents significant challenges. The high reactivity of the acid leads to degradation and a multiplicity of chemical and electrochemical equilibria with HNO_2.

The system was characterised using silver plating to assess the ease of detecting the presence of redox ions by metal stripping/plating in nitric acid. The microelectrodes performed well, displaying low iR drop and low double layer capacitance which made the non-faradaic current negligible. The silver deposition reaction displayed a reduction wave for silver plating, which at slow sweep rates, increased in current response as the plated metal grew in volume, increasing the electroactive surface area.

The feasibility of detecting the amount of HNO_2 and HNO_3 at microelectrodes to determine the nitric-nitrous acid equilibrium was also studied. HNO_2 could be detected at concentrations above 0.001 M, due to a peak of HNO_2 oxidation and HNO_2/HNO_3 reductions, which can be measured quantitatively. This can be attributed to the high sensitivity of the microelectrodes. As the solution degraded the transition of the NO_2^- decay to NO_3^- and NO was identifiable. When the nitric acid solution was made more dilute a change in redox properties showed different reduction mechanisms to be observed.

Initial observations of material resistance indicate that the microelectrode devices can withstand the acidic medium over 5-7 hours. These are very promising results for demonstrating the applicability of microelectrodes in detection in the PUREX process.

6.5 References

---

[1] C. Milhano and D. Pletcher Modern Aspects of Electrochemistry Vol 45, 2009, pp 1-61 The Electrochemistry and Electrochemical Technology of Nitrate **DOI:** 10.1007/978-1-4419-0655-7_1

[2] M. Duca, B. van der Klugt, M.T.M. Koper. Electrochimica Acta 68 (2012) 32– 43 http://dx.doi.org/10.1016/j.electacta.2012.02.037

[3] M. Duca, B. van der Klugt, M.A. Hasnat, M. Machida, M.T.M Koper. Journal of Catalysis 275 (2010) 61-69
http://dx.doi.org/10.1016/j.jcat.2010.07.013

[4] M.T. de Groot, M.T.M. Koper. Journal of Electroanalytical Chemistry 562 (2004) 81-94 http://dx.doi.org/10.1016/j.jelechem.2003.08.011

[5] O.W.J.S. Rutten, A. van Sandwijk, G. van Weert. Journal of Applied Electrochemistry 29 (1999) 87-92 **DOI:** 10.1023/A:1003412613806

[6] Y.-Z. Wei, B. Fang, T. Arai, M. Kumagai. Journal of Radioanalytical and Nuclear Chemistry 262 (2004) 409-415
DOI:10.1023/B:JRNC.0000046770.86000.d6

[7] M. Duca, V. Kavvadia, P. Rodriguez, S.C.S. Lai, T. Hoogenboom, M.T.M Koper. Journal of Electroanalytical Chemistry 649 (2010) 59-68 http://dx.doi.org/10.1016/j.jelechem.2010.01.019

[8] A.C.A. de Vooys, G.L. Beltramo, B. van Riet, J.A.R. van Veen, M.T.M. Koper. Electrochimica Acta 49 (2004) 1307–1314 http://dx.doi.org/10.1016/j.electacta.2003.07.020

Chapter 7: The Characterisation of Platinum Square Microelectrode Arrays

In this chapter the feasibility of using microlithography to make square microelectrode arrays of controlled size and placement is investigated, developed from the characterisation and application of single square microelectrodes in previous chapters. Arrays of square microelectrodes were characterised in potassium ferricyanide solution using cyclic voltammetry, electrical impedance spectroscopy and potential step voltammetry. Observed microelectrode responses were compared to simulated currents to determine whether the arrays had been successfully fabricated.

7.1 Introduction

Arrays allow for the summation of signals from multiple electrodes acting together. With microelectrode arrays this removes the disadvantage of the small currents from microelectrodes, whilst retaining the desirable characteristics of the microelectrodes. The arrays however have an additional factor which can affect performance that needs to be characterised, namely that of the spacing between the electrodes.

It has been determined that there are four possible diffusion regimes for disc microelectrode arrays[2] as shown in Figure 7-1. The first, (a), characteristic linear diffusion to individual microelectrodes, occurs at very short time scales. This rapidly develops into the quintessential hemispherical diffusion characteristic of individual microelectrodes, (b). As each microelectrode acts independently from its neighbours the array then achieves its maximum current efficiency. However, as the diffusion layers grow outward they will eventually overlap, (c). The onset of this overlap will be dependent on the spacing between the electrodes. This means that the microelectrodes begin to interact with each other, competing for the same redox-active material and lowering the overall current. Over longer timescales the diffusion layers then evolve into a final profile, (d) characteristic of linear diffusion over the entire array area, where the array behaves similarly to a macroelectrode.

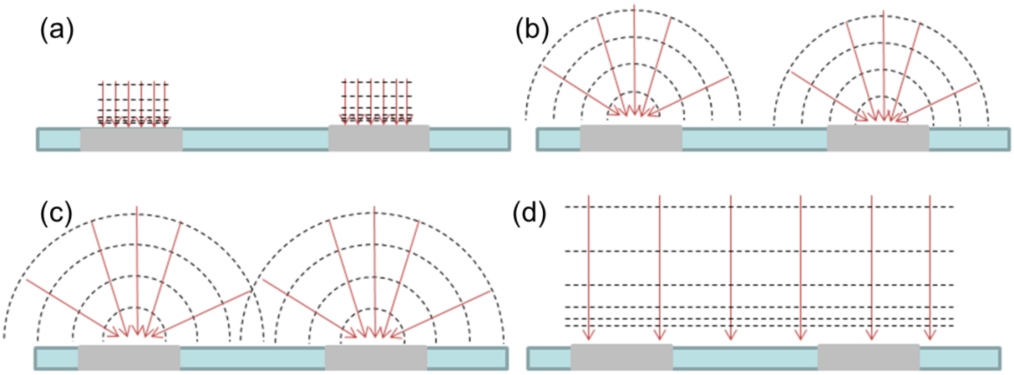

Figure 7-1: The four profiles of diffusion fields at electrodes in an array.

The design of arrays by photolithography allows great control over the spacing and organisation of electrodes on an array. The traditional wire set in glass approach is inefficient for creating multiple electrodes, as discussed in the Introduction (Section 1.3), but it becomes even more challenging when fabricating arrays as there is little or no control of the spacing between the wire microelectrodes. Instead random arrays are produced.[1] Random spacing means that diffusional field overlap can occur over variable time scales, producing a range of current outputs from electrodes within the same array. Quantification is therefore difficult and results are unlikely to be reproducible between different fabricated arrays.

The spacing of electrodes on arrays has been the object of studies by both simulation[2] and experimental determination for disc microelectrodes. The size to spacing ratio[3] and the packing[4] of electrodes in arrays have been found to have an effect on the current response. The disc arrays have been characterised using non-electrochemical methods[5] in addition to cyclic voltammetry[6], impedance[7] and chronoamperometry[8].

In this work, microelectrode arrays were produced using electrodes of square shapes. As these have been shown to produce higher current densities than discs due to the effects of enhanced corner diffusion,[9] this work probes the effects of spacing and electrode size on the array response, with systematic analysis of cyclic voltammetry, electrical impedance spectroscopy and chronoamperometry, correlated with COMSOL simulations.

7.2 Methodology

7.2.1 Electrodes

The arrays were designed and fabricated as described in Chapter 3 (Section 3.1.2.). The twenty arrays characterised in this chapter have individual microelectrodes of square shape with varying edge lengths and spacing between them. All electrodes were arranged with square packing. The edge lengths (D) of the individual microelectrodes were 10, 20, 30, 50 and 100 µm. The minimum spacing between electrodes (S) is given by S = nD where n = 1,2,3,4 and D is the length of the electrode. This is shown schematically in Figure 7-2.

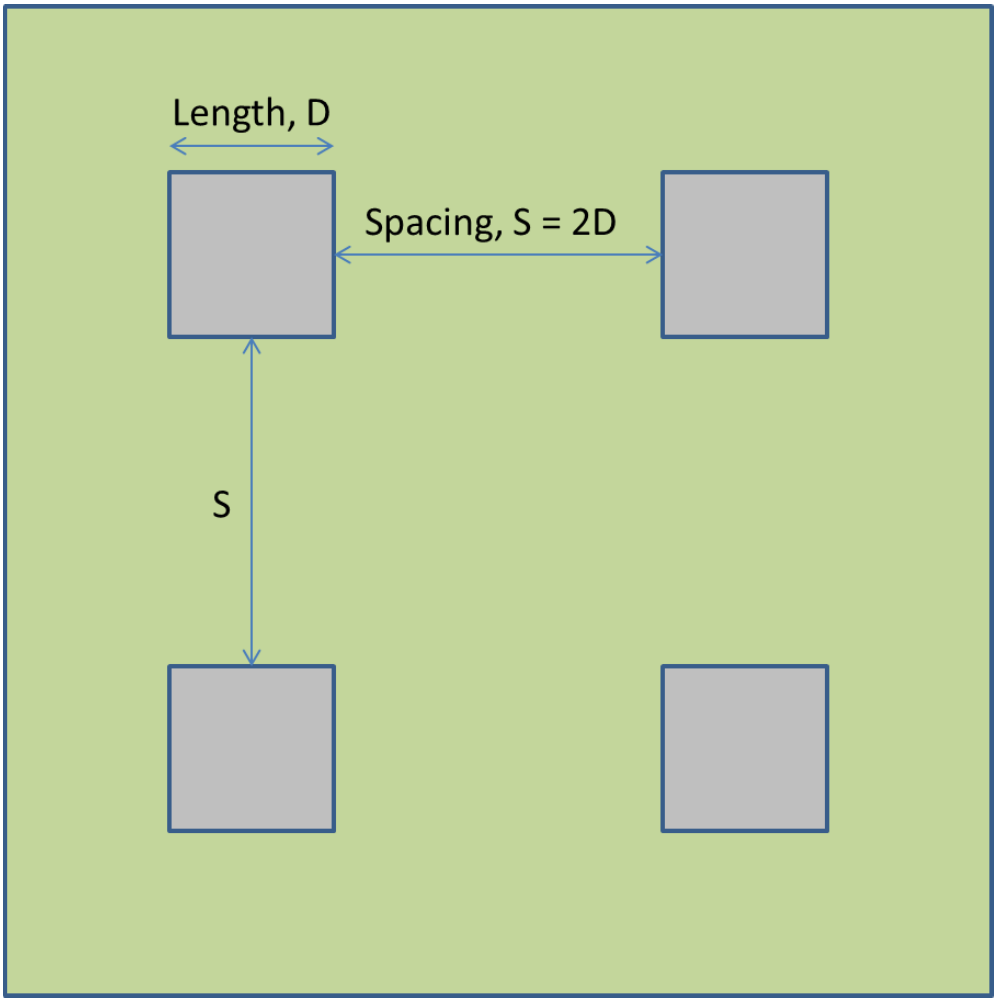

Figure 7-2: Schematic showing the length of an electrode edge (D) and the spacing between electrodes (S).

For example an array with 50 µm length squares and 2D spacing has S = 100 µm between the sides of an electrode and its neighbours in the array. The twenty devices studied are summarised in Table 7-1.

Device acronym	D / µm	S	S / µm
10A1D	10	1D	10
20A1D	20	1D	20
30A1D	30	1D	30
50A1D	50	1D	50
100A1D	100	1D	100
10A2D	10	2D	20
20A2D	20	2D	40
30A2D	30	2D	60
50A2D	50	2D	100
100A2D	100	2D	200
10A3D	10	3D	30
20A3D	20	3D	60
30A3D	30	3D	90
50A3D	50	3D	150
100A3D	100	3D	300
10A4D	10	4D	40
20A4D	20	4D	80
30A4D	30	4D	120
50A4D	50	4D	200
100A4D	100	4D	400

Table 7-1: Technical specifications of the electrode lengths and spacings for the 20 microelectrode array devices.

The array devices produced were 10 mm in length and can be seen in Figure 7-3 along with a microscope image showing 2D spacing between electrodes on the array.

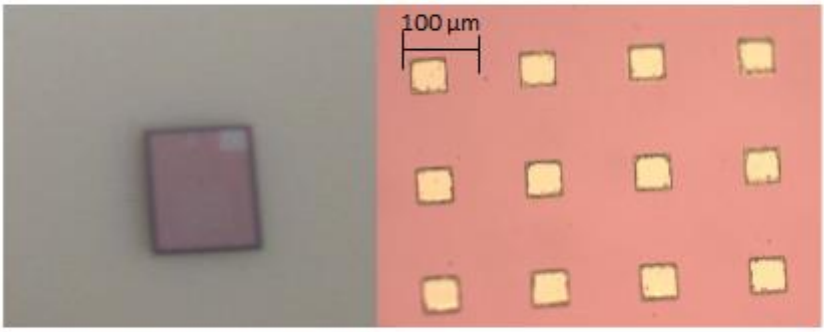

Figure 7-3: An array device with visible contact pad in the top right corner and a microscope image showing the electrodes at S = 2D.

The number of electrodes on each array and total electroactive area are summarised in Table 7-2. The array areas of the devices are designed to take up the same footprint, a 5 x 5 mm area.

Device acronym	Number of electrodes	Σ electrode area / cm^2
10A1D	62500	6.250 x10^{-2}
20A1D	15625	6.250 x10^{-2}
30A1D	6889	6.200 x10^{-2}
50A1D	2500	6.250 x10^{-2}
100A1D	625	6.250 x10^{-2}
10A2D	27889	2.789 x10^{-2}
20A2D	6889	2.756 x10^{-2}
30A2D	3136	2.822 x10^{-2}
50A2D	1089	2.723 x10^{-2}
100A2D	289	2.890 x10^{-2}
10A3D	15625	1.563 x10^{-2}
20A3D	3969	1.588 x10^{-2}
30A3D	1764	1.588 x10^{-2}
50A3D	625	1.563 x10^{-2}
100A3D	169	1.690 x10^{-2}
10A4D	10000	1.000 x10^{-2}
20A4D	2500	1.000 x10^{-2}
30A4D	1156	1.040 x10^{-2}
50A4D	400	1.000 x10^{-2}
100A4D	100	1.000 x10^{-2}

Table 7-2: Technical specifications of the number of electrodes and total electrode area on the 20 microelectrode array devices.

7.2.2 Experimental Techniques

All square microelectrode arrays were pre-treated by cycling in sulfuric acid solution, using the method developed in Chapter 4. The electrodes were characterised electrochemically using cyclic voltammetry, potential step voltammetry and EIS as documented in Chapter 3. Cyclic voltammetry and potential step voltammetry data were collected at ambient laboratory temperature. Electrochemical impedance spectroscopy data was collected in a waterbath set at 25 °C. COMSOL simulations, also discussed in Chapter 3, were compared to the experimental responses.

7.3 Results & Discussion

7.3.1 Using Cyclic Voltammetry to Understand Diffusion Regimes

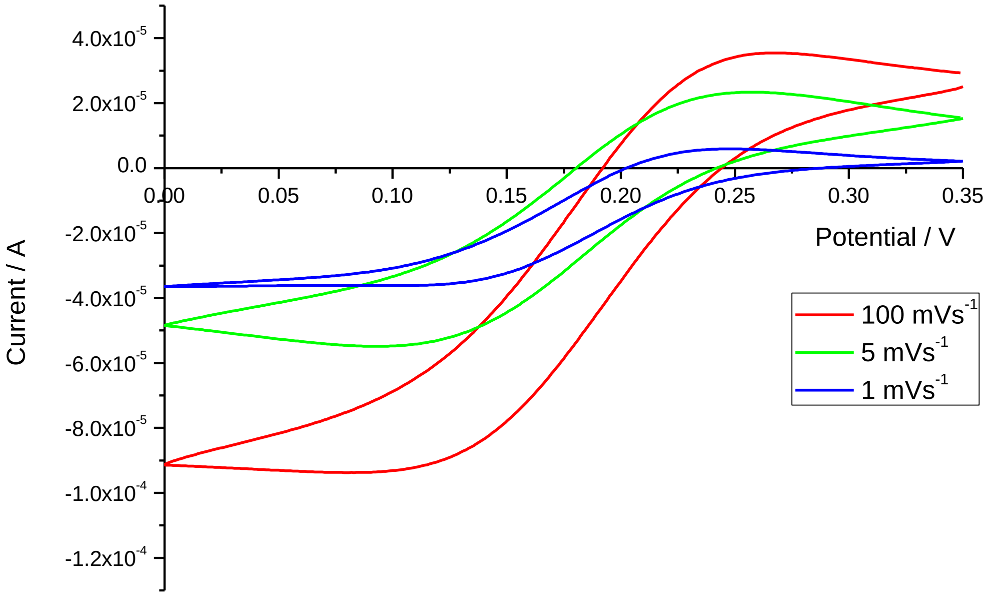

Figure 7-4: Successive cyclic voltammetry scans at various scan rates in potassium ferricyanide solution using the 50A2D square microelectrode array.

Figure 7-4 shows the current-potential response of the 50A2D array in ferricyanide solution at room temperature at various scan rates. This response of increasing maximum current with scan rate is typical of each array. However, beyond that each array current profile differs due to both electrode size and spacing.

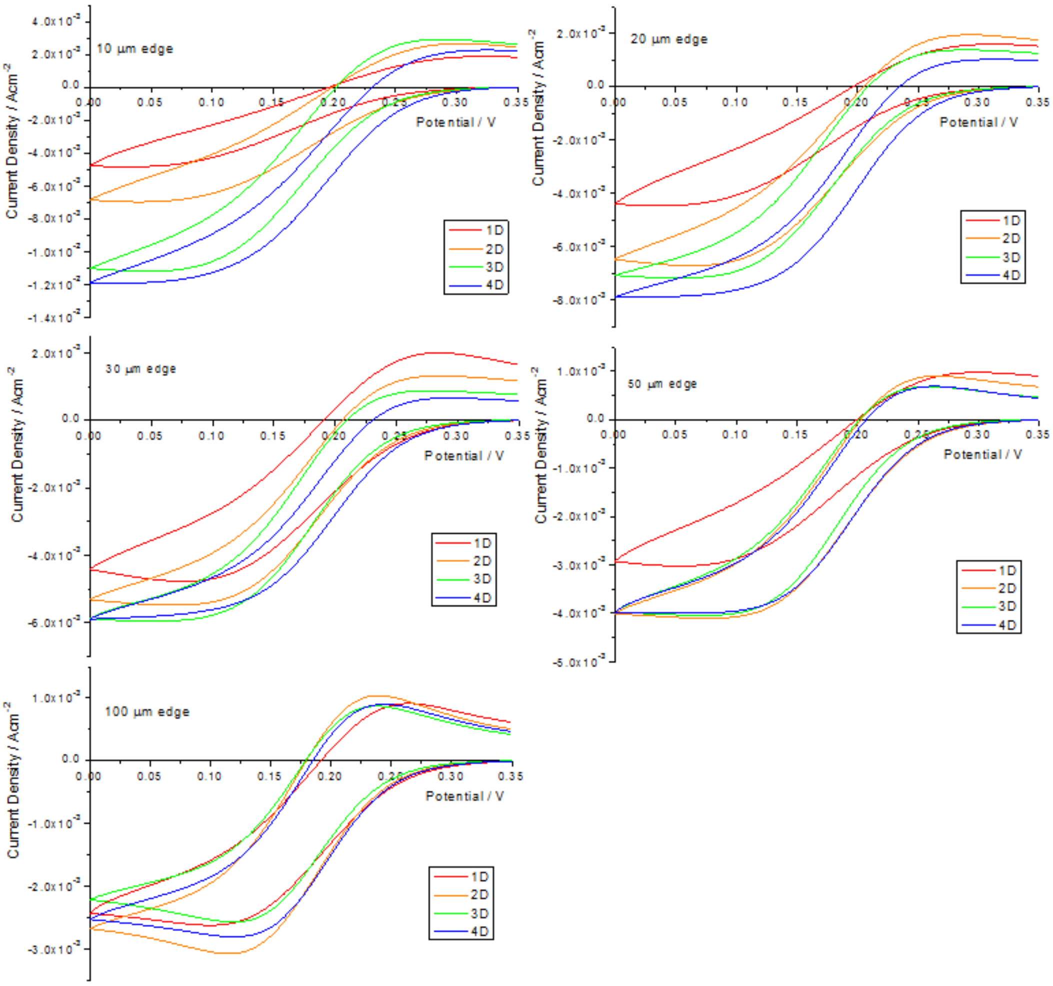

Figure 7-5: Cyclic voltammetry showing current density of arrays with varying D at a fixed S. Scan rate 100 mVs^{-1}.

Figure 7-5 shows each array response at 100 mVs^{-1} scan rate, a relatively fast scan rate. The devices with 100 μm edge electrodes show very similar current density (current for total area of electrodes, as detailed in Table 7-2) and peak shape, effectively demonstrating that each electrode is acting individually, responding to linear diffusion to the individual microelectrodes. This is a demonstration of regime (a). With decreasing edge length the current density responses separate out, as hemispherical diffusion has developed, regime (b), the current density changes related to the spacing.

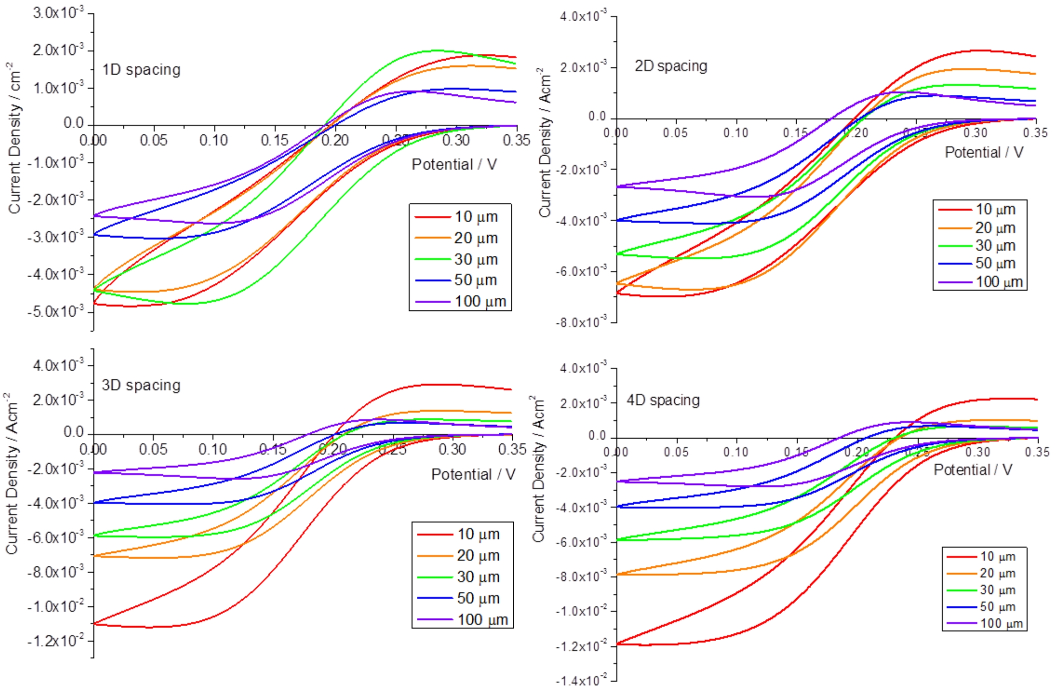

Figure 7-6: Cyclic voltammetry showing current density of arrays with varying S at fixed D. Scan rate 100 mVs^{-1}.

Figure 7-6 shows the same current density responses as Figure 7-5 but collated to demonstrate the effect of changing electrode length on the current response. In the 1D devices it can be seen that the 10A1D and 20A1D devices show very similar current magnitudes, possibly indicating that they are responding to a significant amount of diffusional overlap, regime (c), even developing into regime (d) with linear diffusion over the array.

The differences between profiles (b) and (c), individual and overlapping hemispherical diffusion fields are difficult to see in cyclic voltammograms. Instead the observed peak currents, i_P, were compared to COMSOL simulated limiting currents, i_L. These simulated currents were calculated for individual square microelectrodes. By multiplying by the number of elements in the array a simulated regime (b) could be used to compare to experimental values. If $i_L > i_P$ it indicates that there is overlap of the diffusion layers, regime (c), and the current has decreased from the ideal values. If $i_L < i_P$ it is taken to mean that the current is peaked due to either linear diffusion over a single electrode, regime (a), or over the entire array, regime (d).

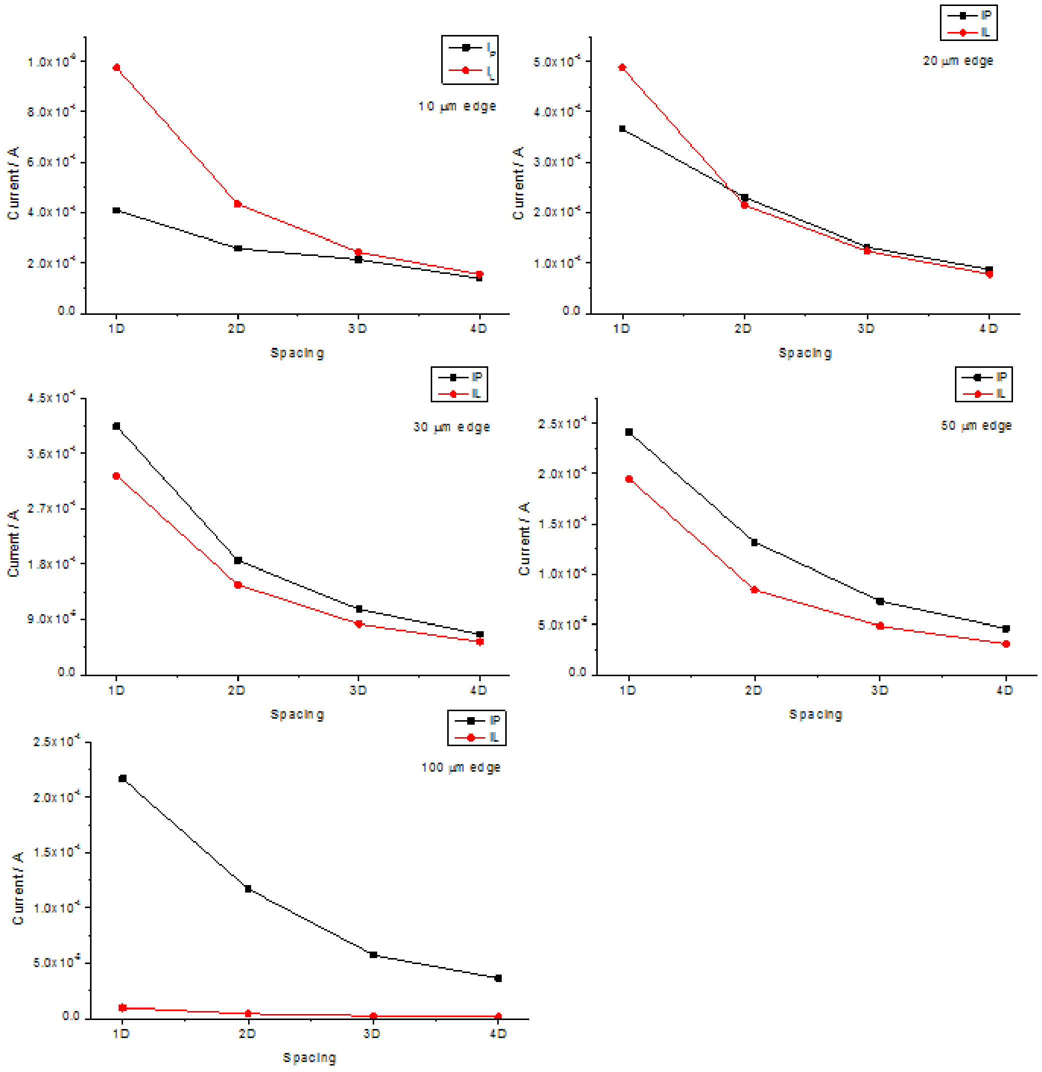

Figure 7-7: Comparisons of the experimentally observed peak current at 100 mVs^{-1} scan rate, i_P, and the COMSOL simulated limiting current, i_L on devices varying D at a fixed S.

Figure 7-7 shows the comparison of the experimentally observed peak current at 100 mVs^{-1} scan rate, i_P, and the simulated limiting current, i_L. It can be seen that the devices of 100 µm edge lengths do not follow the simulated response, as was seen in Figure 7-5. This is also true for the 50 µm and 30 µm edge arrays with i_P greater than i_L. The 20 µm edge 2D to 4D arrays show good agreement with the simulations, indicating that they are responding to the individual hemispherical diffusion regime (b). 20A1D has an i_P less than i_L, indicating that overlap has occurred and current response has dropped with the shared response of regime (c). The 10 µm edge arrays show some of both regime (b) and (c) character with the 10A3D and 10A4D arrays agreeing well with simulation with i_P dropping with smaller spacing.

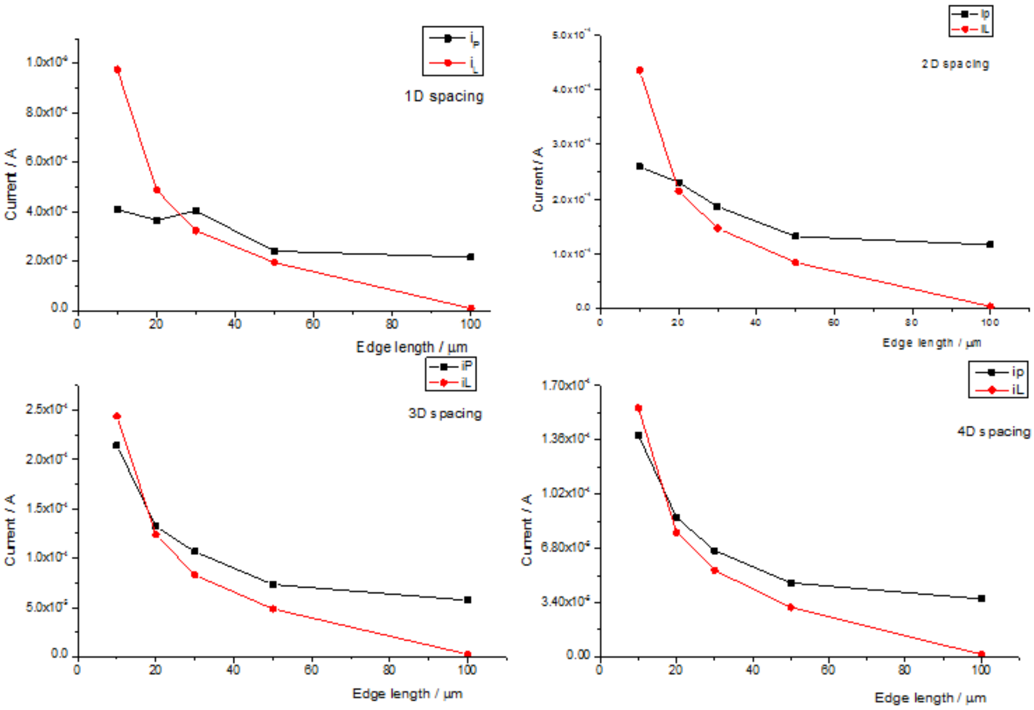

Figure 7-8: Comparisons of the experimentally observed peak current at 100 mVs^{-1} scan rate, i_P, and the COMSOL simulated limiting current, i_L on devices varying S at a fixed D.

Figure 7-8 shows the same data as Figure 7-7 but shows that the 1D spacing fails to demonstrate individual hemispherical diffusion. In addition, it visualises the disparity between the larger electrode edge lengths. Table 7-3 gives as a summary of the most likely diffusion regimes at the 100 mVs^{-1} scan rate to each device.

Diffusion regime / Edge length	**(a)**	**(b)**	**(c)**	**(d)**
10 µm		4D 3D	2D	1D
20 µm		4D 3D 2D	1D	
30 µm	4D 3D	2D 1D		
50 µm	4D 3D 2D	1D		
100 µm	4D 3D 2D 1D			

Table 7-3: The likely diffusion regimes for the 100 mVs^{-1} scan rate to each device given cyclic voltammetry data and comparison to simulated limiting current values.

If, instead, the slower scan rate of 5mVs^{-1} is studied, as shown in Figure 7-9, it can be seen that the devices with 100 µm edge electrodes no longer give the same response, with the 100A1D electrode having a smaller current density. This could indicate at these slower scan rates that hemispherical diffusion can occur even at the larger microelectrodes, though care must be taken to ensure that steady state currents do not result from the influences of natural convection.

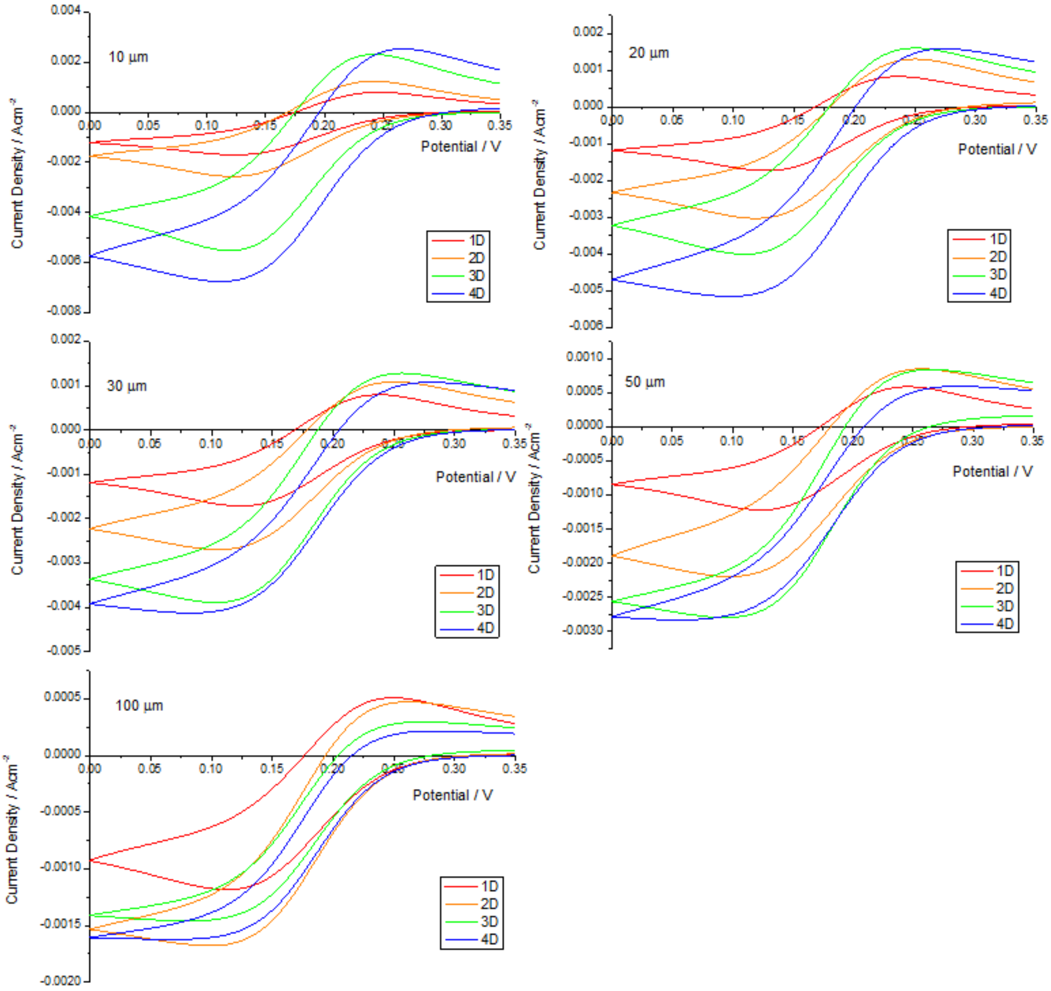

Figure 7-9: Cyclic voltammetry showing current density of arrays with varying S at a fixed D. Scan rate 5 mVs^{-1}.

Figure 7-10 shows the same current density responses as Figure 7-9 but collated to demonstrate the effect of changing electrode length on the current response. With the slower scan rate the spacing effect becomes more important. Figure 7-10 shows that for devices with 1D spacing the current densities are very similar, indicating that linear diffusion is likely occurring over the entire array, as described by regime (d).

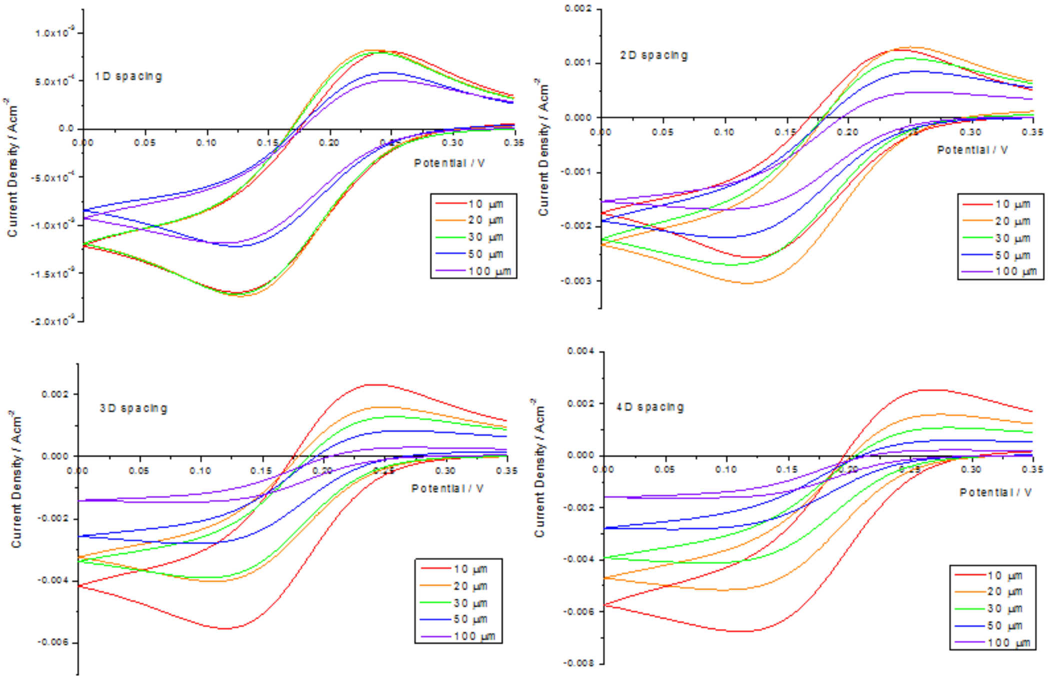

Figure 7-10: Cyclic voltammetry showing current density of arrays with varying D at fixed S. Scan rate 100 mVs^{-1}.

The 5 mVs-1 scan rate allowed the current response to develop further with the longer timescales of the experiment. Figure 7-11 shows the comparison between i_P and i_L at this scan rate.

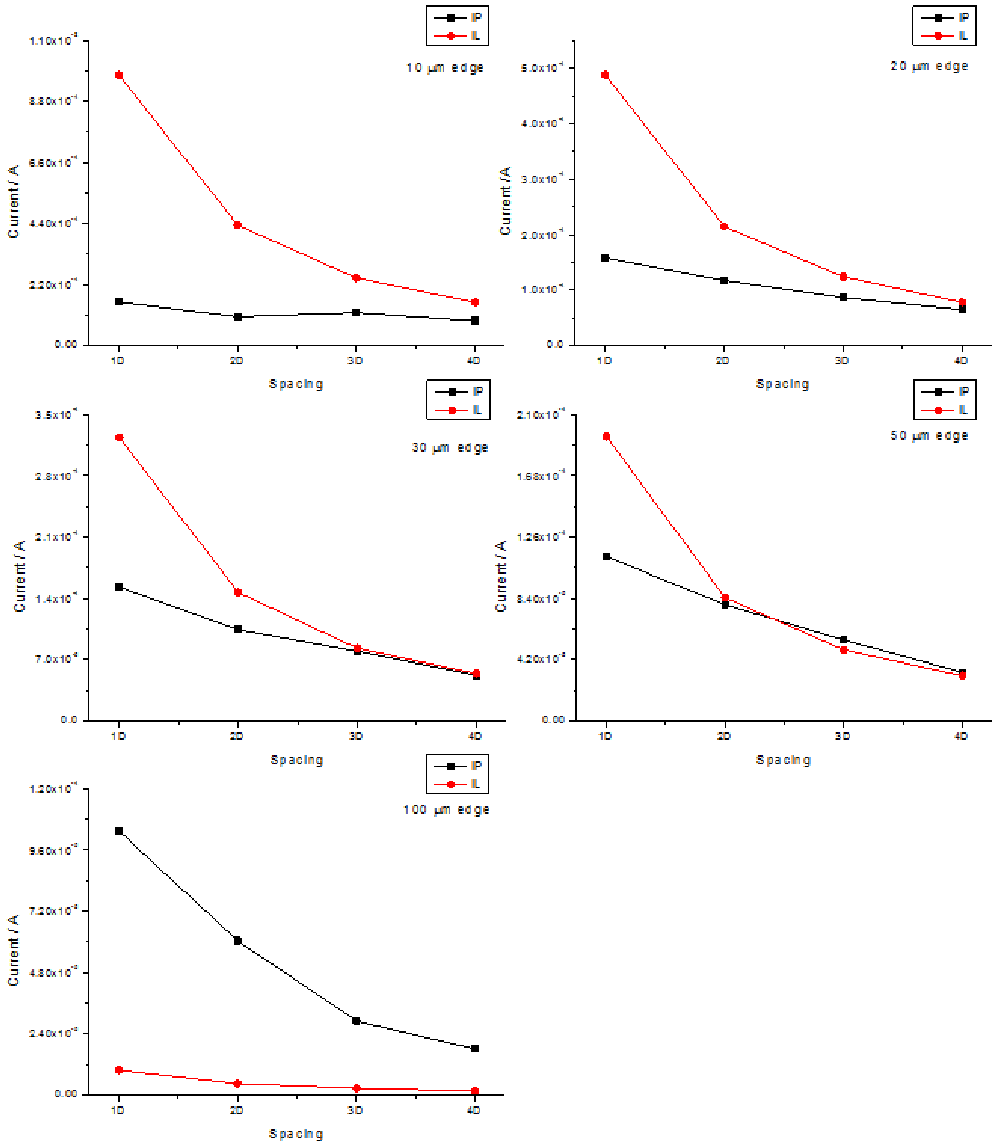

Figure 7-11: Comparisons of the experimentally observed peak current at 5 mVs^{-1} scan rate, i$_P$, and the COMSOL simulated limiting current, i$_L$ on devices varying D at a fixed S.

Here it can be seen that the similar shape of the graphs show hemispherical diffusion, but the i$_P$ is smaller than the limiting current, indicating a large degree of overlap. This reduction from i$_L$ is greatest for the closer spaced arrays and for smaller microelectrodes. The 100 µm edge microelectrode arrays show a high i$_P$ relative to i$_L$ indicating they still are subject to regime (a) diffusion. The 10 µm edge microelectrodes have a low i_P relative to i_L indicating that they are subject to diffusion by regime (d).

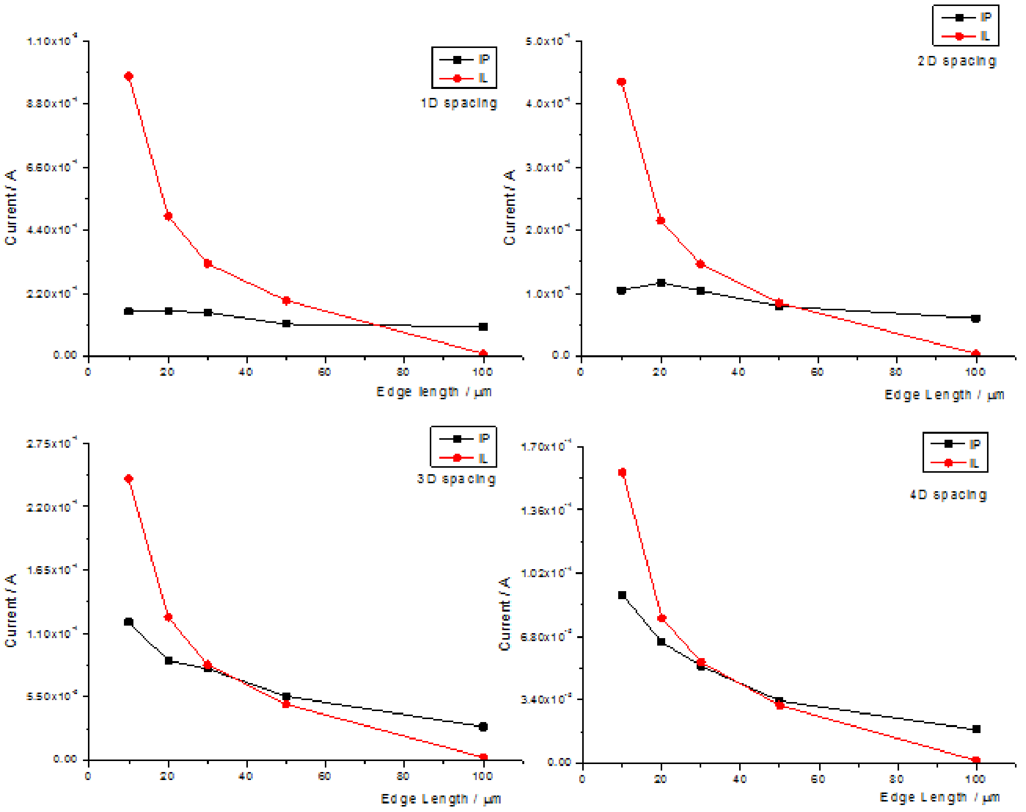

Figure 7-12: Comparisons of the experimentally observed peak current at 5 mVs^{-1} scan rate, i_P, and the COMSOL simulated limiting current, i_L on devices varying S at a fixed D.

Figure 7-12 displays the same data as Figure 7-11 but shows that the 1D spacing, and to some extent the 2D, does not display hemispherical diffusion. Rather it has linear diffusion over the area, regime (d). In addition, it shows that at this slower scan rate even the larger electrode edge lengths have developed hemispherical diffusion for the most part. Table 7-4 gives as a summary of the most likely diffusion regimes at the 5 mVs^{-1} scan rate to each device.

Diffusion regime / Edge length	**(a)**	**(b)**	**(c)**	**(d)**
10 µm				4D 3D 2D 1D
20 µm		4D	3D 2D 1D	
30 µm		4D 3D	2D 1D	
50 µm		4D 3D 2D	1D	
100 µm	4D 3D 2D	1D		

Table 7-4: The likely diffusion regimes at the 5 mVs^{-1} scan rate to each device given cyclic voltammetry data and comparison to simulated limiting current values.

From the cyclic voltammograms and the COMSOL simulated limiting currents it can be seen that there is no ideal spacing or microelectrode size for individual hemispherical diffusion and optimum current density over a square microelectrode array. The optimal diffusion, regime (b), can be achieved most quickly with arrays designed to have smaller electrodes (S) and larger spacing (D). The arrays can be optimised for a specific purpose and the required diffusion regime can be dependent on the microelectrode area, the spacing between the electrodes, the electrochemical technique applied and the diffusion coefficient of the species under analysis. Given the high degree of control this optimisation requires, the production of arrays through microlithography is ideal.

7.3.2 Electrochemical Impedance Spectroscopy

Having seen that there is significant difference in array response with changing the array design and diffusional overlap, EIS was used to characterise and quantify this further. Figure 7-13 shows the changing impedance response as E_{DC} is varied for the 50A3D array. As found previously, the impedance increases as E_{DC} is moved further from E^{θ} for the reaction.[9] The smallest impedance response was found at E^{θ}, as expected, as this produces the largest redox exchange current.

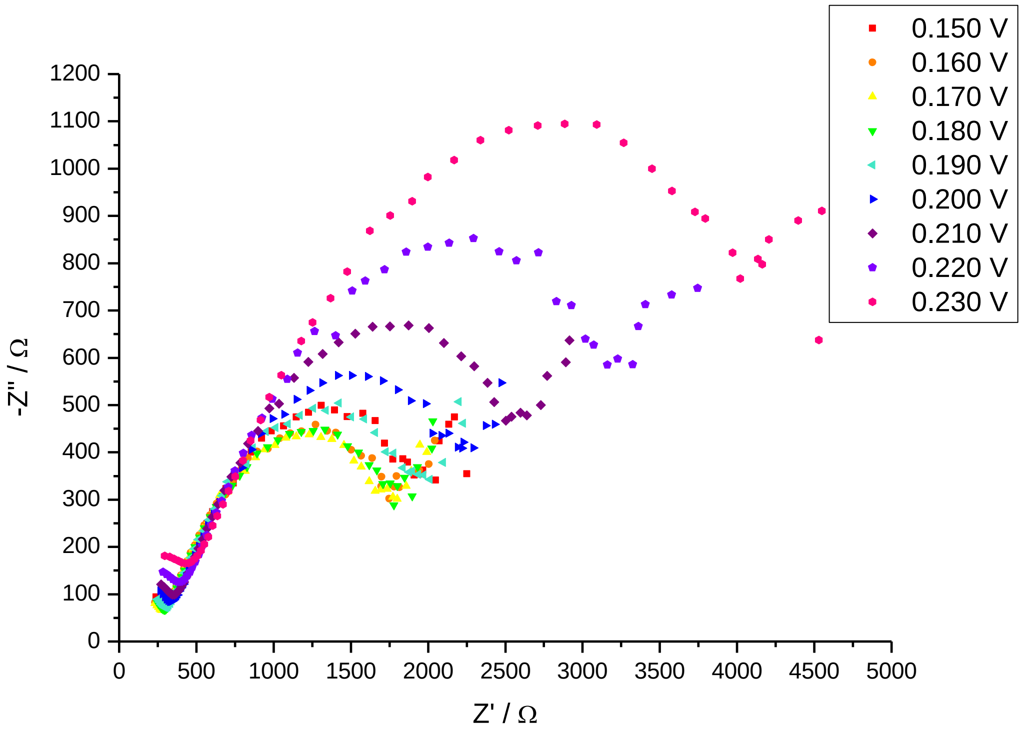

Figure 7-13: EIS response for the 50A3D microelectrode array in potassium ferricyanide at various E_{DC} across the reaction potentials.

The EIS response of arrays with fixed electrode length and differing spacing shows an additional feature to that of the single microelectrode. At low frequencies a prominent 45° line is seen, indicating a Warburg impedance. This extends from the semicircle corresponding to the non-linear resistance, as discussed in Chapter 2 (Section 2.3.2).

The Warburg impedance that develops at lower frequencies occurs after the hemispherical diffusion layers have overlapped and once linear diffusion has evolved over the array, regime (d). The array is now acting as a single electroactive device and the microelectrodes give a shared response.

During microelectrode array response fitting, specific frequencies had to be selected to determine R_{NL} accurately, shown in Figure 7-14. This is due to the modified Randles' circuit accurately describing the EIS response of a disc shaped microelectrode (Section 2.3.2), but not the effects of corner diffusion found with square microelectrodes. The enhanced diffusion produces higher steady state currents than for disc shaped microelectrodes, therefore lower R_{NL} values, and a systematic deviation has been found in the EIS response that required frequency selection to fit to the low frequency response.[9] With the additional diffusion regimes at arrays the EIS develops further into another feature after R_{NL} at low frequencies, making the fitting and frequency selection more challenging.

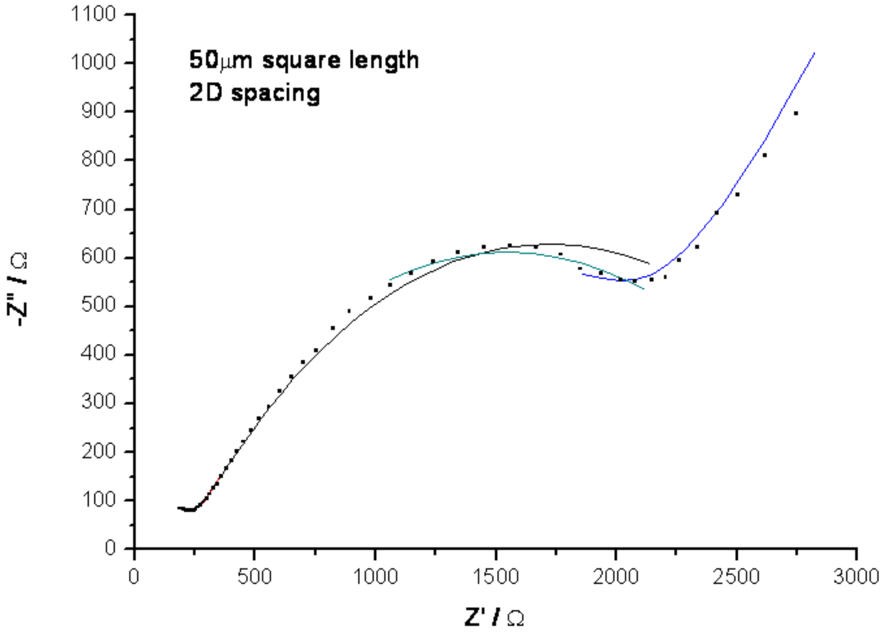

Figure 7-14: The selected frequencies used for fitting the Randles' Circuit and Modified Randles Circuit to determine values for the solution resistance and double layer capacitance (red line), the charge transfer resistance and the micro-Warburg impedance (black line), the non-linear resistance (green line) and the macro-Warburg impedance (blue line).

The various features of the Nyquist plot were fitted using the equivalent circuits seen in Figure 7-15. The modified Randles circuit, containing the non-linear resistance, is typically used to describe a microelectrode circuit, while the standard Randles circuit is used to describe macroelectrodes. Therefore the standard Randles circuit was used to describe the low frequency macroelectrode-like behaviour as the diffusion profile changed from hemispherical to linear diffusion across the entire array.

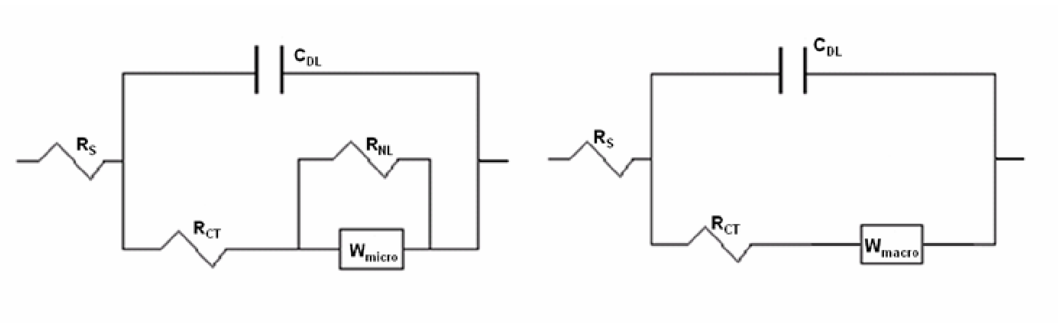

Figure 7-15: Equivalent circuits used to fit the impedance response of the arrays. The modified Randles circuit was used to determine solution resistance (R_{S}), double layer capacitance (C_{DL}), charge transfer resistance (R_{CT}), non-linear resistance (R_{NL}) and micro-Warburg impedance (W_{micro}). The Randles Circuit was used to find macro-Warburg impedance (W_{macro}).

7.3.2.1 Analysis of the Hemispherical Diffusion Regimes at a Square Microelectrode Array

The non-linear resistance of the microelectrode arrays were determined using iterative fitting to the modified Randles' circuit at each E_{DC}. The results of these fits are shown in Figure 7-16, plotted against E_{DC}.

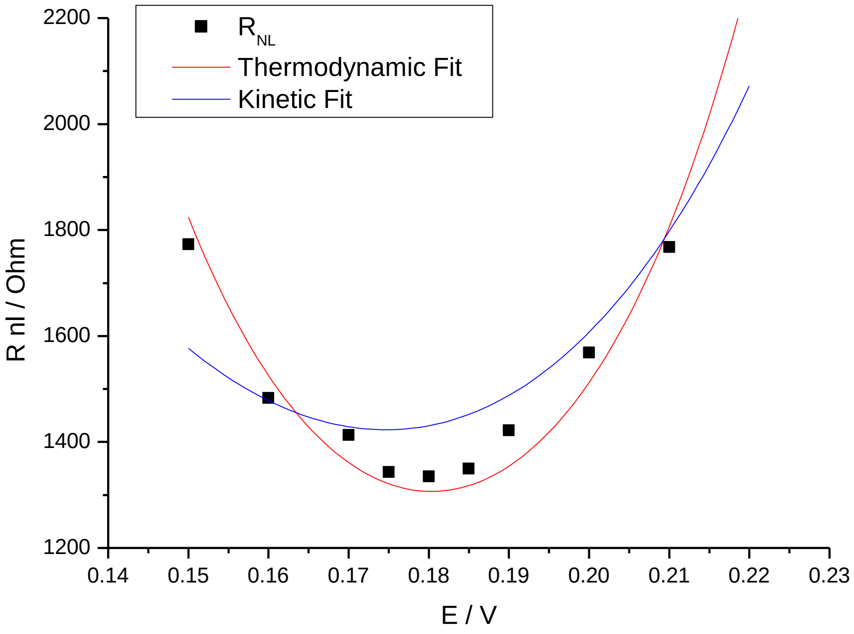

Figure 7-16: R_{NL} vs. E_{DC} for the 30A3D array. The shape of the plot is typical for each array.

Equations previously derived to describe the charge transfer resistance, discussed in Chapter 3 (Section 3.5), were used to describe how the non-linear resistance of the microelectrode changed with E_{DC}. For a single square microelectrode two possible expressions were used, the "thermodynamic fit" (Equation 3-2) and the "kinetic fit" (Equation 3-3). The thermodynamic and kinetic fits gave R^2 values of 0.97 and 0.83 respectively. From this, and a visual inspection of the fits, it is clear that the thermodynamic fit most appropriately describes the array behaviour.

This is reassuring and expected as R_{NL} is determined by the mass transport of redox species whose concentrations are determined by the Nernst equation.

During diffusion regime (b) the microelectrodes on an array are acting independently. Therefore they should be responding to the same diffusion fields and subject to the same non-linear resistance. Therefore the array responses were normalized for number of electrodes on the array and superimposed on each other to see if this were the case. The result can be seen in Figure 7-17.

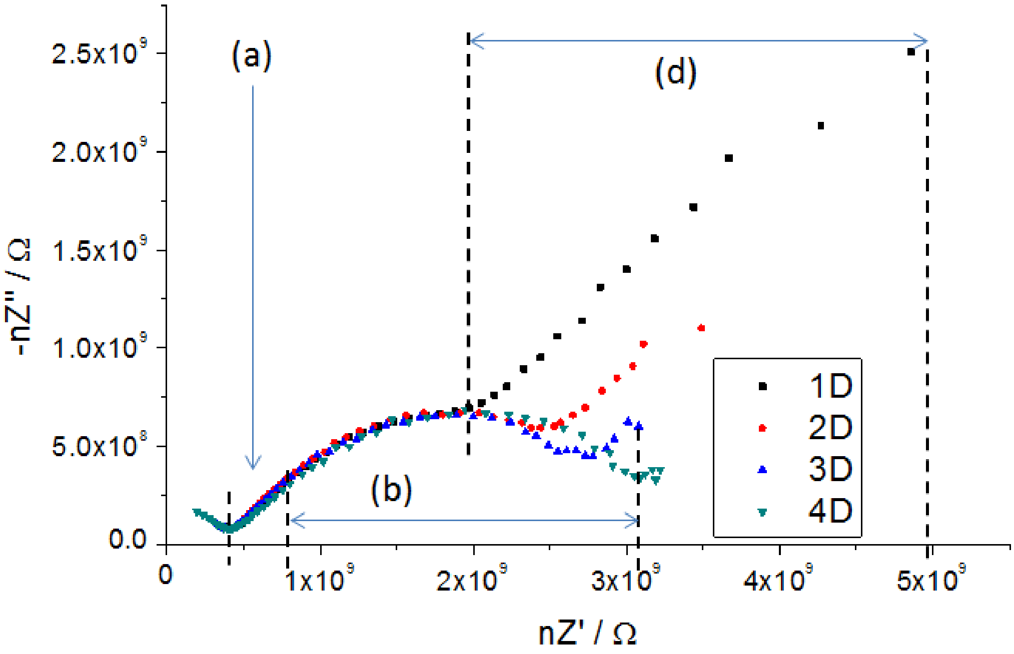

Figure 7-17: Nyquist plot of arrays with D = 50 µm, with varying S at an E_{DC} of 0.170 V normalised for total electrode area (n) showing the diffusion response at low frequencies. Region (a) shows linear diffusion over an electrode, (b) shows hemispherical diffusion and (d) shows linear diffusion over the array area.

It is satisfying that the impedance response for the arrays does indeed show clearly the devices responding to different diffusional profiles and that the individual linear and hemispherical fields of (a) and (b) can be superimposed when normalised for array area. As the frequency is lowered it can be seen that the arrays deviate from the non-linear resistance describing regime (b). A straight line indicating linear diffusion over the array, regime (d), develops. Regime (c) is, as the transition from (b) to (d), identifiable as the transition from R_{NL} to a Warburg response at low frequencies. This occurs at higher frequencies for closer spaced arrays, indicating that the overlap has occurred more quickly, as expected. This demonstrates the independence of the non-linear resistance and hemispherical diffusion from the spacing of the array.

7.3.2.2 Determining the Limiting Current from the Non-Linear Resistance

Given that the non-linear resistance describes independent hemispherical diffusion from each array element, this can be used to understand the array response if the electrodes were sufficiently spaced to not have overlapping diffusion profiles, regime (b). This therefore has a relationship with the limiting current of the array. This relationship was determined and is discussed below.

The modified Tafel equation (Equation 7-1) applies to an electrochemically reversible reaction and is applicable to microelectrode analysis.[10]

$$\ln\left(\frac{i_L}{i}-1\right)=\frac{nF\left(E-E_{\frac{1}{2}}\right)}{RT}$$

Equation 7-1

This can be rearranged to:

$$i=i_L\left[\frac{1}{1+\exp\left[nF\left(E-E_{\frac{1}{2}}\right)/RT\right]}\right]$$

Equation 7-2

If a small change in potential is applied ($\Delta E = E_1 - E_2$) then:

$$i_1 = i_L \left[\frac{1}{1 + \exp\left[nF\left(E_1 - E_{\frac{1}{2}} \right) / RT \right]} \right]$$

Equation 7-3

And:

$$i_2 = i_L \left[\frac{1}{1 + \exp\left[nF\left(E_2 - E_{\frac{1}{2}} \right) / RT \right]} \right]$$

Equation 7-4

Therefore:

$$\frac{i_L}{i_1} - \frac{i_L}{i_2} = 1 + \exp\left[\frac{nF\left(E_1 - E_{\frac{1}{2}} \right)}{RT} \right] - 1 + \exp\left[\frac{nF\left(E_2 - E_{\frac{1}{2}} \right)}{RT} \right]$$

Equation 7-5

Let $P = E_2 - E_{½}$, so that $P + \Delta E = E_1 - E_{½}$. Therefore Equation 7-5 can be written as:

$$\frac{i_L}{i_1} - \frac{i_L}{i_2} = \exp\left[\frac{nF(P + \Delta E)}{RT} \right] - \exp\left[\frac{nFP}{RT} \right]$$

Equation 7-6

$$\frac{i_L}{i_1} - \frac{i_L}{i_2} = \exp\left[\frac{nFP}{RT}\right]\left(\exp\left[\frac{\Delta EnF}{RT}\right] - 1\right)$$

Equation 7-7

If ΔE is small (as in EIS) then the exponential can be linearised, giving:

$$\exp\left[\frac{\Delta EnF}{RT}\right] \approx 1 + \frac{\Delta EnF}{RT}$$

Equation 7-8

So:

$$\frac{i_L}{i_1} - \frac{i_L}{i_2} = \exp\left[\frac{nFP}{RT}\right]\left(\frac{\Delta EnF}{RT}\right)$$

Equation 7-9

This rearranges to:

$$\frac{i_L(i_2 - i_1)}{i_2 i_1} = \exp\left[\frac{nFP}{RT}\right]\left(\frac{\Delta EnF}{RT}\right)$$

Equation 7-10

or

$$\frac{-i_L \Delta i}{i_2 i_1} = \exp\left[\frac{nFP}{RT}\right]\left(\frac{\Delta EnF}{RT}\right)$$

Equation 7-11

Where $\Delta i = i_2 - i_1$.

In EIS $Z = \Delta E / \Delta i$, as explained in Chapter 2, which under these mass transport controlled conditions corresponds to R_{NL}. Therefore:

$$\frac{\Delta E}{\Delta i} = R_{NL} = \frac{-i_L RT}{nFi_2 i_1}\exp\left[\frac{-nFP}{RT}\right]$$

Equation 7-12

Note that there is a minus sign at the beginning of the expression to indicate the reduction reaction.

From Equation 7-3 and Equation 7-4:

$$i_1 i_2 = \left(\frac{i_L}{1 + \exp\left[\frac{nF(P + \Delta E)}{RT} \right]} \right) \left(\frac{i_L}{1 + \exp\left[\frac{nFP}{RT} \right]} \right)$$

Equation 7-13

This can be rearranged to give:

$$i_1 i_2 = i_L^2 \left(\frac{1}{\left(1 + \exp\left[\frac{nF(P + \Delta E}{RT} \right] \right) \left(1 + \exp\left[\frac{nFP}{RT} \right] \right)} \right)$$

Equation 7-14

Again as ΔE is small:

$$i_1 i_2 \approx i_L^2 \left(\frac{1}{\exp\left[\frac{nFP}{RT} \right] + 1} \right)^2$$

Equation 7-15

So Equation 7-15 can be substituted into Equation 7-12:

$$R_{NL} = \frac{-RT}{nFi_L} \exp\left[\frac{-nFP}{RT} \right] \left(\exp\left[\frac{nFP}{RT} \right] + 1 \right)^2$$

Equation 7-16

This rearranges to:

$$R_{NL}=\frac{-RT}{nFi_L}\left(\exp\left[\frac{nFP}{RT}\right]+1\right)\left(1+\exp\left[\frac{-nFP}{RT}\right]\right)$$

Equation 7-17

$$R_{NL}=\frac{-RT}{nFi_L}\left(2+\exp\left[\frac{-nFP}{RT}\right]+\exp\left[\frac{nFP}{RT}\right]\right)$$

Equation 7-18

The general expression for oxidation or reduction is therefore:

$$R_{NL}=\left|\frac{RT}{nFi_L}\right|\left(2+\exp[-nFP/RT]+\exp[nFP/RT]\right)$$

Equation 7-19

To further simplify, as

$$\cosh\theta=\frac{e^{-\theta}+e^{\theta}}{2}$$

Equation 7-20

And

$$\cosh^2\theta=\frac{2+e^{-2\theta}+e^{2\theta}}{4}$$

Equation 7-21

So Equation 7-19 becomes:

$$R_{NL}=\left|\frac{4RT}{nFi_L}\right|\cosh^2\left(\frac{nFP}{2RT}\right)$$

Equation 7-22

This means that the non-linear resistance should be readily be able to be used to determine the limiting current. In the trough of the R_{NL} vs. E_{DC} graph (Figure 7-16) the value of R_{NL} is equal to $R_{NL,min}$, the minimum possible non-linear resistance, found at E^{θ} (P=0).

$$i_L = \frac{4RT}{nFR_{NL,\min}}$$

Equation 7-23

From the thermodynamic fit the values of $R_{NL,min}$, the minimum value for the non-linear resistance, and E^{θ} were found. These were 1306.7 Ω and 0.180 V respectively for the 30A3D device analysed in Figure 7-16.

Using Equation 7-23, the limiting current from the non-linear resistance was determined to be 7.725 x10^{-5} A. Table 7-5 summarises the different current outputs found for the 30A3D array.

	i_L observed experimentally / A	i_L calculated from impedance / A	i_L simulated computationally / A
Total Array	9.357 x10^{-5}	7.73 x10^{-5}	8.29 x10^{-5}
Individual Electrode	5.304 x10^{-8}	4.38 x10^{-8}	4.70 x10^{-8}

Table 7-5: The difference in current response for the 30A3D array found experimentally from cyclic voltammetry at a scan rate 100 mVs^{-1}, calculated from impedance measurements and simulated using COMSOL.

The value of limiting current calculated from the impedance response shows good agreement with the simulated currents for single squares (within 10%). This indicates that the COMSOL simulated response is a good method for predicting the diffusional response of a microelectrode and validates this approach for calculating the limiting current from EIS.

7.3.2.3 Analysis of the Linear Diffusion Regimes at a Square Microelectrode Array

In addition to the non-linear resistance the Warburg coefficients were fitted for each device to see how the values changed with varying array characteristics. The typical changes in the response of W_{micro}, and W_{macro}, the Warburg coefficients describing the first and second linear diffusion profiles are shown in Figure 7-18.

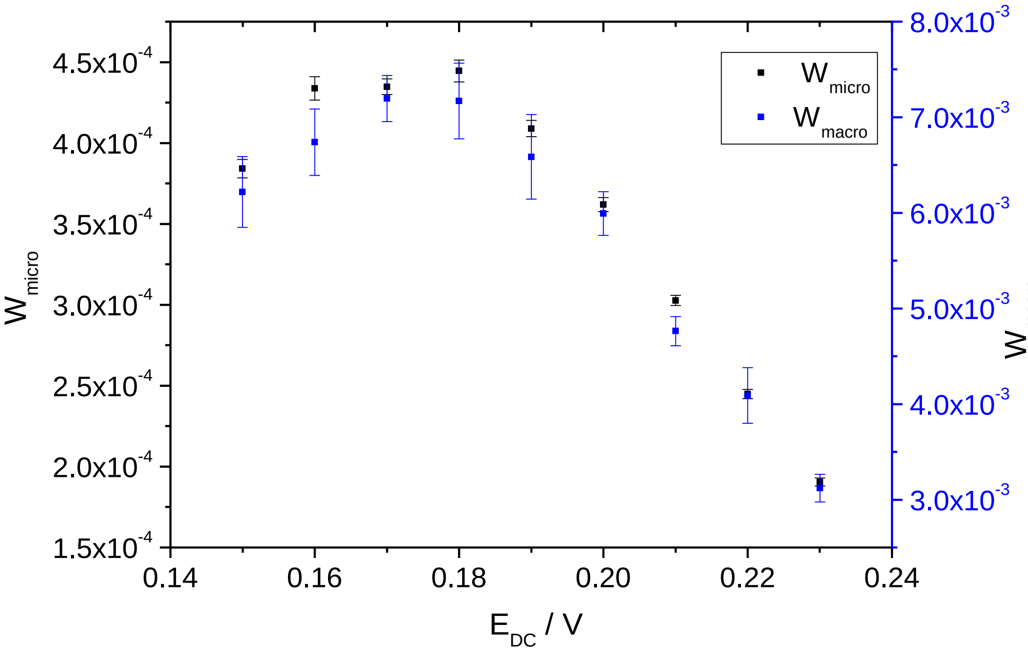

Figure 7-18: W_{micro} and W_{macro} vs. E_{DC} for the 50A3D array. The shape of the plot is typical for each array.

Both W_{micro} and W_{macro} can be seen to be following a similar trend, with a peak around E^0. The error bars are notably larger for the W_{macro} values. This can be attributed to the difficulty of fitting to lower frequency responses, as there are only a small number of data points.

The relationship between W_{macro} and W_{micro} was studied further. Values of Y_0 were obtained at each E_{DC} measured by fitting against a standard

Randles circuit and the modified Randles circuit, respectively. These values were then plotted against each other and revealed a linear relationship, shown in Figure 7-19.

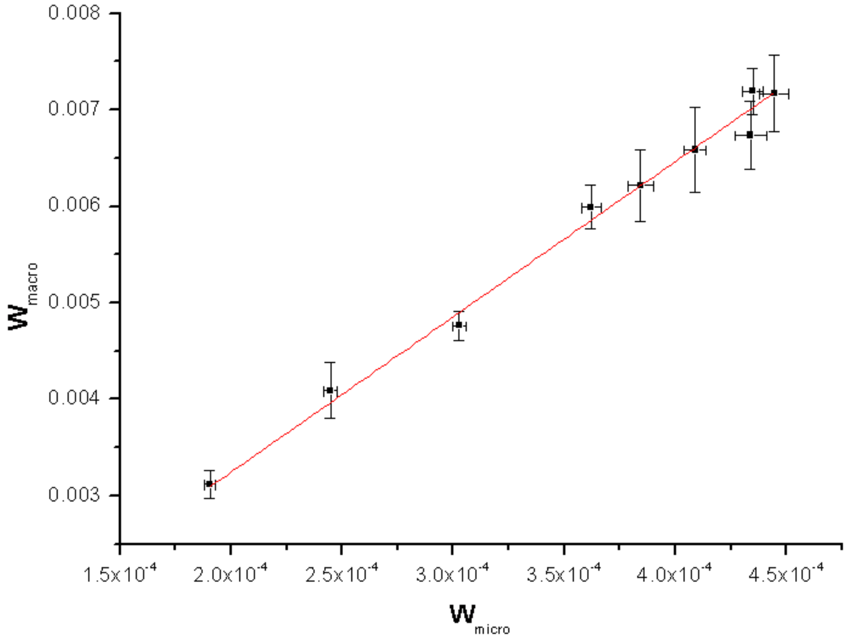

Figure 7-19: The linear relationship between values of W_{micro} and W_{macro} at each E_{DC} for a single array using values of Y_0.

The relationship of this gradient to the array spacing is $(x+1)^2$ where xD is the spacing, so when S = 2D, there is a ratio between W_{micro} and W_{macro} of 9. This is a ratio of linear diffusion over a single electrode and linear diffusion over that electrode's space in the array, shown schematically in Figure 7-20 and is consisten with regimes (a) and (d).

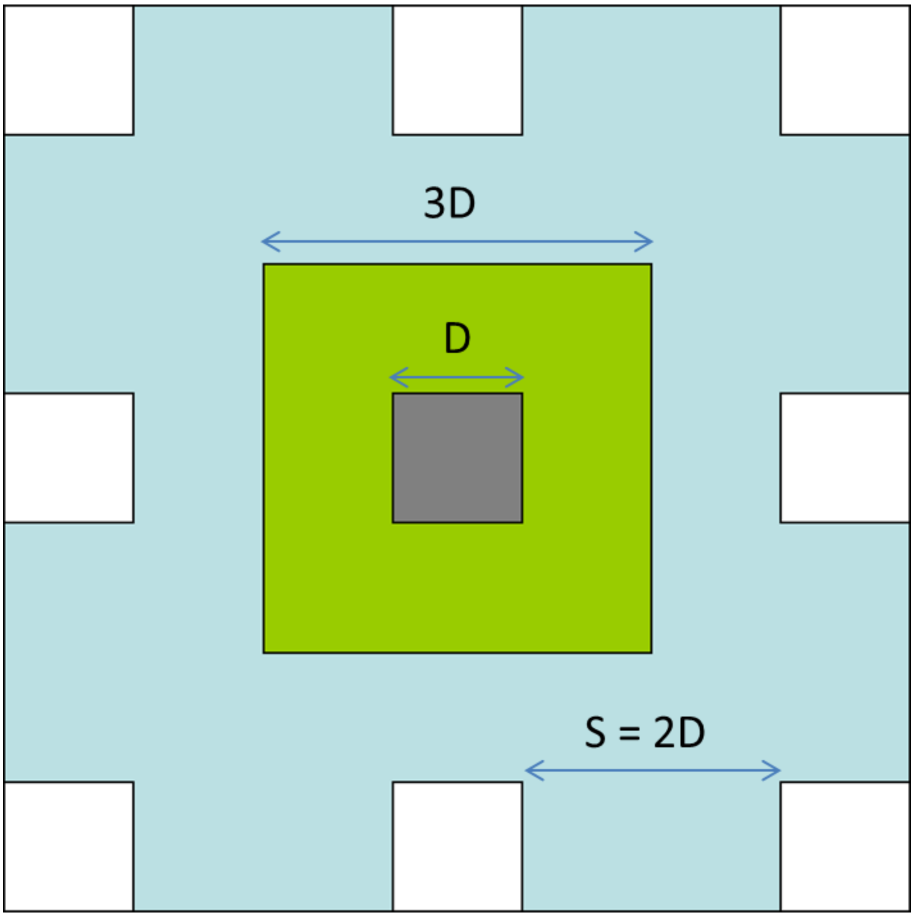

Figure 7-20: Schematic showing the relationship between W_{micro} and W_{macro} on an S = 2D array. W_{micro} describes linear diffusion over a single electrode (grey) of edge length D and W_{macro} describes linear diffusion over the electrode and surrounding space (green) of edge length 3D.

7.3.3 Designing an Equivalent Circuit to Describe the Global Array Response

The relationship between W_{micro} and W_{macro} shows that there is a relationship between the device acting as a single microelectrode and when the array acts as a macroelectrode. Attempts were made to design a global fit that described the array response, at all applicable frequencies, using a single equivalent circuit. It was important in designing a circuit that, rather than fitting the data first and risk over-parameterising, used features that gave insight into the physical processes that may be going on.

Two possible circuits were designed based on the modified Randles Circuit with an additional Warburg impedance in Figure 7-21. The placing of the second Warburg, W_{macro}, to be in parallel with C_{DL} and in series with the other diffusion components to the circuit seemed logical. However, issues with the fit at lower frequencies suggested that C_{DL} had changed. By placing the W_{macro} element in series with the C_{DL} it would minimise the effect of C_{DL} on W_{macro}, so a second circuit was attempted. This was also not the observed case. At low frequencies the fitting of C_{DL} continued to force a different value on the circuit than that found at high frequencies, where it was relevant to the model. Effectively, C_{DL} apparently changed between the array showing microelectrode and macroelectrode behaviour. This makes no physical sense and on reflection there seems no *a priori* reason why the two equivalent circuits should be bridged by this theoretical circuit. Therefore the two separate circuits were used for all fitting.

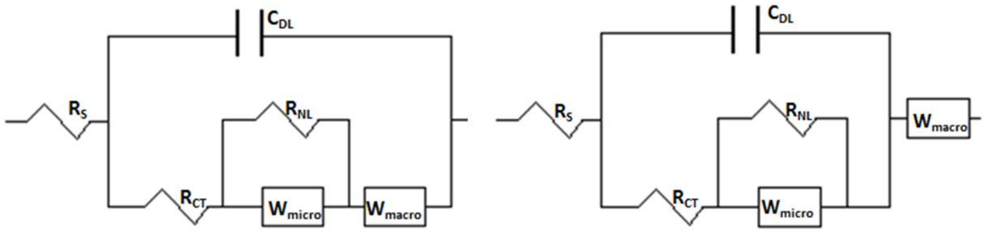

Figure 7-21: Equivalent circuits expected to fit the microelectrode array response over the entire frequency range.

7.3.4 Using Chronoamperometry to Characterise the Diffusion Over a Square Microelectrode Array

In addition to the complete analysis with EIS, potential step voltammetry (or chronoamperometry) was used to characterise the current response from arrays over time. Figure 7-22 shows the current-time transients for the 50A3D array, with the potential being stepped from +0.350 V to mass transport limited reduction of ferricyanide. This is typical of each array response. The magnitude of current is reduced when the potential step is smaller.

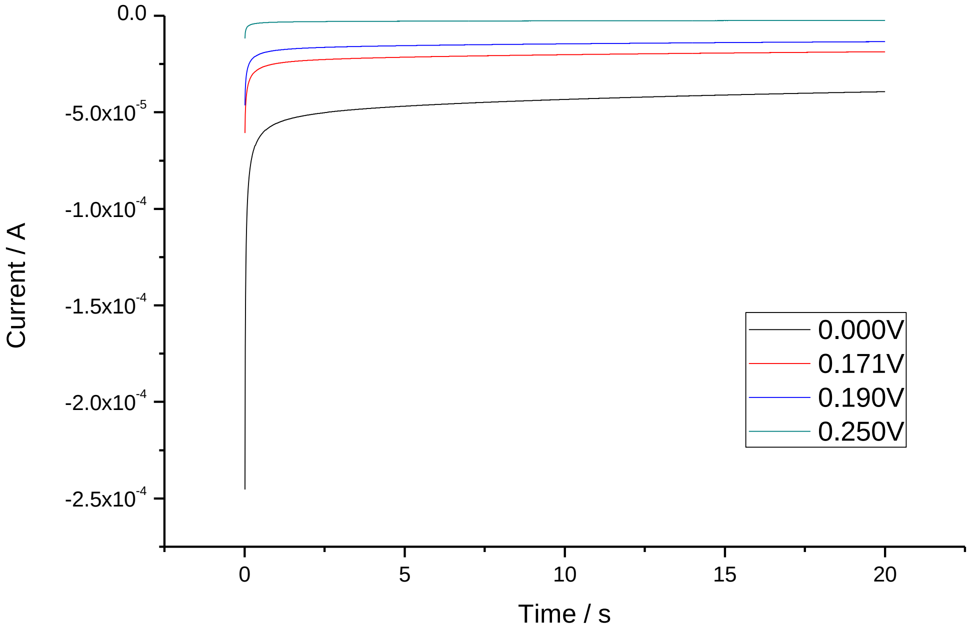

Figure 7-22: Current-time transients for the 50A3D array, with the potential stepped from 0.350 V.

Figure 7-23 shows the effect of spacing on the 50 μm edge arrays. It can be seen that for the 50A1D device current drops more rapidly. This indicates the rapid development to diffusion regimes (c) and (d) due to the close electrode spacing that lower current. With increasing spacing it is seen that the current reduction is less and that the 50A3D and 50A4D arrays show very similar character across 20 seconds, indicating that they are subject to less overlap in that time, as expected.

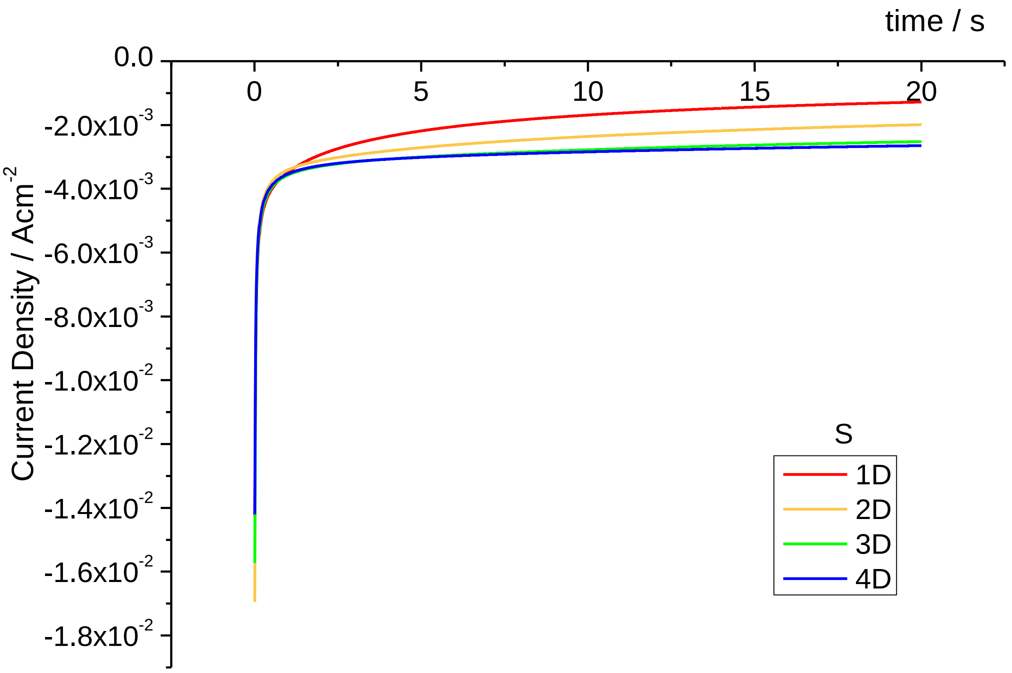

Figure 7-23: Current time transients for D = 50 µm arrays with varying spacing when the potential is stepped from 0.350 V to 0.00 V normalised for total array area.

The measured current-time transients were compared to COMSOL simulated transient responses, discussed in Chapter 3 (Section 3.4). These simulations were based on diffusion to a single square microelectrode in an array using a reactive species with diffusion coefficient $D = 6.98*10^{-10}$ m^2s^{-1} and a bulk concentration of [c] = 10 $molm^{-3}$. The simulated array responses for the devices with microelectrodes of 50 µm edge can be seen, with a single square response, in Figure 7-24.

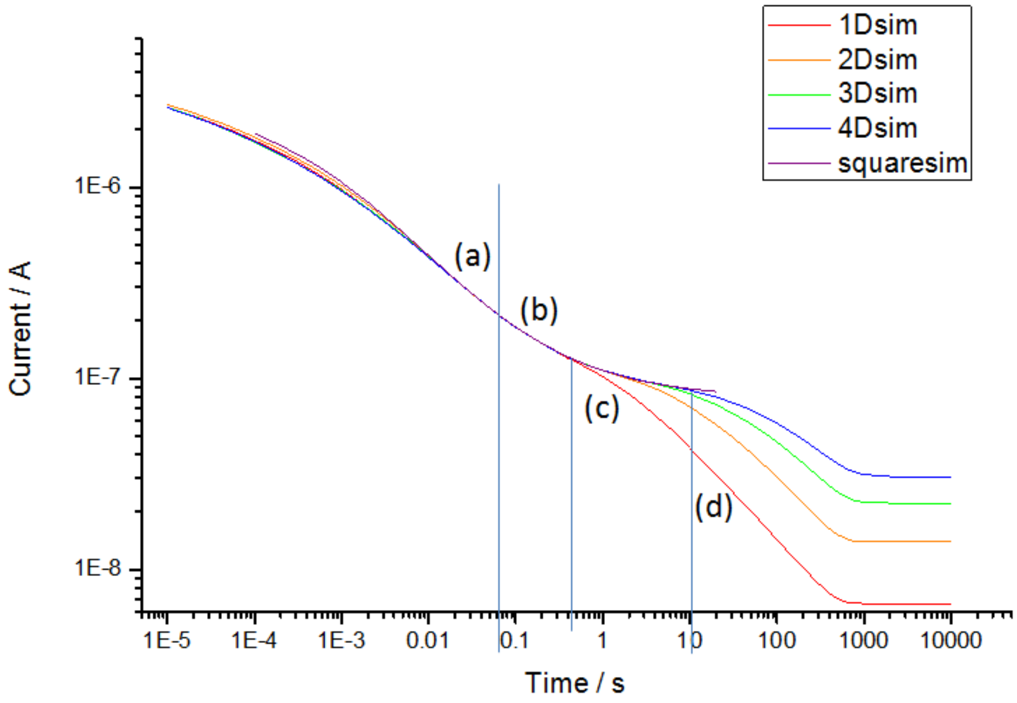

Figure 7-24: COMSOL simulated current-time transients for D = 50 μm array electrodes with varying S. Currents are for one electrode. Potentials were stepped from 0.350 V to 0.000 V. The linear regions (a) & (d) show linear diffusion, while region (b) shows hemispherical diffusion.

The simulations cover the timeframe from $1\text{x}10^{-5}$ – $1\text{x}10^{5}$ seconds, though it is accepted that at very short timescales the diffusion simulations are limited by meshing effects. The currents all follow the same response through linear diffusion over individual electrodes, regime (a), and develop hemispherical diffusion. Eventually the arrays begin to deviate from the square response, as the profile changes from (b) to (c) and the current is less due to the degree of overlap. This is indicated by the current of the 1D array dropping rapidly and this drop occurring sooner than for the larger spaced arrays. Regime (d), complete overlap and linear diffusion, is achieved once the current response decays linearly. In this region the current will obey the Cottrell equation (Equation 2-11). Therefore this linear decrease has a gradient of about -0.5 for all arrays, as:

$$\log(i) = A - \tfrac{1}{2}\log(t)$$

Equation 7-24

It is notable that regime (a) at short timescales also has this gradient, as expected for linear diffusion to individual electrodes. At very long timescales the current plateaus. This is an artefact of the simulation, showing that diffusion has reached the edge of the simulation box. It is a limitation of the defined simulated environment, not a real effect.

The comparison of experimentally observed and simulated device responses can be seen in Figure 7-25. Also shown is the response for a single square, as was discussed in Chapter 5 (Section 5.3.2). The comparison clearly shows a similar response over experimental timeframes as the diffusion changes from regime (b) to (c) as overlap occurs. This occurs more rapidly for closer spaced arrays, with the 1D array even appearing to develop linear diffusion across the array, regime (d). The single square response has a larger current density than expected due to flaws in the passivation layer. However, it shows the two regimes associated with single microelectrodes: (a) and (b) only.

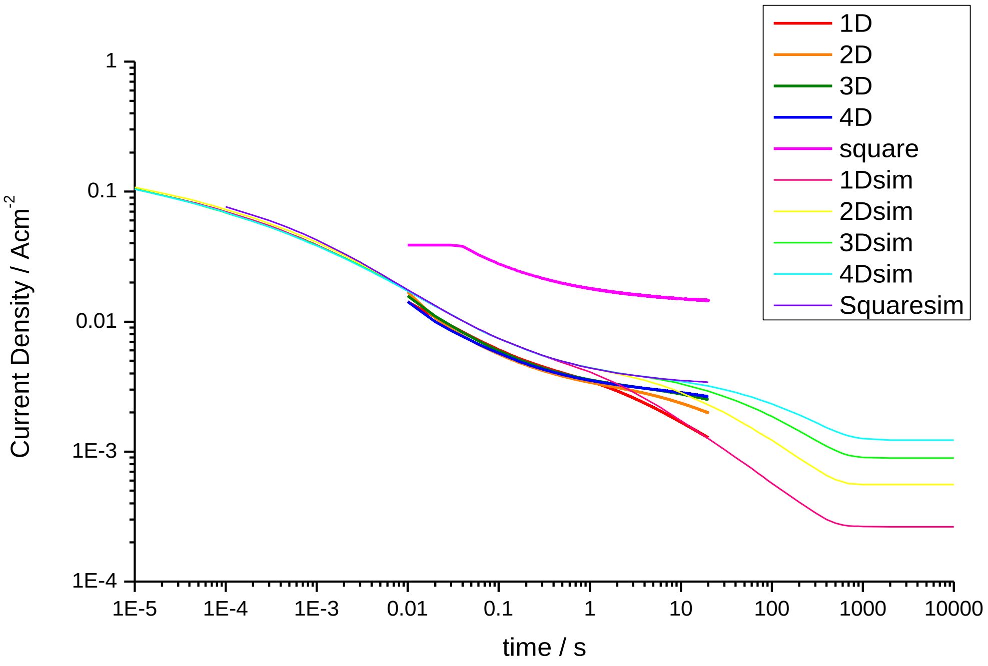

Figure 7-25: Comparison of simulated and experimental current-time transients for D = 50 µm arrays with varying S and a single square. Potentials were stepped from 0.350 V to 0.000 V.

There is a noticeable difference in the current magnitude between experimentally observed and simulated responses. This is attributed to the simulations using a temperature of 25 °C, while the chronoamperometry experiments were performed at ambient laboratory temperature. Using a waterbath to control the temperature would produce external convection that would affect the current response, as was observed in cyclic voltammetry experiments.

Figure 7-26 shows the chronoamperometry response as the potential is swept from 0.350 to 0.00 V with the x-axis as $t^{-1/2}$. The response is different to those found for single squares (Figure 5-14), which was a curved line that did not go through the origin. In this case the arrays have broadly similar current responses over short times, before the current density drops at longer timescales towards the origin.

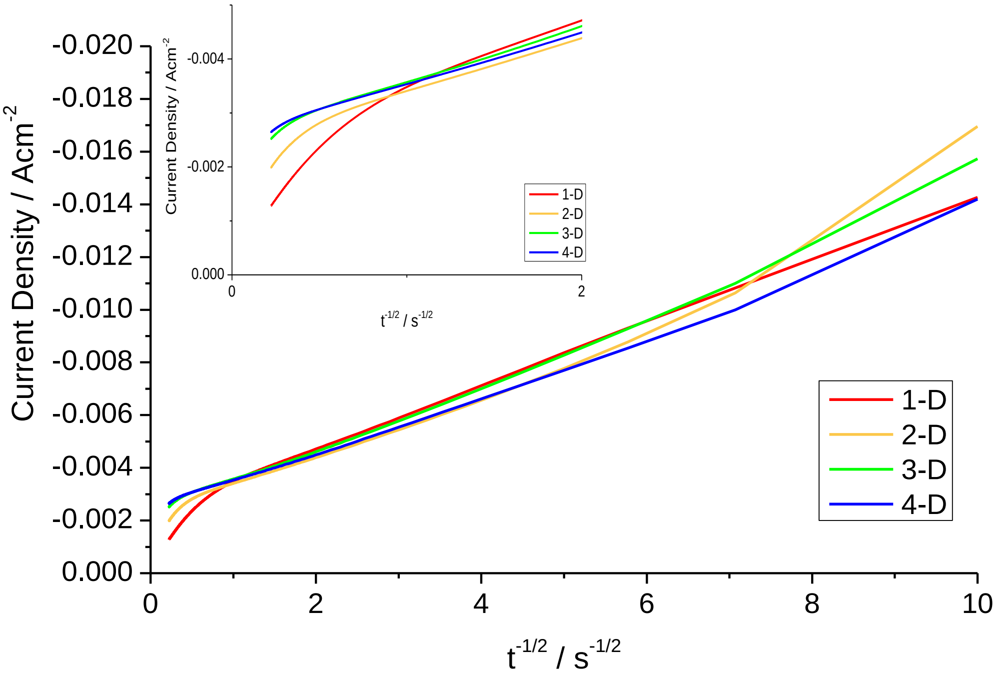

Figure 7-26: t$^{-1/2}$ vs. current density for the array with D = 50 μm and varying spacing. Inset shows response at long timescales, as t$^{-1/2}$→ 0, t→∞.

The drop in current response begins sooner for the closer spaced array (red line), shown in the inset. In addition the curve is steeper, showing the drop in current efficiency for the closer spaced array. As t→∞, the current density of the 50A1D array appears to be tending to 0 Acm^{-2}, which you would find for linear diffusion as described by the Cottrell equation, regime (d). This demonstrates the transition from hemispherical diffusion in regime (b), which has been shown in Chapter 5 to go towards a steady state current as t→∞, to linear diffusion which would tend towards the origin. Though, in reality, this will also go towards a non-zero value of current due to convection in the solution allowing some mass transport of material to the electrode.

7.4 Conclusions

Microelectrode arrays have been fabricated and characterised through various techniques to give a full and systematic analysis of their response for the standard ferri/ferrocyanide electrochemical redox reaction with respect to both the electrode area and the electrode spacing. The time-dependent response has been considered in terms of changes in the growing diffusion layer across the square microelectrode array. More than just the sum of its parts, an array has its own diffusional response to changing electrochemical conditions with two additional regimes compared to a single square microelectrode. Through cyclic voltammetry, EIS and chronoamperometry the array system response has been characterised and these four diffusion regimes have been measured as a function of array parameters.

Cyclic voltammetry confirmed that there is no ideal spacing or microelectrode size for individual hemispherical diffusion and optimum current density over a square microelectrode array. Instead this depends on the type of experiment performed because, for examples, at different scan rates the diffusion profiles vary. The evolution of the diffusion field at the microelectrode was shown to be dependent on both the square microelectrode length and the spacing between electrodes in a reproducible and predictable manner. This opens up the prospect for optimal microelectrode array design and fabrication, tuned to experiment.

EIS also showed clearly the developing response due to diffusion at the microelectrode array. This shows that for closer spaced arrays the linear diffusion response over the entire array occurs more quickly. In addition due to the fact that hemispherical diffusion is a feature of individual electrodes, this response was found to be independent of electrode spacing and could therefore be used to find the theoretical array limiting current when the electrodes were sufficiently spaced apart to act independently. These currents were also in close agreement with the limiting currents predicted by COMSOL simulations.

Potential step experiments were also used to see how the current response changed with time. As expected, as electrode spacing increased the electrodes were seen to act independently for longer. Linear diffusion over the array at longer times reduced the current and the current response became Cottrell in nature (i vs. $t^{\frac{1}{2}}$) more quickly for closer-spaced arrays, consistent with the peak currents, rather than limiting currents, seen in the cyclic voltammetry.

From this work it is clear that photolithographic fabrication techniques can be used to produce arrays of square electrodes with controlled size and spacing, whose fundamental response is as expected theoretically. This opens up the prospect of their application in electroanalytical measurement, and also raises the question as to why this fabrication has not been affected by the flaws in the silicon nitride insulator seen in the previous chapter. This can be understood by the fact that the number of electrodes in these arrays is so large that the contribution of any additional electrode area exposed by flaws to the overall current can be considered to be negligible.

7.5 References

---

[1] S. Fletcher, M.D. Horne. Electrochemistry Communications. Vol. 1, Issue 10, (1999) p502–512
http://dx.doi.org/10.1016/S1388-2481(99)00100-9

[2] T.J. Davies, R.G. Compton. Journal of Electroanalytical Chemistry. Vol. 585, Issue 1 (2005) p63–82
http://dx.doi.org/10.1016/j.jelechem.2005.07.022

[3] S.J. Hood, D. K. Kampouris, R.O. Kadara, N. Jenkinson, F.J. del Campo, F.X. Muñoz and C.E. Banks. Analyst, 2009, 134, 2301-2305
DOI: 10.1039/B911507B

[4] H.J. Lee, C. Beriet, R. Ferrigno, H.H Girault. Journal of Electroanalytical Chemistry. Vol. 502, Issues 1–2 (2001) p138–145
http://dx.doi.org/10.1016/S0022-0728(01)00343-6

[5] G Buß, M.J Schöning, H Lüth, J.W Schultze. Electrochimica Acta
Vol. 44, Issues 21–22 (1999) p3899–3910
http://dx.doi.org/10.1016/S0013-4686(99)00097-3

[6] C. Belmont, M.-L. Tercier, J. Buffle, G.C. Fiaccabrino, M. Koudelka-Hep
Analytica Chimica Acta, Vol. 329, Issue 3 (1996) p203-214
http://dx.doi.org/10.1016/0003-2670(96)00116-X

[7] H.O. Finklea, D.A. Snider , J. Fedyk , E. Sabatani , Y. Gafni , I. Rubinstein. Langmuir, 1993, 9 (12), p3660–3667
DOI: 10.1021/la00036a050

---

[8] W.E. Morf, N.F. de Rooij. Sensors and Actuators B: Chemical, Vol. 44, Issues 1–3 (1997) p538-541 http://dx.doi.org/10.1016/S0925-4005(97)00159-7

[9] H.L. Woodvine, J.G. Terry, A.J. Walton and A.R. Mount, Analyst, 2010 **DOI:** 10.1039/b924342a

[10] H.L. Woodvine. Development and Characterisation of Microelectrode and Nanoelectrode Systems (2011) University of Edinburgh

Chapter 8: The Development of a High Temperature System for Molten Salt Analysis Using Microelectrodes

In this chapter the design, manufacture and development of high temperature compatible microelectrodes for molten salt analysis is described. Apparatus for high temperature electrochemical experiments was first designed and constructed. A simple one electron reversible reaction in the well-known lithium chloride: potassium chloride eutectic salt was used to characterise the developed microelectrode devices for response and robustness to assess their future application to the analysis of pyrochemical nuclear reprocessing reactions.

8.1 Introduction

Molten salt media are of great interest for electrochemical studies, due to their ability to eliminate water as a solvent, dissolve compounds at high concentrations, support oxidation states not readily accessible in aqueous systems and enable enhanced chemical reaction rates due to their higher temperatures[1]. One use of molten salts that is particularly important for addressing future energy concerns is during the re-enrichment processing of nuclear fuels. Various countries across the globe, including South Korea and Russia, use molten salt systems to electrochemically separate uranium from used nuclear fuel for re-enrichment, thereby removing the useful species from the fission products. Various electrochemical studies of redox-active species in molten salts have been studied using macro-sized electrodes to understand the processes that occur under these conditions[2,3].

Microelectrodes are a useful tool to monitor processes in closed systems, such as processes that involve anhydrous, high temperature conditions. Due to their hemispherical diffusion profiles microelectrodes are ideal tools to study diffusion, as discussed previously (Section 2.2). The efficient hemispherical diffusion also reduces or removes the influence of convection in the system, which would need to be controlled to achieve adequate sensing with a macroelectrode. This is an issue because convection in high temperature systems is difficult to control due to the enhanced thermal and mechanical convection in heated industrial systems.

There have been very few studies using microelectrodes in molten salts. Pint and Flengas used a tungsten wire set in glass as a microelectrode for molten salt analysis.[4] They attached it to an oscillator to use as a dropping mercury electrode analogue as mercury has a boiling point of 356.7 °C. While they achieved a microelectrode response, by their own admission the reduction response of silver ions to metal was not well defined. Carlin and Osteryoung used a microelectrode of tungsten wire set in a Pyrex capillary tube to study reduction of lithium and bismuth ions to the liquid metals.[5] They noticed some etching and cracking of the microelectrodes after removal from the melt, most likely due to a combination of corrosive chemical attack of the Pyrex and/or a mechanical failure at the electrode-insulator interface due to mismatched thermal expansion. With the improved fabrication methods of lithography, this opens up the possibility of developing robust microelectrodes for analysis in molten salt environments as a valuable area of study for future applications.

8.2 High Temperature Design Development

A high temperature system was first designed to perform electrochemistry in molten salts. The initial idea was to have a sealed metal reaction vessel with external heating and a controlled atmosphere. To facilitate this, a tube furnace and Schlenk line were procured. The Schlenk line is a dual gas manifold which controls the atmosphere of the system by connection to a vacuum pump or a gas source through pipes.

Initial designs of the experimental set up vessel were developed around an existing stainless steel reaction vessel of height 100 mm. A Carbolite Single Zone Tube Furnace (Model GVA12/100/300) with a heated length of 300 mm was purchased for the high temperature work and so the reaction vessel length was extended to ensure that the molten salt would be within the metal coils heating the furnace. The metal reaction vessel modified to extend the length is shown in Figure 8-1.

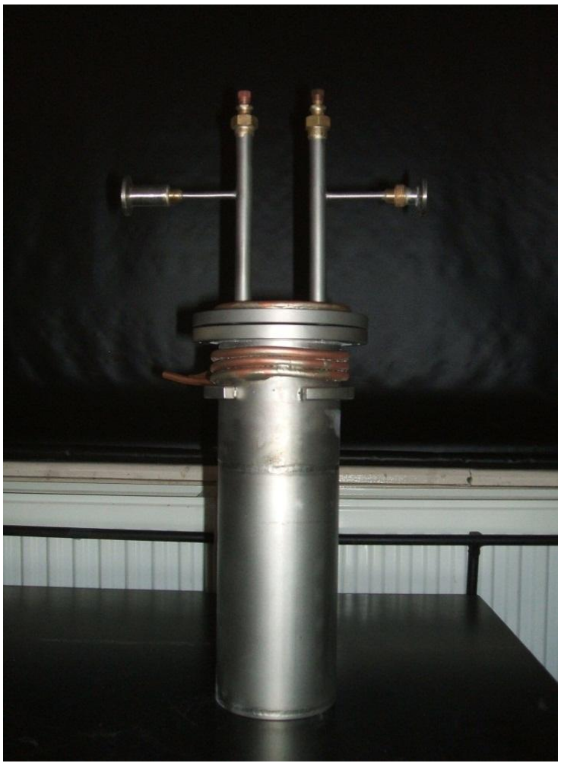

Figure 8-1: The initial metal reaction pot.

This original vessel had several noteworthy features. Inlet and outlet gas pipes are visible, along with cooling coils. The vessel was constructed from stainless steel, which is more robust and a cheaper material than quartz. The top of the vessel was sealed to the bottom by means of a rubber O-ring. At high temperature, given the high thermal conductivity of steel, this required the addition of cooling coils to ensure the O-ring seal was not compromised.

However, this water cooling design would create large thermal gradients which on consideration would be undesirable. In addition, the introduction of electrodes to the system required them to be fed through the metal pipes in the lid. The metal system could therefore create shorting issues, between the cell and the electrical contacts and also shorting between the cell and the metal heating coils of the furnace.

To address these issues a new cell was therefore, similar to those found in other molten salt research described in the literature[6,7] (Figure 8-2). The cell body was manufactured from quartz by YorLab Ltd, whilst the lid was made from borosilicate glass to prevent contact with the electrochemical connections, and also avoids any undesirable contact with the metal heating coils of the furnace. This was considered to benefit both safety and performance. As an additional benefit, quartz allowed visual inspection of the inside of the system.

The metal cell design contained a gas inlet and outlet to connect to the Schlenk line for molten salt purification and evacuation. This aspect of the system was preserved to keep the cell sealed from air, as well as to remove any chlorine gas produced as a by-product during experimentation. Additional ports for the electrode contacts were added. These were screw cap controlled (GL14 Duran Group Gmbh/ Schott

Glass) so that the electrodes could be raised and lowered, as required. An alumina crucible (Almath Crucibles Ltd) was used to contain the molten salt in the cell. The final quartz vessel and associated crucible can be seen in Figure 8-2.

Figure 8-2: The quartz cell with alumina crucible

The quartz vessel and the borosilicate glass lid were joined using a metal collar that fitted around the circumference of the connection. During experiment, it became clear that this collar was not tight enough to seal the system. The choice of seal between the vessel and the lid caused several issues. Initial attempts used a pre-existing Teflon O-ring though this was ineffective in providing an adequate seal. Ultimately vacuum grease was found to provide an adequate seal. This held for a day but prolonged temperatures and maintaining the vessel under vacuum caused bubbles to form in the grease, likely from decomposition of the grease, eventually allowing air into the system. It was, however, sufficient for experimentation over a 1 day period.

8.3 Electrode Design

The counter electrode and working macroelectrode were tungsten rods, sealed in glass at one end. This allowed them to be introduced to the molten salt while maintaining a closed system. The electrodes in position in the vessel lid are shown in Figure 8-3.

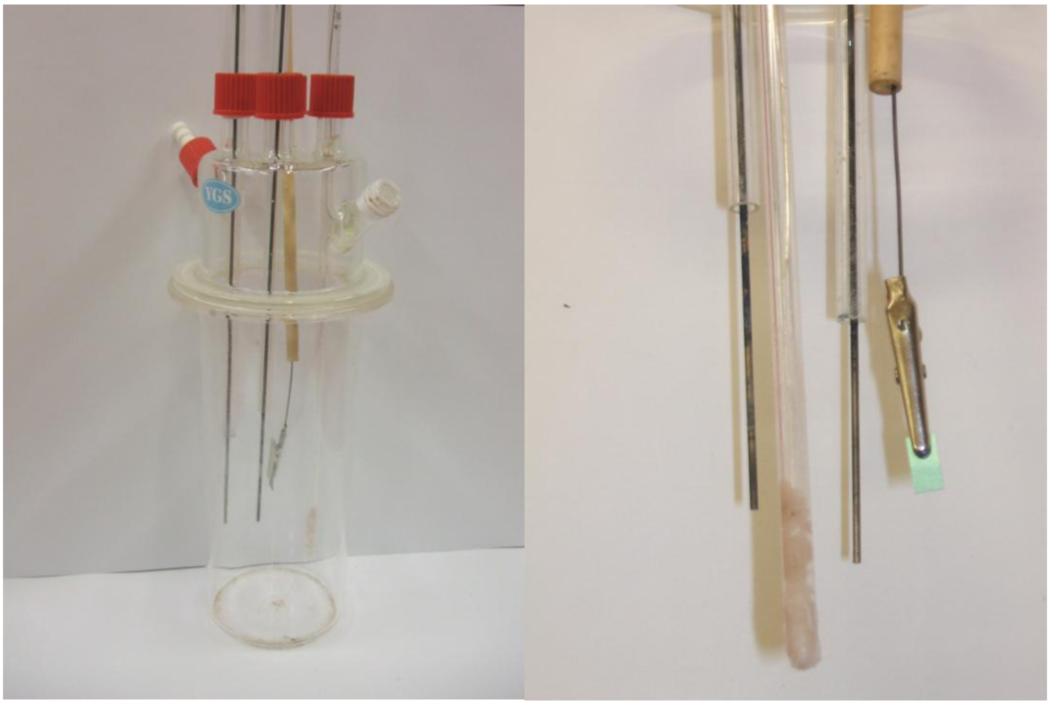

Figure 8-3: The final quartz vessel and lid, with fitted electrodes. Shown here from left-to right are the tungsten rod working electrode, the Ag/AgCl reference electrode, tungsten rod counter electrode and a single tungsten microelectrode device on a crocodile clip. The right side port of the lid connects to the Schlenk line for evacuation.

Two square tungsten microelectrode designs were fabricated as described in Chapter 3 (Section 3.1.3). The first design were devices 10 mm in length with square electrodes of 500 µm edge length. Although these are relatively large for microelectrodes they allowed for proof of concept studies of electrochemical detection. The devices are shown in Figure 8-4.

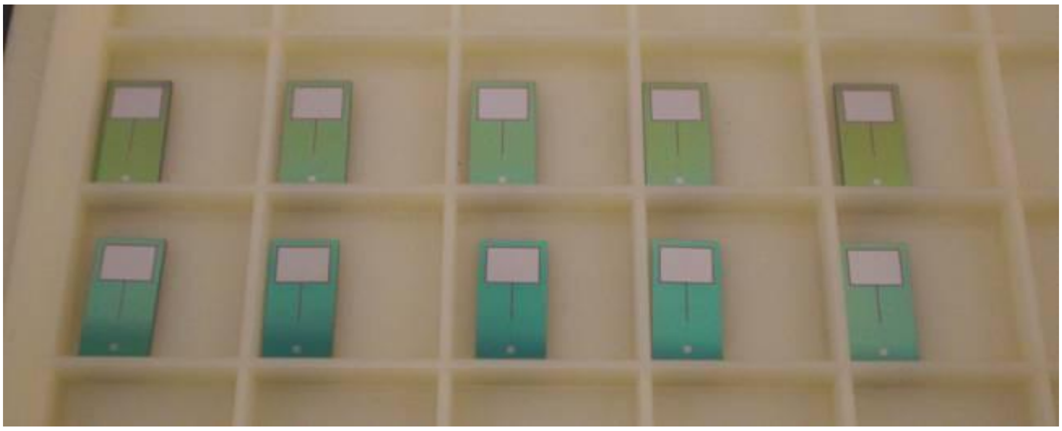

Figure 8-4: The single square microelectrode devices.

The second batch of square electrode devices produced were 35 mm in length, with square electrodes of 50 µm edge. They were based on a design of platinum electrode with eight microelectrodes on a single device, discussed in Chapter 3. These electrodes had contact pads slightly too small for the crocodile clips used in the system. In addition, the electrodes were designed eight to a device and were therefore too wide for the reaction vessel. To solve these issues the device was diced to have two electrodes and complete tracks to the contact pad, with a crocodile clip connecting to two contact pads at the same time, as shown in Figure 8-5.

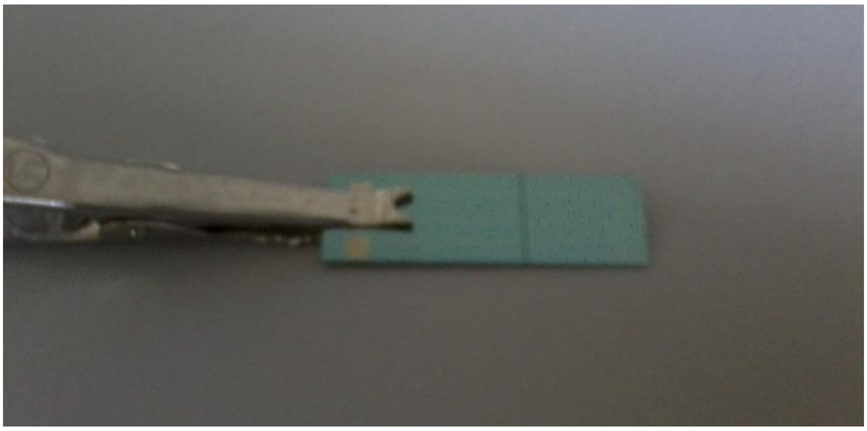

Figure 8-5: The final tungsten microelectrodes, diced to retain only two electrodes per device.

The microelectrodes were connected using a 4 mm nickel plated steel fine wire crocodile clip (Hirschmann) with flattened teeth to ensure a good connection to the contact pad. The other end of the crocodile clip was connected to a 0.75 mm straight tungsten wire (Goodfellow) threaded through a ceramic tube up through the screw cap lid port.

The reference electrode was a silver: silver chloride couple produced by having a 0.75 molkg^{-1} concentration of AgCl in LiCl-KCl held in a thin glass tube. A silver wire was extended to near the base of the tube so it was dipping into this salt mixture. The glass was kept thin so that at high temperatures it would be partially permeable to ions, allowing diffusion through the glass without affecting the bulk concentration of the melt. This design was similar to others found in the literature[8,9] and preferable to metal reference electrode alternatives that act as pseudo reference electrodes. Platinum foil and platinum wire were used historically as pseudo-reference electrodes, but were shown to only be able to maintain a constant potential over a limited timeframe[10,11].

8.4 Redox Material Delivery

A material delivery system was designed to add redox species to the closed system after the molten salt had been dried. This was to enable introduction of the redox species subsequent to the molten salt drying procedure. The initial design involved a capsule made from a glass melting point tube with the intention that on addition of the capsule to the melt it would break either from the impact or from the thermal shock the capsule would be subject to. The capsule was made by sealing the tube at one end before the dried, ground, redox material was added. The remaining tube end was then sealed. Examples of capsules containing silver chloride are shown in Figure 8-6.

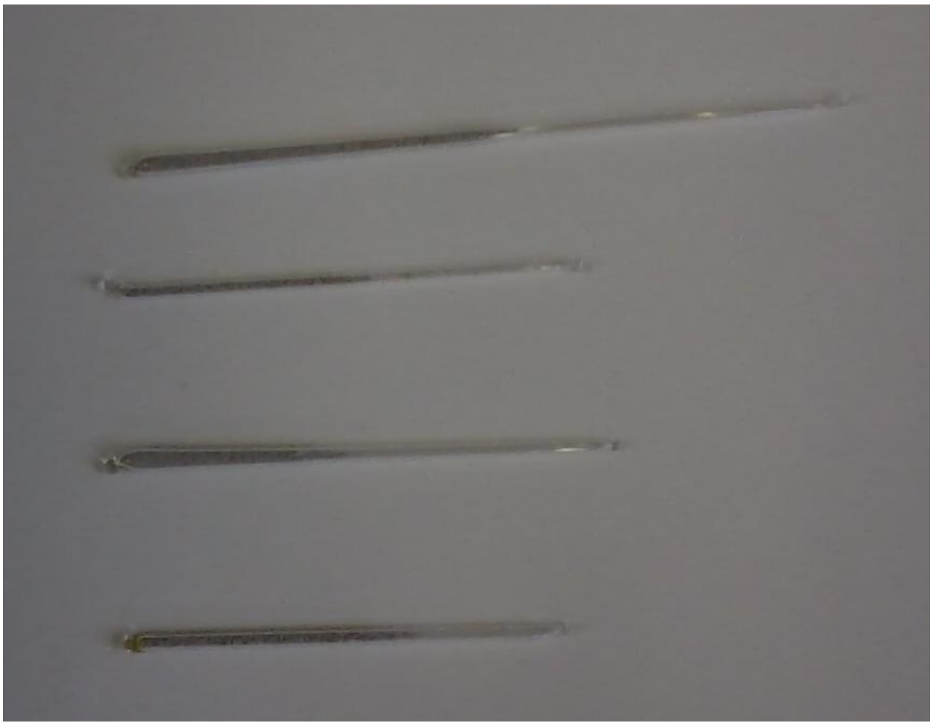

Figure 8-6: The capsules of silver chloride produced from melting point tubes that are designed to break on entry to the molten salt to release the redox active material.

During the high temperature experiments the logistics of redox material delivery into the vessel presented a considerable challenge. Initial attempts involved the use of a glass tube sealed at one end, fixed into a side port of the lid, shown in Figure 8-7. This tube had a notch in the centre that would prevent the redox capsule from falling in to the system until it was required. Unfortunately this proved unreliable and the tube would either not fall into the system at all or do so at unexpected times.

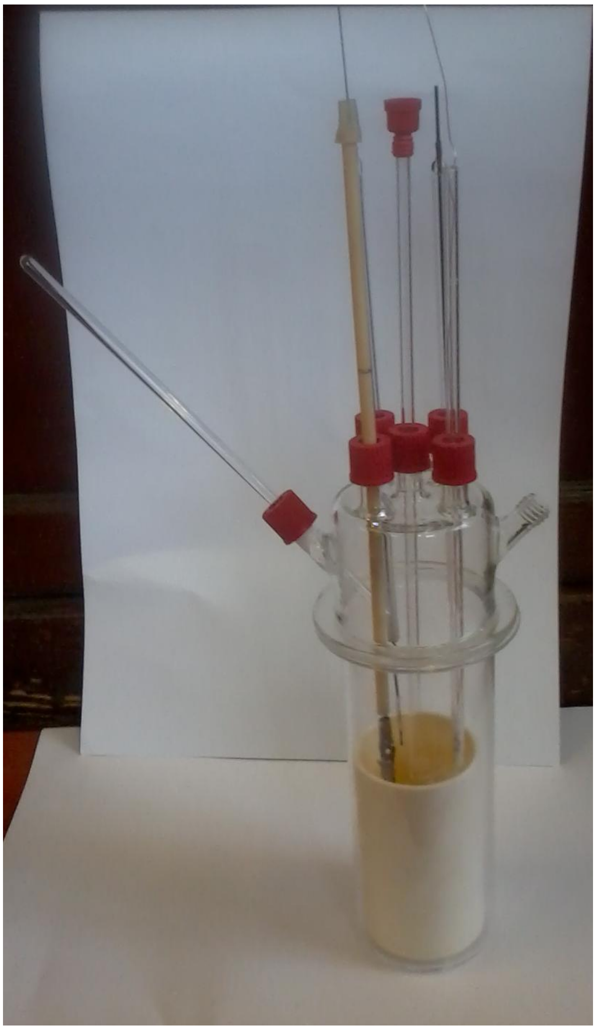

Figure 8-7: The final design of the quartz vessel, alumina crucible and lid. The lid allows control of the descent of the electrodes and has an additional port to drop capsules of redox active materials into the melt. The right side port is connected to the Schlenk line. The left port shows the failed material delivery system.

Subsequently a new vessel lid was commissioned with a fifth port at the top as an alternative delivery method was tried. A vertical tube, with a removable seal was used to drop the capsule down in to the melt after drying. There were also difficulties with this delivery method. If the tube was stationed too high in the vessel the capsule would just sit on the melt without breaking, or the impact of the capsule on the melt led to splashing which wet the electrochemical connections. If the tube was too low in the melt opening the system, even momentarily, to drop the capsule led to exposure of the salt to oxygen and gaseous H_2O again, rendering the previously performed salt drying procedure useless.

8.5 Connection Optimisation

Given the small size of the microelectrode devices, lowering of the electrode in to the molten salt without also wetting the crocodile clip and destroying the connection was very tricky. To protect this connection and prevent creep of the melt up the silicon oxide surfaces a porcelain panel was inserted behind the device. This can be seen in Figure 8-8.

Figure 8-8: The microelectrode device supported by a crocodile clip and porcelain plate to prevent wetting of the connections caused by the melt creeping up the device.

The porcelain plate proved to be inefficient and would occasionally, as the crocodile clip was stretched further open, lead to the device falling off in to the melt.

A more robust solution to this wetting problem was found in the application of a ceramic gum used in repairing car exhausts (Holts Firegum), which was used to seal the connection between the device contact pad and the crocodile clip. After repeated use, it was found that the gum was not subject to leaching of electroactive species or attack from the melt. This meant that the crocodile clip was left unaffected by any electrochemistry in the salt and ensured that the current response was wholly that of the microelectrode. The gum sealing the connection is shown in Figure 8-9.

Figure 8-9: The microelectrode device and crocodile clip sealed in ceramic gum to prevent loss of connection.

Another issue found during experiments was corrosion leading to loss of connectivity. After one experimental session it was found that the crocodile clip and microelectrode device were coated in black residue. This is shown in Figure 8-10. This residue washed off easily in water. It is possible that a reaction caused the coating on the crocodile clip to degrade, although given that the clip does not enter the melt it seems unlikely that it is due to attack from the liquid reagents. Instead, the release of gases from the melt, removed by vacuum, must cause corrosion. The most likely source is O_2/H_2O which could lead to black nickel (III) oxide formation on the nickel-coated crocodile clip.[12]

Figure 8-10: A crocodile clip and microelectrode device coated in black residue produced during high temperature experiments.

Corrosion of the microelectrode device, the electrodes and the connections would affect reproducibility and lifetimes of the equipment. Figure 8-11 shows the build-up of residue after high temperature experiments. This affected the electrochemistry by producing very high resistances.

Figure 8-11: Other visible signs of corrosion on the apparatus after high temperature experiments.

The way to minimise this was to coat the clip in the gum used to seal the microelectrode-crocodile clip connection to protect it. The electrode and the crocodile clip were also placed as highly as possible in the quartz cell before use to remove them from any stream of gases produced by the salt during the drying procedure.

8.6 System Optimisation

Another design issue found during use of the high temperature system was electrical noise produced in the tube furnace during heating and while maintaining a constant temperature. This noise was manifest in periodic bursts of induced current as the coils were heating to maintain temperature. Such effects were more pronounced on microelectrodes than macroelectrodes as the Faradaic current were smaller. This meant that a systematic noise signal was seen in the electrochemical response during experiments. Figure 8-12 shows the effect of this noise on the current signal for both a macroelectrode and a microelectrode.

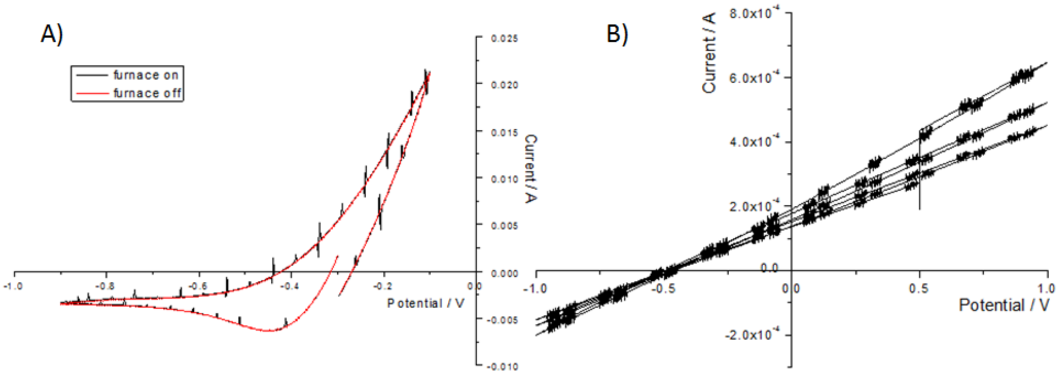

Figure 8-12: CVs displaying the effect of electrochemical noise from the furnace heating element on A) a macroelectrode and B) a microelectrode signal.

A pseudo-Faraday cage was therefore designed to cover the areas of the vessel that would be subject to the noise to see if this signal could be blocked. This cage is shown in Figure 8-13.

Figure 8-13: Metal cage designed to act as a pseudo-faraday cage.

Unfortunately, while the cage showed some reduction in noise, it did not completely remove the signal from the tube furnace. In addition the metal gauze heated up to such an extent that the quartz cracked and broke where the cage was in contact with the vessel. It was therefore decided not to pursue electrical shielding further at this point. Instead when cyclic voltammetry was performed on systems for analysis the furnace was turned off. This limited the cyclic voltammetry to timeframes which ensured the melt did not drop in temperature significantly, and certainly not below 400 °C, giving approximately 5 minutes to gather data.

8.7 Electrochemistry in Molten Salts

8.7.1 Experimental

All tungsten square microelectrodes were handled and pre-treated as described in Chapter 4 (Section 4.5). In pre-treatment the time was minimised between removal of the protective photoresist layer and onset of electrochemical measurement to minimise tungsten oxide build up on the surface.

A 45:55 wt.% mixture, typical mass of 100 grams, of lithium chloride: potassium chloride was placed in the alumina crucible. This was then heated at 120 °C overnight to dry the salt before use. The cell was then assembled and placed in the tube furnace. A vacuum was applied using the Schlenk line with a good seal (as shown by the vacuum gauge registering and maintaining a pressure equal or less than 0.1 mbar). Heating was performed under vacuum in the furnace in stages to 120 °C, 220 °C, 320 °C and 450 °C, with twenty minutes between reaching each temperature and beginning the next heating step. This was to allow adequate time for any water species to be driven off and ensure the melt was at the furnace-controlled temperature. The salt was then finally typically heated to 500 °C to ensure it was fully molten before electrodes were lowered into the crucible.

All cyclic voltammetry was performed under vacuum. Voltammetry to dry the molten salt was performed using a tungsten rod macroelectrode by scanning the potential across the solvent window. Once dry, silver deposition and stripping was chosen as a well-documented[13,14,15,] one electron, reversible reaction to study in the melt. Silver studies were performed by dropping capsules of silver chloride into the melt after drying, while allowing time for the silver chloride to sufficiently mix with the LiCl-KCl eutectic before performing cyclic voltammetry across the redox reaction.

8.7.2 Macroelectrode Reactions in the Molten Salt

8.7.2.1 Molten Salt Drying

Having a pure LiCl: KCl molten salt is important beyond simply having the ability to monitor a clear response of a redox material. While it is generally accepted to be a eutectic salt of choice due to its high stability and conductivity, whilst avoiding fluoride salt corrosive properties, it does have one disadvantage. Water and oxygen impurities in the salt mixture can react with the alkali earth ions, particularly lithium[16], to form oxide and hydroxide. The hydroxide species are corrosive[17] and lower the salt's efficiency as a solvent. The equations for producing these oxygen containing contaminants are:

$$H_2O + LiCl \rightleftarrows LiOH + HCl$$

Equation 8-1

$$H_2O + 2LiCl \rightleftarrows Li_2O + 2HCl$$

Equation 8-2

Before redox reactions could be investigated it was necessary to remove any remaining oxy- and hydroxy- containing species within the molten salt, effectively further drying it to purity. Typically molten salts are purified by using large amounts of hydrogen chloride in the system to shift the equilibria to the left. However for this work an electrochemical drying method was developed for ease of use. Cyclic voltammetry was used to repeatedly scan across the solvent window of the LiCl: KCl eutectic, as shown in Figure 8-14, using a tungsten rod working electrode at a scan rate of 100 mVs^{-1}. Note that there is repeated periodic noise in the current signal from the furnace heating element.

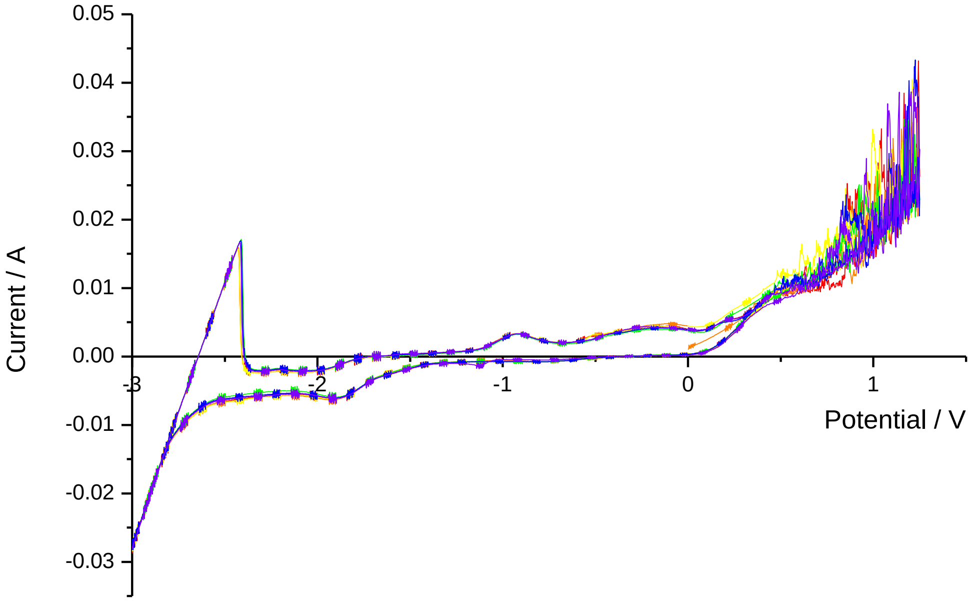

Figure 8-14: CV of the molten salt with oven-dried lithium chloride: potassium chloride eutectic.

Chlorine gas production can be seen as an oxidation more positive than 1.0 V and occurs by the reaction:

$$2Cl^- \rightarrow Cl_{2(g)} + 2e^-$$

Equation 8-3

This gas production tends to make the current response very noisy, as pockets of gas block regions of active electrode surface. The lithium plating process is a reduction at potentials more negative than -2.0 V for the salt and occurs by the reaction:

$$Li^+ + e^- \rightarrow Li_{(l)}$$

Equation 8-4

The oxidation of lithium is seen as a stripping peak when the potential sweep is reversed and the lithium returns as ions into the melt. If this peak is not observed/present it is a good indication that the melt contains oxidising agents that react chemically with the newly reduced lithium metal. Possible equations for these chemical reactions are:

$$Li_{(l)} + H_2O_{(l)} \rightarrow Li^+_{(l)} + OH^-_{(l)} + \frac{1}{2}H_{2(g)}$$

Equation 8-5

$$Li_{(l)} + OH^-_{(l)} \rightarrow Li^+_{(l)} + O^{2-}_{(l)} + \frac{1}{2}H_{2(g)}$$

Equation 8-6

Over a number of scans (from twenty to two thousand) the current response across the solvent window was found to change indicating electrochemical drying of the molten salt. The features present in Figure 8-14 within the solvent window decrease in magnitude until they are no longer visible. This leaves the solvent window clear of background reactions that may impede electrochemical analysis in the melt. These peaks are likely due to hydrogen and oxygen gas being produced at the negative and positive potentials respectively, removing the water based contaminants. A plot of current response from a salt going through the electrochemical drying process is shown in Figure 8-15.

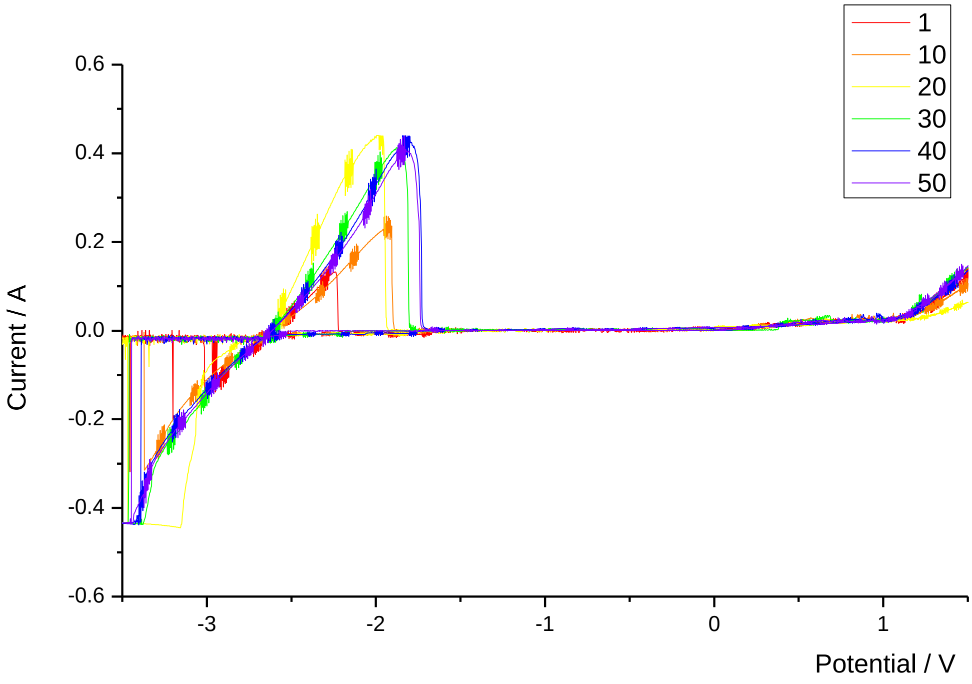

Figure 8-15: Cyclic voltammetry scans with growing lithium stripping peak height, indicating electrochemical molten salt drying.

At very negative potentials over subsequent scans the lithium stripping peak increases, indicating that the liquid lithium metal is no longer chemically reacting to oxide and hydroxide species present in the system. The procedure was stopped when the lithium plating/stripping peaks appeared to be no longer increasing with subsequent scans.

Electrochemical drying is preferable to chemical removal of water species from the molten salt using gas due to safety, as well as removing the requirement for a necessary atmosphere the melt is subjected to via the Schlenk line a dual gas manifold. The exclusion of hydrogen chloride gas allows for an alternative gas to be introduced to the system such as Argon after cleaning.

8.7.2.2 Macroelectrode Detection of Silver

Capsules of silver chloride were added to the melt after drying to see if the electrodes could detect the redox species. These reactions on a macroelectrode were used to ensure that the capsule had broken and that silver ions were present in the melt. Figure 8-16 shows one of the responses after a capsule has been added and given twenty minutes for material to diffuse into the melt.

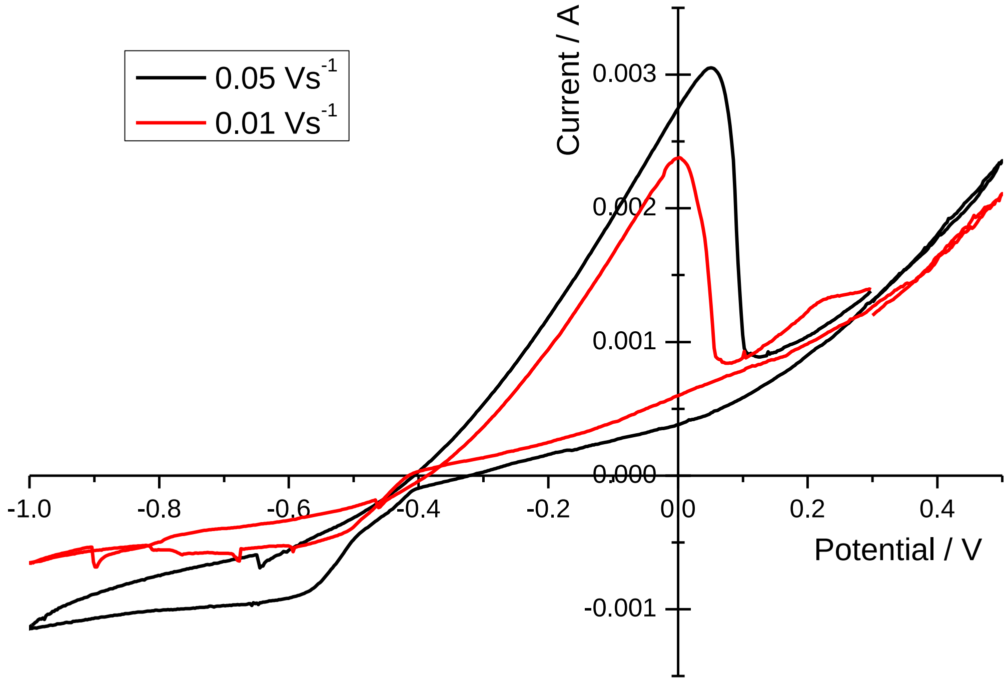

Figure 8-16: CV of silver deposition and stripping in the molten salt on a tungsten macroelectrode.

The CV shows the silver plating and stripping. The deposition occurs at potentials more negative than -0.40 V. As the potential is swept forward towards zero the current magnitude is higher, indicating that the silver deposition is favourable on the tungsten electrode, rather than the already deposited silver. The current response shows quite broad peaks indicating there is significant resistance within the system.

8.7.3 Microelectrode Response in Molten Salt

Microelectrode responses were very difficult to achieve in initial experiments. A typical response found in a dry salt after switching from tungsten rod to microelectrode as working electrode is shown in Figure 8-17 below.

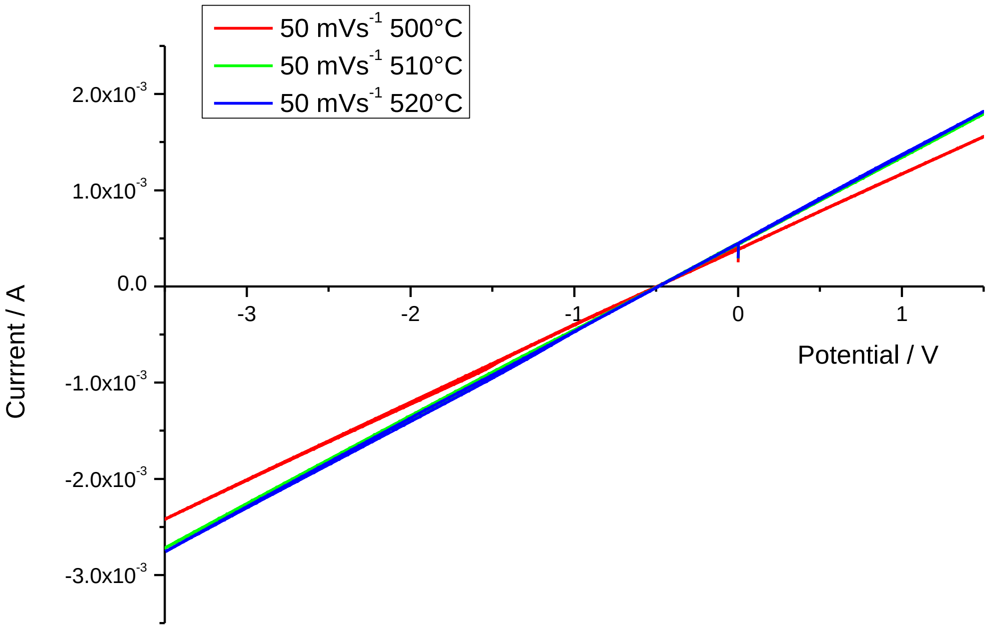

Figure 8-17: A typical cyclic voltammetry response from a microelectrode indicating high resistances.

The relatively high currents for a microelectrode and shape of the CV suggested that there was a very high resistance associated with the system. This resistance decreased as the temperature increased, as can be seen by the change in gradient of the linear response due to Ohm's law.

The molten salt is an extreme environment for a microelectrode device. The susceptibility to attack from the melt was judged by inspecting the electrodes and passivation layer under a microscope after experimental work. This involved raising the electrodes out of the salt after use, letting the melt solidify (typically overnight) before deconstructing the assembly, cleaning the equipment and washing off any remaining salt mixture with water.

Figure 8-18 shows an image of microelectrode device that produced the resistive response. It is worth noting that this system required prolonged drying overnight and so the device had been subject to high temperatures and vacuum for 24 hours before characterisation in the melt was attempted.

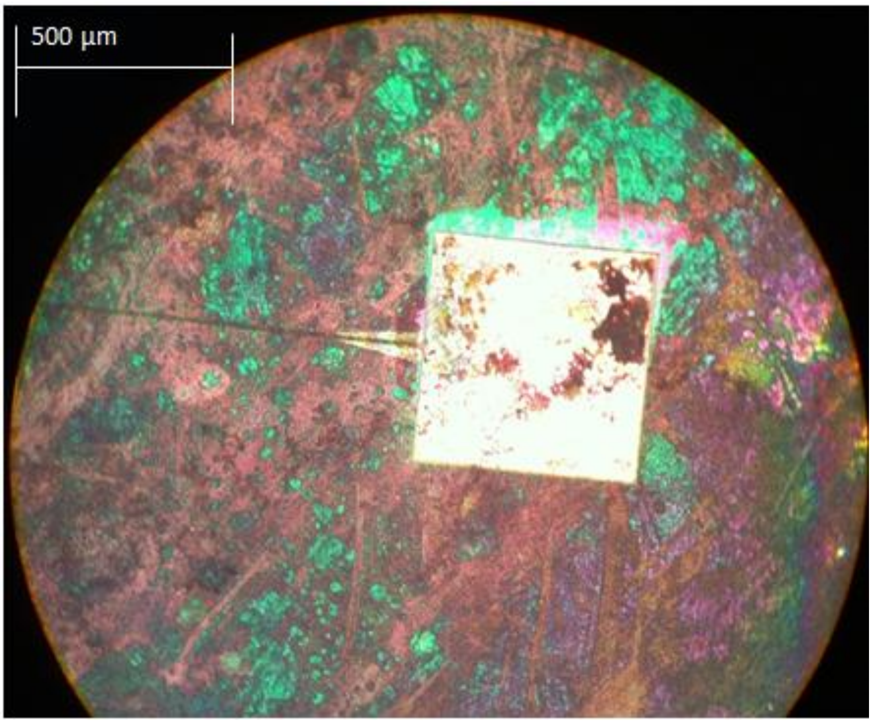

Figure 8-18: Tungsten microelectrode after prolonged times in high temperature.

This shows that the passivation layer, although mottled, still covers the device. The electrode is still well defined and even appears to have a relatively clean and shiny surface.

The "resistive line" response from microelectrodes occurred in the majority of attempted experiments. Another, seen in Figure 8-19 below, covered the potential window of silver detection after adding a capsule, rather than sweeping across the entire solvent window.

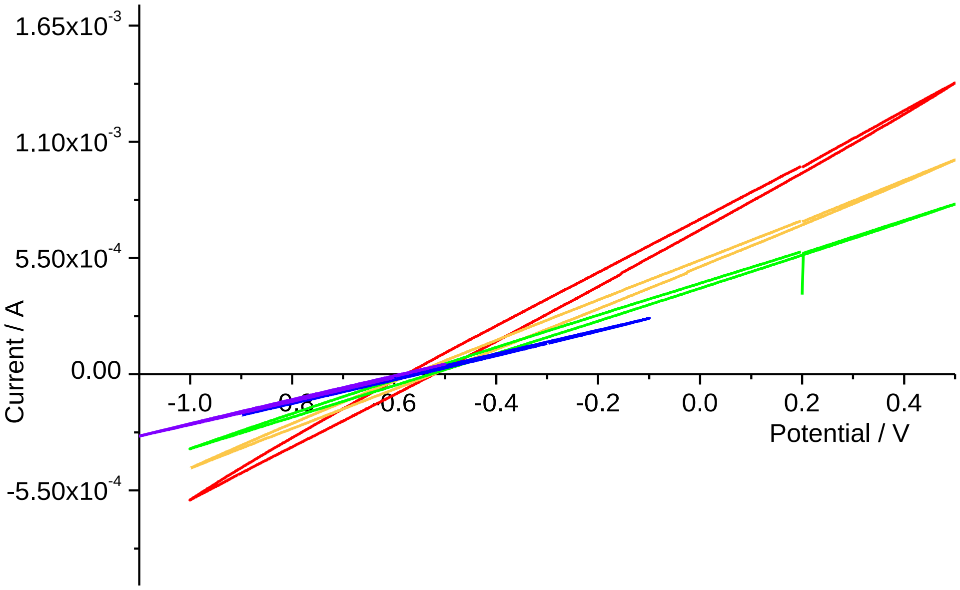

Figure 8-19: A cyclic voltammetry response from a microelectrode indicating high resistances with no silver detected.

The resistive line appeared to be decreasing in gradient over the course of several hours (red line through to violet). No characteristic silver plating or stripping peaks were observed, masked by the high resistances in the system. Figure 8-20 shows an image of microelectrode device that produced this response. Dark silver deposits can clearly be seen on the surface of the device, even though the current response did not reveal a reaction. The green colour is assumed to be the electrode, which has oxidised over time. Tungsten oxide formation will also have increased with the washing of the device in water to remove the chloride salt mixture. The surface of the passivation layer appears to have been attacked during the course of the experiment, but the electrode area is still well-defined. It is unknown as to why the passivation layer is not as colourful as observed in Figure 8-18.

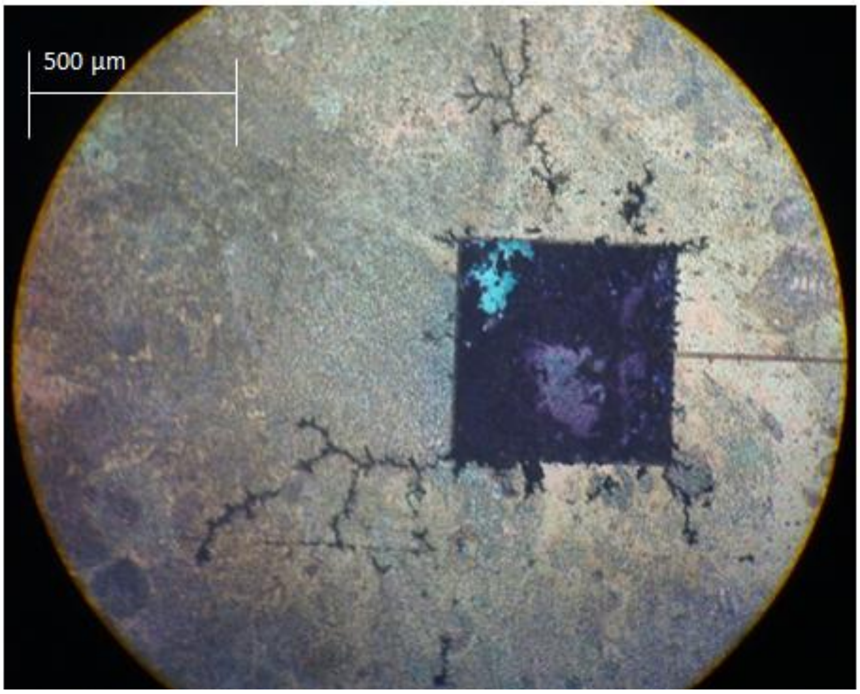

Figure 8-20: Tungsten microelectrode after attempts at silver deposition.

Through improvement of the connection to the microelectrode using the cement gum to seal the contact pad to the crocodile clip an improved response was observed which can be seen in Figure 8-21.

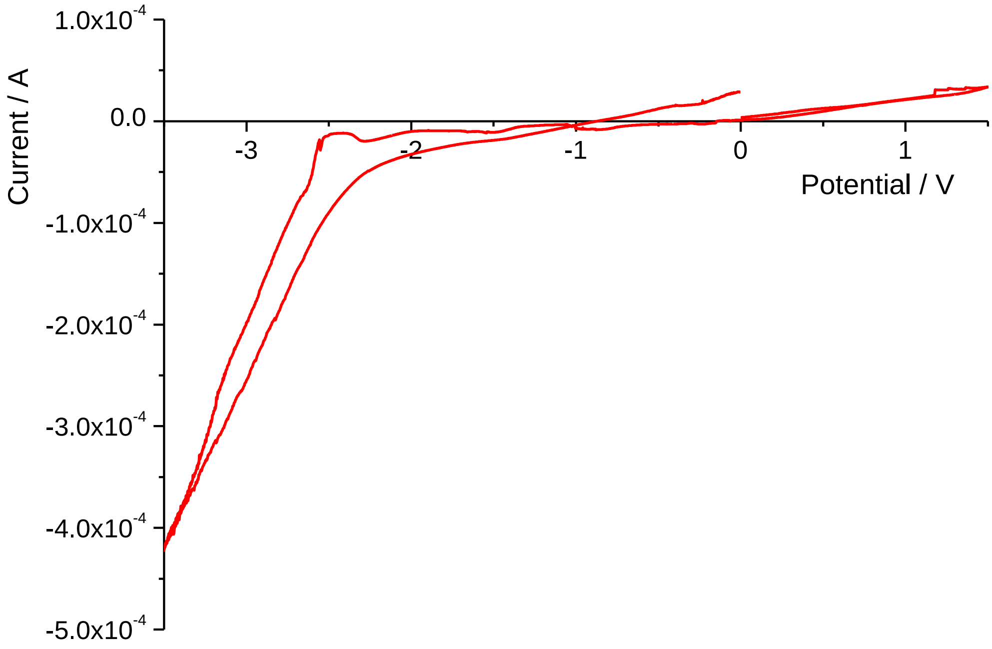

Figure 8-21: A cyclic voltammetry response from a microelectrode showing non-resistive responses.

Although the currents are much less, features have developed in the CV. Most notably is that of a lithium plating peak. In this case the potential was first swept forwards to 1.5 V before going to negative potentials, which indicates that the lithium plating peak starts after -2.5 V. As the potential is then swept more positive towards zero the current magnitude is greater and there is no stripping peak. Unfortunately, addition of silver chloride capsules to the melt did not produce any silver detection, demonstrating the issues with delivery system discussed (Section 7.4). In this case it was assumed the lack of response was due to the capsule not breaking on entry to the melt.

Lithium plating on a microelectrode has been reported in the literature. Carlin and Osteryoung saw a small reproducible stripping peak; however it was still not equal in size to the deposition peak. They attribute the discrepancy to the reaction of lithium with their Pyrex vessel.

Interestingly, they cycled through the reaction repeatedly before they could achieve a reproducible response. They attribute this to cleaning the tungsten, possibly removing an oxide layer. This would release oxides in to the melt, undoing the work of the salt drying process. This reinforces the importance of pre-treatment of electrodes and the need to develop a method suitable for tungsten electrodes.

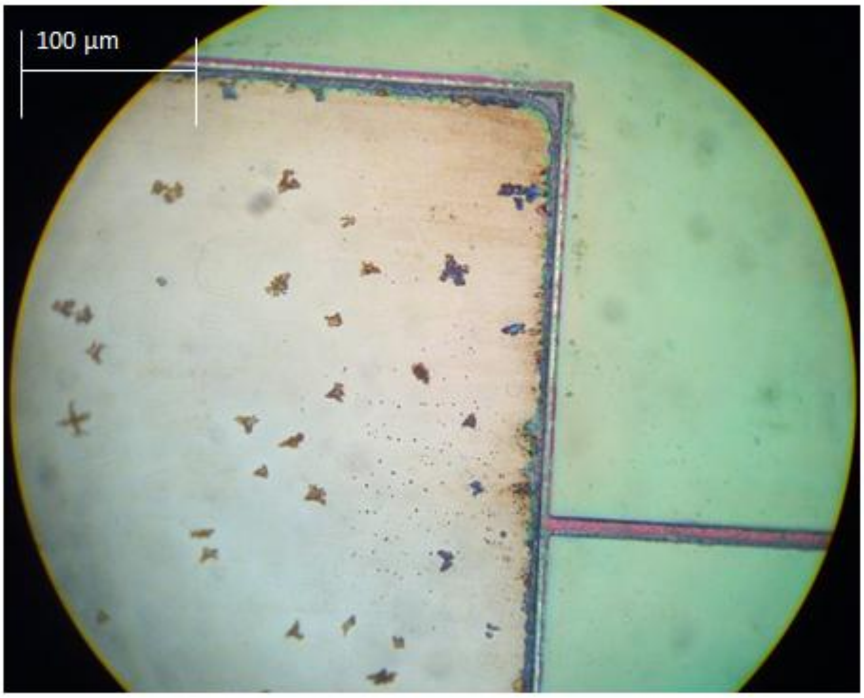

Figure 8-22: Tungsten microelectrode after lithium deposition.

Figure 8-22 shows an image of microelectrode device that produced these responses. It can again be seen that the electrode is well defined and relatively clean. This device showed electrochemical responses to the reactive materials, notably lithium, in the melt. However it did not detect the silver reaction. It is surprising then that the photo appears to show small deposits on the surface near the edges which could be silver as any lithium would have been washed off during deconstruction and clean-up of the experiment. The passivation layer is much more uniform in colour which suggests that it has been attacked less by this melt.

Using the 50 µm edge microelectrode a response was detected across the solvent window, as seen in Figure 8-23. This current response was very noisy and the signal was smoothed using the Origin software for clarity. The signal smoothing was performed using the Savitzky–Golay smoothing filter with 5 points of window and a polynomial order of 2. The microelectrode response showed large features in the apparently clean melt. The first scan shows two large reductions. The peak at -2.35 V could be a response from a contaminant, now visible due to the high sensitivity of the microelectrode. The peak at -3.00 V shows the reduction of lithium ions, though with no reverse peak. No silver reaction was detected. The red line, the first scan, shows the noise apparent when the oven is left on heating. It was turned off to prevent interference with the current response.

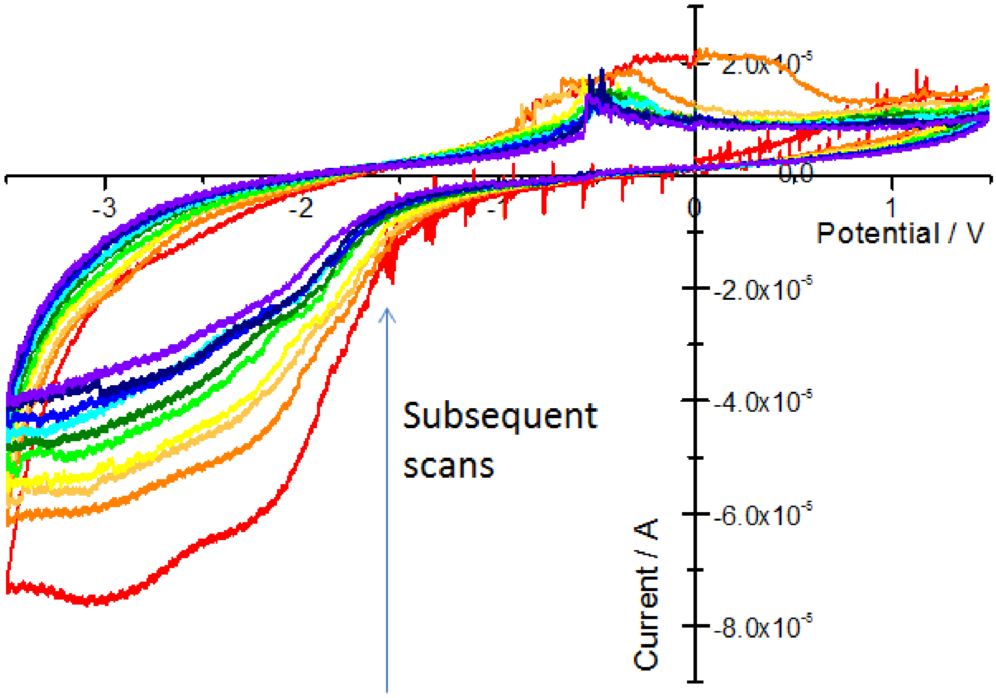

Figure 8-23: A non-resistive cyclic voltammetry response of a tungsten microelectrode.

Interestingly, subsequent scans show a decrease in current. The cause of this is unknown. Figure 8-24 shows images of the device after removal from the melt. It can be seen clearly that the track between the electrodes and the contact pad has become damaged. In addition, the microelectrode itself shows that little or no tungsten remains in the patterned area. This indicates that, in all likelihood, the titanium adhesion layer failed, causing the tungsten to come away from the device.

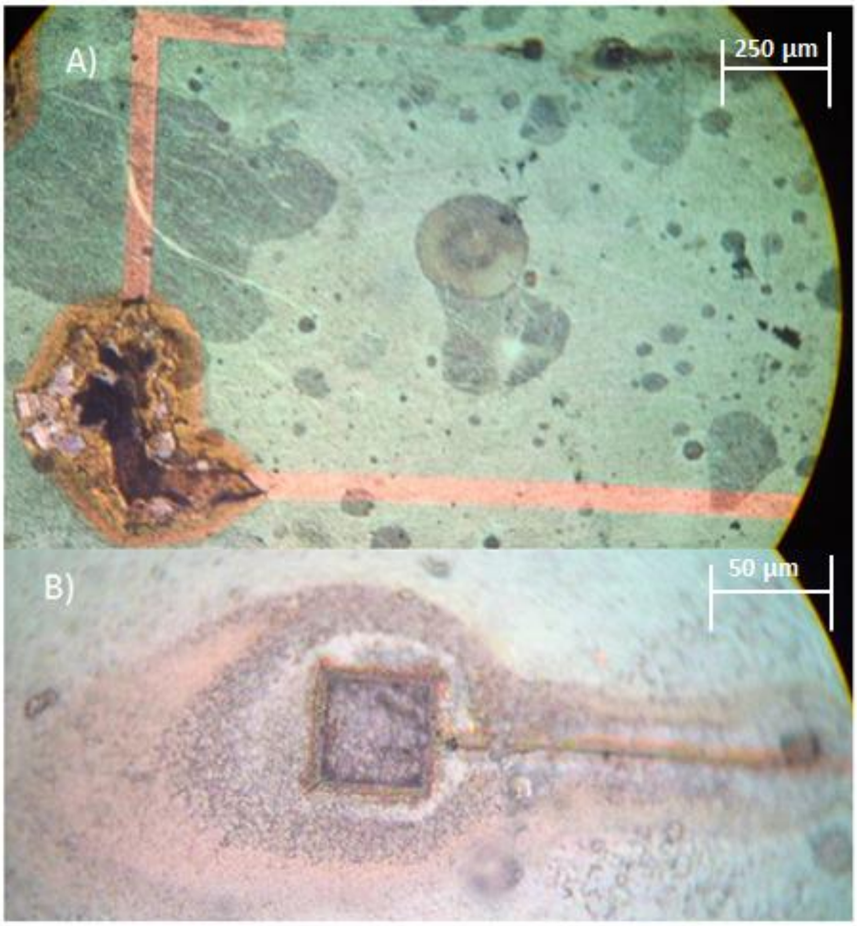

Figure 8-24: Tungsten microelectrode and device. A) The black squares at the top are the remains of the microelectrodes and the pink tungsten track runs to the contact pad, showing damage. B) The remains of the microelectrode on the left of A). There appears to be no tungsten remaining.

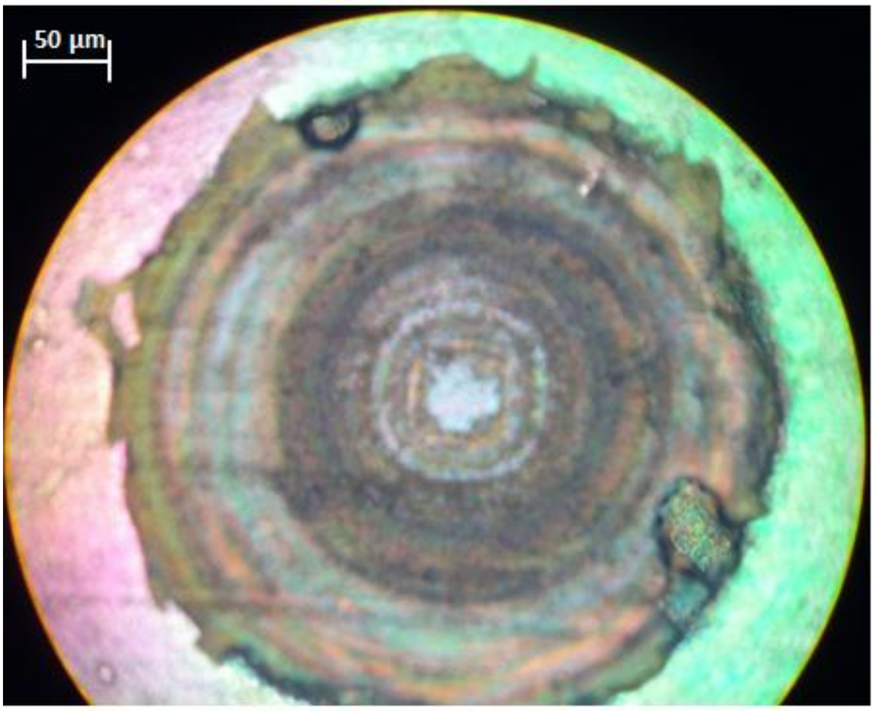

Figure 8-25: Platinum microelectrode showing severe degradation of the device.

Figure 8-25 is added as an aside in that, a single attempt was made to use a platinum microelectrode in the molten salt set-up. The electrode was akin to that used in the nitric acid studies seen in Chapter 6. This is the result of that experiment. Electrochemically only a resistive line was observed, of the same magnitudes and shapes as seen with the tungsten microelectrodes. However it can be seen that the platinum reacted in the melt and this reaction attacked the passivation layer. This image is included as it nicely shows the developing hemispherical diffusion from a square electrode. This does however demonstrate the importance of selecting appropriate materials for high temperature studies and that tungsten is a much more suitable electrode.

8.8 Conclusions

Molten salt media are of great interest in electrochemical studies. Nuclear material is separated in molten salts for future reprocessing in several countries around the world and the importance of understanding the systems involved cannot be underestimated. In-line monitoring of the system and being able to sense changes quickly and with great sensitivity requires the development of appropriate devices.

To that end, a high temperature system has been designed and built to analyse the electrochemical reactions in molten salt. The design and development of the system has been summarised here along with failed designs worthy of mention.

An electrochemical process for drying the molten lithium chloride-potassium chloride eutectic was developed that prevents a highly corrosive build-up of oxides. This allows the salt to be used in conjunction with microelectrode devices. Robust microelectrodes were designed and developed for the molten salt studies using tungsten as the electrode metal. Some preliminary studies using these electrodes are presented here and the lithium plating reaction was detected. There are no issues with the silicon nitride passivation layer and intact tungsten electrodes remained well defined. A delivery route for redox active material within the closed system, added after the salt is dried has proved difficult and silver deposition studies have had poor results.

Electrochemical analysis using the high temperature system will now continue within the research group and studies using lanthanide analogues for nuclear reactions and a variety of electrochemical sensors will be developed.

8.9 References

---

[1] S. V. Volkov. Chem. Soc. Rev., 1990,19, 21-28
DOI: 10.1039/CS9901900021

[2] Y. Sakamura, T. Hijikata, K. Kinoshita, T. Inoue, T.S. Storvick, C.L. Krueger, J.J. Roy, D.L. Grimmett, S.P. Fusselman, R.L. Gay. Journal of Alloys and Compounds. Volumes 271–273, 12 June 1998, Pages 592–596
http://dx.doi.org/10.1016/S0925-8388(98)00166-2

[3] B. H. Park, S. B. Park, S. M. Jeong, C.-S. Seo, S.-W. Park. Journal of Radioanalytical and Nuclear Chemistry December 2006, Volume 270, Issue 3, pp 575-583 **DOI:** 10.1007/s10967-006-0464-3

[4] P. Pint, S. N. Flengas. J. Electrochem. Soc. 1976 123(7): 1042-1047; **DOI:**10.1149/1.2132988

[5] Richard T. Carlin, Robert A. Osteryoung. Journal of the Electrochemical Society, 136 (5), 1989 p1249-1255
http://dx.doi.org/10.1149/1.2096900

[6] M.R. Bermejo et al. Journal of Electroanalytical Chemistry, 588, 2006 p253–266 http://dx.doi.org/10.1016/j.jelechem.2005.12.031

[7] O. Shirai, T. Iwai, Y. Suzuki, Y. Sakamura, H. Tanaka. Journal of Alloys and Compounds. Volumes 271–273, 12 June 1998, Pages 685–688
http://dx.doi.org/10.1016/S0925-8388(98)00187-X

[8] M. Mohamedi, J. Bouteillon, J.C. Poignet. Electrochimica Acta, Volume 41, Issue 9, June 1996, Pages 1495-1504
http://dx.doi.org/10.1016/0013-4686(95)00401-7

---

[9] M.R. Bermejo, E. Barrado, A.M. Martínez, Y. Castrillejo. Journal of Electroanalytical Chemistry, Volume 617, Issue 1, 1 June 2008, Pages 85-100. http://dx.doi.org/10.1016/j.jelechem.2008.01.017

[10] H.C. Gaur, H.L. Jindal. Curr. Sci. 37 (2), 1968 p49-50
http://www.ias.ac.in/j_archive/currsci/37/2/49-50/viewpage.html

[11] K.K. Kasem, S. Jones. Platinum Metals Review. 52 (2), 2008 p100-106 **DOI:** 10.1595/147106708X297855

[12] F.A. Cotton, G. Wilkinson, C. A. Murillo, M. Bochmann. Advanced Inorganic Chemistry. 6th Edition. Section 17-G-5.

[13] G. J. Hills, D. J. Schiffrin, J. Thompson. J. Electrochem. Soc. 1973 120(2): 157-164; **DOI:**10.1149/1.2403413

[14] T. B. Reddy. J. Electrochem. Soc. 1966 113(2): 117-123; **DOI:**10.1149/1.2423882

[15] W. K. Behl. J. Electrochem. Soc. 1973 120(12): 1692-1694; **DOI:**10.1149/1.2403332

[16] W.J. Burkhard , J.D. Corbett J. Am. Chem. Soc., 1957, 79 (24), pp 6361–6363 **DOI:** 10.1021/ja01581a005

[17] H. A. Laitinen, W. S. Ferguson, R. A. Osteryoung. J. Electrochem. Soc. 1957 104(8): 516-520; **DOI:**10.1149/1.2428639

Chapter 9: Conclusions

Within the scope of this body of research single square microelectrodes and arrays have been fabricated and characterised using a variety of techniques. The electrodes are studied in pre-treatment, characterised using standard redox couples and then used to sense changes in more complex systems akin to industrial processes. These electrodes were designed for use in extreme conditions, namely strong acidic environments and molten salts, similar to those used in nuclear fuel reprocessing.

Microelectrodes were fabricated by photolithography to produce robust electrodes of square shape. Devices fabricated by this method are reproducible due to the high control of the electrode size and shape in the method. This gives the potential for reproducible measurements and greater reliability than alternative fabrication techniques. The benefit of square shaped microelectrode over alternative 2 dimensional shapes due to enhanced diffusion at corners has been documented previously and so square microelectrodes were the focus of these studies.

In Chapter 4 the pre-treatment of microelectrode devices before their use in analysis of systems was discussed. Little previous work has been done to fully understand the importance of this step and so the treatment of the electrodes was studied. The pre-treatment of microelectrodes is a valuable, often ignored, area of development that can be critical to the performance of a device. The sensitivity and rapid response of an electrode can be greatly improved by preparing the surface appropriately.

Before use in aqueous systems “activation” of the platinum electrode surface was performed electrochemically. This was performed by cycling potentials between the limits of the solvent window in aqueous solutions.

By extending the potentials to these limits the reaction at the electrode surface was the production of hydrogen and oxygen gases. The bubbles of gases allow any dust or particulate matter on the surface to be lifted off. The optimal cleaning regime for platinum microelectrodes was found to be an aqueous solution of sulfuric acid, monitored by the repeated measurements of a platinum oxide formation and removal in the cyclic voltammetry.

In solutions with a redox couple present for study the cleanliness of an electrode could be recognised as insufficient cleaning resulted in lower current responses during voltammetry. In electrical impedance spectroscopy (EIS) uncleanliness was observed by the magnitudes of the resistance and reactance, which affected the Nyquist plot. This demonstrates the importance of adequate pre-treatment and the variability that insufficient cleaning can produce in electrode response.

The ease of cleanliness is affected greatly by the size of the microelectrode in question. Smaller sizes of electrodes take more repeated cycles of potential sweeps, effectively meaning they are harder to clean. This is likely due to difficulties in removing particulate matter of sizes similar to that of the electrodes. With the higher current densities found at the corners of square microelectrodes smaller electrodes show more efficient current response due to a higher ratio of corner and edge to area. It is therefore very important to ensure good cleaning in the pre-treatment step of the device before use.

In Chapter 5 single platinum squares of 10, 20, 30, 50 and 100 μm lengths were studied using the reversible potassium ferricyanide – ferrocyanide couple using cyclic voltammetry, potential step voltammetry and EIS. Characterisation of the squares showed fabrication issues with individual flaws in the silicon nitride passivation layers. The flaws increased the effective electrode area, producing higher current magnitudes than expected from theory.

These flaws in the passivation layer introduced variability in the response. In addition to the difficulties with unknown electrode areas exposed, the cleanliness of these areas was also difficult to quantify. Fabrication of robust microelectrodes therefore requires selection of durable materials and care in handling is very important to achieving reproducible and reliable measurements with these devices. Of critical importance is development of a robust insulator layer.

In Chapter 6 the characterised platinum microelectrode devices were used to study highly concentrated nitric acid solutions. This was used as a model system of the PUREX process where fissile nuclides in used nuclear fuel are separated from fission products for future recycling. The microelectrode devices showed minimal degradation from the acidic media and were sensitive and responsive to small concentrations of silver ions with a strong potential for detection of other metals. These microelectrodes were able to detect changes in concentrations of nitrous acid, a product of nitric acid decay, and nitric acid making it potentially a valuable sensing device within the recycling of nuclear fuel, for measuring the stability of the aqueous phase during the liquid-liquid extraction.

Corrosion of the microelectrode was an import factor to consider in developing a device for extreme environments. Observation of the devices after use in the nitric acid solutions determined that there was a dark build up on platinum metal electrodes and where additional metal had been revealed at pre-existing flaws in the passivation layer. However, there appeared to be no degradation of the silicon nitride across the device surface and electrodes remained well defined square shapes, reinforcing the importance of an inert and chemically resistant passivation layer for extreme conditions.

In Chapter 7 arrays of microelectrodes were characterised. With the low currents associated with single square microelectrodes the area of microelectrode arrays was the natural development for device production. The significant increase in number of electroactive areas on the device minimises the effect of any passivation flaws. Arrays allow for higher currents but, with sufficient spacing, still have individual diffusion profiles, providing all the benefits of the single electrodes. Closer spacing electrodes on arrays lower current density as the diffusion layers overlap, leading to changing responses from the array. The further the spacing between electrodes the longer it takes for the diffusion field to overlap.

Arrays of electrodes with different lengths and spacing were fully and systematically characterised. From the voltammetry it was apparent that the diffusion profile at an array changed the current response noticeably. The diffusion response at a fixed scan rate was dependent on both the electrode size, as had been seen previously and the spacing between electrodes. This indicated that arrays could be fabricated in the future for specific applications, maximising the array efficiency of space and optimising the current magnitude.

Using the electrochemical techniques of EIS and potential step voltammetry the diffusion across an array was studied and the development of linear and hemispherical diffusion fields was observed. The hemispherical diffusion was found to be independent of the spacing using EIS and so from this the optimal limiting current of an array could be determined. This will allow development of the microelectrode array devices for future work.

In Chapter 8 microelectrodes were fabricated and characterised for use in corrosive, high temperature environments associated with the pyroprocessing of nuclear fuel. Molten salts used in high temperature extraction of nuclear fuel are a corrosive and difficult media to work with. Developing sensitive analytical tools for such conditions is challenging and selection of appropriate materials is critical.

A high temperature set-up was successfully designed and built to characterise tungsten microelectrodes in molten salts using a lithium chloride potassium chloride eutectic salt. A process for cleaning the molten salt electrochemically has been developed to minimise corrosive oxygen containing species that could attack the apparatus and microelectrode device. The microelectrodes were used to detect small concentrations of metal ions with lithium deposition visible in cyclic voltammetry. Observation of the devices after use in the molten salt determined that there appeared to be no degradation of the silicon nitride across the device surface and electrodes remained well defined square shapes, indicating the material resistances under the extreme conditions.

Microelectrodes have successfully been shown to be responsive in molten salt media and can now be used to probe the systems used in nuclear fuel conditioning during pyroprocessing. Having established methods for analysis, the way is now clear to develop sensor systems for specific species and deploy them for electroanalysis and on-line monitoring. This is the subject of further work in the group.